EINDHOVEN UNIVERSITY OF TECHNOLOGY

&

UTRECHT UNIVERSITY

Master Thesis Project

Optimising for the Delayed Onset of Trapped-Electron Modes in Stellarator Geometry

---

By

Paul Mulholland

Under the Supervision of

Dr. Josefine H.E. Proll

and

Prof. dr. Rembert A. Duine

Daily Supervisor:	TU/e	Josefine Proll
Primary Supervisor:	UU	Rembert Duine
Secondary Supervisor:	UU	Henk Stoof

Abstract

Nuclear fusion is a promising candidate for the generation of clean energy in future societies. This is an exciting research area which shares an intersection with other fields of academia, including but not limited to engineering, computer science and environmental science. The method to achieving fusion of primary interest to us is known as magnetic confinement fusion (MCF). In particular, we will focus on a certain branch of toroidal MCF devices, known as stellarators. These are lesser known but quickly catching up to the more ubiquitous tokamaks. A problem still facing all MCF devices is plasma heat loss due to particle and energy transport from the hot core to the cold edge. This reduces confinement, which inhibits our plasma reaching the necessary fusion-temperatures. A primary cause of transport is turbulent behaviour due to plasma micro-instabilities. The instability mode of interest to this project is the trapped-electron mode (TEM). This mode has a critical threshold for when it first becomes manifest, and it subsequently becomes problematic. For the TEM, this threshold is known as the critical density gradient. The nature and behaviour of this instability mode is heavily dependent on the geometry in which it exists, and thus, it is desirable to create an optimal geometry that extends this threshold. This would in turn delay the onset of unwanted TEM-driven turbulence. Technically, gyrokinetic simulations could be run for a myriad of different geometries which vary in configuration space. This would involve starting with a simple tokamak geometry and gently deforming it until the optimum configuration was found. However, this approach is easier said than done, and would be far too costly in terms of time and money to be realistically feasible. Thus, we turn to the theoretical framework which describes these micro-instabilities, and seek to find an analytical expression predicting their behaviour. This expression will be dependent on the geometrical characteristics of the stellarator configuration. In particular, we require a geometry-dependent expression for the critical density gradient of the mode - which we wish to maximise. This is the end goal of the project. Beyond this work, our results would be utilised in a stellarator optimisation code (STELLOPT) to see if an optimal geometry can be found in configuration space which maximises the critical density gradient. Further investigation would then be required to see if turbulent transport is indeed reduced by this newly TEM-optimised geometry.

Contents

Part I

Introduction, Background, and Mathematical Framework

Chapter 1

Introduction

Nuclear fusion has the potential to revolutionise energy production in our societies worldwide. It is projected to be a clean, safe and high-yield form of energy generation, if it is successfully put into operation. The method of operation we will focus on here is called magnetic confinement fusion. Specifically, the magnetic confinement fusion device of interest to us is the stellarator, which is the modest toroidal sibling of the better-known tokamak. All toroidal magnetic confinement fusion devices aim to confine the fusion plasma within a magnetic cage, which follows a (twisted) toroidal geometry. Sustaining this confinement is the main aim of this field. More specifically, we are trying to maximise the confinement time of the plasma within this cage. Longer confinement times should then improve the probability of enabling a self-sustaining fusion reaction in our devices.

A major challenge to this effort is unwanted energy and particle transport from the hot and dense plasma core to the cold thin edge. This leads to unwanted mixing and the subsequent reduction to the core plasma temperature. A major cause of such transport is known as turbulent transport. The turbulent behaviour that leads to this transport is driven by micro-instabilities in the plasma. These micro-instabilities take place at orders of magnitude comparable to the particle gyro-radius (Larmor radius). They feed off of the free energy supplied by the inevitable temperature and density gradients in the plasma. The instability mode of interest to this project is the trapped-electron mode (TEM), which exists and grows due to the density gradient. This mode has a particular starting point at a certain critical density gradient, which is determined by the geometry under consideration. Beyond this point, the mode grows increasingly unstable, leading to turbulence and eventually to energy transport.

This project aims to delay the onset of the TEM by increasing the value of this critical density gradient. The strategy for doing this is to develop an analytical proxy for the critical density gradient, which depends on the wavenumber of the mode, the mode frequency, and the geometrical characteristics of the toroidal configuration being considered. In the end, we would like to utilise

this proxy in an optimisation code, so as to maximise the value of this critical density gradient by manipulating the geometry into some optimal configuration.

A necessary step to getting to this end point is to find a suitable analytical expression for the mode frequency, which depends on the structure of the instability mode. Thus, we implement a variational principle technique to obtain a proxy for this mode frequency, with the trial function input being the mode structure. In order to be able to work independently of costly simulation data, we predict the shape of this mode structure based on the geometry the mode exists in, and use this prediction as our trial function input for the variational principle. This variational principle then yields a proxy for the mode frequency, which we then insert into our proxy for the critical density gradient. This then means that our only remaining inputs are the wavenumber of the mode and the geometric quantities of the configuration at hand - both of which are known to us without any need for costly simulations.

With this ultimate goal in mind, we now provide an overview of what this project report contains. The contents of this thesis have been compartmentalised into three distinct parts. This structure will be discussed in the next section.

1.1 Thesis Structure

In this section, we provide a guide to the overall structure of this thesis report. The report consists of three main parts.

Part 1 gives a very basic introduction and some background to the field of nuclear fusion, including the physical process itself and how it may be put into practice in future. We also discuss the structure of fusion plasma, and the nature of particle motion in such a system. These are important concepts to grasp in order to fully appreciate and understand the later work of the project. This is followed by the introduction of the essential mathematical framework that the main body of this project will be built upon. This includes the use of gyrokinetic theory and the derivation of the gyrokinetic equation. The results of this framework form the building blocks for the original work carried out later in Part 2.

In Part 2, we provide the full methodology of this project, including all of the relevant analytical derivations needed to obtain the original results of this work. The methodology consists of two main derivations. Both derivations are carried out to obtain useful proxies for certain key quantities possessed by the instability mode we are interested in. The first of these proxies, known as the mode frequency proxy, is a necessary ingredient for evaluating the second proxy, known as the critical-density-gradient proxy.

Finally, Part 3 of this project comprises the full set of results for the various different components of the project. Specifically, we provide the numerical results which are based upon the analytical proxies derived in Part 2. We end each set of results with a discussion of their interpretation, and means to improvement. Following this, we come to the final conclusion of this report, accompanied by a brief outlook of what the next steps should be beyond this thesis project.

Additional analytical derivations which were carried out, but not utilised or needed in the main body of work, have been relegated to the Appendices. All work contained here is purely surplus material, with the exception of section B.2, which supports the results of section 5.2.

1.2 Research Question

The research question that motivates this project can be broken into two consecutive parts:

1. Is it possible to accurately predict the critical density gradient of trapped-electron modes (TEMs) by analytical means for stellarators, using only geometric information?

2. If yes, can this analytical prediction be utilised in geometrical optimisation to then delay the onset of turbulent transport caused by the TEM instability?

Only the first of these two questions will be addressed directly in this project, as answering the second requires the use of stellarator optimisation software (STELLOPT), and this goes beyond the scope of this work. However, this latter question has been stated here to give some broader context in as to how the results of this project could be further developed and investigated, in order to determine the overall efficacy of this work.

Chapter 2

Background

In this chapter, we will discuss the motivations, mechanisms, and challenges of nuclear fusion, as they stand today. The sections covered in this chapter are as follows. We start by briefly describing the motivation behind researching nuclear fusion in the first place. This motivation is followed by a look at the physics of fusion, and in particular, magnetic confinement fusion, which is the method of fusion we are concerned with in this project. We will conclude this chapter with a description of one of the main obstacles encountered in magnetic confinement fusion, that being energy loss due to transport in the plasma. To put this into context, the overall aim of this project is to find a means to reducing the levels of transport in the plasma, by investigating one of the mechanisms that cause it. It is the goal of this chapter to provide some background knowledge of nuclear fusion as a whole, and to help contextualise the work of this project in the wider framework of fusion research.

2.1 Why fusion?

In this section, we will briefly discuss the fundamental motivation behind researching nuclear fusion as a potential means to providing sustainable and clean energy.

Fusion is projected to be an invaluable source of energy production, once successfully put into operation. There are numerous significant incentives for researching this field of physics and technology, some of which will be mentioned here briefly. Four main factors that should be considered are the energy yield, fuel reserves, environmental impact, and safety.

When considering the energy generated from a nuclear reaction (fission or fusion) compared to a fossil fuel chemical reaction, the former produces an order of one million times more energy per elementary particle than the latter [1]. Regarding fuel reserves, and taking into account

our current rate of electricity consumption, nuclear fusion would be able to sustain our energy demands on the earth for over a billion years [1]. When it comes to environmental impact, fusion reactions do not produce any carbon dioxide or other greenhouse gases, and no harmful chemicals are emitted into the atmosphere. The main product of a fusion reaction is helium gas, which is safe and chemically inactive. The fusion process is also very safe. A meltdown, as can occur in a fission power plant, is physically impossible in a fusion device. At any given time, a fusion reactor contains only a very small amount of fuel, and is gradually fed to sustain the reaction. And so, the possibility of a runaway chain-reaction is non-existent [1].

2.2 Physics of Fusion & Magnetic Confinement Fusion

In this section, we first discuss the physical mechanism of fusion in general, as can be found in nature. Following this, we adapt the process to how it can be made achievable on earth as a practical form of energy generation. The method to be focused on here is magnetic confinement fusion.

Thermonuclear fusion is a naturally occurring process, which takes place in environments of extremely high temperature and pressure, such as at the core of stars like our sun. In simple terms, light nuclei - such as hydrogen - fuse together due to their very close proximity, which is a result of these extreme conditions. To do this, they must overcome their intrinsic repulsive response due to the Coulomb force. The nuclei have to collide with a large kinetic energy, which must in principle exceed the maximum of the Coulomb barrier, that being at a value of 415 keV [2]. Fortunately, due to the quantum tunneling effect, the energy required for a collision to take place is substantially reduced. This means that there is a finite probability of penetrating the Coulomb wall, even if a particle's energy is actually smaller than the barrier energy. With this in mind, necessary collisions can occur, and due to the short-range strong nuclear force, the original hydrogen nuclei combine to form the larger nuclei of helium. When such a fusion reaction takes place, a large amount of energy is released as a result. The released energy corresponds to the difference between the total masses of reactants, and the reaction products. This follows in accordance with Einstein's famous relation $E = mc^2$, describing the conversion of mass to energy. The energy released is in the form of kinetic energy, which is distributed between the reaction products ($\sim$ 80% goes to the neutron due to conservation of momentum). The newly formed nuclei can then also fuse to form even larger nuclei, and this process continues along the periodic table of elements. At the centre of stars, the end point of this fusion-chain tends to be iron - our most stable element in the periodic table. For elements lighter than iron, these fusion reactions often involve an energy release, since the binding energy of their products is larger than that of the initial nuclei, as can be seen in Fig. 2.1. On the other hand, nuclear fission works by splitting heavy atoms into lighter ones, which also leads to a release in energy. This can be easily seen from the peaked shape of the binding energy curve.

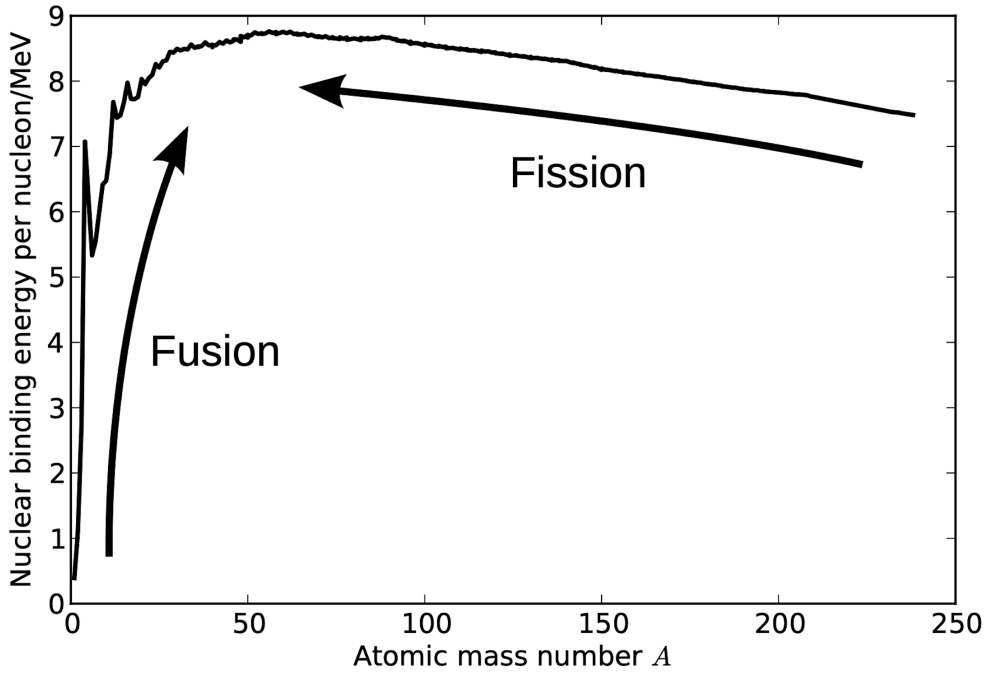

Figure 2.1: *Graph depicting energy obtained by fusion and by fission due to different nuclear binding energies. Source: [3]*

The form of fusion we will focus on takes a slightly altered process than how it occurs in stars. As already mentioned, the fusion reactions in the sun are occurring under conditions of extremely high temperature, density and gravitational force, and are fuelled by basic hydrogen - or protium. On earth, however, this extremely large system with enormous gravitational force and plasma pressure is absent. This means that alterations have to be made to the standard fusion reaction. And so, the reaction with the highest cross section under the achievable circumstances on earth is as follows [1]:

$$D_1^2 + T_1^3 \rightarrow He_2^4 + n_0^1 + 17.59Mev \tag{2.1}$$

This D–T reaction involves the fusion of a deuterium nucleus with a tritium nucleus. It is the easiest of all the fusion reactions to initiate (although its initiation is still much more difficult than that of U^{235} fission reactions) [1]. For ground-based fusion to work, we will need this higher rate of reaction to take place to meet our needs of a continuous, sustained form of energy production.

Although the above D–T reaction gives the highest chances of a fusion reaction occurring, the average temperature of the plasma is still required to be on the order of 100 million Kelvin [1]. This is gargantuan when one considers that the temperature of the core of our sun is approximately 15 million Kelvin. This is obviously far too high a temperature for any containment vessel to withstand. In addition, we want our reactor to work in a self-sustaining manner, so as to eventually have a greater output energy than input energy. Achieving this can be aided in

the following way. Once the plasma has been initially heated to the required thermonuclear conditions, helium is being produced, which possesses a certain amount of kinetic energy. If the helium is kept within the plasma, as desired, then this energy can be distributed to the rest of the plasma particles through collisions. These collisions cause extra heating of the plasma from within, without external energy input. Thus, when sufficient plasma confinement conditions are met, it is possible to reach a point where the temperature of the plasma is maintained due to this internal helium-heating, despite some energy losses [4].

The confinement conditions we need to consider depend on the density of the plasma (n), and the length of time that the plasma particles can be confined for, also known as the energy confinement time (τ_E). To understand exactly what conditions are required, we will introduce an extension of the Lawson criterion [4]:

$$n\tau_E T > 3 \times 10^{21} \text{keV}\cdot\text{s}\cdot\text{m}^{-3}$$

This is a modification of the original criterion given by Lawson in [5]. This above expression tells us that when the triple product of our plasma density, confinement time and temperature is above a certain critical threshold, then the energy output is equal to energy losses for the required plasma temperature of $\sim$100MK. This defines the minimum bound for a self-sustaining fusion setup. For a fixed required temperature, this minimum threshold can be achieved by having low density and high confinement times, or vice versa. The former strategy is used in magnetic confinement fusion, whereas the latter is applied in inertial confinement fusion [6]. This leads us to our discussion of magnetic confinement fusion, which aims to maximise confinement times in order to achieve the Lawson criterion. A limiting factor to long confinement times in a fusion reactor is the presence of transport. The details of this phenomenon will be described in the following section.

As the name would suggest, magnetic confinement fusion is a method of thermonuclear fusion whereby a plasma is confined and controlled by a shaped magnetic field. This method allows for control of the plasma's motion without any direct contact between the plasma itself and the containment vessel walls, which is necessary due to the extremely high temperature of the plasma. To confine the plasma, two directions of confinement must be considered. This consideration is what determines the general geometry of our magnetic confinement fusion devices, i.e., their toroidal shape. When using a magnetic field to control the motion of a plasma, it must be confined both perpendicular and parallel to that magnetic field. Fortunately, the former is mostly guaranteed due to the Lorentz force. To see this, let's consider a single charged particle entering a magnetic field $\mathbf{B}$, moving with some velocity $\mathbf{v}$. Assuming the particle's velocity has components both parallel ($v_\parallel$) and perpendicular ($v_\perp$) to the magnetic field, then the particle will move along a magnetic field line with a speed equal to $v_\parallel$, and it will orbit that field line due to the Lorentz force:

$$F_L = q\mathbf{v} \times \mathbf{B} = qv_\perp B$$

The charged particle then follows a helical path due to this combination of $v_{||}$ and the Lorentz force. The particle is confined to the field line within a distance of its orbiting radius, known as the Larmor radius ρ. This can be clearly seen in Fig. 2.2.

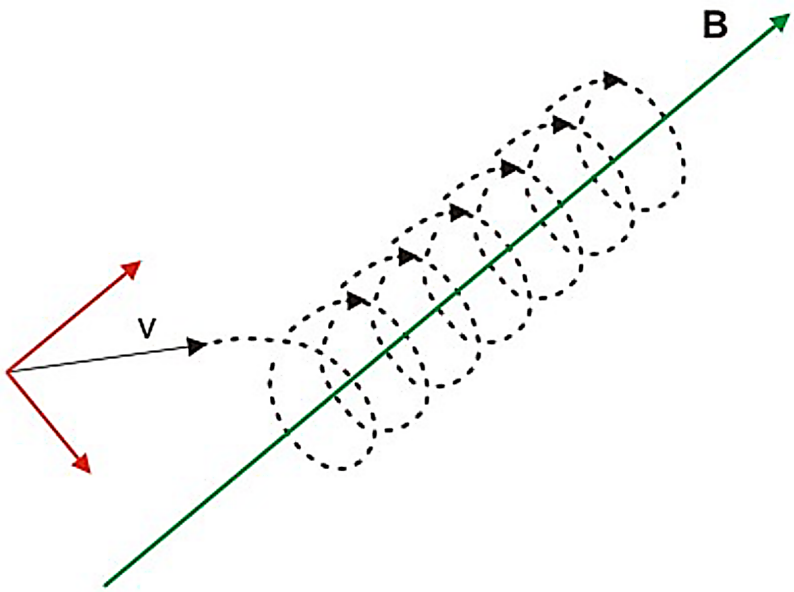

Figure 2.2: *Perpendicular confinement of a charged particle to a field line. Source: saburchill.com*

For parallel confinement, we need to ensure that the field lines do not end abruptly by meeting the walls of the containment vessel. Thus, roughly speaking, the field lines are bent around such that they form a ring. This enables the plasma particles to follow the field lines indefinitely, so long as they remain in the magnetic field region. This requirement leads us to designing toroidally-shaped devices (see Fig. 2.3). Magnetic confinement fusion is the method used for both the tokamak and stellarator designs of fusion reactor - both of which will be introduced in a later section. The ultimate goal of magnetic confinement fusion is to maintain the plasma at a sufficiently high temperature and density to enable particle collisions - and subsequent fusion reactions - to occur. Thus, it is vital to prevent the particles in the hot plasma core from drifting outward continuously in the radial direction, as this would lead to unwanted particle loss and heat loss. Such losses would reduce the density and temperature of the plasma core, leading to a lower probability of fusion reactions occurring. The level to which the fusion device can minimise these losses helps to determine the allowed confinement time for the plasma, which we wish to maximise. The loss of energy or particles from the plasma core is described by different transport phenomena. This brings us to the topic of the next section.

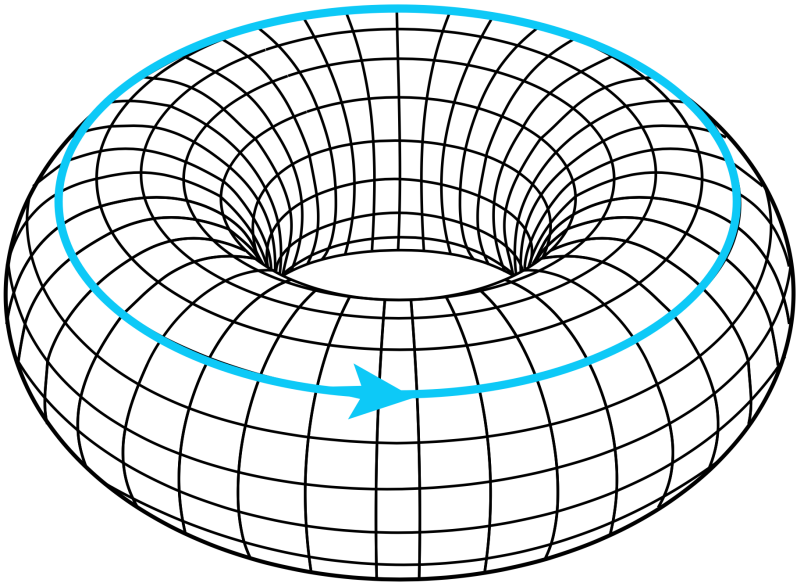

Figure 2.3: *Parallel confinement ensured by toroidal shape. Source: wikipedia.org*

2.3 Transport

In this section, we will give a very brief description of two important forms of transport in magnetic confinement fusion. The first of these is neoclassical transport, which will not be discussed further in this report. The second is known as turbulent transport, which is of primary interest to this project.

Transport is the term given to energy or particle losses in a fusion plasma. The two types of transport to be briefly discussed here are neoclassical transport, and turbulent transport. The former has been optimised for in contemporary fusion devices, lowering its negative effects to a tolerable level [1]. Thus, with neoclassical effects rendered relatively low, turbulence has become the main limiting factor to increasing confinement times. It is for this reason that turbulence is the primary focus of transport optimisation today.

Neoclassical transport theory combines the model of classical diffusion with effects of the toroidal geometry. Classical diffusion describes how particles orbiting adjacent magnetic field lines can collide and scatter, leading to a random walk process, and possibly to a loss of particles to regions outside of the magnetic field. These Coulomb collisions can occur in a simple cylindrical geometry. However, in our toroidal fusion devices, we have to account for extra effects that alter this classical process. These effects take the form of particle drifts, which are due to the curvature of the device, and also, due to an inhomogeneity of the magnetic field [1]. The field inhomogeneity can occur due to the magnetic coil arrangement. For instance, the coils at the centre of the torus are closer together than on the outer side of the device, which leads to a gradient in the magnetic field (∇B)

pointing toward the central toroidal axis. The radial drifts due to curvature and ∇B lead to an increase in the step-size after a Coulomb collision. This increases the overall level of transport when compared to classical diffusion alone.

Turbulent transport is very different in nature to neoclassical transport. Turbulence is caused by micro-instabilities in the plasma, which are induced by a density or temperature perturbation to the plasma profile. These perturbations can be caused by ambient vibrations in or near the device, and so they must be expected. The micro-instabilities can then cause turbulent eddies to form, which can transport heat from the hot core of the plasma out to the cooler edge, reducing our levels of confinement. The two main mechanisms of instability are the ion-temperature-gradient mode (ITGM) and the trapped-electron mode (TEM). Both of these modes will be discussed in detail later in this report. Several approaches for potential optimisation of these turbulent modes will also be described.

Chapter 3

Fusion in Practice

In this chapter, we will take a look beyond the fundamental physics of fusion, and discuss how this process is attempted in practice. The sections covered in this chapter are as follows. We first discuss the main magnetic confinement fusion devices relevant to this project, those being the toroidally shaped designs known as the tokamak and the stellarator. This is followed by a discussion of some relevant concepts for understanding the plasma structure and particle motion within the plasma. With this knowledge of the fusion plasma at hand, we are better able to understand the challenges occurring within it. This takes us to discussing the problem of turbulence, and the negative impacts it has on our efforts to confine the plasma. We follow this with a more detailed explanation of the different mechanisms underlying this turbulent behaviour, which in turn leads to turbulent transport. We conclude this chapter with an overview of how this unwanted turbulence could potentially be optimised for, which is of primary interest to us in this project.

3.1 Toroidal Magnetic Confinement Fusion

In this section, we describe the nature of toroidal magnetic confinement fusion, and the two different types of devices that aim to utilise this method of nuclear fusion. These devices are known as the tokamak and the stellarator, and both are of interest to the main body of work in this project.

In a toroidal magnetic confinement fusion device, a balancing of forces must be maintained to ensure magneto-hydrodynamic (MHD) equilibrium. The details of MHD is not within the scope of this project, but we will mention the importance of establishing a stable plasma equilibrium, and the method to achieving this. We will then see how this requirement significantly influences the design of our fusion devices in different ways. To produce this desired equilibrium, there are

two different types of forces to be considered. Firstly, there are radial expansion forces, which naturally occur due to the tendency of hot gases (and plasma) to expand [1]. These radial forces can be balanced sufficiently by the toroidal and poloidal magnetic fields of the reactor. Here, the toroidal and poloidal directions refer to going the long and short way around the torus, respectively (see Fig. 3.1). Secondly, there are forces arising exclusively due to the toroidal

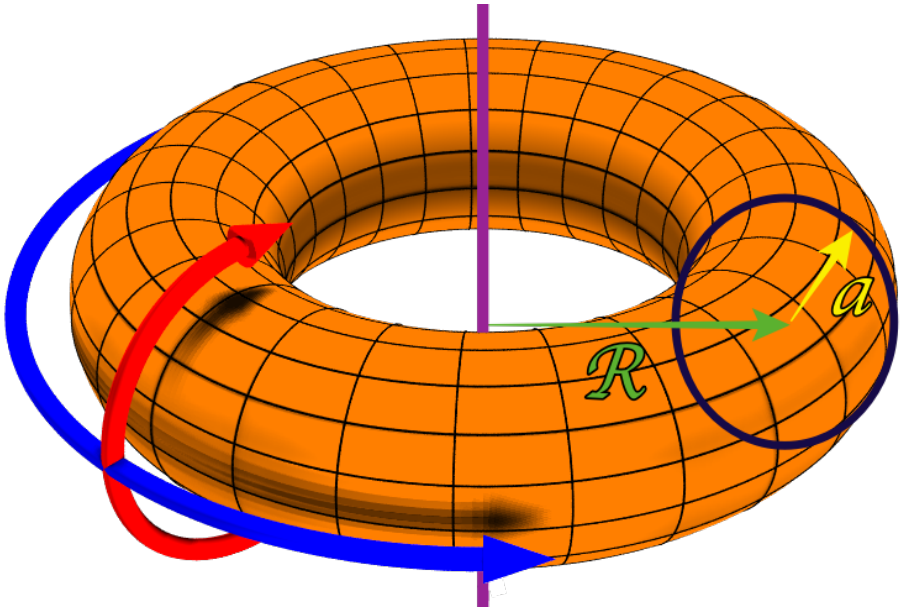

Figure 3.1: *Toroidal direction in blue and poloidal direction in red, with major radius R and minor radius a. Source: wikipedia.org*

geometry, which cause the ring of plasma to expand and have a gradually increasing major radius. In this case, only the poloidal magnetic fields can counteract this expansion. The magnetic field must then possess a critical property to account for the toroidal force balance: a poloidal twist. This twisted property is known as the rotational transform (ι) [1]. It is sometimes better known by its inverse value, q, which is called the safety factor. This is defined as follows:

$$q = \frac{m}{n} = \frac{\text{Number of toroidal turns}}{\text{Number of poloidal turns}}$$

In words, it is the ratio of the number of times a particular magnetic field line makes a complete journey the long way around the device (toroidally), to the number of times it completes a journey the short way around (poloidally). This twisting of the field lines can be achieved by different means, and we will explore those differences now when discussing our two main fusion devices of interest.

Stellarators and tokamaks are both toroidal magnetic confinement fusion devices, whose plasmas are topologically equivalent. However, the tokamak's plasma possesses axisymmetry about the

central axis through the centre of the torus, whereas the stellarator loses this axisymmetry. A stellarator plasma can be visualised externally as a helically-twisted torus in shape, analogous to a 3D Möbius strip. The stellarator's twisted shape leads to a more complex magnetic coil - and magnetic field - configuration than the tokamak. Both the stellarator and tokamak must aim to confine the plasma sufficiently, and maintain the adequate force balance, as already discussed. The stellarator relies primarily on external superconducting magnetic coils to confine the plasma, and it manages to twist the field lines purely by its intrinsic contorted 3D-geometry. In contrast, the tokamak relies on external magnet coils along with an additional internal toroidal current within the plasma, to produce a sufficient confinement field. This induced current adds a poloidal magnetic field to artificially twist the field lines in the plasma, which helps to maintain adequate force balance [1]. In present tokamaks, this plasma current is driven by a toroidal electric field, induced by transformer action. This transformer has its primary coil in the centre of the torus, and the plasma itself acts as the secondary coil. The plasma current is then induced by continuously increasing the current in the primary coil. This is an inherently pulsed process, as there is an upper limit to the allowed magnitude of current through the primary coil. Tokamaks must therefore operate for only brief periods, or rely upon alternative means of current drive [1].

Stellarators have both advantages and disadvantages when compared to the tokamak. For one thing, due to the aforementioned transformer action and its inherently pulsed nature, tokamaks cannot run in steady-state which prevents continuous operation. This poses a substantial problem, as continuous operation is likely to be an inevitable requirement for a practical reactor. The stellarator, however, is an inherently steady-state device, which has several advantages from an engineering standpoint. Moreover, the large plasma current induced in tokamaks can disappear due to disruptive plasma instabilities, which lead to an immediate loss of confinement, and can sometimes cause severe damage to the plasma-facing components in the device [7]. This issue is absent in stellarators. For stellarators, the lack of an internal current eliminates some of the instabilities of the tokamak, meaning the stellarator should be more stable at similar operating conditions. On the downside, the absence of this internal current means that the stellarator must compensate by using more powerful external magnets to reach the same confinement levels achievable by the tokamak. The stellarator has one main disadvantage compared to the tokamak. The coil system needed to generate a stellarator magnetic field is substantially more technologically complicated than the tokamak coil system. This leads to an increased cost and possibly also to stricter limitations on the maximum achievable magnetic field [1].
The axisymmetry which tokamaks possess is lost in stellarators, which have an inherently 3D geometry. This led to the first stellarator experiments performing poorly compared with tokamaks when it came to confinement. However, stellarator designs have since been optimised to account for these initial issues, such that their confinement performance is now comparable with modern tokamaks. The details of these issues, and the optimisation that was introduced to counteract them, will be discussed later.

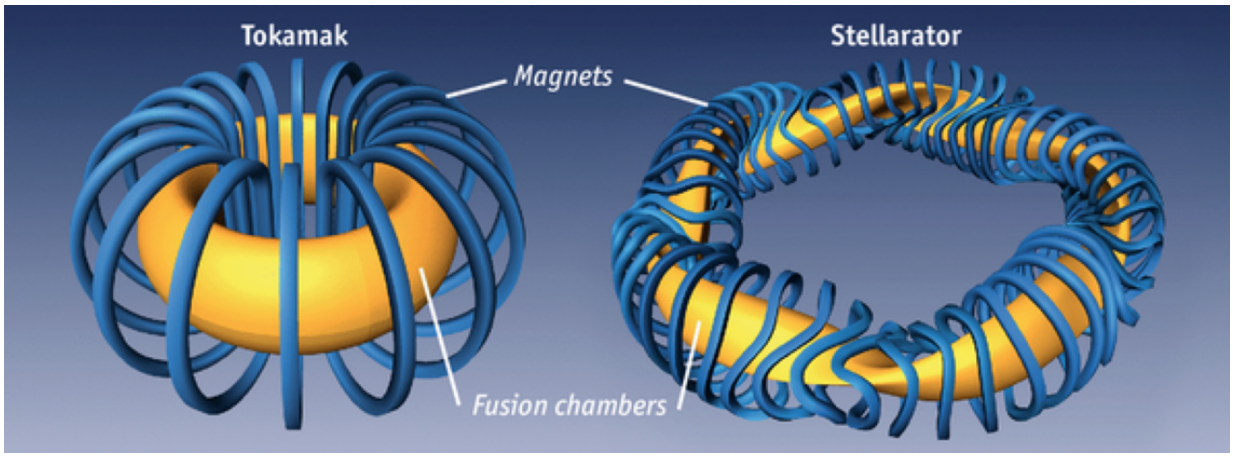

Figure 3.2: *Comparison of plasma/magnetic-coil geometries between the Tokamak and the Stellarator. Source: Economist.com*

3.2 Plasma Structure and Particle Motion

In this section, we describe the overall structure of a fusion plasma, and the motion of particles within that structure. We also introduce an important coordinate system for toroidal configurations, which we will depend on in later chapters.

An important feature of the plasma structure to understand is the nature of a flux surface. Following from [1], if one considers a magnetically-confined plasma at equilibrium, flux surfaces can be easily visualised as nested contours of constant pressure, as shown in Fig. 3.3. Clearly, for a contour of constant pressure p, which is nested between other contours of different constant pressure, ∇p must be perpendicular to that original contour everywhere on its surface. This ∇p can then be related to a normal vector of the constant pressure surface: $\nabla p \sim \mathbf{n}$. Here, we have ignored a potential minus sign, which would arise due to the direction of the pressure gradient (pointing radially inward) being opposite to the normal of the surface (pointing radially outward). Neglecting this sign detail, a magnetic flux surface can be defined as a surface satisfying the following property:

$$\mathbf{B} \cdot \nabla p \sim \mathbf{B} \cdot \mathbf{n} = 0 \tag{3.1}$$

This expression then implies that the magnetic field lines, which are aligned with the vector $\mathbf{B}$, must lie within a surface of constant pressure. The field lines then do not traverse from one surface of constant pressure p_i to another distinct surface of constant pressure p_j, for $i \neq j$. Now, with the concept of a flux surface solidified, let's describe the different possible types of flux surface. Specifically, we will make the distinction between rational and irrational flux surfaces.

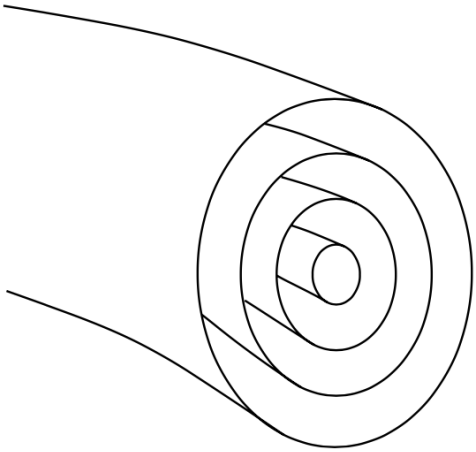

Figure 3.3: *Nested Flux Surfaces: Defined by contours of constant pressure in toroidal-plasma equilibrium. Source: [1]*

This is most easily understood when considering the safety factor q, which we have already established to be:

$$q = \frac{m}{n} = \frac{\text{Number of toroidal turns}}{\text{Number of poloidal turns}}$$

Every flux surface has its own value for q. For a flux surface to be rational, the value for q must be a rational number. In other words, after a finite number of turns toroidally and poloidally around the torus, the field line will end up where it started and eat its own tail. In contrast, for an irrational flux surface, q must be an irrational number, and so it cannot be written as a fraction. This implies that for this case, a magnetic field line will never close back on itself, but rather, it winds around the torus infinitely many times until the entire flux surface has been covered by its path.

With these concepts in mind, we can describe different features of the plasma concisely with the help of a convenient coordinate system, in terms of (ψ, ζ, θ). The conventions shown here are analogous to those in [8]. ψ denotes the flux surface label (or minor-radial coordinate), ζ is the toroidal angle (about the central axis through the torus), and θ is the poloidal angle. A particular point on a chosen flux surface can then be described by the angular coordinates ζ and θ. See Fig. 3.4 for a clear visualisation.

Now, we will discuss the nature of particle motion in our fusion devices of interest, and how

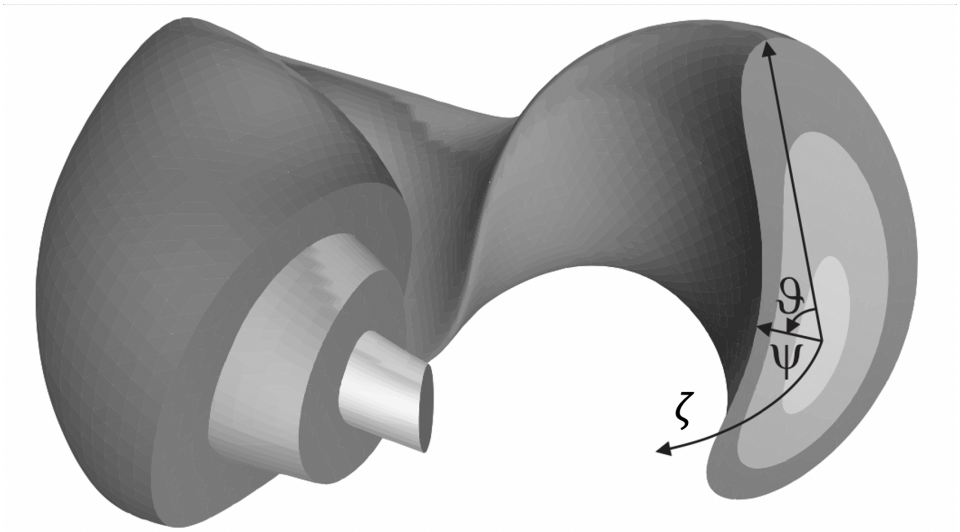

Figure 3.4: *Nested flux surfaces in a stellarator plasma, with coordinate system (ψ, ζ, θ). Source: [9]*

the specific design of these configurations influences this motion. Due to the toroidal shape of tokamaks and stellarators, there exist regions of high and low magnetic field density. The field is stronger on the inside curve than the outside simply due to the magnets being closer together in that area. This inhomogeneity of the magnetic field - as well as other field inhomogeneities, to be described later - leads to the plasma particles being divided into two classes. These classes are commonly referred to as trapped and passing particles [1, 4]. Trapped particles are those that are periodically reflected between regions of high magnetic field with a characteristic frequency, known as the bounce frequency. This occurs when particles enter a region of low magnetic field strength, and do not have sufficient parallel velocity to escape the region. Such a region can be thought of as a magnetic-field well, bounded by regions of higher magnetic field. This reflective motion of trapped particles is also known as the mirror-effect, which will be qualitatively described in more detail later. Passing particles, on the other hand, are those whose parallel velocity is large enough that they can overcome these barriers of higher magnetic field, and so, they mostly follow a magnetic field line around the torus without being reflected - or trapped in a well [1].

This concept of the mirror-effect can be more precisely described by introducing the first adiabatic invariant, μ. This quantity can be thought of as the gyro-averaged magnetic moment of a charged particle moving in a helical path [1]. This can be clearly seen if we think of the standard definition of the magnetic moment, when describing some current I moving through a wire loop of area A, such that $\mu = IA$. Now, in our case, for particles undergoing gyro-motion in a magnetic field, the averaged current over one period of this motion can be expressed as:

$$I = \frac{q}{\tau_c} = \frac{q\omega_c}{2\pi}$$

where τ_c and ω_c are the cyclotron (gyro-motion) period and angular frequency, respectively. Also,

the area of the motion can be expressed as:

$$A = \pi\rho^2 = \pi\left(\frac{mv_\perp}{qB}\right)^2$$

The expression for ρ that we have inserted here can be obtained from equating the Lorentz force with centripetal force, shown below. With these expressions for I and A, this then leads us to the following form for μ:

$$\mu = IA = \left(\frac{q\omega_c}{2\pi}\right)\left[\pi\left(\frac{mv_\perp}{qB}\right)^2\right] = \underbrace{\left(\frac{\omega_c m}{qB}\right)}_{=1}\left(\frac{mv_\perp^2}{2B}\right) = \frac{mv_\perp^2}{2B}$$

where we have made use of the fact that the Lorentz force and centripetal force are equivalent, combined with expressing the Larmor radius in terms of cyclotron angular frequency:

$$F_L = qv_\perp B = \frac{mv_\perp^2}{\rho} \quad \text{and} \quad \rho = \frac{v_\perp}{\omega_c} \implies \omega_c m = qB$$

According to [1], when averaging over the gyro-period, μ can be taken as a constant of the motion, i.e.,

$$\mu = \frac{mv_\perp^2(t)}{2B(t)} = \text{constant}$$

The invariance of μ can be interpreted as follows. As the B field changes along a particle's motion, its perpendicular velocity $v_\perp$ and corresponding gyro-radius ρ must changed accordingly to maintain a constant μ. More accurately, μ is an approximate constant of the motion, since its derivation involves averaging over the gyro-period of the particle, under the assumption that the magnetic field is varying slowly, i.e., adiabatically [1]. This concept of having a conserved quantity of the motion will now enable us to describe the mirror-effect, which was roughly discussed earlier.

A magnetic field inhomogeneity, leading to a $\nabla_\parallel B$ effect, can be induced by the magnetic coil arrangement shown in Fig. 3.5. In such an arrangement, and in the limit that the Larmor radius ρ is small compared to the field variation length, μ is an adiabatic invariant, and a gyro-averaged force acts parallel to $\nabla_\parallel B$. This force can have a significant impact on the guiding-centre motion in the direction parallel to the magnetic field, and this force leads to the aforementioned mirror-effect. The derivation of this force is carried out in full in [1], and only the result will be stated here for brevity:

$$F_\parallel = m\frac{dv_\parallel}{dt} = -\mu\nabla_\parallel B$$

Let's now discuss how this force can lead to the mirror-effect, which causes a total reversal of the guiding-centre's parallel motion. This can also be clearly visualised in Fig. 3.6. In (a) of the

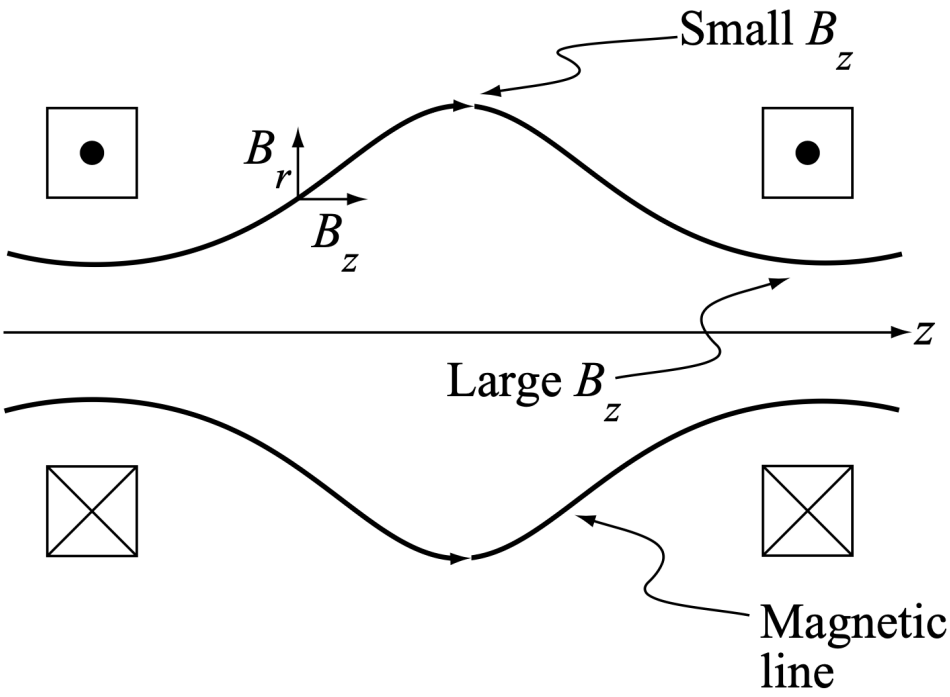

Figure 3.5: *Toroidal direction follows z-axis. Magnetic coils here are coming out of screen above z-axis, and entering into the screen below this axis. Field strength is stronger inside coil region, and weaker between separate coils. Source: [1]*

figure, a particle starts in a region of lower B, possessing certain values of $v_\perp$ and $v_\parallel$. The particle undergoes its gyro-motion and its guiding-centre travels parallel to **B** into a region of higher field strength. Remember,

$$\mu = \frac{mv_\perp^2(t)}{2B(t)} = \text{constant}$$

which means that $v_\perp$ must also increase as B increases. Note, that in a static magnetic field, a particle's kinetic energy is also an exact constant of the motion:

$$E_{(Kinetic)} = \frac{m(v_\perp^2 + v_\parallel^2)}{2} = \text{constant}$$

Due to this, as $v_\perp$ goes up, $v_\parallel$ must go down accordingly. If the magnitude of B increases sufficiently, then there will come a point when $v_\parallel = 0$. This defines the mirror point, as can be seen in (b) of Fig. 3.6. Once reaching this point, the parallel velocity of the guiding-centre is reversed, and the particle moves to the left in our graph. The force causing this behaviour is $F_\parallel = -\mu\nabla_\parallel B$. As shown in (c), this forces slows down the particle's parallel guiding-centre motion [1]. This concludes our explanation of how mirroring can occur to charged particles in an inhomogeneous magnetic field.

The plasma particles can also experience a radial drift that is due to the inhomogeneous toroidal

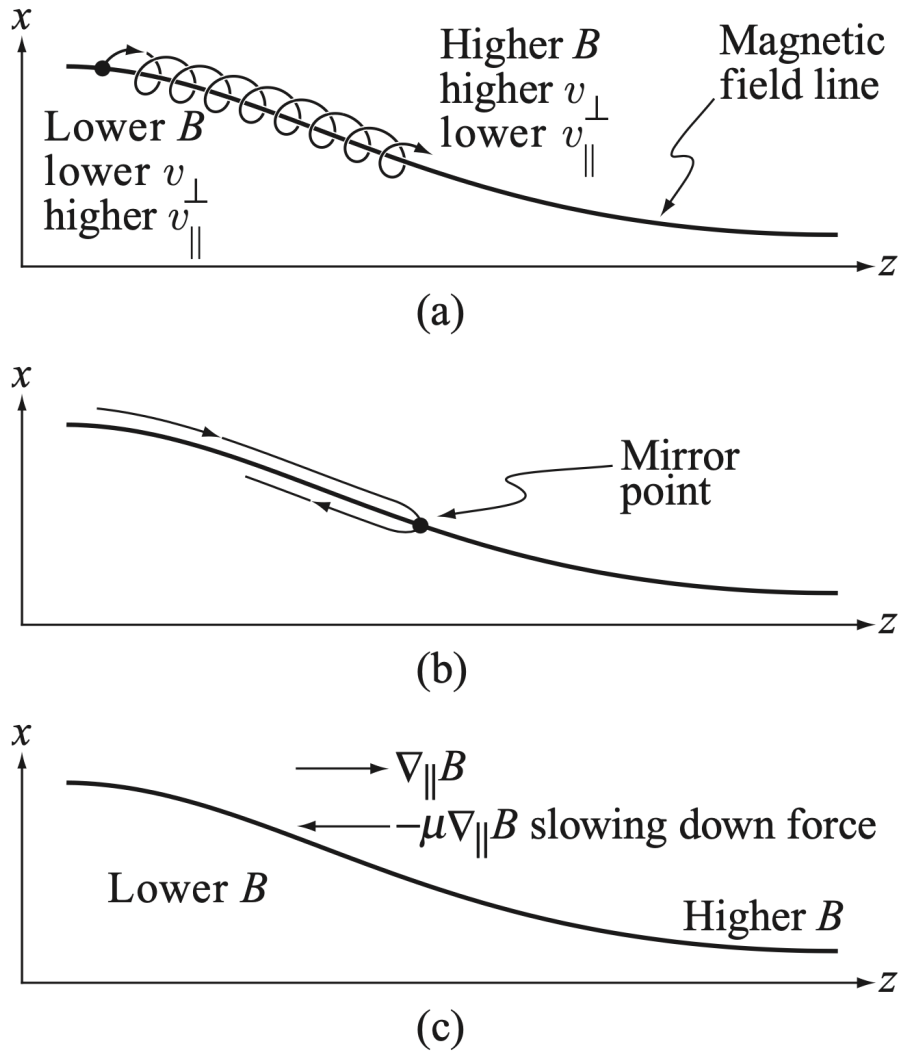

Figure 3.6: *Mirroring effect experienced by charged particles due to inhomogeneous magnetic fields along the toroidal axis. (a) shows the particle trajectory, (b) shows the guiding-centre motion at the mirror point, and (c) shows the parallel force acting on the guiding-centre. Source: [1]*

magnetic field. As will be seen later during our derivation of the gyrokinetic equation, the drift velocity arising due to the gradient of the magnetic field strength and the curvature of the field, can be expressed as follows:

$$\mathbf{v}_d = \frac{\hat{\mathbf{b}}}{\Omega_a} \times \left(\frac{v_\perp^2}{2} \nabla \ln B + v_\parallel^2 \kappa \right) \tag{3.2}$$

where $\kappa = \hat{\mathbf{b}} \cdot \nabla \hat{\mathbf{b}}$ indicates the curvature present, and $\Omega_a = \frac{e_a B}{m_a}$ is the gyro-frequency, where the subscript a refers to the different particle species. The details of how to arrive to this result will be seen in Chapter 4. The level of drift a particle experiences depends heavily on its position, and so the overall net drift depends on the particle's path around the device. The radial drift for passing particles is almost negligible, as any drift experienced at a given point in the device is eventually

averaged out over the full path taken. Trapped particles, on the other hand, can experience a finite net radial drift [1]. This finite drift is what led to particles being lost in classical stellarators, which are those that preceded our current geometrically-optimised design. These losses are described by the aforementioned neoclassical transport theory. Recent optimised stellarator geometries, however, promise to reduce the neoclassical transport down to the level of tokamaks. This can be achieved by different geometrical optimisation designs. One such way is by ensuring that the trapped particles precess around the torus poloidally and do not experience any net radial drift. These types of magnetic fields whereby the time-averaged radial drift vanishes are known as omnigeneous fields. More specifically, the example that has been described here is a quasi-isodynamic field, which is omnigeneous and has poloidally, but not toroidally, closed contours of the magnetic field strength B. In these optimised stellarators, the neoclassical transport becomes small enough so that turbulent transport may limit the confinement instead [1]. An example of a fusion device that as been optimised with such a geometry is the Wendelstein 7-X (W7-X). This is an experimental stellarator device, located in Greifswald, Germany. It was developed and built by the Max Planck Institute of Plasma Physics (IPP), and is currently the flagship for stellarator fusion devices today.

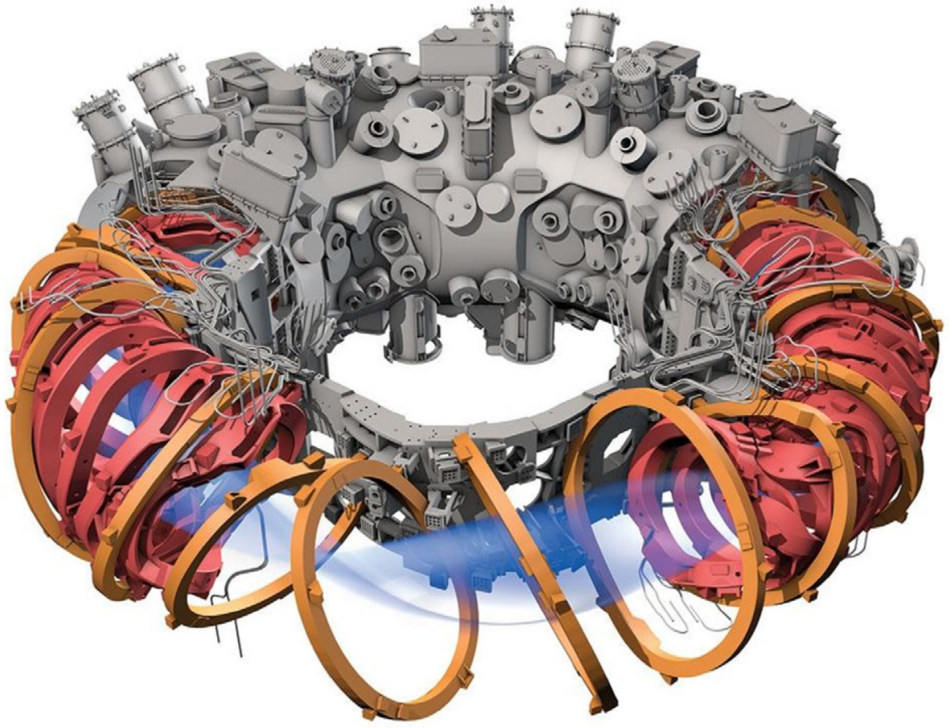

Figure 3.7: *Schematic diagram of the superconducting stellarator device Wendelstein 7-X. The 50 non-planar (red) and the 20 planar (orange) superconducting coils are operated in an evacuated cryostat volume between the plasma vessel and the outer vessel. Source: [10]*

3.3 Turbulence and its Negative Impacts

In this section, we give a brief overview of the nature of turbulence in fusion plasmas, and the negative impacts such behaviour has on magnetic confinement fusion devices.

When levels of neoclassical transport are at a low and tolerable level, turbulence is the dominant mechanism for heat loss in the plasma. Small fluctuations in the plasma lead to turbulence, and turbulent eddies can very effectively transport heat from the hot core across confining magnetic field lines out to the cooler plasma edge, degrading the plasma performance. This lowers our confinement time, which is a quantity we wish to maximise. The turbulence is driven by small-scale instabilities, also known as micro-instabilities. These micro-instabilities grow by tapping into the available free energy supplied by the density and temperature gradients in the plasma [11]. Some of these instabilities are driven by the trapped particles and therefore depend strongly on the magnetic geometry. With this in mind, we then have to consider how the chosen geometrical optimisation of the system is affecting the over stability of the fusion plasma. While large scale instabilities should not be a major problem in geometrically optimised stellarators, the small scale instabilities do threaten successful fusion experiments. These so-called micro-instabilities are on the scale of the Larmor radius, $\mathcal{O}(\rho)$. The transport they tend to cause - known as turbulent transport - is expected to play a major role in stellarators where the neoclassical transport is rendered small by the optimisation [12]. With this overview of turbulence in mind, we will now look closely at the mechanisms of instabilities that cause it.

3.4 Mechanisms of Instabilities

In this section, we introduce two important modes of micro-instabilities relevant to magnetic confinement fusion plasma. These are the trapped-particle mode (TPM) and the ion-temperature-gradient mode (ITGM). Specifically, we will describe the underlying mechanisms governing the manifestation and subsequent behaviour of these modes. Trapped-particle modes and ion-temperature-gradient modes cause most of the turbulent transport in toroidal fusion devices [13, 14]. Before describing the causes of these instabilities, however, the concept of the drift wave must first be understood. Only electrostatic instabilities will be focused on here, meaning that perturbations to the magnetic field are neglected [13]. The descriptions of the following mechanisms follow directly from [4, 12]. To end this section, we will give a brief but important introduction to the mathematical description of these modes, in particular, regarding their frequency ω. This will aid us in explaining the concept of marginal stability, which is crucial to understanding the primary goal of this project.

3.4.1 Drift Waves due to a Density Perturbation:

For drift waves to occur, we require that the plasma has a background density gradient, which we will call ∇n_0. Ambient vibrations or disturbances to the plasma can cause a density perturbation to be induced. This perturbation to the density, up to first order, can take the following form: $n = n_0 + n_1$. This perturbation can lead to a periodic increase and decrease in the plasma density along the poloidal direction (when looking at a cross section of the torus). The electrons, which are significantly lighter than the ions, are then free to move on the time scale of the perturbation. They move along the field lines in the toroidal direction. They respond adiabatically to this change in density of the plasma, and they move from a higher density region to fill the lower density regions. This relocation of the electrons creates an electrostatic potential, as the regions with more electrons become negative, and the regions where electrons have moved away from are now more positive. This potential continues to build until the Boltzmann level is reached:

$$\phi = \frac{n_1}{n_0}\frac{T}{e}$$

where T is the temperature and e is the electron charge. These potentials are in phase with the initial density perturbation, as seen in Fig. 3.8. Hence, an electric field $\mathbf{E}$ is established. This field $\mathbf{E}$ is perpendicular to the magnetic field $\mathbf{B}$, and an $\mathbf{E}\times\mathbf{B}$ effect develops. This then causes the so-called $\mathbf{E}\times\mathbf{B}$ drift in the plasma. This drift has a maximum which is a $\frac{\pi}{2}$ shift away from the maximum of the initial density perturbation. The periodic wave form - seen in the density gradient - then shifts to the right (positive y-direction) due to the location of the $\mathbf{E}\times\mathbf{B}$ drift (which points in the $\pm$x directions, midway between the regions of positive and negative electric potential). A drift occurs, but the amplitude of the density perturbation remains unchanged. This means the perturbation does not grow, but oscillates in a steady-state. With the drift wave mechanism now explained, the main two modes of turbulence can now be understood. Rather than discussing the TEM specifically, the more general case of the trapped-particle mode (TPM) is described. Following this is an explanation of the ITGM.

3.4.2 Trapped-Particle Mode (TPM):

The TPM can be regarded as a drift wave that is driven unstable, but they are both initiated in a similar way. Once again, a density perturbation is induced. This time, however, both ions and electrons react kinetically, not adiabatically. Both particles experience a magnetic curvature drift, and thus a drift velocity given by Eqn. 3.2. We can restate that expression here:

$$\mathbf{v}_d = \frac{\hat{\mathbf{b}}}{\Omega_a} \times \left(\frac{v_\perp^2}{2} \nabla \ln B + v_\parallel^2 \kappa \right) \tag{3.3}$$

where $\Omega_a = \frac{e_a B}{m_a}$, and the subscript a refers to the different particle species. This species dependence indicates that the ions and electrons drift in opposite poloidal directions ($\pm$y directions)

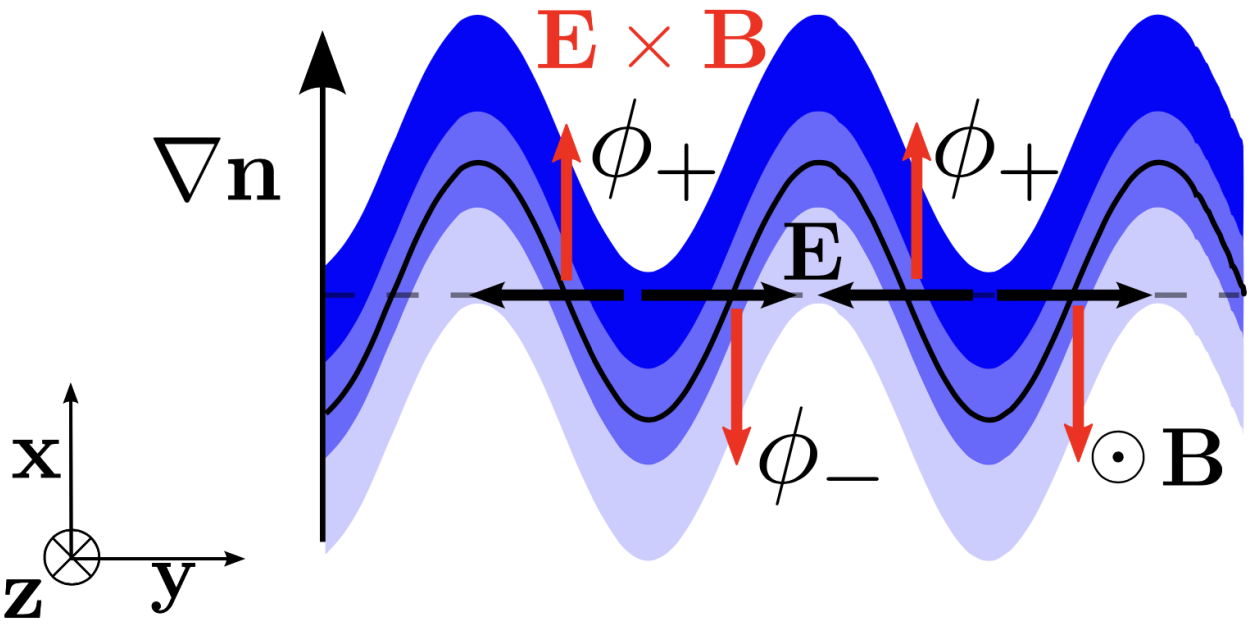

Figure 3.8: *Drift Waves. Source: [12]*

due to their opposite charge. We can see that in our example schematic, Fig. 3.9, the electrons drift to the right (+y direction) from the higher density region (dark blue), and the ions behave oppositely. In a tokamak, trapped particles spend most of their time on the outboard side where the magnetic field is weakest, which leads to the magnetic curvature drift of these particles having a preferred net direction [4]. Having this preferred net direction leads to these particles experiencing a finite net drift over the course of their bounce motion. In contrast, passing particles circulate the full torus and therefore are not constrained to only experiencing the outboard side. This leads to them having negligible net drift, as any drift they experience averages out over time. Returning to our schematic, we see that a charge separation occurs due to the congregation of oppositely charged trapped particles in the $\pm$y directions. As before, this charge separation leads to the emergence of an electric field, and thus an $\mathbf{E}\times\mathbf{B}$ drift develops. Note, however, that in this case, there is a phase shift between the potentials (positive and negative) and the density perturbation. This is seen clearly in Fig. 3.9. The maximum of the $\mathbf{E}\times\mathbf{B}$ drift coincides with the maximum of the density perturbation, and thus the perturbation is enhanced and the instability grows. A temperature gradient can also lead to a trapped-particle instability.

For a more detailed review of TPMs, and trapped-electron modes (TEMs) in particular, the following literature is recommended. On the stability properties of the TEM, see [15, 16]. On the resilience of quasi-isodynamic stellarators to the TEM, see [17]. For an analytical and numerical analysis of TPMs in stellarators, see [18, 19]. Finally, for TEM turbulence optimisation and suppression, see [20, 21]. It should be noted that this selection of literature is by no means exhaustive.

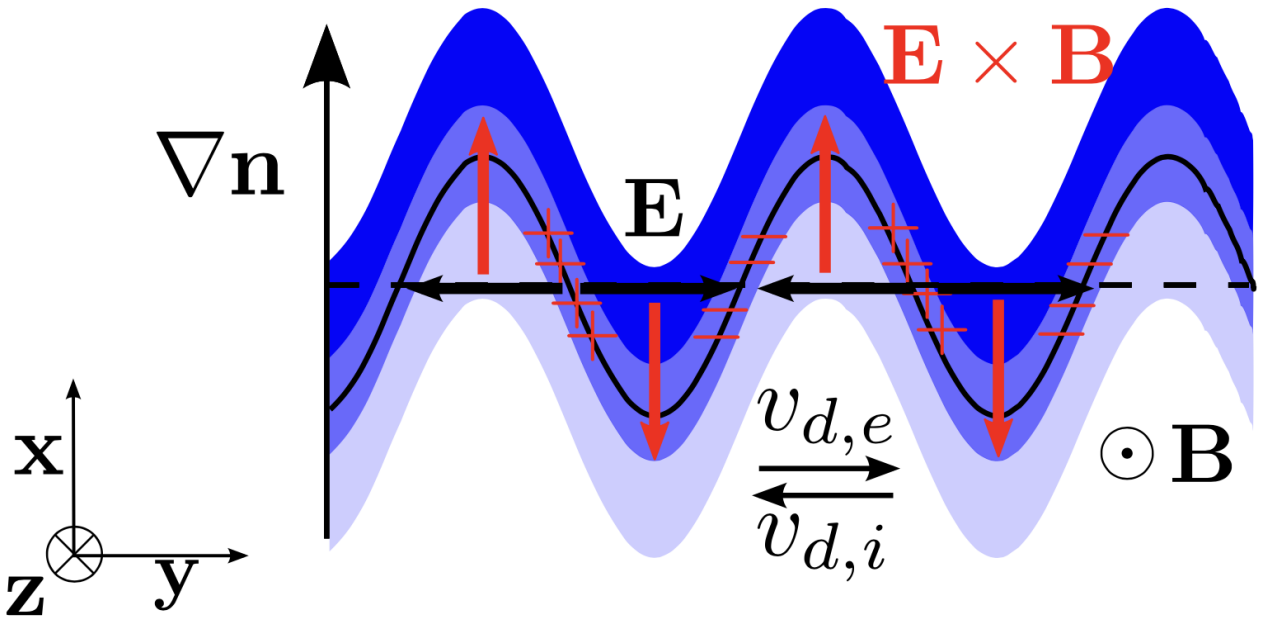

Figure 3.9: *Trapped-Particle Mode. Source: [12]*

3.4.3 Ion-Temperature-Gradient Mode (ITG Mode):

In this case, only the kinetic response of the ions is considered, while the electron response is neglected. Again a perturbation - this time in the temperature - is induced. If we now assume a negative y-directed drift velocity proportional to the temperature, it can be observed that this drift will be larger in regions of high temperatures than in regions of low temperatures. An electrostatic potential will thus build up, as the ions leave the regions of higher temperature faster than they can stream out from the lower temperature regions to the other side. See Fig. 3.10 for clarity. Analogous to the TPM, the resulting $\mathbf{E}\times\mathbf{B}$ drift is in phase with the temperature perturbation, and the instability grows. If the direction of the drift velocity were reversed with respect to the underlying temperature gradient, for example on the inner side of the torus, the perturbation would be reduced and there would be no unstable mode. If there is a density gradient as well as an ion-temperature gradient, which is expected in a fusion device, the drift wave mechanism will compete with the ITG mechanism. The phase between the perturbation and the $\mathbf{E}\times\mathbf{B}$ drift will be changed, so that the ITG mode is stabilised if the density gradient is high enough. The roles of ions and electrons could also be reversed if electrons but not ions are considered kinetically. This would happen for instabilities with frequencies so high that the ions are practically non-magnetised. In this case, and if the underlying temperature gradient is in the electron temperature, an analogous mode arises, which is called the electron-temperature gradient mode (ETG).

For a more detailed review of the ITGM, the following literature is recommended. A general discussion on the ITGM and the turbulence caused by it can be found in [22, 23, 24]. A gyrofluid description of turbulent transport in tokamaks, including transport caused by the ITGM, can be found in [25, 26]. The threshold of destabilisation of the ITGM is described in [27]. Finally, a study of the geometric stabilisation of ITG-driven instabilities in nearly axisymmetric and non-axisymmetric configurations is discussed in [28] and [29], respectively. It should be noted that this selection of literature is by no means exhaustive.

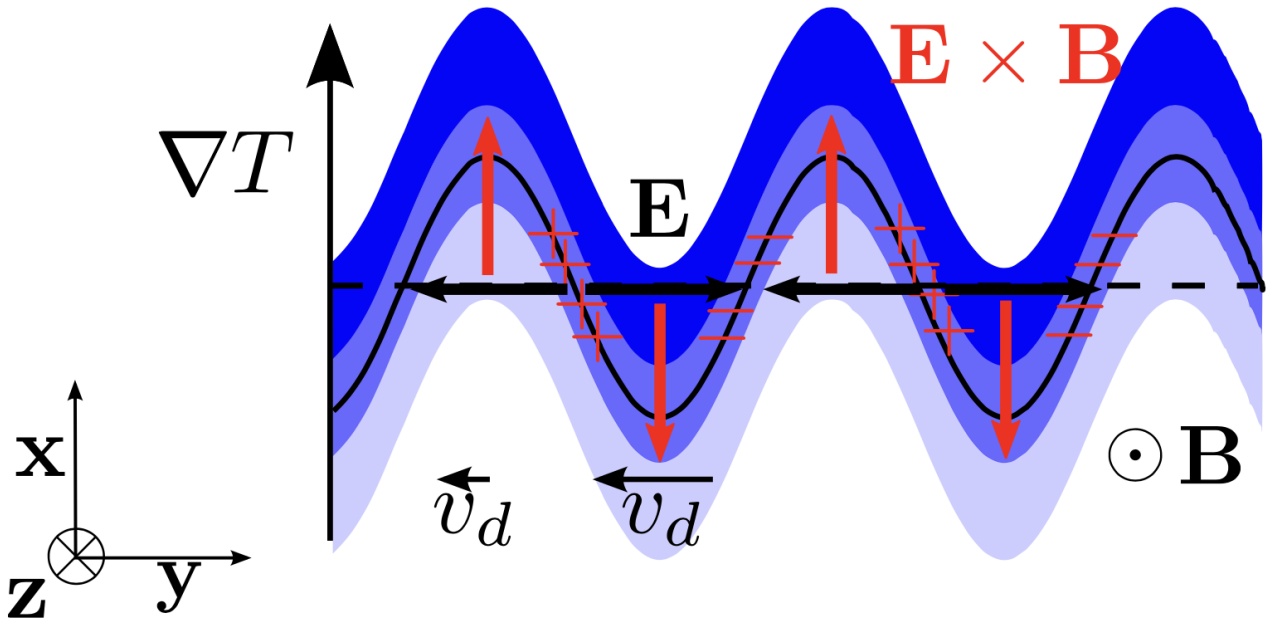

Figure 3.10: *Ion-Temperature-Gradient Mode. Source: [12]*

The Mode Frequency and Marginal Stability

Let's consider some plasma perturbation which varies in space and time, $Q(\mathbf{x}, t)$. We can extract the time dependence of this perturbation by means of a normal mode expansion [1, 4, 30]. This means that our perturbed quantity can be written as

$$Q(\mathbf{x}, t) = Q(\mathbf{x})e^{-i\omega t} \tag{3.4}$$

where $Q(\mathbf{x})$ is the time-independent amplitude, and ω is the frequency of the perturbation, which may be complex. In the case that ω is complex, and takes the form

$$\omega = \omega_r + i\gamma \tag{3.5}$$

then the time-dependent exponential term in our perturbation becomes

$$e^{-i\omega t} = e^{-i\omega_r t + \gamma t} \tag{3.6}$$

Thus, our perturbation can be written fully as

$$Q(\mathbf{x}, t) = Q(\mathbf{x})e^{-i\omega_r t+\gamma t} \tag{3.7}$$

whereby ω_r determines the real frequency of the perturbation in question, and the sign of γ determines the stability. If $\gamma > 0$, the system is rendered unstable since the perturbation grows exponentially in time. If $\gamma \leq 0$, then the system either remains stable as the perturbation decays exponentially, or it oscillates in a steady-state with no growth [1]. This imaginary component γ of the mode frequency is thus known as the growth rate.

It is desirable to know when a perturbation is on the brink of becoming unstable, and so this threshold of interest where $\gamma \to 0^+$ is defined as the point of marginal stability. In the case of the TEM, which is of primary interest in this project, this point occurs for a particular density gradient value known as the critical density gradient. For density gradients below this critical value, the growth rate γ is less than or equal to zero, meaning we either have a decaying perturbation or a steady-state drift-wave. When γ becomes finite and positive, the drift-wave has been driven unstable, and continues to grow [1].

Thus, if one were to maximise the value of this critical density gradient, then this would delay the onset of the TEM instability, and with it any subsequent turbulent transport caused by its behaviour. This method of optimisation is the ultimate goal of this project. In the following section, we will give a brief overview of turbulence optimisation strategies in stellarators.

3.5 Turbulence Optimisation

In this section, we provide a brief overview of some different approaches to turbulence optimisation in magnetic confinement fusion devices.

Turbulence optimisation is a pressing issue in magnetic confinement fusion research today. With the optimisation of neoclassical transport achieved to a tolerable level in contemporary fusion devices, transport driven by turbulent behaviour is now the main obstacle that limits plasma confinement times [14]. Evidence of this is clear from experimental measurements of turbulent transport levels in magnetic confinement fusion devices. Results have shown that these transport levels surpass those predicted by neoclassical transport theory by approximately a factor of 10 for ions, and up to a factor of 1000 for electrons [11]. As stellarators possess many degrees of freedom when it comes to their geometrical design, optimisation can potentially be achieved by manipulating the magnetic field configuration of the device to influence the level of stability [31, 32]. Being able to manipulate the field means having more control over drift levels in the plasma, which are due to the ∇B and curvature effects mentioned earlier. If not regulated, these effects can lead to unwanted plasma instabilities. If successful manipulation of the fields

is achieved, this could then heighten the stability properties of the plasma, reduce transport from turbulence, and improve confinement overall [33]. The primary aim is then to analyse the behaviour of turbulent modes, and extrapolate an optimum geometry from the analysis. There are certain important characteristics of the instabilities that we can investigate in order to gain this insight, which we will now discuss here.

As already mentioned in the previous section, the two main modes of instabilities that lead to turbulence (TPM and ITGM) are dependent on having a gradient in either the plasma density or plasma temperature. An important characteristic of the TEM and ITGM, in particular, is that they both possess a critical instability threshold [13]. The existence of such a threshold was foreshadowed at the end of the previous section, when introducing the concept of marginal stability. As stated there, this critical threshold is defined as the density/temperature gradient value beyond which instabilities begin to grow. Growth occurs as the instabilities tap into the free energy made available by these plasma gradients [11]. This, of course, means that the modes possess a certain positive growth rate ($\gamma > 0$). The higher the growth rate, the more quickly the instability becomes an issue. This then gives rise to the current research directions of turbulence optimisation. Two such approaches will be described briefly here. First, is to lower the slope of the growth rate of the mode past the critical gradient, as was investigated for the TEM in [20]. See Fig. 3.11 for a graph of TEM linear growth rates present in different stellarator devices. The point of this strategy is to slow down the rate at which energy is lost from the plasma, and thus, improving its performance by increasing the confinement time. Second, would be to extend the critical gradient value to a higher density/temperature gradient value, such that transport due to the turbulent mode is not a significant factor for a larger part of the stellarator's operational parameter space. This would delay the overall onset of turbulence, and allow the reactor to run for a longer time before the effects of turbulent transport become too high. This then would also improve the plasma's performance by increasing the confinement time. The latter strategy described here is precisely the goal of this project, with the TEM being the instability mode of interest.

For a more detailed review of turbulence and its optimisation, the following literature is recommended. A general introduction to turbulence can be found in [13]. For a discussion on improving confinement in stellarators, and a study of the geometric dependence of turbulence in stellarators, see [33, 34]. The means to controlling such turbulence in stellarators is also discussed in [31, 32]. Finally, further material on the suppression and optimisation of turbulence can be found in [35, 14, 36, 21]. It should be noted that this selection of literature is by no means exhaustive.

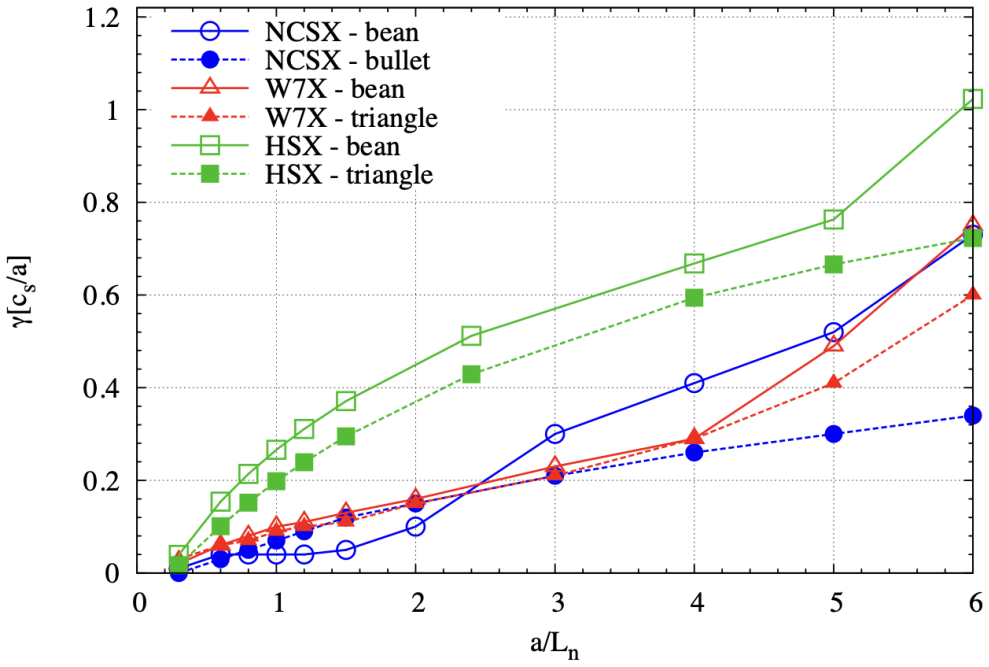

Figure 3.11: *Linear growth rates of density-gradient-driven TEMs in different types of simulated flux tubes in NCSX, HSX and W7-X. At each simulated density gradient $\frac{a}{L_n}$, where a is the minor radius of the device and L_n the density-gradient scale length, the growth rate of the most unstable mode is displayed. Source: [20]*

Chapter 4

Gyrokinetic Theory

In this chapter, we give an introduction to gyrokinetic theory, and some motivation for why we need to rely on this framework. The sections covered in this chapter are as follows. We begin by discussing why kinetic theory is chosen as our starting point to describe turbulent behaviour in fusion plasma. This leads us to formulate a kinetic description of a plasma. As we will see, this description will lead to some difficulty, which is partially alleviated by the implementation of gyrokinetic theory. The benefits of using this gyrokinetic theory are described, before we tackle the complete derivation of the gyrokinetic equation. We end the chapter by deriving the quasi-neutrality condition, which completes our set of equations required for the remainder of this project.

4.1 Kinetic Theory

In this section, we will first motivate our efforts to understand turbulence by explaining why kinetic theory is used for describing this phenomenon. With this motivation in hand, we will then formulate a mathematical description of the plasma using kinetic theory, leading to a kinetic equation. Finally, we will discuss the necessity of introducing gyrokinetic theory, along with the accompanying benefits of this advancement.

4.1.1 Kinetic Theory to Describe Turbulence

There are several different approaches to take when dealing with the many-particle problem of magnetic confinement fusion. When considering large scale phenomena, such as plasma waves with wavelengths on the order of the plasma device dimensions, a fluid approach can be practical. This works on the basis that the plasma, being composed of charge-carrying particles, behaves

like an electrically conducting fluid due to its collective behaviour.

The plasma can be described by the following fluid quantities: the particle density $n_a(x,t)$ at the position x and time t, the macroscopic fluid velocity $V_a(x,t)$, and further tensor expressions related to the kinetic energy of the plasma and fluxes of energy and momentum. Once again, a denotes the particle species of interest, which can be e for the electrons, i for the hydrogen ions, and other subscripts for impurity species. Equations linking these quantities are derived by employing conservation laws for the total number of particles and the total momentum. However, the fluid description has its limitations, as some phenomena - in low-collisionality plasmas especially - are not easily described. A kinetic treatment of the problem is therefore required [30].

4.1.2 Kinetic Description of a Plasma

The formulation presented here follows from [12, 30]. We begin by noting that each particle species a can be described by a particle distribution function $f_a(\mathbf{x},\mathbf{v},t)$, where $\mathbf{x}$ and $\mathbf{v}$ are the 3-dimensional position and velocity vectors, respectively. In particular, the zeroth moment, with respect to which the other moments are normalised, yields the particle density of each species a:

$$n_a(\mathbf{x},t) = \int f_a(\mathbf{x},\mathbf{v},t)d^3v \tag{4.1}$$

where we have integrated over velocity space here. The quantity $f_a(\mathbf{x},\mathbf{v},t)d^3xd^3v$ can therefore be interpreted as the number of particles of species a in the volume element d^3xd^3v surrounding the position $(\mathbf{x},\mathbf{v})$ in the phase space of position $\mathbf{x}$ and velocity $\mathbf{v}$. Other fluid quantities can be obtained by taking higher orders of the distribution function. For instance, by taking the first moment, we obtain the macroscopic fluid velocity

$$\mathbf{V}_a(\mathbf{x},t) = \frac{\int \mathbf{v} f_a(\mathbf{x},\mathbf{v},t)d^3v}{\int f_a(\mathbf{x},\mathbf{v},t)d^3v} = \frac{1}{n_a(\mathbf{x},t)}\int \mathbf{v} f_a(\mathbf{x},\mathbf{v},t)d^3v \tag{4.2}$$

In the 6-dimensional phase space, particle numbers must be conserved. So we can use the continuity equation to describe the evolution of the distribution function.
Let's now focus on a particular element in phase space surrounding the point $(\mathbf{x},\mathbf{v}) = \mathbf{z}$. As in hydrodynamics, the change in the number of particles in $\mathbf{z}$ can only occur through fluxes into and out of $\mathbf{z}$, or because of collisions, which reults in the following 6D continuity equation

$$\frac{\partial f_a}{\partial t} + \nabla_{\mathbf{z}}(\dot{\mathbf{z}} f_a) = C_a(f_a) \tag{4.3}$$

where C_a denotes the collision operator describing small-scale Coulomb interactions between the particles, and $\dot{\mathbf{z}} = (\dot{\mathbf{x}},\dot{\mathbf{v}})$ denotes the flow velocity of particles in phase space. By neglecting other forces, such as gravity, the acceleration of the charged particles is given by the Lorentz force

$$\dot{\mathbf{v}} = \frac{e_a}{m_a}(\mathbf{E} + \mathbf{v}\times\mathbf{B}) \tag{4.4}$$

where m_a and e_a denote the particle mass and charge, respectively. By inserting this expression into Eqn. 4.3, and focusing only the second term on the left-hand side, we obtain

$$\begin{aligned}
\nabla_{\mathbf{z}}(\dot{\mathbf{z}} f_a) &= (\dot{\mathbf{z}} \cdot \nabla_{\mathbf{z}} f_a) + (\nabla_{\mathbf{z}} \dot{\mathbf{z}} \cdot f_a) \\
&= (\dot{\mathbf{x}} \cdot \nabla_{\mathbf{x}} f_a + \dot{\mathbf{v}} \cdot \nabla_{\mathbf{v}} f_a) + (\nabla_{\mathbf{x}} \dot{\mathbf{x}} \cdot f_a + \nabla_{\mathbf{v}} \dot{\mathbf{v}} \cdot f_a) \\
&= \left(\mathbf{v} \cdot \nabla_{\mathbf{x}} f_a + \frac{e_a}{m_a} (\mathbf{E} + \mathbf{v} \times \mathbf{B}) \cdot \nabla_{\mathbf{v}} f_a \right) + \left(\underbrace{\nabla_{\mathbf{x}} \mathbf{v}}_{=0} \cdot f_a + \frac{e_a}{m_a} \underbrace{\nabla_{\mathbf{v}} (\mathbf{E} + \mathbf{v} \times \mathbf{B})}_{=0} \right) \cdot f_a \\
&= \mathbf{v} \cdot \nabla_{\mathbf{x}} f_a + \frac{e_a}{m_a} (\mathbf{E} + \mathbf{v} \times \mathbf{B}) \cdot \nabla_{\mathbf{v}} f_a
\end{aligned}$$

We thus obtain the kinetic equation

$$\frac{\partial f_a}{\partial t} + \mathbf{v} \cdot \nabla_{\mathbf{x}} f_a + \frac{e_a}{m_a} (\mathbf{E} + \mathbf{v} \times \mathbf{B}) \cdot \nabla_{\mathbf{v}} f_a = C_a(f_a) \tag{4.5}$$

Depending on which type of collision operator C_a is used here, we obtain different equations. For describing a gas, the Boltzmann operator is suitable, and we get the Boltzmann equation. In plasmas, the dominant collision processes are Coulomb interactions, which are described by the Fokker-Planck operator, and the resulting equation is called the Fokker-Planck equation. In very hot plasmas, however, the collision frequency is very small. This is due to Spitzer resistivity, which shows that the electrical resistance in a plasma decreases in proportion to the particle species temperature as $T_a^{-\frac{3}{2}}$ [37]. Therefore, neglecting collisions altogether can be a valid approximation. The equation with $C_a = 0$ is called the Vlasov equation.

Obtaining a complete and exact solution to Eqn. 4.5 is not practically feasible. The reasoning for the difficulties behind this will be further explained in the next section. Due to these difficulties, approximations are needed in order to simplify the problem. The key approach in kinetic theory is to utilise a suitable ordering scheme, which, if successful, makes it possible to distinguish the relevant terms for the problem at hand from those small terms that don't affect the solution in a significant way, and that we can ultimately neglect. Determining which ordering assumptions to make depends on the phenomena one wishes to study. In this report, the ordering scheme we will implement is the gyrokinetic ordering scheme, which is particularly beneficial and frequently used in magnetised plasma research [7].

4.1.3 Benefits of Gyrokinetic Theory

Turbulence is driven by pressure gradients, which results in a change in the distribution function of particles. These changes can affect the particle density, temperature, momentum, and flux within the plasma. In order to predict plasma turbulence, the 6D Fokker-Planck equation (Eqn. 4.5, for C_a representing Coulomb collisions) needs to be solved for each species. This 6D equation, as it stands, results in a major practical issue when it comes to the simulation of fusion plasmas.

The spatio-temporal scales in fusion plasmas span an enormous range of orders, and this makes it impractical to simulate all phenomena in a realistic time-frame [7, 2].

Gyrokinetics aims to solve the this issue by reducing the Fokker-Planck equation to a 5D problem, which is much more manageable to solve when compared to the previous 6D problem [38]. It achieves this by eliminating the fast cyclotron time scale, as most interesting turbulent phenomena occur at much slower time scales [7, 38]. This transform, which is essentially a change of coordinates, is licit when the frequency of fluctuations is smaller than cyclotron frequencies. This ordering is well justified in most fusion devices [2, 39]. The remaining 5 dimensions are allocated as follows: three coordinates to describe the gyro-centre position, one parallel velocity or energy coordinate, which is aligned with the magnetic field, and one for the magnetic moment μ, an adiabatic invariant which effectively describes the velocity perpendicular to the magnetic field [39]. This procedure eventually leads us to the generalised gyrokinetic equation, which will be derived in the next section.

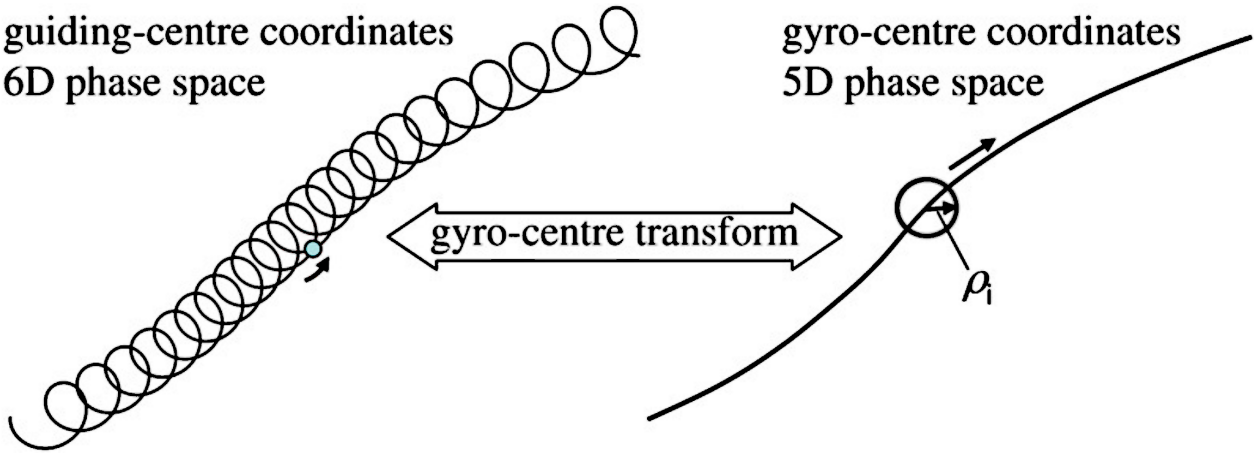

Figure 4.1: *Applying the gyro-centre transform to reduce the problem from 6D to 5D. This transformation reduces the trajectory of the particle to charged rings centred about the gyro-centre of radius ρ. Source: [39]*

4.2 The Gyrokinetic Equation

The content of this section, which includes the full derivation of the gyrokinetic equation, follows primarily from [12, 2, 7]. Throughout the derivation, assumptions about the magnitude of various quantities are implemented. These assumptions are motivated by experimental observations, as well as by some basic properties of plasmas. For instance, our equations will consider small perturbations of the distribution function about a Maxwellian background, and potential energy perturbations that are small compared to the background temperature, which we will characterise by an expansion parameter denoted by δ [2]. With this in mind, we will introduce the assumed

the gyrokinetic ordering

$$\frac{e_a\phi}{T_a} \sim \frac{\rho}{L} \sim \frac{\omega}{\Omega_a} \sim \delta \ll 1$$

where ω and L denote the typical frequency and length scale of the perturbation, respectively.

In a magnetic field, the charged particles gyrate around the field lines with the gyro-radius, given by

$$\rho_a = \frac{\sqrt{2m_aT_a}}{e_aB} \tag{4.6}$$

where T_a is the temperature. In magnetic confinement fusion, the plasma is usually highly magnetised, so the gyro-radius is much smaller than any macroscopic scale length L, i.e., $\frac{\rho_a}{L} \ll 1$.

For magnetised plasmas we choose convenient variables. We define the energy $\mathcal{E}$ that consists of kinetic energy and electrostatic potential energy, the magnetic moment μ and the gyro-centre $\mathbf{R}$

$$\mathcal{E} = \frac{m_av^2}{2} + e_a\phi \tag{4.7}$$

$$\mu = \frac{m_av_\perp^2}{2B} \tag{4.8}$$

$$\mathbf{R} = \mathbf{r} + \frac{\hat{\mathbf{b}} \times \mathbf{v}}{\Omega_a} \tag{4.9}$$

where $\Omega_a = \frac{e_aB}{m_a}$ is defined as the gyro-frequency (or cyclotron frequency) and $\hat{\mathbf{b}}$ is the unit vector pointing in the direction of the magnetic field. Additionally, we use θ to represent the gyro-angle. Then the gyrokinetic equation (Eqn. 4.5) becomes

$$\frac{\partial f_a}{\partial t} + \dot{\mathbf{R}} \cdot \frac{\partial f_a}{\partial \mathbf{R}} + \dot{\theta}\frac{\partial f_a}{\partial \theta} + \dot{\mathcal{E}}\frac{\partial f_a}{\partial \mathcal{E}} + \dot{\mu}\frac{\partial f_a}{\partial \mu} = C_a \tag{4.10}$$

Now note that the gyro-angle varies as $\dot{\theta} \simeq -\Omega_a$. The change of energy can be derived by noting that $m_a\dot{\mathbf{v}} = e_a(\mathbf{E} + \mathbf{v} \times \mathbf{B})$, such that

$$\begin{aligned}
\dot{\mathcal{E}} &= \frac{d}{dt}\left(\frac{m_av^2}{2}\right) + e_a\left(\frac{\partial\phi}{\partial t}_{\mathbf{r}}\right) + e_a\frac{\partial\phi}{\partial\mathbf{r}} \cdot \frac{d\mathbf{r}}{dt} \\
&= m_a\dot{\mathbf{v}} \cdot \mathbf{v} + e_a\left(\frac{\partial\phi}{\partial t}_{\mathbf{r}}\right) + e_a\mathbf{v} \cdot \nabla\phi \\
&= -e_a\mathbf{v} \cdot \nabla\phi + e_a\left(\frac{\partial\phi}{\partial t}_{\mathbf{r}}\right) + e_a\mathbf{v} \cdot \nabla\phi \\
&= e_a\left(\frac{\partial\phi}{\partial t}\right)_{\mathbf{r}}
\end{aligned}$$

where in the third step, we inserted the above expression for $m_a\dot{\mathbf{v}}$, and we used $\mathbf{E} = -\nabla\phi$.

We now decompose the distribution function into

$$f_a = f_{a0} + g_a,$$

where f_{a0} denotes the equilibrium distribution function including adiabatic responses to small electric fields $\left(\propto -\frac{e_a\phi}{T_a}\right)$, and g_a is the small non-adiabatic part of the perturbed distribution function, $g_a \ll f_{a0}$ $\left(\frac{g_a}{f_{a0}} \sim \delta\right)$. If we assume that the equilibrium distribution function varies slowly in time compared with the perturbed part

$$\frac{\partial g_a}{\partial t} > \frac{\partial f_{a0}}{\partial t}$$

but allow

$$\nabla_\rho(g_a) \sim \nabla_L(f_{a0})$$

where ρ and L denote scale lengths that g_a and f_{a0} vary on, respectively - we obtain in lowest order $\frac{\partial f_{a0}}{\partial \theta} = 0$. That is, the equilibrium part is independent of the gyro-angle.

In next order, we obtain

$$\frac{\partial f_{a0}}{\partial t} + \frac{\partial g_a}{\partial t} + \dot{\mathbf{R}} \cdot \frac{\partial}{\partial \mathbf{R}}(f_{a0} + g_a) - \Omega_a \frac{\partial g_a}{\partial \theta} + e\frac{\partial \phi}{\partial t}\frac{\partial f_{a0}}{\partial \mathcal{E}} + \dot{\mu}\frac{\partial f_a}{\partial \mu} = C_a, \tag{4.11}$$

where we assumed that

$$\frac{\partial g_a}{\partial \mathcal{E}} \ll \frac{\partial f_{a0}}{\partial \mathcal{E}}$$

$$\frac{\partial g_a}{\partial \mu} \ll \frac{\partial f_{a0}}{\partial \mu}$$

As mentioned at the beginning of this section, we choose the equilibrium distribution function to be represented by a Maxwellian distribution

$$\begin{aligned} f_{a0} &= n_a(\psi)\left(\frac{m_a}{2\pi T_a(\psi)}\right)^{\frac{3}{2}} e^{-\frac{\mathcal{E}}{T_a(\psi)}} \\ &\simeq n_a(\psi)\left(\frac{m_a}{2\pi T_a(\psi)}\right)^{\frac{3}{2}} e^{-\frac{m_a v^2}{2T_a(\psi)}}\left(1 - \frac{e_a\phi}{T_a}\right) \end{aligned} \tag{4.11}$$

In the final step, we have inserted Eqn. 4.7 for $\mathcal{E}$. Here, $n_a(\psi)$ is the density and $T_a(\psi)$ is the temperature, and both of these quantities are assumed to be constant on a flux surface with the flux surface label ψ. The approximation in the exponential term is only possible if we assume the potential to be small, i.e., $\frac{e_a\phi}{T_a} \sim \delta \ll 1$, which will result in the extra term containing the adiabatic response. Noticing that Eqn. 4.11 is independent of both t and μ, it follows that

$$\frac{\partial f_{a0}}{\partial t} = 0$$

$$\frac{\partial f_{a0}}{\partial \mu} = 0$$

and also

$$\frac{\partial f_{a0}}{\partial \mathcal{E}} = -\frac{f_{a0}}{T_a}.$$

Anticipating that the velocity will largely follow the magnetic field lines,

$$\dot{\mathbf{R}} = v_{\parallel}\hat{\mathbf{b}} + \mathcal{O}(\delta v_T)$$

where v_T represents the thermal velocity, we obtain

$$\frac{\partial g_a}{\partial t} + \dot{\mathbf{R}} \cdot \frac{\partial}{\partial \mathbf{R}}(f_{a0} + g_a) - \Omega_a \frac{\partial g_a}{\partial \theta} - \frac{e_a}{T_a}\left(\frac{\partial \phi}{\partial t}\right)_{\mathbf{r}} f_{a0} = C_a \tag{4.12}$$

Before continuing, we will need to introduce gyro-averaging.

> ASIDE
>
> We can now perform the gyro-averaging, which allows us to describe the motion of the gyro-centre **R**. When carrying out the following integral, μ and $\mathcal{E}$ are kept constant. What we are essentially doing, is taking an average over the charged ring (shown in Fig. 4.1), which is centred about **R**
>
> $$\langle f(\mathbf{v}, \mathbf{r}, t, ...)\rangle_{\mathbf{R}} = \frac{1}{2\pi}\int_0^{2\pi} f(\mathbf{v}, \mathbf{r}, t, ...)d\theta$$

We will now return to Eqn. 4.12. Neglecting the $\frac{\partial}{\partial \theta}$ term for now, we can estimate the order of the remaining terms as follows:

$$\left(\frac{\partial g_a}{\partial t} \sim \Omega_a g_a\right) \quad ; \quad (\dot{\mathbf{R}} \sim v_T \simeq \Omega_a \rho) \quad ; \quad \left(\frac{\partial f_{a0}}{\partial \mathbf{R}} \sim \frac{f_{a0}}{L}\right) \quad ; \quad \left(\frac{\partial g_a}{\partial \mathbf{R}} \sim \frac{g_a}{\rho}\right)$$
$$\left(\frac{e_a}{T_a}\left(\frac{\partial \phi}{\partial t}\right)_{\mathbf{r}} f_{a0} \sim \frac{e_a}{T_a}(\Omega_a \phi) f_{a0}\right)$$

To make things clearer, we can multiply each of these terms by a factor of $\frac{1}{\Omega_a f_{a0}}$, which leaves the approximate ordering of the left-hand side of Eqn. 4.12 as follows:

$$\frac{1}{\Omega_a f_{a0}}\left[\Omega_a g_a + \Omega_a \rho \frac{f_{a0}}{L} + \Omega_a \rho \frac{g_a}{\rho} - \Omega_a \frac{\partial g_a}{\partial \theta} - \frac{e_a}{T_a}(\Omega_a \phi) f_{a0}\right]$$
$$\rightarrow \left[\frac{g_a}{f_{a0}} + \frac{\rho}{L} + \frac{g_a}{f_{a0}} + \frac{1}{f_{a0}}\frac{\partial g_a}{\partial \theta} - \frac{e_a \phi}{T_a}\right]$$

Here, all terms are of order $\mathcal{O}(\delta)$, except for $\frac{1}{f_{a0}}\frac{\partial g_a}{\partial \theta}$, which is the largest term. We can thus expand $g_a = g_{a0} + g_{a1} + ...$, yielding in the lowest order

$$\frac{\partial g_{a0}}{\partial \theta} = 0$$

Keeping this in mind, we return to Eqn. 4.12. In the next order, after gyro-averaging while keeping the gyro-centre constant (denoted by $\langle ... \rangle_{\mathbf{R}}$)

$$\frac{\partial g_{a0}}{\partial t} + \langle \dot{\mathbf{R}} \rangle_{\mathbf{R}} \cdot \frac{\partial}{\partial \mathbf{R}} (f_{a0} + g_{a0}) - \frac{e_a}{T_a} \left\langle \left(\frac{\partial \phi}{\partial t} \right)_{\mathbf{r}} \right\rangle_{\mathbf{R}} f_{a0} = \langle C_a \rangle_{\mathbf{R}}. \tag{4.13}$$

We have therefore eliminated the $\frac{\partial}{\partial \theta}$ term. The gyro-averaged velocity can be split into different contributions:

$$\langle \dot{\mathbf{R}} \rangle_{\mathbf{R}} = \frac{1}{2\pi} \oint \dot{\mathbf{R}} d\theta = v_{\parallel} \hat{\mathbf{b}} + \mathbf{v}_E + \mathbf{v}_d$$

where the $\mathbf{E} \times \mathbf{B}$ drift $\mathbf{v}_E$ is

$$\mathbf{v}_E = \frac{\hat{\mathbf{b}} \times \nabla \langle \phi \rangle_{\mathbf{R}}}{B} \tag{4.14}$$

and the magnetic drift $\mathbf{v}_{da}$ is

$$\mathbf{v}_{da} = \frac{\hat{\mathbf{b}}}{\Omega_a} \times \left(\frac{v_{\perp}^2}{2} \nabla \ln B + v_{\parallel}^2 \kappa \right) \tag{4.15}$$

where the latter arises due to the gradient of the magnetic field strength, and the curvature is given by $\kappa = \hat{\mathbf{b}} \cdot \nabla \hat{\mathbf{b}}$.

Using the fact that f_{a0} is a flux function and thus does not vary along the magnetic field lines, $\hat{\mathbf{b}} \cdot \nabla f_{a0} = 0$, and sorting terms containing g_{a0} onto the left-hand side, Eqn. 4.13 becomes

$$\frac{\partial g_{a0}}{\partial t} + \left(v_{\parallel} \hat{\mathbf{b}} + \underbrace{\mathbf{v}_E}_{A} + \mathbf{v}_{da} \right) \cdot \nabla g_{a0} - \langle C_a \rangle_{\mathbf{R}} = - \left(\mathbf{v}_E + \underbrace{\mathbf{v}_{da}}_{B} \right) \cdot \nabla f_{a0} + \frac{e_a}{T_a} \left\langle \left(\frac{\partial \phi}{\partial t} \right)_{\mathbf{r}} \right\rangle_{\mathbf{R}} f_{a0}. \tag{4.16}$$

where the term A is nonlinear in the fluctuations, which means it can be neglected when focusing on a linear stability analysis. The term B gives the neoclassical response in g_{a0}, which simply adds to the fluctuations driven by the other two terms on the right.

It is common convention, as can be seen in [40, 41, 42, 43, 44], that when fluctuations are slowly varying parallel to the magnetic field lines, but vary rapidly across them, it is natural to separate these components and write the perturbation in the following way:

$$\phi(\mathbf{r}, t) = \hat{\phi}(\mathbf{r}) e^{i(\mathbf{k} \cdot \mathbf{x})} = \hat{\phi}(\mathbf{r}) e^{i\left(\frac{S(\mathbf{r})}{\delta} - \omega t \right)} \tag{4.17}$$

where $\hat{\phi}(\mathbf{r})$ is the slowly varying amplitude of the perturbation, which is assumed to vary on the long spatial scale ($\mathcal{O}(L)$) parallel with the field, and the fast variation is found in the phase factor $\left(\frac{S(\mathbf{r})}{\delta} - \omega t \right)$, which varies on the short spatial scale ($\mathcal{O}(\rho)$) perpendicular with the field. This phase factor can be obtained as follows:

$$(\mathbf{k} \cdot \mathbf{x}) = (\mathbf{k}_{\mu} \mathbf{x}^{\mu}) = (- \underbrace{k_0}_{\omega} t + \overrightarrow{\mathbf{k}} \underbrace{\overrightarrow{\mathbf{x}}}_{\mathbf{r}}) = (-\omega t + \overrightarrow{\mathbf{k}} \mathbf{r}) = \left(\frac{S(\mathbf{r})}{\delta} - \omega t \right)$$

Here, we can think of the spatial component of the wavevector $\overrightarrow{\mathbf{k}}$ comprising parallel and perpendicular components, $\mathbf{k}_{\parallel}$ and $\mathbf{k}_{\perp}$, respectively.

$$\overrightarrow{\mathbf{k}} = \mathbf{k}_{\parallel} + \mathbf{k}_{\perp}$$

If we take a spatial derivative (∇) of Eqn. 4.17, we can see that

$$\overrightarrow{\mathbf{k}} = \frac{\nabla S}{\delta} = \frac{1}{\delta}\left(\nabla_{\parallel} S + \nabla_{\perp} S\right) \implies \left(\mathbf{k}_{\parallel} = \frac{\nabla_{\parallel} S}{\delta}\right) \quad \text{and} \quad \left(\mathbf{k}_{\perp} = \frac{\nabla_{\perp} S}{\delta}\right) \tag{4.18}$$

It can be seen from utilising the work of [8, 40, 41, 42, 45, 46, 47, 48, 49], that the ballooning transform allows us to assume $\nabla_{\parallel} S \simeq 0$, i.e.,

$$(\nabla_{\parallel} S \ll \nabla_{\perp} S) \equiv (\mathbf{k}_{\parallel} \ll \mathbf{k}_{\perp})$$

and so,

$$\mathbf{k}_{\perp} \simeq \frac{\nabla S}{\delta}. \tag{4.19}$$

where $\mathbf{k}_{\perp}\rho = \mathcal{O}(1)$, as the perturbations perpendicular to the field lines are on the order of the Larmor radius, ρ. The ballooning transform is a highly non-trivial mathematical tool widely used in magnetic confinement fusion literature, but it will not be discussed further in this report. A detailed explanation of this abstract concept can be found in [50].

Then we can write

$$\left\langle \left(\frac{\partial \phi}{\partial t}\right)_{\mathbf{r}} \right\rangle_{\mathbf{R}} = -i\omega \langle \phi(\mathbf{R}+\rho)\rangle_{\mathbf{R}} \simeq -i\omega \hat{\phi}(\mathbf{R}) e^{-i\omega t} \left\langle e^{\frac{iS(\mathbf{R}+\rho)}{\delta}} \right\rangle_{\mathbf{R}}$$

where

$$\left\langle e^{\frac{iS(\mathbf{R}+\rho)}{\delta}} \right\rangle_{\mathbf{R}} \simeq e^{\frac{iS(\mathbf{R})}{\delta}} \left\langle e^{i\mathbf{k}_{\perp}\cdot\rho} \right\rangle_{\mathbf{R}} = J_0\left(\frac{k_{\perp} v_{\perp}}{\Omega_a}\right) e^{\frac{iS(\mathbf{R})}{\delta}}$$

so that

$$\left\langle \left(\frac{\partial \phi}{\partial t}\right)_{\mathbf{r}} \right\rangle_{\mathbf{R}} = -i\omega J_0\left(\frac{k_{\perp} v_{\perp}}{\Omega_a}\right) \phi(\mathbf{R}, t)$$

Here, we have used the integral defining the Bessel Function of zeroth order

$$\int_0^{2\pi} e^{ix\sin\theta} d\theta = \int_0^{2\pi} \cos(x\sin\theta) d\theta + \underbrace{\int_0^{2\pi} \sin(x\sin\theta) d\theta}_{=0} = 2\pi J_0(x).$$

Now consider the remaining terms on the right-hand side of Eqn. 4.16

$$\begin{aligned} -\mathbf{v}_E \cdot \nabla f_{a0} &= -\frac{\hat{\mathbf{b}} \times \nabla \langle \phi \rangle_{\mathbf{R}}}{B} \cdot \nabla f_{a0} \\ &= \frac{\nabla \langle \phi \rangle_{\mathbf{R}} \times \hat{\mathbf{b}}}{B} \cdot \nabla f_{a0} \\ &= \frac{\nabla \langle \phi \rangle_{\mathbf{R}}}{B} \cdot \hat{\mathbf{b}} \times \nabla f_{a0} \end{aligned}$$

Here

$$\begin{aligned}
\nabla\langle\phi\rangle_{\mathbf{R}} &= \nabla\langle\phi(\mathbf{R}+\rho)\rangle_{\mathbf{R}} \\
&\simeq \nabla\left[\hat{\phi}(\mathbf{R})\left\langle e^{\frac{iS(\mathbf{R}+\rho)}{\delta}}\right\rangle_{\mathbf{R}} e^{-i\omega t}\right] \\
&\simeq \nabla\left[\hat{\phi}(\mathbf{R})e^{-i\omega t}e^{\frac{iS(\mathbf{R})}{\delta}}J_0\left(\frac{k_\perp v_\perp}{\Omega_a}\right)\right] \\
&\simeq \underbrace{\hat{\phi}(\mathbf{R})e^{-i\omega t}e^{\frac{iS(\mathbf{R})}{\delta}}}_{\phi(\mathbf{R},t)} i\frac{\nabla S}{\delta}J_0\left(\frac{k_\perp v_\perp}{\Omega_a}\right) \quad \text{because} \quad \frac{\nabla S}{\delta} \gg \frac{\nabla\hat{\phi}(\mathbf{R})}{\hat{\phi}(\mathbf{R})} \\
&\simeq i\mathbf{k}_\perp J_0\left(\frac{k_\perp v_\perp}{\Omega_a}\right)\phi(\mathbf{R},t).
\end{aligned}$$

Thus, we obtain

$$-\mathbf{v}_E\cdot\nabla f_{a0} = iJ_0\left(\frac{k_\perp v_\perp}{\Omega_a}\right)\phi(\mathbf{R},t)\left(\frac{1}{B}\right)\mathbf{k}_\perp\cdot\hat{\mathbf{b}}\times\nabla f_{a0} \tag{4.20}$$

Also, we can see that

$$\left(\frac{k_\perp v_\perp}{\Omega_a}\right) = k_\perp\rho = \mathcal{O}(1).$$

Since the equilibrium distribution function f_{a0} is a flux-function, the spatial derivative can be expressed as

$$\nabla f_{a0} = \frac{\partial f_{a0}}{\partial\psi}\nabla\psi$$

where ψ is a radial coordinate within the plasma, which indicates which nested flux surface we are considering. We can think of ψ as a flux surface label, and so $\nabla\psi$ points in the direction of increasing minor radius.

If the magnetic field has the form

$$\mathbf{B} = B\cdot\hat{\mathbf{b}} = \nabla\psi\times\nabla\alpha$$

where α can be thought of as a field line labelling coordinate (with $\nabla\alpha$ pointing tangential to the flux surface, and perpendicular to the magnetic field lines), the perpendicular wave vector can be written in terms of the two components perpendicular to $\mathbf{B}$

$$\mathbf{k}_\perp = k_\psi\nabla\psi + k_\alpha\nabla\alpha$$

Accordingly, Eqn. 4.20 can be simplified further

$$\begin{aligned}
-\mathbf{v}_E \cdot \nabla f_{a0} &= iJ_0\phi \frac{\hat{\mathbf{b}} \cdot (\nabla\psi \times \mathbf{k}_\perp)}{B} \frac{\partial f_{a0}}{\partial \psi} \\
&= iJ_0\phi k_\alpha \frac{\hat{\mathbf{b}} \cdot (\nabla\psi \times \nabla\alpha)}{B} \frac{\partial f_{a0}}{\partial \psi} \\
&= iJ_0\phi k_\alpha \frac{\hat{\mathbf{b}} \cdot (B \cdot \hat{\mathbf{b}})}{B} \frac{\partial f_{a0}}{\partial \psi} \\
&= iJ_0\phi k_\alpha \frac{\partial f_{a0}}{\partial \psi}
\end{aligned}$$

Now, focusing on the partial derivative of the equilibrium distribution function, we can insert the first line of Eqn. 4.11 for f_{a0} here

$$\begin{aligned}
\frac{\partial f_{a0}}{\partial \psi} &= \frac{\partial}{\partial \psi}\left(n_a(\psi)\left(\frac{m_a}{2\pi T_a(\psi)}\right)^{\frac{3}{2}}\right) e^{-\frac{\mathcal{E}}{T_a(\psi)}} + \underbrace{\left(n_a(\psi)\left(\frac{m_a}{2\pi T_a(\psi)}\right)^{\frac{3}{2}}\right) e^{-\frac{\mathcal{E}}{T_a(\psi)}}}_{f_{a0}} \cdot \left(\frac{\mathcal{E}\frac{\partial T_a}{\partial \psi}}{T_a(\psi)^2}\right) \\
&= \left[\frac{\partial n_a}{\partial \psi}\left(\frac{m}{2\pi T(\psi)}\right)^{\frac{3}{2}} + n_a(\psi)\left(\frac{3}{2}\left(\frac{m}{2\pi T_a(\psi)}\right)^{\frac{1}{2}} \cdot \underbrace{\left(\frac{-2\pi m \frac{\partial T_a}{\partial \psi}}{(2\pi T_a(\psi))^2}\right)}_{=-\left(\frac{m}{2\pi T_a(\psi)}\right)\frac{\partial \ln T_a}{\partial \psi}}\right)\right] e^{-\frac{\mathcal{E}}{T_a(\psi)}} + f_{a0}\underbrace{\left(\frac{\mathcal{E}\frac{\partial T_a}{\partial \psi}}{T_a(\psi)^2}\right)}_{\frac{\mathcal{E}}{T_a(\psi)}\frac{\partial \ln T_a}{\partial \psi}}
\end{aligned}$$

Now simplifying the term in square brackets, including the exponential outside it, we obtain

$$\underbrace{\frac{1}{n_a(\psi)}\frac{\partial n_a}{\partial \psi}}_{\frac{\partial \ln n_a}{\partial \psi}} \underbrace{\left(n_a(\psi)\left(\frac{m_a}{2\pi T_a(\psi)}\right)^{\frac{3}{2}}\right) e^{-\frac{\mathcal{E}}{T_a(\psi)}}}_{f_{a0}} + \left(-\frac{3}{2}\frac{\partial \ln T_a}{\partial \psi}\right) \underbrace{\left(n_a(\psi)\left(\frac{m_a}{2\pi T_a(\psi)}\right)^{\frac{3}{2}}\right) e^{-\frac{\mathcal{E}}{T_a(\psi)}}}_{f_{a0}}$$

Finally, this gives us our expression for $\frac{\partial f_{a0}}{\partial \psi}$

$$\frac{\partial f_{a0}}{\partial \psi} = \left[\frac{d \ln n_a}{d\psi} + \left(\frac{\mathcal{E}}{T_a} - \frac{3}{2}\right)\frac{d \ln T_a}{d\psi}\right] f_{a0}$$

where we have replaced the partial derivatives with full derivatives, as n and T are functions of ψ only. We can now return to our simplified form of Eqn. 4.20, inserting this result for $\frac{\partial f_{a0}}{\partial \psi}$,

$$\begin{aligned}
-\mathbf{v}_E \cdot \nabla f_{a0} &= iJ_0\phi k_\alpha \left[\frac{d \ln n_a}{d\psi} + \left(\frac{\mathcal{E}}{T_a} - \frac{3}{2}\right)\frac{d \ln T_a}{d\psi}\right] f_{a0} \\
&= iJ_0 \frac{e_a \phi}{T_a} \omega_{*a}^T f_{a0}
\end{aligned}$$

where we define the velocity dependent diamagnetic drift frequency ω_{*a}^T as follows

$$\begin{aligned}\omega_{*a}^T &= \omega_{*a}\left[1+\eta_a\left(\frac{\mathcal{E}}{T_a}-\frac{3}{2}\right)\right]\\ \omega_{*a} &= \frac{T_a k_\alpha}{e_a}\frac{d\ln n_a}{d\psi}\\ \eta_a &= \frac{d\ln T_a}{d\psi}\Big/\frac{d\ln n_a}{d\psi}\end{aligned} \tag{4.21}$$

For the remaining terms, we Fourier transform g_{a0} and separate the slow and fast variation

$$g_{a0}(\mathbf{R},\mathcal{E},\mu,t) = \hat{g}_a(\mathbf{R},\mathcal{E},\mu)e^{i\left(\frac{S(\mathbf{R})}{\delta}-\omega t\right)} \tag{4.22}$$

Hence

$$\begin{aligned}\frac{\partial g_{a0}}{\partial t}+\left(v_\parallel\hat{\mathbf{b}}+\mathbf{v}_{da}\right)\cdot\nabla g_{a0} &\simeq \left[-i\omega\hat{g}_a+v_\parallel\nabla_\parallel\hat{g}_a+\mathbf{v}_{da}\cdot\underbrace{\frac{\nabla S}{\delta}}_{\mathbf{k}_\perp}\hat{g}_a\right]e^{i\left(\frac{S(\mathbf{R})}{\delta}-\omega t\right)}\\ &\simeq \left[v_\parallel\nabla_\parallel\hat{g}_a-i(\omega-\omega_{da})\hat{g}_a\right]e^{i\left(\frac{S(\mathbf{R})}{\delta}-\omega t\right)}\end{aligned}$$

where we define the magnetic drift frequency as

$$\omega_{da} = \mathbf{k}_\perp\cdot\mathbf{v}_{da}$$

and we also used the fact that

$$\nabla_\parallel S = 0 \quad \text{and} \quad \frac{\nabla S}{\delta} \gg \frac{\nabla\hat{g}_a(\mathbf{R})}{\hat{g}_a(\mathbf{R})}$$

With the terms A and B introduced in Eqn. 4.16, the gyrokinetic equation becomes

$$v_\parallel\nabla_\parallel\hat{g}_a-i(\omega-\omega_{da})\hat{g}_a-e^{-i\left(\frac{S(\mathbf{R})}{\delta}\right)}\left\langle C_a\left(\hat{g}_a e^{+i\left(\frac{S(\mathbf{R})}{\delta}\right)}\right)\right\rangle_{\mathbf{R}} = -\frac{ie_a}{T_a}J_0\hat{\phi}\left(\omega-\omega_*^T a\right)f_{a0}$$

In fact, collisions can be neglected, since the collision frequency is usually small compared with the frequencies of the observed instability modes. So we can set $C_a \simeq 0$. Also the hats will be omitted from both the perturbed distribution function and the electrostatic potential. The dependence on the frequency ω and the slow variation in space will be implied. Therefore, the gyrokinetic equation can be written in the following form:

$$v_\parallel\nabla_\parallel g_a-i(\omega-\omega_{da})g_a = -\frac{ie_a}{T_a}J_0\phi\left(\omega-\omega_{*a}^T\right)f_{a0} \tag{4.23}$$

This concludes the derivation of the gyrokinetic equation. In the next section, we complete our set of equations by implementing the quasi-neutrality condition. This will conclude the establishment of our mathematical framework, which will be built upon to perform the main derivations of this project in Chapters 5 and 6.

4.3 The Quasi-Neutrality Condition

In this section, we formulate the quasi-neutrality (QN) condition, which is based on the principle that our plasma has a net charge of zero. The derivation carried out here is taken directly from [12]. This condition will prove very important in later chapters, as it completes our set of equations required for further derivations.

We start with the Poisson equation

$$\nabla^2\phi = \frac{e(n_e - n_i)}{\epsilon_0}$$

where n_e and n_i denote the electron and ion densities, respectively. Assuming a typical plasma temperature T_0, we can define a dimensionless potential

$$\varphi = \frac{e\phi}{T_0} \tag{4.24}$$

hence

$$\nabla^2\varphi = \frac{e^2(n_e - n_i)}{\epsilon_0 T_0}$$

We will now assume that the ion and electron densities are approximately equal to the common value n_0, but each having a small deviation of δn_a

$$n_e = n_0 + \delta n_e$$
$$n_i = n_0 + \delta n_i$$

The Poisson equation then becomes

$$\nabla^2\varphi = \frac{n_0 e^2}{\epsilon_0 T_0}\frac{(\delta n_e - \delta n_i)}{n_0} = \frac{(\delta n_e - \delta n_i)}{n_0 \lambda_D^2}$$

where we have inserted the Debye length, given by

$$\lambda_D = \sqrt{\frac{\epsilon_0 T_0}{n_0 e^2}}$$

which is a shielding parameter that denotes the length after which the electrostatic potential of a point charge has dropped to $\frac{1}{e}$ of its Coulomb value. In fusion plasmas, the Debye length is usually one of the smallest length scales in the system.

Noting that $\varphi \leq \mathcal{O}(1)$ and that the potential varies on a length scale L, such that $\nabla\varphi \sim \frac{1}{L}$, we find

$$\frac{(\delta n_e - \delta n_i)}{n_0} = \lambda_D^2 \nabla^2 \varphi \sim \left(\frac{\lambda_D}{L}\right)^2 \tag{4.25}$$

Therefore, we have two options presented to us. Firstly, we can think of the deviations from QN being large, which means that the two increments in particle density differ by a substantial amount (i.e., $\Delta\delta n_a$ is large), which means that the resulting electric potential needs to vary on length scales comparable to λ_D, in order for the above equation to be satisfied. On the other hand, if the length scales of the potential are large compared with λ_D (i.e., $L \gg \lambda_D$), then the density increments must cancel ($\Delta\delta n_a \overset{!}{=} 0$). Thus, we obtain the QN condition

$$\begin{aligned}
\sum_{a=i,e} e_a \delta n_a &= e_i \delta n_i + e_e \delta n_e \\
&= +e\delta n_i - e\delta n_e \\
&= e\underbrace{(\delta n_i - \delta n_e)}_{=0} \\
&= 0
\end{aligned}$$

which we will state more concisely as

$$\boxed{\sum_{a=i,e} e_a \delta n_a = 0} \tag{4.26}$$

The density perturbations can be calculated as follows

$$\delta n_a(\mathbf{r}, t) = \int_{r=const} (f_{a0} + g_{a0}) d\mathbf{v} - n_a(\mathbf{r})$$

where

$$\begin{aligned}
\int f_{a0} d\mathbf{v} &= n_a \left(1 - \frac{e_a \phi}{T_a}\right) \\
&= n_a - \frac{n_a e_a \phi}{T_a}
\end{aligned}$$

and

$$\begin{aligned}
\int g_{a0} d\mathbf{v} &= \int_{r=const} \hat{g}_a(\mathbf{R}, \mathcal{E}, \mu) e^{i\left(\frac{S(\mathbf{R})}{\delta} - \omega t\right)} d\mathbf{v} \\
&\simeq \int \hat{g}_a(\mathbf{R}, \mathcal{E}, \mu) e^{i\left(\frac{S(\mathbf{r})}{\delta} - \mathbf{k}_\perp \cdot \rho - \omega t\right)} v_\perp dv_\perp dv_\parallel d\theta \\
&= e^{i\left(\frac{S(\mathbf{r})}{\delta} - \omega t\right)} \int \hat{g}_a(\mathbf{R}, \mathcal{E}, \mu) J_0\left(\frac{k_\perp v_\perp}{\Omega_a}\right) 2\pi v_\perp dv_\perp dv_\parallel
\end{aligned}$$

where in the intermediate step, we applied the following

$$\begin{aligned}
\mathbf{R} &= \mathbf{r} + \frac{\hat{\mathbf{b}} \times \mathbf{v}}{\Omega_a} \\
&= \mathbf{r} - \frac{v_\perp}{\Omega_a} \\
&= \mathbf{r} - \rho
\end{aligned}$$

and inserted this into

$$\begin{aligned}\frac{S(\mathbf{R})}{\delta} &= \frac{S(\mathbf{r}-\rho)}{\delta} \\ &\simeq \frac{S(\mathbf{r})}{\delta} - \frac{S(\rho)}{\delta} \\ &= \frac{S(\mathbf{r})}{\delta} - \mathbf{k}_\perp \cdot \rho\end{aligned}$$

With all of this now expanded, let's insert everything into the QN condition (Eqn. 4.26)

$$\begin{aligned}\sum_{a=i,e} e_a \delta n_a &= \sum_{a=i,e} e_a \left[\int_{r=const} (f_{a0} + g_{a0}) d\mathbf{v} - n_a(\mathbf{r}) \right] \\ &= \sum_{a=i,e} e_a \left[\int_{r=const} (g_{a0}) d\mathbf{v} + n_a(\mathbf{r}) - \frac{n_a e_a \phi}{T_a} - n_a(\mathbf{r}) \right] \\ &= \sum_{a=i,e} e_a \left[e^{i\left(\frac{S(\mathbf{r})}{\delta} - \omega t\right)} \int \hat{g}_a(\mathbf{R}, \mathcal{E}, \mu) J_0 \left(\frac{k_\perp v_\perp}{\Omega_a} \right) 2\pi v_\perp dv_\perp dv_\parallel d\mathbf{v} - \frac{n_a e_a \phi}{T_a} \right]\end{aligned} \tag{4.27}$$

where in the final step, we used the following expression for g_{a0}

$$g_{a0}(\mathbf{R}, \mathcal{E}, \mu, t) = \hat{g}_a(\mathbf{R}, \mathcal{E}, \mu) e^{i\left(\frac{S(\mathbf{R})}{\delta} - \omega t\right)}$$

Now, as in accordance with Eqn. 4.26, the result of Eqn. 4.27 must equal zero. With this in mind, and using the fact that ϕ can be expressed using

$$\phi(\mathbf{r}, t) = \hat{\phi}(\mathbf{r}) e^{i\left(\frac{S(\mathbf{r})}{\delta} - \omega t\right)}$$

Eqn. 4.27, becomes

$$\sum_{a=i,e} \frac{n_a e_a^2}{T_a} \hat{\phi}(\mathbf{r}) e^{i\left(\frac{S(\mathbf{r})}{\delta} - \omega t\right)} = \sum_{a=i,e} e_a \left[e^{i\left(\frac{S(\mathbf{r})}{\delta} - \omega t\right)} \int \hat{g}_a(\mathbf{R}, \mathcal{E}, \mu) J_0 \left(\frac{k_\perp v_\perp}{\Omega_a} \right) 2\pi v_\perp dv_\perp dv_\parallel d\mathbf{v} \right]$$

Now, we can see that the fast variation captured by the exponential terms $\left(e^{i\left(\frac{S(\mathbf{r})}{\delta} - \omega t\right)} \right)$ will cancel on both sides, and we will subsequently drop the hats for the slowly varying amplitudes of ϕ and g_a, giving us our final result

$$\boxed{\sum_{a=i,e} \frac{n_a e_a^2}{T_a} \phi = \sum_{a=i,e} e_a \int g_a(\mathbf{R}, \mathcal{E}, \mu) J_0 \left(\frac{k_\perp v_\perp}{\Omega_a} \right) d\mathbf{v}} \tag{4.28}$$

making our set of equations complete.

This result will be essential for the upcoming analytical derivations in this report, whereby we use Eqn. 4.28 as the starting point for deriving approximations to the TEM ω proxy (Chapter 5), as well as for developing a proxy for the critical density gradient (Chapter 6).

Part II

Methodology

Methodology Overview

We begin this part of the report by first providing a brief overview of our strategy for obtaining a suitable proxy for the critical density gradient of the TEM. This will concisely describe our methods for achieving the main goals of this project, and thus will help to motivate the following chapters. Our methodology from here relies on the results of our gyrokinetic framework, which was established in Chapter 4. From this starting point, we wish to find an analytical expression for the dispersion relation $\omega(k)$, and calculate this relation at the point of marginal stability. This point of marginal stability occurs for

$$\omega = \omega_r + i\gamma \text{ when } \gamma \to 0^+ \tag{4.29}$$

where ω is the mode frequency of the instability, ω_r is the real part of this frequency, and γ is the growth rate of the mode. This is carried out for two separate approaches in sections 6.1 and 6.2. The relevant results from those sections are Eqn. 6.66 and Eqn. 6.71, respectively. It should be noted that the latter of these results needs to be combined with Eqn. 5.105 in order to be meaningful. We find that these results are dependent on the geometric quantities (magnetic field strength B and curvature profile κ), the perpendicular wavenumber ($k_\perp$), and the density gradient $\left(\frac{a}{L_n}\right)$. This implies that for a particular geometric configuration and chosen wavenumber, our results at marginal stability can only be satisfied by the critical density gradient. If the density gradient is above or below this value, then we are no longer considering the point of marginal stability.

We also see that our results, Eqn. 6.66 and Eqn. 6.71, depend on the real part of the mode frequency ω_r, which is not immediately known to us. Therefore, we make use of a variational principle technique in section 5.2, which allows us to develop an analytical proxy for this quantity. However, developing this approximation requires knowledge of the mode structure, given by ϕ. To first test the validity of our mode frequency proxy, we can utilise ϕ-data output from gyrokinetic simulations. Specifically, we utilise data output from the GENE code (Gyrokinetic Electromagnetic Numerical Experiment). This GENE software carries out 5D gyrokinetic supercomputer simulations to obtain data on micro-instabilities [13]. Although turbulence is an intrinsically non-linear phenomenon, GENE can be run in a linear and non-linear way to simulate the behaviour of the underlying micro-instabilities [12]. For this project, only a linear investigation is undertaken. Ideally, we would like to be able to complete this procedure without any dependence on such simulation data. Thus, we can attempt to predict the mode structure profile, based on our knowledge of the TEM instability and its dependence on the geometry at hand. When this has been achieved, we insert our proxy for the mode frequency into our aforementioned results, Eqn. 6.66 and Eqn. 6.71, and subsequently, we extract our proxy for the critical density gradient. All numerical results produced from our analytical methods are presented in Chapter 7.

Chapter 5

The Mode Frequency Proxy

In this chapter, we explore how the mode frequency ω of our TEM instability can be estimated analytically by use of a variational principle technique. This exploration is carried out in consecutive stages. To begin, we foreshadow the use of the variational principle by looking at a very general case, which is explained heuristically for now. A more rigorous and detailed approach is given later in the chapter, when we need to actively put this procedure into practice. This is followed by our full analytical derivation for the mode frequency ω, whereby it is assumed that the ions and electrons are behaving as passing and trapped particles, respectively. The resulting expression for ω is to be used in Chapter 6 as a proxy function for the actual mode frequency of the TEM instability. The accuracy of this proxy function is measured qualitatively by comparing the analytical results with gyrokinetic simulation output from the aforementioned GENE code. The mode frequency proxy procedure has already been shown to work sufficiently well in the simpler tokamak geometry [18, 19, 12], yet it has not been tested hitherto for the more complicated stellarator geometries. The results of this investigation will be presented for various geometrical configurations in Chapter 7. An alternative mode frequency proxy derivation can be found in Appendix A, whereby both particle species are treated solely as trapped particles. This alternative derivation is not utilised in the remainder of this body of work, but has been included in this report for completion's sake.

5.1 Understanding the Variational Principle

In this section, we will give a brief heuristic argument of why and how the variational principle is used in our analytical procedure. This argument is taken primarily from [18]. A better understanding of this principle will be gained in later sections when we implement it directly during our upcoming derivations - in particular, see section 5.2. However, we will foreshadow its later use in this section, to help familiarise ourselves with the concept before engaging with it in

practice.

We start by looking at the following general integral equation

$$\boxed{f(\omega,l)\phi(l) = B\int_{\frac{1}{B_{max}}}^{\frac{1}{B_{min}}} g(\omega,\lambda)\overline{\phi}(\lambda)\frac{d\lambda}{\sqrt{1-\lambda B}}} \tag{5.1}$$

which will be explored in greater detail later in this report. For now, all we need to know is that the left-hand side corresponds to the ions in the system, whilst the right-hand side corresponds to the electrons. It should be noted that in this particular example, the ions are being treated as passing particles and the electrons are being treated as trapped particles [12]. It seems that this integral equation is not solvable by analytical means. However, it can be reformulated as a variational principle, whereby the variational quantity is the mode frequency ω [18].

To reformulate Eqn. 5.1 as a variational principle, we first obtain a real expression by multiplying across by $\frac{\phi^*}{B}$, and subsequently we integrate along the field line $\int dl$, giving

$$\int_{-\infty}^{\infty} f(\omega,l)|\phi|^2\frac{dl}{B} = \int_{\frac{1}{B_{max}}}^{\frac{1}{B_{min}}}\int_{-\infty}^{\infty}\frac{dl}{\sqrt{1-\lambda B}}g(\omega,\lambda)|\overline{\phi}|^2 d\lambda \tag{5.2}$$

We can rearrange this slightly and write it as a functional as follows:

$$S[\phi,\omega] \equiv \int_{-\infty}^{\infty} f(\omega,l)|\phi|^2\frac{dl}{B} - \int_{\frac{1}{B_{max}}}^{\frac{1}{B_{min}}}\int_{-\infty}^{\infty}\frac{dl}{\sqrt{1-\lambda B}}g(\omega,\lambda)|\overline{\phi}|^2 d\lambda = 0 \tag{5.3}$$

which is a quadratic equation for the mode frequency ω when the mode structure ϕ is known. We can now vary this functional with respect to ϕ to give

$$\delta S[\phi,\omega] = \int_{-\infty}^{\infty}\left(\frac{\delta f}{\delta\omega}\delta\omega|\phi|^2 + 2f\phi\delta\phi\right)\frac{dl}{B} - \int_{\frac{1}{B_{max}}}^{\frac{1}{B_{min}}}\int_{-\infty}^{\infty}\frac{dl}{\sqrt{1-\lambda B}}\left(\frac{\delta g}{\delta\omega}\delta\omega|\overline{\phi}|^2 + 2g\overline{\phi}\delta\overline{\phi}\right)d\lambda = 0 \tag{5.4}$$

where some intermediate steps have not been shown, but will be detailed later in section 5.2. This varied expression can now be rearranged to give

$$\begin{aligned}\delta\omega\left(\int_{-\infty}^{\infty}\frac{\delta f}{\delta\omega}|\phi|^2\frac{dl}{B} - \int_{\frac{1}{B_{max}}}^{\frac{1}{B_{min}}}\int_{-\infty}^{\infty}\frac{dl}{\sqrt{1-\lambda B}}\frac{\delta g}{\delta\omega}|\overline{\phi}|^2 d\lambda\right)\\ = -2\int_{-\infty}^{\infty} f\phi\delta\phi\frac{dl}{B} + 2\int_{\frac{1}{B_{max}}}^{\frac{1}{B_{min}}}\int_{-\infty}^{\infty}\frac{dl}{\sqrt{1-\lambda B}}g\overline{\phi}\delta\overline{\phi}d\lambda\end{aligned} \tag{5.5}$$

and this can be rewritten to obtain an expression for $\delta\omega$:

$$\delta\omega = \frac{-2\int_{-\infty}^{\infty}\delta\phi\frac{dl}{B}\left(f\phi - B\int_{\frac{1}{B_{max}}}^{\frac{1}{B_{min}}}\frac{g\overline{\phi}}{\sqrt{1-\lambda B}}d\lambda\right)}{\left(\int_{-\infty}^{\infty}\frac{\delta f}{\delta\omega}|\phi|^2\frac{dl}{B} - \int_{\frac{1}{B_{max}}}^{\frac{1}{B_{min}}}\int_{-\infty}^{\infty}\frac{dl}{\sqrt{1-\lambda B}}\frac{\delta g}{\delta\omega}|\overline{\phi}|^2 d\lambda\right)} \tag{5.6}$$

We can now see that the expression in parenthesis in our numerator here is simply the integral equation we started with, Eqn. 5.1. Thus, we obtain $\delta\omega = 0$ when Eqn. 5.1 is satisfied by the correct inputs for (ϕ, ω). Conversely, if $\delta\omega = 0$ for all variations $\delta\phi$, then Eqn. 5.1 is fulfilled [18]. This latter case is then somewhat equivalent to a variational principle. And so, instead of needing to solve Eqn. 5.1 - which cannot be done analytically, as already mentioned - a decent approximation to the value of ω should be obtainable by inserting an appropriately chosen trial function for ϕ into Eqn. 5.3. If one utilises the Rayleigh-Ritz optimisation technique, then the systematic way of finding a suitable mode structure ϕ is to create a trial function containing one or more free parameters p_i, such that our trial function becomes $\phi(l, p_1, p_2, ...)$ [51]. This trial function would then be inserted into our functional expression $S[\phi, \omega]$, which then becomes a function of ω and the free parameters p_i. The aim would then be to minimise this functional with respect to these free parameters, such that our system of equations becomes:

$$\begin{aligned} S[\omega, p_1, p_2, ...] &= 0 \\ \frac{\partial S}{\partial p_i} &= 0 \end{aligned} \tag{5.7}$$

Completing this procedure would then yield an approximate solution for the eigenvalue problem, Eqn. 5.1, by generating sufficient approximations for ϕ and ω.

This very useful technique means that we circumvent the need to solve the difficult integral equation we started with, Eqn. 5.1, and also, we obtain the eigenvalue ω with enhanced precision. This is due to the fact that if there is an error of order ϵ made in the trial eigenfunction ϕ (where $\epsilon < 1$), then the resulting error to the eigenvalue ω is of order ϵ^2.

5.2 Developing the Mode Frequency Proxy

In this section, we derive a proxy for the mode frequency ω of the TEM instability in stellarator geometry, where it is assumed that the ions are behaving as passing particles and the electrons are behaving as trapped particles. The approach taken here is a rederivation of the work carried out in [18, 12, 52], with some steps expanded for clarity. In those works, this procedure was applied to the simpler tokamak geometry only. In this project, however, the results of this section are applied to the more complex geometry of stellarators.

We begin our derivation by reminding ourselves of the QN condition result:

$$\boxed{\sum_{a=i,e} \frac{n_a e_a^2}{T_a}\phi = \sum_{a=i,e} e_a \int g_a(\mathbf{R}, \mathcal{E}, \mu) J_0 \left(\frac{k_\perp v_\perp}{\Omega_a}\right) d\mathbf{v}} \tag{5.8}$$

Expanding the sum over each particle species a gives

$$\frac{n_i e_i^2}{T_i}\phi + \frac{n_e e_e^2}{T_e}\phi = e_i \int g_i(\mathbf{R},\mathcal{E},\mu) J_0\left(\frac{k_\perp v_\perp}{\Omega_i}\right) d\mathbf{v} + e_e \int g_e(\mathbf{R},\mathcal{E},\mu) J_0\left(\frac{k_\perp v_\perp}{\Omega_e}\right) d\mathbf{v} \tag{5.9}$$

Now, using that

$$\begin{aligned} n_i &= n_e = n \\ e_i^2 &= e_e^2 = e^2 \end{aligned} \tag{5.10}$$

changes the equation to

$$\frac{ne^2}{T_i}\phi + \frac{ne^2}{T_e}\phi = (+e) \int g_i(\mathbf{R},\mathcal{E},\mu) J_0\left(\frac{k_\perp v_\perp}{\Omega_i}\right) d\mathbf{v} + (-e) \int g_e(\mathbf{R},\mathcal{E},\mu) J_0\left(\frac{k_\perp v_\perp}{\Omega_e}\right) d\mathbf{v} \tag{5.11}$$

and subsequently multiplying across by $\frac{T_e}{ne^2}$ gives

$$\frac{T_e}{T_i}\phi + \phi = \frac{T_e}{ne} \int g_i(\mathbf{R},\mathcal{E},\mu) J_0\left(\frac{k_\perp v_\perp}{\Omega_i}\right) d\mathbf{v} - \frac{T_e}{ne} \int g_e(\mathbf{R},\mathcal{E},\mu) J_0\left(\frac{k_\perp v_\perp}{\Omega_e}\right) d\mathbf{v} \tag{5.12}$$

As done in [12], the following distinct expressions for g_i and g_e are used, which correspond to the non-adiabatic portion of the distribution function for the ions and electrons, respectively. At this point, it is important to mention again that the ions are treated solely as passing particles, and the electrons are treated solely as trapped particles. There are, in reality, both passing and trapped portions of both particle species, but this assumption is suitable for the purpose of this derivation. The g_a expressions are as follows:

$$\begin{aligned} g_{i(passing)} &= \frac{e_i\phi}{T_i}\frac{(\omega-\omega_{*i}^T)}{(\omega-\omega_{di})} J_0 f_{i0} \\ g_{e(trapped)} &= \frac{e_e}{T_e}\overline{J_0\phi}\frac{(\omega-\omega_{*e}^T)}{(\omega-\overline{\omega}_{de})} f_{e0} \end{aligned} \tag{5.13}$$

Inserting these expressions into Eqn. 5.12, and using $e_i = -e_e = e$, gives

$$\begin{aligned} \left(\frac{T_e}{T_i}+1\right)\phi &= \frac{T_e}{ne}\int \frac{e\phi}{T_i}\frac{(\omega-\omega_{*i}^T)}{(\omega-\omega_{di})} J_0 f_{i0} J_0\left(\frac{k_\perp v_\perp}{\Omega_i}\right) d\mathbf{v} + \frac{T_e}{ne}\int_{trapped} \frac{e}{T_e}\overline{J_0\phi}\frac{(\omega-\omega_{*e}^T)}{(\omega-\overline{\omega}_{de})} f_{e0} J_0\left(\frac{k_\perp v_\perp}{\Omega_e}\right) d\mathbf{v} \\ &= \frac{\phi T_e}{nT_i}\int \frac{(\omega-\omega_{*i}^T)}{(\omega-\omega_{di})} J_0^2 f_{i0} d\mathbf{v} + \frac{1}{n}\int_{trapped} \overline{J_0\phi}\frac{(\omega-\omega_{*e}^T)}{(\omega-\overline{\omega}_{de})} f_{e0} J_0 d\mathbf{v} \end{aligned} \tag{5.14}$$

To simplify matters, the Bessel function J_0 for the electron part of this equation can be set equal to one [12]. This approximation is suitable for long perpendicular wavelengths, $k_\perp \rho_a \ll 1$. Making this change to Eqn. 5.14 then gives

$$\left(\frac{T_e}{T_i}+1\right)\phi = \frac{\phi T_e}{nT_i}\int \frac{(\omega-\omega_{*i}^T)}{(\omega-\omega_{di})} J_0^2 f_{i0} d\mathbf{v} + \frac{1}{n}\int_{trapped} \frac{(\omega-\omega_{*e}^T)}{(\omega-\overline{\omega}_{de})}\overline{\phi} f_{e0} d\mathbf{v} \tag{5.15}$$

Now, care must be taken in treating the passing ions and trapped electrons differently. In the main body of our derivation, we will only present how the ion result is obtained. For the electron part, we will simply state the end result here, as the full derivation for treating trapped particles can be found in Appendix A. Thus, we can rewrite the electron part of Eqn. 5.15 as follows:

$$\frac{1}{n}\int_{trapped}\frac{(\omega-\omega_{*e}^{T})}{(\omega-\overline{\omega}_{de})}\overline{\phi}f_{e0}d\mathbf{v}=B\int_{\frac{1}{B_{max}}}^{\frac{1}{B_{min}}}U_e(\omega,\lambda)\overline{\phi}\frac{d\lambda}{\sqrt{1-\lambda B}} \tag{5.16}$$

where we have used the method described in Appendix A leading to Eqn. A.50. To be explicit, we are using the following expression for $U_e(\omega,\lambda)$:

$$U_e(\omega,\lambda)=\frac{1}{2}\left[1-\frac{\omega_{*e}}{\omega}+\frac{3}{2}\frac{F_e\overline{G(\lambda)}}{\omega}\left(1-\frac{\omega_{*e}}{\omega}\left[1+\eta_e\right]\right)\right] \tag{5.17}$$

For the ion term in Eqn. 5.15, we take the same approach as carried out in [12], which will differ considerably from the trapped particle derivation seen in Appendix A. As done in [12], we will be assuming that we have a vanishing plasma pressure gradient, $\nabla p=0$, which then enables the curvature vector to be written as the perpendicular derivative of the magnetic field strength:

$$\vec{\kappa}=\hat{\mathbf{b}}\cdot\nabla\hat{\mathbf{b}}=\frac{\nabla_\perp B}{B}=\nabla_\perp \ln B \tag{5.18}$$

This allows us to transform the ion magnetic drift expression as follows:

$$\begin{aligned}\omega_{di}&=\mathbf{k}_\perp\cdot\mathbf{v}_{di}\\&=\mathbf{k}_\perp\cdot\left[\hat{\mathbf{b}}\times\left(\frac{v_\perp^2}{2}\nabla\ln B+v_\parallel^2\vec{\kappa}\right)\frac{1}{\Omega_i}\right]\\&=\mathbf{k}_\perp\cdot\left[\hat{\mathbf{b}}\times\left(\frac{v_\perp^2}{2}\nabla\ln B+v_\parallel^2\vec{\kappa}\right)\frac{1}{\Omega_i}\right]\\&=\mathbf{k}_\perp\cdot\left[\hat{\mathbf{b}}\times\frac{\nabla_\perp B}{B}\left(\frac{v_\perp^2}{2}+v_\parallel^2\right)\frac{1}{\Omega_i}\right]\\&=\hat{\omega}_{di}\left(\frac{x_\perp^2}{2}+x_\parallel^2\right)\end{aligned} \tag{5.19}$$

where we have used for the ions:

$$\begin{aligned}v_\parallel^2&=v_{Ti}^2x_\parallel^2\\v_\perp^2&=v_{Ti}^2x_\perp^2\end{aligned} \tag{5.20}$$

and we have defined

$$\hat{\omega}_{di}\equiv\frac{\mathbf{k}_\perp v_{Ti}^2}{\Omega_i}\cdot\left(\hat{\mathbf{b}}\times\frac{\nabla_\perp B}{B}\right) \tag{5.21}$$

We can once again make the assumption of having a small magnetic drift frequency, which means that $\omega_{di} \ll \omega$, such that we can write

$$\frac{(\omega - \omega_{*i}^T)}{(\omega - \omega_{di})} = \frac{\omega}{\omega} \frac{\left(1 - \frac{\omega_{*i}^T}{\omega}\right)}{\left(1 - \frac{\omega_{di}}{\omega}\right)} \simeq \left(1 - \frac{\omega_{*i}^T}{\omega}\right)\left(1 + \frac{\omega_{di}}{\omega} + \mathcal{O}\left(\frac{\omega_{di}^2}{\omega^2}\right)\right) \tag{5.22}$$

which can be expanded to first order in ω_{di} to give

$$\frac{(\omega - \omega_{*i}^T)}{(\omega - \omega_{di})} \simeq \left(1 - \frac{\omega_{*i}^T}{\omega} + \frac{\omega_{di}}{\omega} - \frac{\omega_{*i}^T \omega_{di}}{\omega^2}\right) \tag{5.23}$$

This then allows us to rewrite the ion part of Eqn. 5.15 as

$$\frac{\phi T_e}{n T_i} \int \frac{(\omega - \omega_{*i}^T)}{(\omega - \omega_{di})} J_0^2 f_{i0} d\mathbf{v} = \frac{\phi T_e}{n T_i} \int \left(1 - \frac{\omega_{*i}^T}{\omega} + \frac{\omega_{di}}{\omega} - \frac{\omega_{*i}^T \omega_{di}}{\omega^2}\right) J_0^2 f_{i0} d\mathbf{v} \tag{5.24}$$

We can insert the following expression for our equilibrium ion Maxwellian distribution

$$f_{i0} = \left[n \left(\frac{1}{\pi v_{Ti}^2}\right)^{\frac{3}{2}} e^{-x^2} \right] \tag{5.25}$$

and also use the fact that, for the ions:

$$v = v_{Ti} x \implies dv = v_{Ti} dx \implies d\mathbf{v} = d^3 v = (v_{Ti})^3 d^3 x \tag{5.26}$$

These changes then transform Eqn. 5.24 as follows:

$$\begin{aligned} &\frac{\phi T_e}{n T_i} \int \left(1 - \frac{\omega_{*i}^T}{\omega} + \frac{\omega_{di}}{\omega} - \frac{\omega_{*i}^T \omega_{di}}{\omega^2}\right) J_0^2 f_{i0} d\mathbf{v} \\ &= \frac{\phi T_e}{n T_i} \int \left(1 - \frac{\omega_{*i}^T}{\omega} + \frac{\omega_{di}}{\omega} - \frac{\omega_{*i}^T \omega_{di}}{\omega^2}\right) J_0^2 \left[n \left(\frac{1}{\pi v_{Ti}^2}\right)^{\frac{3}{2}} e^{-x^2} \right] (v_{Ti})^3 d^3 x \\ &= \frac{\phi T_e}{\pi^{\frac{3}{2}} T_i} \int \underbrace{\left(1 - \frac{\omega_{*i}^T}{\omega} + \frac{\omega_{di}}{\omega} - \frac{\omega_{*i}^T \omega_{di}}{\omega^2}\right)}_{\ddagger} J_0^2 e^{-x^2} d^3 x \end{aligned} \tag{5.27}$$

Now, using of the definition of the temperature-dependent ion diamagnetic drift frequency

$$\omega_{*i}^T = \omega_{*i} \left[1 + \eta_i \left(\frac{\mathcal{E}_i}{T_i} - \frac{3}{2}\right)\right] \tag{5.28}$$

and also

$$\frac{\mathcal{E}_i}{T_i} = \frac{m_i v^2}{2 T_i} = \frac{v^2}{v_{Ti}^2} = x^2 \tag{5.29}$$

then Eqn. 5.28 becomes

$$\omega_{*i}^T = \omega_{*i} \left[1 + \eta_i \left(x^2 - \frac{3}{2}\right)\right] = \left[\omega_{*i} + \omega_{*i} \eta_i x^2 - \frac{3}{2} \omega_{*i} \eta_i\right] \tag{5.30}$$

For the ions, we will switch to cylindrical velocity coordinates, such that

$$\begin{aligned} \int d^3x &\equiv 2\pi \int_{-\infty}^{\infty} dx_{\parallel} \int_0^{\infty} x_{\perp} dx_{\perp} \\ x^2 &= x_{\parallel}^2 + x_{\perp}^2 \end{aligned} \tag{5.31}$$

This changes Eqn. 5.30 to

$$\omega_{*i}^T = \left[\omega_{*i} + \omega_{*i}\eta_i x_{\parallel}^2 + \omega_{*i}\eta_i x_{\perp}^2 - \frac{3}{2}\omega_{*i}\eta_i\right] \tag{5.32}$$

which we can now insert into ‡ from Eqn. 5.27, as follows

$$\begin{aligned} &\left(1 - \frac{\omega_{*i}^T}{\omega} + \frac{\omega_{di}}{\omega} - \frac{\omega_{*i}^T \omega_{di}}{\omega^2}\right) = \\ &\left(1 - \frac{\left[\omega_{*i} + \omega_{*i}\eta_i x_{\parallel}^2 + \omega_{*i}\eta_i x_{\perp}^2 - \frac{3}{2}\omega_{*i}\eta_i\right]}{\omega} + \frac{\omega_{di}}{\omega} - \frac{\left[\omega_{*i} + \omega_{*i}\eta_i x_{\parallel}^2 + \omega_{*i}\eta_i x_{\perp}^2 - \frac{3}{2}\omega_{*i}\eta_i\right]\omega_{di}}{\omega^2}\right) = \\ &\left(1 - \frac{\omega_{*i}}{\omega} - \frac{\omega_{*i}\eta_i x_{\parallel}^2}{\omega} - \frac{\omega_{*i}\eta_i x_{\perp}^2}{\omega} + \frac{3\omega_{*i}\eta_i}{2\omega} + \frac{\omega_{di}}{\omega} - \frac{\omega_{*i}\omega_{di}}{\omega^2} - \frac{\omega_{*i}\eta_i x_{\parallel}^2 \omega_{di}}{\omega^2} - \frac{\omega_{*i}\eta_i x_{\perp}^2 \omega_{di}}{\omega^2} + \frac{3\omega_{*i}\eta_i \omega_{di}}{2\omega^2}\right) \end{aligned} \tag{5.33}$$

We will now also insert the following expression for the ion magnetic drift frequency

$$\omega_{di} = \hat{\omega}_{di}\left(\frac{x_{\perp}^2}{2} + x_{\parallel}^2\right) = \hat{\omega}_{di}\frac{x_{\perp}^2}{2} + \hat{\omega}_{di}x_{\parallel}^2 \tag{5.34}$$

such that the result of Eqn. 5.33 becomes

$$\begin{aligned} &1 - \frac{\omega_{*i}}{\omega} - \frac{\omega_{*i}\eta_i x_{\parallel}^2}{\omega} - \frac{\omega_{*i}\eta_i x_{\perp}^2}{\omega} + \frac{3\omega_{*i}\eta_i}{2\omega} + \frac{\hat{\omega}_{di}}{\omega}\frac{x_{\perp}^2}{2} + \frac{\hat{\omega}_{di}}{\omega}x_{\parallel}^2 - \frac{\omega_{*i}\hat{\omega}_{di}}{\omega^2}\frac{x_{\perp}^2}{2} - \frac{\omega_{*i}\hat{\omega}_{di}}{\omega^2}x_{\parallel}^2 \\ &- \frac{\omega_{*i}\eta_i x_{\parallel}^2 x_{\perp}^2 \hat{\omega}_{di}}{2\omega^2} - \frac{\omega_{*i}\eta_i x_{\parallel}^4 \hat{\omega}_{di}}{\omega^2} - \frac{\omega_{*i}\eta_i x_{\perp}^4 \hat{\omega}_{di}}{2\omega^2} - \frac{\omega_{*i}\eta_i x_{\perp}^2 x_{\parallel}^2 \hat{\omega}_{di}}{\omega^2} + \frac{3\omega_{*i}\eta_i \hat{\omega}_{di} x_{\perp}^2}{4\omega^2} + \frac{3\omega_{*i}\eta_i \hat{\omega}_{di} x_{\parallel}^2}{2\omega^2} \end{aligned} \tag{5.35}$$

Let's attempt to organise this verbose expression based on the different degrees of $x_{\parallel}$ and $x_{\perp}$ in each of the terms. When we eventually carry out the integration, we will first calculate those integrals pertaining to $x_{\parallel}$ before working out the $x_{\perp}$ integrals, so we will prioritise our groupings here with this in mind.

$$\begin{aligned} &\left(1 - \frac{\omega_{*i}}{\omega} + \frac{3\omega_{*i}\eta_i}{2\omega}\right) \\ &+ x_{\perp}^2\left(-\frac{\omega_{*i}\eta_i}{\omega} + \frac{\hat{\omega}_{di}}{2\omega} - \frac{\omega_{*i}\hat{\omega}_{di}}{2\omega^2} + \frac{3\omega_{*i}\eta_i\hat{\omega}_{di}}{4\omega^2}\right) \\ &- x_{\perp}^4\left(\frac{\omega_{*i}\eta_i\hat{\omega}_{di}}{2\omega^2}\right) \\ &+ x_{\parallel}^2\left(-\frac{\omega_{*i}\eta_i}{\omega} + \frac{\hat{\omega}_{di}}{\omega} - \frac{\omega_{*i}\hat{\omega}_{di}}{\omega^2} - \frac{3\omega_{*i}\eta_i x_{\perp}^2\hat{\omega}_{di}}{2\omega^2} + \frac{3\omega_{*i}\eta_i\hat{\omega}_{di}}{2\omega^2}\right) \\ &- x_{\parallel}^4\left(\frac{\omega_{*i}\eta_i\hat{\omega}_{di}}{\omega^2}\right) \end{aligned} \tag{5.36}$$

If we now consider the final line of Eqn. 5.27, and take into account our switch to cylindrical coordinates as outlined in Eqn. 5.31, we can see that our integration looks roughly as follows:

$$\int \underbrace{\left(1 - \frac{\omega_{*i}^T}{\omega} + \frac{\omega_{di}}{\omega} - \frac{\omega_{*i}^T \omega_{di}}{\omega^2}\right)}_{\ddagger} J_0^2 e^{-x^2} d^3x = \int_0^\infty \int_{-\infty}^\infty (\ddagger)\, J_0^2\left(a x_\perp\right) e^{-\left(x_\parallel^2 + x_\perp^2\right)} dx_\parallel x_\perp dx_\perp$$

$$= \int_0^\infty \int_{-\infty}^\infty (\ddagger)\, J_0^2\left(a x_\perp\right) e^{-x_\parallel^2} e^{-x_\perp^2} dx_\parallel x_\perp dx_\perp \tag{5.37}$$

where we have left out the following prefactor for neatness:

$$\frac{\phi T_e}{\pi^{\frac{3}{2}} T_i} \times \underbrace{2\pi}_{Cylindrical} = \frac{2\phi T_e}{\sqrt{\pi} T_i} \tag{5.38}$$

Also, the argument of the Bessel function will be explained quickly in the following aside.

Aside

Our Bessel function usually has an argument as follows:

$$J_0\left(\frac{k_\perp v_\perp}{\Omega_a}\right) \tag{5.39}$$

We can make use of the following relation:

$$x = \frac{v}{v_{Ta}} \implies v = v_{Ta} x \implies v_\perp = v_{Ta} x_\perp \tag{5.40}$$

and reinsert this into the Bessel function to give:

$$J_0\left(\frac{k_\perp v_\perp}{\Omega_a}\right) = J_0\left(\underbrace{\frac{k_\perp v_{Ta}}{\Omega_a}}_{a} x_\perp\right) = J_0\left(a x_\perp\right) \tag{5.41}$$

We can now evaluate our $x_\parallel$ integrals line by line for the terms in Eqn. 5.36, using the following:

$$\begin{aligned} \int_{-\infty}^\infty e^{-x_\parallel^2} dx_\parallel &= \sqrt{\pi} \\ \int_{-\infty}^\infty x_\parallel^2 e^{-x_\parallel^2} dx_\parallel &= \frac{\sqrt{\pi}}{2} \\ \int_{-\infty}^\infty x_\parallel^4 e^{-x_\parallel^2} dx_\parallel &= \frac{3\sqrt{\pi}}{4} \end{aligned} \tag{5.42}$$

With this done, Eqn. 5.37 becomes

$$\begin{aligned}
&\int_0^\infty \int_{-\infty}^\infty (\ddagger)\, J_0^2\left(a x_\perp\right) e^{-x_\parallel^2} e^{-x_\perp^2} dx_\parallel x_\perp dx_\perp = \\
&\sqrt{\pi} \int_0^\infty \left[\left(1 - \frac{\omega_{*i}}{\omega} + \frac{3\omega_{*i}\eta_i}{2\omega}\right) + x_\perp^2 \left(-\frac{\omega_{*i}\eta_i}{\omega} + \frac{\hat{\omega}_{di}}{2\omega} - \frac{\omega_{*i}\hat{\omega}_{di}}{2\omega^2} + \frac{3\omega_{*i}\eta_i\hat{\omega}_{di}}{4\omega^2}\right) - x_\perp^4 \left(\frac{\omega_{*i}\eta_i\hat{\omega}_{di}}{2\omega^2}\right) \right] \\
&\times J_0^2 e^{-x_\perp^2} x_\perp dx_\perp \\
&+ \frac{\sqrt{\pi}}{2} \int_0^\infty \left(-\frac{\omega_{*i}\eta_i}{\omega} + \frac{\hat{\omega}_{di}}{\omega} - \frac{\omega_{*i}\hat{\omega}_{di}}{\omega^2} - \frac{3\omega_{*i}\eta_i x_\perp^2 \hat{\omega}_{di}}{2\omega^2} + \frac{3\omega_{*i}\eta_i\hat{\omega}_{di}}{2\omega^2}\right) J_0^2 e^{-x_\perp^2} x_\perp dx_\perp \\
&+ \frac{3\sqrt{\pi}}{4} \int_0^\infty \left(-\frac{\omega_{*i}\eta_i\hat{\omega}_{di}}{\omega^2}\right) J_0^2 e^{-x_\perp^2} x_\perp dx_\perp
\end{aligned} \tag{5.43}$$

Before evaluating the remaining $x_\perp$ integrals, let's reorganise our result by grouping terms together with a common degree of $x_\perp$. To start, we will gather together all the terms containing a $x_\perp$ of degree one:

$$x_\perp \left(1 - \frac{\omega_{*i}}{\omega} + \frac{3\omega_{*i}\eta_i}{2\omega} - \frac{\omega_{*i}\eta_i}{2\omega} + \frac{\hat{\omega}_{di}}{2\omega} - \frac{\omega_{*i}\hat{\omega}_{di}}{2\omega^2} + \frac{3\omega_{*i}\eta_i\hat{\omega}_{di}}{4\omega^2} - \frac{3\omega_{*i}\eta_i\hat{\omega}_{di}}{4\omega^2}\right) \tag{5.44}$$

which simplifies to

$$x_\perp \left(1 - \frac{\omega_{*i}}{\omega} + \frac{\omega_{*i}\eta_i}{\omega} + \frac{\hat{\omega}_{di}}{2\omega} - \frac{\omega_{*i}\hat{\omega}_{di}}{2\omega^2}\right) \tag{5.45}$$

Now, we will gather together all the terms containing a $x_\perp$ of degree three:

$$x_\perp^3 \left(-\frac{\omega_{*i}\eta_i}{\omega} + \frac{\hat{\omega}_{di}}{2\omega} - \frac{\omega_{*i}\hat{\omega}_{di}}{2\omega^2} + \frac{3\omega_{*i}\eta_i\hat{\omega}_{di}}{4\omega^2} - \frac{3\omega_{*i}\eta_i\hat{\omega}_{di}}{4\omega^2}\right) \tag{5.46}$$

which simplifies to

$$x_\perp^3 \left(-\frac{\omega_{*i}\eta_i}{\omega} + \frac{\hat{\omega}_{di}}{2\omega} - \frac{\omega_{*i}\hat{\omega}_{di}}{2\omega^2}\right) \tag{5.47}$$

Finally, we have only one term left unaccounted for, which contains a $x_\perp$ of degree five:

$$x_\perp^5 \left(-\frac{\omega_{*i}\eta_i\hat{\omega}_{di}}{2\omega^2}\right) \tag{5.48}$$

Let's now gather everything together, which gives us our simplified version of Eqn. 5.43

$$\begin{aligned}
\sqrt{\pi} \int_0^\infty \Bigg[& x_\perp \left(1 - \frac{\omega_{*i}}{\omega} + \frac{\omega_{*i}\eta_i}{\omega} + \frac{\hat{\omega}_{di}}{2\omega} - \frac{\omega_{*i}\hat{\omega}_{di}}{2\omega^2}\right) \\
& + x_\perp^3 \left(-\frac{\omega_{*i}\eta_i}{\omega} + \frac{\hat{\omega}_{di}}{2\omega} - \frac{\omega_{*i}\hat{\omega}_{di}}{2\omega^2}\right) \\
& + x_\perp^5 \left(-\frac{\omega_{*i}\eta_i\hat{\omega}_{di}}{2\omega^2}\right) \Bigg] \times J_0^2(a x_\perp) e^{-x_\perp^2} dx_\perp
\end{aligned} \tag{5.49}$$

To evaluate our final integrals here, we will make use of the following:

$$\begin{aligned}
\int_0^\infty x_\perp e^{-x_\perp^2} J_0^2(ax_\perp)dx_\perp &= \frac{1}{2}e^{-\frac{a^2}{2}} I_0\left(\frac{a^2}{2}\right) \\
\int_0^\infty x_\perp^3 e^{-x_\perp^2} J_0^2(ax_\perp)dx_\perp &= \frac{1}{2}e^{-\frac{a^2}{2}} \left[-\left(\frac{a^2}{2}-1\right) I_0\left(\frac{a^2}{2}\right) + \frac{a^2}{2} I_1\left(\frac{a^2}{2}\right)\right] \\
\int_0^\infty x_\perp^5 e^{-x_\perp^2} J_0^2(ax_\perp)dx_\perp &= \frac{1}{4}e^{-\frac{a^2}{2}} \left[\left(a^2-2\right)^2 I_0\left(\frac{a^2}{2}\right) - a^2\left(a^2-3\right) I_1\left(\frac{a^2}{2}\right)\right]
\end{aligned} \tag{5.50}$$

where $I_0(x)$ is the modified Bessel function. If we make use of the following convenient redefinition

$$b \equiv \frac{a^2}{2} \tag{5.51}$$

then our integral results in Eqn. 5.50 can be more neatly written as

$$\begin{aligned}
\int_0^\infty x_\perp e^{-x_\perp^2} J_0^2(x_\perp\sqrt{2b})dx_\perp &= \frac{1}{2}e^{-b} I_0(b) \\
\int_0^\infty x_\perp^3 e^{-x_\perp^2} J_0^2(x_\perp\sqrt{2b})dx_\perp &= \frac{1}{2}e^{-b} \left[-(b-1) I_0(b) + b I_1(b)\right] \\
\int_0^\infty x_\perp^5 e^{-x_\perp^2} J_0^2(x_\perp\sqrt{2b})dx_\perp &= \frac{1}{4}e^{-b} \left[(2b-2)^2 I_0(b) - 2b(2b-3) I_1(b)\right]
\end{aligned} \tag{5.52}$$

Furthermore, we can tidy up our result even further by making use of the following definition:

$$\Gamma_n(b) \equiv I_n(b)e^{-b} \tag{5.53}$$

which changes our integrals as follows:

$$\begin{aligned}
\int_0^\infty x_\perp e^{-x_\perp^2} J_0^2(x_\perp\sqrt{2b})dx_\perp &= \frac{1}{2}\Gamma_0(b) \\
\int_0^\infty x_\perp^3 e^{-x_\perp^2} J_0^2(x_\perp\sqrt{2b})dx_\perp &= \frac{1}{2}\left[\Gamma_0(b) - b\left(\Gamma_0(b) - \Gamma_1(b)\right)\right] \\
\int_0^\infty x_\perp^5 e^{-x_\perp^2} J_0^2(x_\perp\sqrt{2b})dx_\perp &= \frac{1}{2}\left[2(b-1)^2\Gamma_0(b) - 2b\left(b-\frac{3}{2}\right)\Gamma_1(b)\right]
\end{aligned} \tag{5.54}$$

Using these results, we can now finally evaluate Eqn. 5.49 to give us the following

$$\begin{aligned}
&\frac{\sqrt{\pi}}{2}\Gamma_0(b)\left(1 - \frac{\omega_{*i}}{\omega} + \frac{\omega_{*i}\eta_i}{\omega} + \frac{\hat{\omega}_{di}}{2\omega} - \frac{\omega_{*i}\hat{\omega}_{di}}{2\omega^2}\right) + \\
&\frac{\sqrt{\pi}}{2}\left[\Gamma_0(b) - b\left(\Gamma_0(b) - \Gamma_1(b)\right)\right]\left(-\frac{\omega_{*i}\eta_i}{\omega} + \frac{\hat{\omega}_{di}}{2\omega} - \frac{\omega_{*i}\hat{\omega}_{di}}{2\omega^2}\right) + \\
&\frac{\sqrt{\pi}}{2}\left[2(b-1)^2\Gamma_0(b) - 2b\left(b-\frac{3}{2}\right)\Gamma_1(b)\right]\left(-\frac{\omega_{*i}\eta_i\hat{\omega}_{di}}{2\omega^2}\right)
\end{aligned} \tag{5.55}$$

For now, we will leave out the prefactor of $\frac{\sqrt{\pi}}{2}$ for neatness, so we can more easily tidy up the remaining result. Let's group our result based on the different $\Gamma_n(b)$ terms. Starting with $\Gamma_0(b)$,

we have

$$\begin{aligned}
&\Gamma_0(b)\left[1-\frac{\omega_{*i}}{\omega}+\frac{\hat{\omega}_{di}}{\omega}-\frac{\omega_{*i}\hat{\omega}_{di}}{\omega^2}-b\left(-\frac{\omega_{*i}\eta_i}{\omega}+\frac{\hat{\omega}_{di}}{2\omega}-\frac{\omega_{*i}\hat{\omega}_{di}}{2\omega^2}\right)\underbrace{-(b-1)^2}_{(-b^2+2b-1)}\frac{\omega_{*i}\eta_i\hat{\omega}_{di}}{\omega^2}\right]\\
&=\Gamma_0(b)\left[1-\frac{\omega_{*i}}{\omega}+\frac{\hat{\omega}_{di}}{\omega}-\frac{(1+\eta_i)\omega_{*i}\hat{\omega}_{di}}{\omega^2}+b\left(\frac{\omega_{*i}\eta_i}{\omega}-\frac{\hat{\omega}_{di}}{2\omega}+\frac{\omega_{*i}\hat{\omega}_{di}}{2\omega^2}+\frac{2\omega_{*i}\eta_i\hat{\omega}_{di}}{\omega^2}\right)-b^2\frac{\omega_{*i}\eta_i\hat{\omega}_{di}}{\omega^2}\right]\\
&=\Gamma_0(b)\left[1-\frac{\omega_{*i}}{\omega}+\frac{\hat{\omega}_{di}}{\omega}-\frac{(1+\eta_i)\omega_{*i}\hat{\omega}_{di}}{\omega^2}+b\left(\frac{\omega_{*i}\eta_i}{\omega}-\frac{\hat{\omega}_{di}}{2\omega}+\frac{(1+4\eta_i)\omega_{*i}\hat{\omega}_{di}}{2\omega^2}\right)-b^2\frac{\omega_{*i}\eta_i\hat{\omega}_{di}}{\omega^2}\right]\\
&\equiv Y_0
\end{aligned} \tag{5.56}$$

For $\Gamma_1(b)$, we have

$$\begin{aligned}
&\Gamma_1(b)\left[b\left(-\frac{\omega_{*i}\eta_i}{\omega}+\frac{\hat{\omega}_{di}}{2\omega}-\frac{\omega_{*i}\hat{\omega}_{di}}{2\omega^2}\right)+2b\left(b-\frac{3}{2}\right)\left(\frac{\omega_{*i}\eta_i\hat{\omega}_{di}}{2\omega^2}\right)\right]\\
&=\Gamma_1(b)\left[b\left(-\frac{\omega_{*i}\eta_i}{\omega}+\frac{\hat{\omega}_{di}}{2\omega}-\frac{\omega_{*i}\hat{\omega}_{di}}{2\omega^2}-\frac{3\omega_{*i}\eta_i\hat{\omega}_{di}}{2\omega^2}\right)+b^2\frac{\omega_{*i}\eta_i\hat{\omega}_{di}}{\omega^2}\right]\\
&=\Gamma_1(b)\left[b\left(-\frac{\omega_{*i}\eta_i}{\omega}+\frac{\hat{\omega}_{di}}{2\omega}-\frac{(1+3\eta_i)\omega_{*i}\hat{\omega}_{di}}{2\omega^2}\right)+b^2\frac{\omega_{*i}\eta_i\hat{\omega}_{di}}{\omega^2}\right]\\
&\equiv Y_1
\end{aligned} \tag{5.57}$$

With all of this complete, we have finally obtained the ion part of Eqn. 5.15,where we will now reintroduce our prefactor from Eqn. 5.38, and the newly found factor of $\frac{\sqrt{\pi}}{2}$:

$$\begin{aligned}
\frac{\phi T_e}{nT_i}\int\frac{(\omega-\omega_{*i}^T)}{(\omega-\omega_{di})}J_0^2 f_{i0}d\mathbf{v}&=\frac{2\phi T_e}{\sqrt{\pi}T_i}\frac{\sqrt{\pi}}{2}\left[Y_0+Y_1\right]\\
&=\frac{\phi T_e}{T_i}\left[Y_0+Y_1\right]
\end{aligned} \tag{5.58}$$

Looking at the full expression of Eqn. 5.15, we have

$$\begin{aligned}
\left(\frac{T_e}{T_i}+1\right)\phi&=\frac{\phi T_e}{nT_i}\int\frac{(\omega-\omega_{*i}^T)}{(\omega-\omega_{di})}J_0^2 f_{i0}d\mathbf{v}+\frac{1}{n}\int_{trapped}\frac{(\omega-\omega_{*e}^T)}{(\omega-\overline{\omega}_{de})}\overline{\phi}f_{e0}d\mathbf{v}\\
&=\frac{\phi T_e}{T_i}\left[Y_0+Y_1\right]+B\int_{\frac{1}{B_{max}}}^{\frac{1}{B_{min}}}U_e(\omega,\lambda)\overline{\phi}\frac{d\lambda}{\sqrt{1-\lambda B}}
\end{aligned} \tag{5.59}$$

which can be rearranged slightly and more neatly written by using $\tau\equiv\frac{T_e}{T_i}$:

$$\begin{aligned}
(\tau+1)\,\phi-\phi\tau\left[Y_0+Y_1\right]&=B\int_{\frac{1}{B_{max}}}^{\frac{1}{B_{min}}}U_e(\omega,\lambda)\overline{\phi}\frac{d\lambda}{\sqrt{1-\lambda B}}\\
\implies\left[1+\tau\left(1-\left[Y_0+Y_1\right]\right)\right]\phi&=B\int_{\frac{1}{B_{max}}}^{\frac{1}{B_{min}}}U_e(\omega,\lambda)\overline{\phi}\frac{d\lambda}{\sqrt{1-\lambda B}}
\end{aligned} \tag{5.60}$$

where the left-hand side describes the ions, and the right-hand side describes the electrons. This integral equation can now be rewritten in the following more general form:

$$\boxed{f(\omega,l)\phi(l)=B\int_{\frac{1}{B_{max}}}^{\frac{1}{B_{min}}}g(\omega,\lambda)\overline{\phi}(\lambda)\frac{d\lambda}{\sqrt{1-\lambda B}}} \tag{5.61}$$

In the next subsection, we will show the variational property of this general integral equation, before applying it to our specific result in Eqn. 5.60.

Variational Property of General Integral Equation

We now take a brief, but relevant, detour from our main derivation to prove the variational property of the general integral equation, given by the following expression:

$$\boxed{f(\omega,l)\phi(l) = B\int_{\frac{1}{B_{max}}}^{\frac{1}{B_{min}}} g(\omega,\lambda)\overline{\phi}(\lambda)\frac{d\lambda}{\sqrt{1-\lambda B}}} \tag{5.62}$$

The variational property of this general equation can be demonstrated if we multiply Eqn. 5.62 by $\frac{\phi^*}{B}$ and integrate along the entire field line. The left-hand side is straightforward and looks as follows:

$$\int_{-\infty}^{\infty}\frac{\phi^*}{B}\left[f(\omega,l)\phi(l)\right]dl = \int_{-\infty}^{\infty} f(\omega,l)|\phi|^2\frac{dl}{B} \tag{5.63}$$

The right-hand side is slightly more complicated, but can be clearly seen to work as follows:

$$\int_{-\infty}^{\infty}\frac{\phi^*}{B}\left[B\int_{\frac{1}{B_{max}}}^{\frac{1}{B_{min}}} g(\omega,\lambda)\overline{\phi}(\lambda)\frac{d\lambda}{\sqrt{1-\lambda B}}\right]dl = \int_{\frac{1}{B_{max}}}^{\frac{1}{B_{min}}} g(\omega,\lambda)\overline{\phi}(\lambda)\underbrace{\int_{-\infty}^{\infty}\phi^*\frac{dl}{\sqrt{1-\lambda B}}}_{A}d\lambda \tag{5.64}$$

where for trapped particles, it should be noted that $\int_{-\infty}^{\infty} \equiv \sum_{\text{wells}}\oint$. On the right-hand side of this expression, we can make use of the following bounce-averaging procedure:

$$\overline{\phi^*} = \frac{1}{\oint\frac{dl}{\sqrt{1-\lambda B}}}\oint\phi^*\frac{dl}{\sqrt{1-\lambda B}} \implies \overline{\phi^*}\oint\frac{dl}{\sqrt{1-\lambda B}} = \oint\phi^*\frac{dl}{\sqrt{1-\lambda B}} \tag{5.65}$$

such that

$$A \equiv \sum_{\text{wells}}\oint\phi^*\frac{dl}{\sqrt{1-\lambda B}} = \sum_{\text{wells}}\overline{\phi^*}\oint\frac{dl}{\sqrt{1-\lambda B}} = \overline{\phi^*}\int_{-\infty}^{\infty}\frac{dl}{\sqrt{1-\lambda B}} \tag{5.66}$$

Thus, we can rewrite the right-hand side of Eqn. 5.64 as follows:

$$\int_{\frac{1}{B_{max}}}^{\frac{1}{B_{min}}} g(\omega,\lambda)\overline{\phi}(\lambda)\underbrace{\int_{-\infty}^{\infty}\phi^*\frac{dl}{\sqrt{1-\lambda B}}}_{A}d\lambda = \int_{\frac{1}{B_{max}}}^{\frac{1}{B_{min}}} g(\omega,\lambda)\overline{\phi}(\lambda)\overline{\phi^*}(\lambda)\int_{-\infty}^{\infty}\frac{dl}{\sqrt{1-\lambda B}}d\lambda \tag{5.67}$$

Combining Eqn. 5.63 and Eqn. 5.67 then gives

$$\int_{-\infty}^{\infty} f(\omega,l)|\phi|^2\frac{dl}{B} = \int_{\frac{1}{B_{max}}}^{\frac{1}{B_{min}}}\int_{-\infty}^{\infty}\frac{dl}{\sqrt{1-\lambda B}}g(\omega,\lambda)|\overline{\phi}|^2 d\lambda \tag{5.68}$$

where on the right-hand side, we have used $(\overline{\phi})(\overline{\phi^*}) = |\overline{\phi}|^2$.

Now, in order to show how the variational principle can be applied to our general integral equation, we must vary our new expression with respect to ϕ. Noting that we have:

$$\begin{aligned}\omega &= \omega(\phi)\\ f &= f[\omega] = f[\omega(\phi)]\end{aligned} \tag{5.69}$$

such that

$$\frac{\delta f}{\delta\phi} \equiv \frac{\delta f}{\delta\omega}\frac{\delta\omega}{\delta\phi} \implies \delta f \equiv \frac{\delta f}{\delta\omega}\frac{\delta\omega}{\delta\phi}\delta\phi = \frac{\delta f}{\delta\omega}\delta\omega \tag{5.70}$$

we can vary Eqn. 5.68 with respect to ϕ to obtain

$$\int_{-\infty}^{\infty}\left(\frac{\delta f}{\delta\omega}\delta\omega|\phi|^2 + 2f\phi\delta\phi\right)\frac{dl}{B} = \int_{\frac{1}{B_{max}}}^{\frac{1}{B_{min}}}\int_{-\infty}^{\infty}\frac{dl}{\sqrt{1-\lambda B}}\left(\frac{\delta g}{\delta\omega}\delta\omega|\overline{\phi}|^2 + 2g\overline{\phi}\delta\overline{\phi}\right)d\lambda \tag{5.71}$$

which can be rearranged to give

$$\begin{aligned}&\delta\omega\left(\int_{-\infty}^{\infty}\frac{\delta f}{\delta\omega}|\phi|^2\frac{dl}{B} - \int_{\frac{1}{B_{max}}}^{\frac{1}{B_{min}}}\int_{-\infty}^{\infty}\frac{dl}{\sqrt{1-\lambda B}}\frac{\delta g}{\delta\omega}|\overline{\phi}|^2 d\lambda\right)\\ &= -2\int_{-\infty}^{\infty} f\phi\delta\phi\frac{dl}{B} + 2\int_{\frac{1}{B_{max}}}^{\frac{1}{B_{min}}}\int_{-\infty}^{\infty}\frac{dl}{\sqrt{1-\lambda B}}g\overline{\phi}\delta\overline{\phi}d\lambda\end{aligned} \tag{5.72}$$

Let's look more closely at the second term on the right-hand side. We can rewrite $\delta\overline{\phi}$ using the familiar bounce-averaging procedure once again:

$$\delta\overline{\phi} = \frac{1}{\oint\frac{dl}{\sqrt{1-\lambda B}}}\oint\delta\phi\frac{dl}{\sqrt{1-\lambda B}} \tag{5.73}$$

where once again, we will note that $\int_{-\infty}^{\infty} \equiv \sum_{\text{wells}}\oint$. Using this then changes the relevant term in

Eqn. 5.72 in the following way

$$
\begin{aligned}
2\int_{\frac{1}{B_{min}}}^{\frac{1}{B_{max}}}\int_{-\infty}^{\infty}\frac{dl}{\sqrt{1-\lambda B}}g\bar{\phi}\delta\bar{\phi}d\lambda &= 2\int_{\frac{1}{B_{max}}}^{\frac{1}{B_{min}}}\overbrace{\sum_{\text{wells}}\oint}^{\int_{-\infty}^{\infty}}\frac{dl}{\sqrt{1-\lambda B}}g\bar{\phi}\frac{1}{\oint\frac{dl}{\sqrt{1-\lambda B}}}\oint\delta\phi\frac{dl}{\sqrt{1-\lambda B}}d\lambda \\
&= 2\int_{\frac{1}{B_{max}}}^{\frac{1}{B_{min}}}g\bar{\phi}\sum_{\text{wells}}\oint\delta\phi\frac{dl}{\sqrt{1-\lambda B}}d\lambda \\
&= 2\int_{\frac{1}{B_{max}}}^{\frac{1}{B_{min}}}g\bar{\phi}\int_{-\infty}^{\infty}\delta\phi\frac{dl}{\sqrt{1-\lambda B}}d\lambda \\
&= 2\int_{-\infty}^{\infty}\delta\phi\frac{dl}{B}B\int_{\frac{1}{B_{max}}}^{\frac{1}{B_{min}}}\frac{g\bar{\phi}}{\sqrt{1-\lambda B}}d\lambda
\end{aligned}
\tag{5.74}
$$

where in the final step, we pulled the $\delta\phi$ outside of the λ-integral, as it only depends on the field line l. We also multiplied and divided by B. Returning now to Eqn. 5.72, we can now see we have

$$
\begin{aligned}
&\delta\omega\left(\int_{-\infty}^{\infty}\frac{\delta f}{\delta\omega}|\phi|^2\frac{dl}{B}-\int_{\frac{1}{B_{max}}}^{\frac{1}{B_{min}}}\int_{-\infty}^{\infty}\frac{dl}{\sqrt{1-\lambda B}}\frac{\delta g}{\delta\omega}|\bar{\phi}|^2d\lambda\right) \\
&\quad= -2\int_{-\infty}^{\infty}f\phi\delta\phi\frac{dl}{B}+2\int_{-\infty}^{\infty}\delta\phi\frac{dl}{B}B\int_{\frac{1}{B_{max}}}^{\frac{1}{B_{min}}}\frac{g\bar{\phi}}{\sqrt{1-\lambda B}}d\lambda \\
&\quad= -2\int_{-\infty}^{\infty}\delta\phi\frac{dl}{B}\underbrace{\left(f\phi-B\int_{\frac{1}{B_{max}}}^{\frac{1}{B_{min}}}\frac{g\bar{\phi}}{\sqrt{1-\lambda B}}d\lambda\right)}_{\dagger}
\end{aligned}
\tag{5.75}
$$

We can now clearly see here that we obtain $\delta\omega = 0$ when the general integral equation (Eqn. 5.62) is fulfilled, as this leads to $\dagger = 0$. This means that the correct mode structure solution ϕ to the integral equation minimises the expression obtained for the mode frequency ω, and inserting a suitable trial function for the mode structure should then give a decent approximation to the true value of ω.

Final Mode Frequency Proxy

Let's take a moment to remind ourselves of what we have achieved so far, and of what we would still like to show. Up to now, we have established that our ω proxy derivation result, given by Eqn. 5.60:

$$
\left[1+\tau\left(1-\left[Y_0+Y_1\right]\right)\right]\phi = B\int_{\frac{1}{B_{max}}}^{\frac{1}{B_{min}}}U_e(\omega,\lambda)\bar{\phi}\frac{d\lambda}{\sqrt{1-\lambda B}}
\tag{5.76}
$$

can be written in the form of a more general integral equation, given by Eqn. 5.62:

$$
\boxed{f(\omega,l)\phi(l) = B\int_{\frac{1}{B_{max}}}^{\frac{1}{B_{min}}}g(\omega,l)\bar{\phi}(\lambda)\frac{d\lambda}{\sqrt{1-\lambda B}}}
\tag{5.77}
$$

such that we have

$$\begin{aligned} f(\omega,l) &\equiv [1+\tau\,(1-[Y_0+Y_1])] \\ g(\omega,l) &\equiv U_e(\omega,l) = \frac{1}{2}\left[1-\frac{\omega_{*e}}{\omega}+\frac{3}{2}\frac{F_e\overline{G(\lambda)}}{\omega}\left(1-\frac{\omega_{*e}}{\omega}\left[1+\eta_e\right]\right)\right] \end{aligned} \tag{5.78}$$

As mentioned in the previous section, we can make use of the variational property of Eqn. 5.77 by multiplying by $\frac{\phi^*}{B}$ and integrating along the entire field line, to give the following:

$$\int_{-\infty}^{\infty} f(\omega,l)|\phi|^2\frac{dl}{B} = \int_{\frac{1}{B_{max}}}^{\frac{1}{B_{min}}}\int_{-\infty}^{\infty}\frac{dl}{\sqrt{1-\lambda B}}g(\omega,l)|\overline{\phi}|^2 d\lambda \tag{5.79}$$

We would now like to use this property to find our final ω proxy expression for passing ions and trapped electrons. This can be achieved by inserting our definitions given in Eqn. 5.78 into Eqn. 5.79:

$$\begin{aligned} &\int_{-\infty}^{\infty}\left[1+\tau\,(1-[Y_0+Y_1])\right]|\phi|^2\frac{dl}{B} = \\ &\int_{\frac{1}{B_{max}}}^{\frac{1}{B_{min}}}\int_{-\infty}^{\infty}\frac{dl}{\sqrt{1-\lambda B}}\frac{1}{2}\left[1-\frac{\omega_{*e}}{\omega}+\frac{3}{2}\frac{F_e\overline{G(\lambda)}}{\omega}\left(1-\frac{\omega_{*e}}{\omega}\left[1+\eta_e\right]\right)\right]|\overline{\phi}|^2 d\lambda \end{aligned} \tag{5.80}$$

When inserting our expressions for Y_0 and Y_1, this expression will become very verbose, so we will consider Eqn. 5.80 line by line. Considering the first line to start with, we can expand this out to obtain

$$\begin{aligned} \int_{-\infty}^{\infty}\left[1+\tau\,(1-[Y_0+Y_1])\right]|\phi|^2\frac{dl}{B} &= \int_{-\infty}^{\infty}\left(1+\tau-\tau\,[Y_0+Y_1]\right)|\phi|^2\frac{dl}{B} \\ &= \int_{-\infty}^{\infty}(1+\tau)\,|\phi|^2\frac{dl}{B} - \int_{-\infty}^{\infty}\tau\,[Y_0+Y_1]\,|\phi|^2\frac{dl}{B} \end{aligned} \tag{5.81}$$

Before continuing, let's work out the $[Y_0+Y_1]$ term separately. Instead of using the fully expanded individual terms for Y_0 and Y_1, we will rely on the more compact form written earlier in Eqn. 5.55, but we will ignore the prefactors of $\frac{\sqrt{\pi}}{2}$ as we know they cancel later. So we have

$$\begin{aligned} &[Y_0+Y_1] = \\ &\Gamma_0(b)\left(1-\frac{\omega_{*i}}{\omega}+\frac{\omega_{*i}\eta_i}{\omega}+\frac{\hat{\omega}_{di}}{2\omega}-\frac{\omega_{*i}\hat{\omega}_{di}}{2\omega^2}\right)+ \\ &\left[\Gamma_0(b)-b\,(\Gamma_0(b)-\Gamma_1(b))\right]\left(-\frac{\omega_{*i}\eta_i}{\omega}+\frac{\hat{\omega}_{di}}{2\omega}-\frac{\omega_{*i}\hat{\omega}_{di}}{2\omega^2}\right)+ \\ &\eta_i\left[2\,(b-1)^2\,\Gamma_0(b)-2b\left(b-\frac{3}{2}\right)\Gamma_1(b)\right]\left(-\frac{\omega_{*i}\hat{\omega}_{di}}{2\omega^2}\right) \end{aligned} \tag{5.82}$$

Let's now do some relabelling to aid the process of grouping terms together. We will use the following redefinitions to keep our calculations tidy:

$$\begin{aligned} Z_1 &\equiv \Gamma_0(b) \\ Z_2 &\equiv [\Gamma_0(b)-b\,(\Gamma_0(b)-\Gamma_1(b))] \\ Z_3 &\equiv \eta_i\left[2\,(b-1)^2\,\Gamma_0(b)-2b\left(b-\frac{3}{2}\right)\Gamma_1(b)\right] \end{aligned} \tag{5.83}$$

So these redefinitions transform Eqn. 5.82 as follows:

$$\begin{aligned}&[Y_0 + Y_1] = \\ &Z_1\left(1 - \frac{\omega_{*i}}{\omega} + \frac{\omega_{*i}\eta_i}{\omega} + \frac{\hat{\omega}_{di}}{2\omega} - \frac{\omega_{*i}\hat{\omega}_{di}}{2\omega^2}\right) + \\ &Z_2\left(-\frac{\omega_{*i}\eta_i}{\omega} + \frac{\hat{\omega}_{di}}{2\omega} - \frac{\omega_{*i}\hat{\omega}_{di}}{2\omega^2}\right) + \\ &Z_3\left(-\frac{\omega_{*i}\hat{\omega}_{di}}{2\omega^2}\right)\end{aligned} \tag{5.84}$$

Now grouping based on the degree of ω gives:

$$\begin{aligned}&[Y_0 + Y_1] = \\ &Z_1 + \frac{1}{\omega}\left[Z_1\left(-\omega_{*i} + \omega_{*i}\eta_i + \frac{\hat{\omega}_{di}}{2}\right)\right] + \frac{1}{\omega^2}\left[Z_1\left(-\frac{\omega_{*i}\hat{\omega}_{di}}{2}\right)\right] + \\ &\frac{1}{\omega}\left[Z_2\left(-\omega_{*i}\eta_i + \frac{\hat{\omega}_{di}}{2}\right)\right] + \frac{1}{\omega^2}\left[Z_2\left(-\frac{\omega_{*i}\hat{\omega}_{di}}{2}\right)\right] + \\ &\frac{1}{\omega^2}\left[Z_3\left(-\frac{\omega_{*i}\hat{\omega}_{di}}{2}\right)\right]\end{aligned} \tag{5.85}$$

and continuing to group in this way gives

$$\begin{aligned}&[Y_0 + Y_1] = \\ &Z_1 + \frac{1}{\omega}\left[Z_1\left(-\omega_{*i} + \omega_{*i}\eta_i + \frac{\hat{\omega}_{di}}{2}\right) + Z_2\left(-\omega_{*i}\eta_i + \frac{\hat{\omega}_{di}}{2}\right)\right] + \\ &\frac{1}{\omega^2}\left[Z_1\left(-\frac{\omega_{*i}\hat{\omega}_{di}}{2}\right) + Z_2\left(-\frac{\omega_{*i}\hat{\omega}_{di}}{2}\right) + Z_3\left(-\frac{\omega_{*i}\hat{\omega}_{di}}{2}\right)\right]\end{aligned} \tag{5.86}$$

which can be tidied up further as follows

$$\begin{aligned}&[Y_0 + Y_1] = \\ &Z_1 + \frac{1}{\omega}\left[Z_1\left(-\omega_{*i} + \omega_{*i}\eta_i + \frac{\hat{\omega}_{di}}{2}\right) + Z_2\left(-\omega_{*i}\eta_i + \frac{\hat{\omega}_{di}}{2}\right)\right] + \\ &\frac{1}{\omega^2}\left[\left(-\frac{\omega_{*i}\hat{\omega}_{di}}{2}\right) \times (Z_1 + Z_2 + Z_3)\right]\end{aligned} \tag{5.87}$$

Now, we can insert our result into Eqn. 5.81 to give

$$\begin{aligned}&\int_{-\infty}^{\infty}(1+\tau)\,|\phi|^2\frac{dl}{B} - \int_{-\infty}^{\infty}\tau\,[Y_0 + Y_1]\,|\phi|^2\frac{dl}{B} = \\ &\int_{-\infty}^{\infty}(1+\tau)\,|\phi|^2\frac{dl}{B} - \\ &\int_{-\infty}^{\infty}\tau\,[Z_1]\,|\phi|^2\frac{dl}{B} - \\ &\int_{-\infty}^{\infty}\frac{\tau}{\omega}\left[Z_1\left(-\omega_{*i} + \omega_{*i}\eta_i + \frac{\hat{\omega}_{di}}{2}\right) + Z_2\left(-\omega_{*i}\eta_i + \frac{\hat{\omega}_{di}}{2}\right)\right]|\phi|^2\frac{dl}{B} - \\ &\int_{-\infty}^{\infty}\frac{\tau}{\omega^2}\left[\left(-\frac{\omega_{*i}\hat{\omega}_{di}}{2}\right) \times (Z_1 + Z_2 + Z_3)\right]|\phi|^2\frac{dl}{B}\end{aligned} \tag{5.88}$$

So Eqn. 5.88 is the full expansion of the first line in the following equation:

$$\begin{aligned}&\int_{-\infty}^{\infty}\left[1+\tau\left(1-\left[Y_0+Y_1\right]\right)\right]|\phi|^2\frac{dl}{B}=\\&\int_{\frac{1}{B_{max}}}^{\frac{1}{B_{min}}}\int_{-\infty}^{\infty}\frac{dl}{\sqrt{1-\lambda B}}\frac{1}{2}\left[1-\frac{\omega_{*e}}{\omega}+\frac{3}{2}\frac{F_e\overline{G(\lambda)}}{\omega}\left(1-\frac{\omega_{*e}}{\omega}\left[1+\eta_e\right]\right)\right]|\overline{\phi}|^2d\lambda\end{aligned}\tag{5.89}$$

We now need to work out the second line. Let's focus on expanding and reorganising the terms in the square brackets:

$$\begin{aligned}&\left[1-\frac{\omega_{*e}}{\omega}+\frac{3}{2}\frac{F_e\overline{G(\lambda)}}{\omega}\left(1-\frac{\omega_{*e}}{\omega}\left[1+\eta_e\right]\right)\right]=\\&\left[1+\frac{1}{\omega}\left(-\omega_{*e}+\frac{3}{2}F_e\overline{G(\lambda)}\right)+\frac{1}{\omega^2}\left(-\frac{3}{2}F_e\overline{G(\lambda)}\omega_{*e}\left[1+\eta_e\right]\right)\right]\end{aligned}\tag{5.90}$$

Now, the second line in Eqn5.89 becomes

$$\begin{aligned}&\int_{\frac{1}{B_{max}}}^{\frac{1}{B_{min}}}\int_{-\infty}^{\infty}\frac{dl}{\sqrt{1-\lambda B}}\frac{1}{2}\left[1-\frac{\omega_{*e}}{\omega}+\frac{3}{2}\frac{F_e\overline{G(\lambda)}}{\omega}\left(1-\frac{\omega_{*e}}{\omega}\left[1+\eta_e\right]\right)\right]|\overline{\phi}|^2d\lambda=\\&\int_{\frac{1}{B_{max}}}^{\frac{1}{B_{min}}}\int_{-\infty}^{\infty}\frac{dl}{\sqrt{1-\lambda B}}\frac{1}{2}|\overline{\phi}|^2d\lambda+\\&\int_{\frac{1}{B_{max}}}^{\frac{1}{B_{min}}}\int_{-\infty}^{\infty}\frac{dl}{\sqrt{1-\lambda B}}\frac{1}{2}\left[\frac{1}{\omega}\left(-\omega_{*e}+\frac{3}{2}F_e\overline{G(\lambda)}\right)\right]|\overline{\phi}|^2d\lambda+\\&\int_{\frac{1}{B_{max}}}^{\frac{1}{B_{min}}}\int_{-\infty}^{\infty}\frac{dl}{\sqrt{1-\lambda B}}\frac{1}{2}\left[\frac{1}{\omega^2}\left(-\frac{3}{2}F_e\overline{G(\lambda)}\omega_{*e}\left[1+\eta_e\right]\right)\right]|\overline{\phi}|^2d\lambda\end{aligned}\tag{5.91}$$

Thus, putting everything together into Eqn. 5.89 gives

$$\begin{aligned}&\int_{-\infty}^{\infty}\left(1+\tau\right)|\phi|^2\frac{dl}{B}-\int_{-\infty}^{\infty}\tau\left[Z_1\right]|\phi|^2\frac{dl}{B}-\\&\int_{-\infty}^{\infty}\frac{\tau}{\omega}\left[Z_1\left(-\omega_{*i}+\omega_{*i}\eta_i+\frac{\hat{\omega}_{di}}{2}\right)+Z_2\left(-\omega_{*i}\eta_i+\frac{\hat{\omega}_{di}}{2}\right)\right]|\phi|^2\frac{dl}{B}-\\&\int_{-\infty}^{\infty}\frac{\tau}{\omega^2}\left[\left(-\frac{\omega_{*i}\hat{\omega}_{di}}{2}\right)\times\left(Z_1+Z_2+Z_3\right)\right]|\phi|^2\frac{dl}{B}=\\&\int_{\frac{1}{B_{max}}}^{\frac{1}{B_{min}}}\int_{-\infty}^{\infty}\frac{dl}{\sqrt{1-\lambda B}}\frac{1}{2}|\overline{\phi}|^2d\lambda+\\&\int_{\frac{1}{B_{max}}}^{\frac{1}{B_{min}}}\int_{-\infty}^{\infty}\frac{dl}{\sqrt{1-\lambda B}}\frac{1}{2}\left[\frac{1}{\omega}\left(-\omega_{*e}+\frac{3}{2}F_e\overline{G(\lambda)}\right)\right]|\overline{\phi}|^2d\lambda+\\&\int_{\frac{1}{B_{max}}}^{\frac{1}{B_{min}}}\int_{-\infty}^{\infty}\frac{dl}{\sqrt{1-\lambda B}}\frac{1}{2}\left[\frac{1}{\omega^2}\left(-\frac{3}{2}F_e\overline{G(\lambda)}\omega_{*e}\left[1+\eta_e\right]\right)\right]|\overline{\phi}|^2d\lambda\end{aligned}\tag{5.92}$$

Now, let's rearrange our result so that the ω-independent terms are all on one side of the equals sign, and the remaining terms are on the opposite side:

$$\begin{aligned}
&\int_{-\infty}^{\infty}(1+\tau)\,|\phi|^2\frac{dl}{B}-\int_{-\infty}^{\infty}\tau\,[Z_1]\,|\phi|^2\frac{dl}{B}-\int_{\frac{1}{B_{max}}}^{\frac{1}{B_{min}}}\int_{-\infty}^{\infty}\frac{dl}{\sqrt{1-\lambda B}}\frac{1}{2}|\overline{\phi}|^2d\lambda=\\
&\int_{-\infty}^{\infty}\frac{\tau}{\omega}\left[Z_1\left(-\omega_{*i}+\omega_{*i}\eta_i+\frac{\hat{\omega}_{di}}{2}\right)+Z_2\left(-\omega_{*i}\eta_i+\frac{\hat{\omega}_{di}}{2}\right)\right]|\phi|^2\frac{dl}{B}+\\
&\int_{\frac{1}{B_{max}}}^{\frac{1}{B_{min}}}\int_{-\infty}^{\infty}\frac{dl}{\sqrt{1-\lambda B}}\frac{1}{2}\left[\frac{1}{\omega}\left(-\omega_{*e}+\frac{3}{2}F_e\overline{G(\lambda)}\right)\right]|\overline{\phi}|^2d\lambda+\\
&\int_{-\infty}^{\infty}\frac{\tau}{\omega^2}\left[\left(-\frac{\omega_{*i}\hat{\omega}_{di}}{2}\right)\times(Z_1+Z_2+Z_3)\right]|\phi|^2\frac{dl}{B}+\\
&\int_{\frac{1}{B_{max}}}^{\frac{1}{B_{min}}}\int_{-\infty}^{\infty}\frac{dl}{\sqrt{1-\lambda B}}\frac{1}{2}\left[\frac{1}{\omega^2}\left(-\frac{3}{2}F_e\overline{G(\lambda)}\omega_{*e}\left[1+\eta_e\right]\right)\right]|\overline{\phi}|^2d\lambda
\end{aligned}\tag{5.93}$$

We can pull out the ω terms also, to give

$$\begin{aligned}
&\int_{-\infty}^{\infty}(1+\tau)\,|\phi|^2\frac{dl}{B}-\int_{-\infty}^{\infty}\tau\,[Z_1]\,|\phi|^2\frac{dl}{B}-\int_{\frac{1}{B_{max}}}^{\frac{1}{B_{min}}}\int_{-\infty}^{\infty}\frac{dl}{\sqrt{1-\lambda B}}\frac{1}{2}|\overline{\phi}|^2d\lambda=\\
&\frac{1}{\omega}\left\{\int_{-\infty}^{\infty}\tau\left[Z_1\left(-\omega_{*i}+\omega_{*i}\eta_i+\frac{\hat{\omega}_{di}}{2}\right)+Z_2\left(-\omega_{*i}\eta_i+\frac{\hat{\omega}_{di}}{2}\right)\right]|\phi|^2\frac{dl}{B}+\right.\\
&\left.\int_{\frac{1}{B_{max}}}^{\frac{1}{B_{min}}}\int_{-\infty}^{\infty}\frac{dl}{\sqrt{1-\lambda B}}\frac{1}{2}\left(-\omega_{*e}+\frac{3}{2}F_e\overline{G(\lambda)}\right)|\overline{\phi}|^2d\lambda\right\}+\\
&\frac{1}{\omega^2}\left\{\int_{-\infty}^{\infty}\tau\left[\left(-\frac{\omega_{*i}\hat{\omega}_{di}}{2}\right)\times(Z_1+Z_2+Z_3)\right]|\phi|^2\frac{dl}{B}+\right.\\
&\left.\int_{\frac{1}{B_{max}}}^{\frac{1}{B_{min}}}\int_{-\infty}^{\infty}\frac{dl}{\sqrt{1-\lambda B}}\frac{1}{2}\left(-\frac{3}{2}F_e\overline{G(\lambda)}\omega_{*e}\left[1+\eta_e\right]\right)|\overline{\phi}|^2d\lambda\right\}
\end{aligned}\tag{5.94}$$

We will now make use of the fact that:

$$\begin{aligned}
\omega_{*i}&=-\frac{\omega_{*e}}{\tau}\\
\tau&=\frac{T_e}{T_i}
\end{aligned}\tag{5.95}$$

such that we obtain

$$\begin{aligned}
&\int_{-\infty}^{\infty}(1+\tau)\,|\phi|^2\frac{dl}{B}-\int_{-\infty}^{\infty}\tau\,[Z_1]\,|\phi|^2\frac{dl}{B}-\int_{\frac{1}{B_{max}}}^{\frac{1}{B_{min}}}\int_{-\infty}^{\infty}\frac{dl}{\sqrt{1-\lambda B}}\frac{1}{2}|\overline{\phi}|^2d\lambda=\\
&\frac{1}{\omega}\left\{\int_{-\infty}^{\infty}\tau\left[Z_1\left(\frac{\omega_{*e}}{\tau}-\frac{\omega_{*e}}{\tau}\eta_i+\frac{\hat{\omega}_{di}}{2}\right)+Z_2\left(\frac{\omega_{*e}}{\tau}\eta_i+\frac{\hat{\omega}_{di}}{2}\right)\right]|\phi|^2\frac{dl}{B}+\right.\\
&\left.\int_{\frac{1}{B_{max}}}^{\frac{1}{B_{min}}}\int_{-\infty}^{\infty}\frac{dl}{\sqrt{1-\lambda B}}\frac{1}{2}\left(-\omega_{*e}+\frac{3}{2}F_e\overline{G(\lambda)}\right)|\overline{\phi}|^2d\lambda\right\}+\\
&\frac{1}{\omega^2}\left\{\int_{-\infty}^{\infty}\tau\left[\left(\frac{\omega_{*e}\hat{\omega}_{di}}{2\tau}\right)\times(Z_1+Z_2+Z_3)\right]|\phi|^2\frac{dl}{B}+\right.\\
&\left.\int_{\frac{1}{B_{max}}}^{\frac{1}{B_{min}}}\int_{-\infty}^{\infty}\frac{dl}{\sqrt{1-\lambda B}}\frac{1}{2}\left(-\frac{3}{2}F_e\overline{G(\lambda)}\omega_{*e}\left[1+\eta_e\right]\right)|\overline{\phi}|^2d\lambda\right\}
\end{aligned}\tag{5.96}$$

and now, if we multiply out the terms involving τ, and pull out the ω_{*e} terms, we get

$$\begin{aligned}
&\int_{-\infty}^{\infty}(1+\tau)\left|\phi\right|^2\frac{dl}{B}-\int_{-\infty}^{\infty}\tau\left[Z_1\right]\left|\phi\right|^2\frac{dl}{B}-\int_{\frac{1}{B_{max}}}^{\frac{1}{B_{min}}}\int_{-\infty}^{\infty}\frac{dl}{\sqrt{1-\lambda B}}\frac{1}{2}|\overline{\phi}|^2d\lambda=\\
&\frac{\omega_{*e}}{\omega}\left\{\int_{-\infty}^{\infty}\left[Z_1\left(1-\eta_i+\frac{\hat{\omega}_{di}\tau}{2\omega_{*e}}\right)+Z_2\left(\eta_i+\frac{\hat{\omega}_{di}\tau}{2\omega_{*e}}\right)\right]\left|\phi\right|^2\frac{dl}{B}+\right.\\
&\left.\int_{\frac{1}{B_{max}}}^{\frac{1}{B_{min}}}\int_{-\infty}^{\infty}\frac{dl}{\sqrt{1-\lambda B}}\frac{1}{2}\left(-1+\frac{3}{2}\frac{F_e\overline{G(\lambda)}}{\omega_{*e}}\right)|\overline{\phi}|^2d\lambda\right\}+\\
&\frac{\omega_{*e}^2}{\omega^2}\left\{\int_{-\infty}^{\infty}\left[\left(\frac{\hat{\omega}_{di}}{2\omega_{*e}}\right)\times\left(Z_1+Z_2+Z_3\right)\right]\left|\phi\right|^2\frac{dl}{B}+\right.\\
&\left.\int_{\frac{1}{B_{max}}}^{\frac{1}{B_{min}}}\int_{-\infty}^{\infty}\frac{dl}{\sqrt{1-\lambda B}}\frac{1}{2}\left(-\frac{3}{2}\frac{F_e\overline{G(\lambda)}}{\omega_{*e}}\left[1+\eta_e\right]\right)|\overline{\phi}|^2d\lambda\right\}
\end{aligned}\tag{5.97}$$

Now, if we multiply everything by $\frac{\omega^2}{\omega_{*e}^2}$ and tidy up some of our terms, we finally obtain:

$$\begin{aligned}
&\frac{\omega^2}{\omega_{*e}^2}\left\{\int_{-\infty}^{\infty}\left(1+\tau\left[1-Z_1\right]\right)\left|\phi\right|^2\frac{dl}{B}-\int_{\frac{1}{B_{max}}}^{\frac{1}{B_{min}}}\int_{-\infty}^{\infty}\frac{dl}{\sqrt{1-\lambda B}}\frac{1}{2}|\overline{\phi}|^2d\lambda\right\}=\\
&\frac{\omega}{\omega_{*e}}\left\{\int_{-\infty}^{\infty}\left[Z_1\left(1-\eta_i+\frac{\hat{\omega}_{di}\tau}{2\omega_{*e}}\right)+Z_2\left(\eta_i+\frac{\hat{\omega}_{di}\tau}{2\omega_{*e}}\right)\right]\left|\phi\right|^2\frac{dl}{B}+\right.\\
&\left.\int_{\frac{1}{B_{max}}}^{\frac{1}{B_{min}}}\int_{-\infty}^{\infty}\frac{dl}{\sqrt{1-\lambda B}}\frac{1}{2}\left(-1+\frac{3}{2}\frac{F_e\overline{G(\lambda)}}{\omega_{*e}}\right)|\overline{\phi}|^2d\lambda\right\}+\\
&\int_{-\infty}^{\infty}\left[\left(\frac{\hat{\omega}_{di}}{2\omega_{*e}}\right)\times\left(Z_1+Z_2+Z_3\right)\right]\left|\phi\right|^2\frac{dl}{B}+\\
&\int_{\frac{1}{B_{max}}}^{\frac{1}{B_{min}}}\int_{-\infty}^{\infty}\frac{dl}{\sqrt{1-\lambda B}}\frac{1}{2}\left(-\frac{3}{2}\frac{F_e\overline{G(\lambda)}}{\omega_{*e}}\left[1+\eta_e\right]\right)|\overline{\phi}|^2d\lambda
\end{aligned}\tag{5.98}$$

We can now complete our derivation by reinserting our Z_n expressions. Let's look at expanding the following term from the second line of Eqn. 5.98:

$$\begin{aligned}
&\left[Z_1\left(1-\eta_i+\frac{\hat{\omega}_{di}\tau}{2\omega_{*e}}\right)+Z_2\left(\eta_i+\frac{\hat{\omega}_{di}\tau}{2\omega_{*e}}\right)\right]=\\
&\left[\Gamma_0\left(1-\eta_i+\frac{\hat{\omega}_{di}\tau}{2\omega_{*e}}\right)+\left[\Gamma_0-b\left(\Gamma_0-\Gamma_1\right)\right]\left(\eta_i+\frac{\hat{\omega}_{di}\tau}{2\omega_{*e}}\right)\right]=\\
&\left[\Gamma_0-\Gamma_0\eta_i+\Gamma_0\frac{\hat{\omega}_{di}\tau}{2\omega_{*e}}+\Gamma_0\eta_i+\Gamma_0\frac{\hat{\omega}_{di}\tau}{2\omega_{*e}}-\eta_i b\left(\Gamma_0-\Gamma_1\right)-b\left(\Gamma_0-\Gamma_1\right)\frac{\hat{\omega}_{di}\tau}{2\omega_{*e}}\right]=\\
&\left[\left[\Gamma_0-\eta_i b\left(\Gamma_0-\Gamma_1\right)\right]+\left[2\Gamma_0-b\left(\Gamma_0-\Gamma_1\right)\right]\frac{\hat{\omega}_{di}\tau}{2\omega_{*e}}\right]
\end{aligned}\tag{5.99}$$

Let's now expand the following term from the fourth line of Eqn. 5.98:

$$\begin{aligned}
&Z_1+Z_2+Z_3=\\
&\Gamma_0+\Gamma_0-b\left(\Gamma_0-\Gamma_1\right)+\eta_i\left[2\left(b-1\right)^2\Gamma_0(b)-2b\left(b-\frac{3}{2}\right)\Gamma_1(b)\right]=\\
&2\Gamma_0-b\left(\Gamma_0-\Gamma_1\right)+\eta_i\left[2\left(b-1\right)^2\Gamma_0+b\left(3-2b\right)\Gamma_1\right]
\end{aligned}\tag{5.100}$$

Let's insert everything into Eqn. 5.98:

$$\begin{aligned}
&\frac{\omega^2}{\omega_{*e}^2}\left\{\int_{-\infty}^{\infty}\left(1+\tau\left[1-\Gamma_0\right]\right)|\phi|^2\frac{dl}{B}-\frac{1}{2}\int_{\frac{1}{B_{max}}}^{\frac{1}{B_{min}}}\int_{-\infty}^{\infty}\frac{dl}{\sqrt{1-\lambda B}}|\overline{\phi}|^2 d\lambda\right\}= \\
&\frac{\omega}{\omega_{*e}}\left\{\int_{-\infty}^{\infty}\left[\left[\Gamma_0-\eta_i b\left(\Gamma_0-\Gamma_1\right)\right]+\left[2\Gamma_0-b\left(\Gamma_0-\Gamma_1\right)\right]\frac{\hat{\omega}_{di}\tau}{2\omega_{*e}}\right]|\phi|^2\frac{dl}{B}-\right. \\
&\left.\frac{1}{2}\int_{\frac{1}{B_{max}}}^{\frac{1}{B_{min}}}\int_{-\infty}^{\infty}\frac{dl}{\sqrt{1-\lambda B}}|\overline{\phi}|^2 d\lambda+\frac{1}{2}\int_{\frac{1}{B_{max}}}^{\frac{1}{B_{min}}}\int_{-\infty}^{\infty}\frac{dl}{\sqrt{1-\lambda B}}\left(\frac{3}{2}\frac{F_e\overline{G(\lambda)}}{\omega_{*e}}\right)|\overline{\phi}|^2 d\lambda\right\} \\
&+\int_{-\infty}^{\infty}\left[2\Gamma_0-b\left(\Gamma_0-\Gamma_1\right)+\eta_i\left[2\left(b-1\right)^2\Gamma_0+b\left(3-2b\right)\Gamma_1\right]\right]\left(\frac{\hat{\omega}_{di}}{2\omega_{*e}}\right)|\phi|^2\frac{dl}{B} \\
&-\frac{1}{2}\int_{\frac{1}{B_{max}}}^{\frac{1}{B_{min}}}\int_{-\infty}^{\infty}\frac{dl}{\sqrt{1-\lambda B}}\left(\frac{3}{2}\frac{F_e\overline{G(\lambda)}}{\omega_{*e}}\left[1+\eta_e\right]\right)|\overline{\phi}|^2 d\lambda
\end{aligned} \tag{5.101}$$

We have now obtained an expression that is quadratic in $\frac{\omega}{\omega_{*e}}$, which can be solved numerically by inserting an appropriate trial function ϕ, or GENE simulation data for ϕ. We have also already shown how the variational principle is appropriate for this ω proxy result by looking at the more general integral equation, Eqn. 5.77. However, in Appendix B.2, it is shown explicitly how Eqn. 5.101 possesses the required variational property for this principle.

Before concluding this section, let's look at how Eqn. 5.101 can be solved as a quadratic equation. We will label the distinct terms that make up this equation as follows:

- $a_1 \rightarrow \int_{-\infty}^{\infty}\left(1+\tau\left[1-\Gamma_0\right]\right)|\phi|^2\frac{dl}{B}$
- $a_2 \rightarrow \frac{1}{2}\int_{\frac{1}{B_{max}}}^{\frac{1}{B_{min}}}\int_{-\infty}^{\infty}\frac{dl}{\sqrt{1-\lambda B}}|\overline{\phi}|^2 d\lambda$
- $b_1+b_2 \rightarrow \int_{-\infty}^{\infty}\left[\left[\Gamma_0-\eta_i b\left(\Gamma_0-\Gamma_1\right)\right]+\left[2\Gamma_0-b\left(\Gamma_0-\Gamma_1\right)\right]\frac{\hat{\omega}_{di}\tau}{2\omega_{*e}}\right]|\phi|^2\frac{dl}{B}$
- $b_3 \rightarrow \frac{1}{2}\int_{\frac{1}{B_{max}}}^{\frac{1}{B_{min}}}\int_{-\infty}^{\infty}\frac{dl}{\sqrt{1-\lambda B}}\left(\frac{3}{2}\frac{F_e\overline{G(\lambda)}}{\omega_{*e}}\right)|\overline{\phi}|^2 d\lambda$
- $c_1 \rightarrow \int_{-\infty}^{\infty}\left[2\Gamma_0-b\left(\Gamma_0-\Gamma_1\right)+\eta_i\left[2\left(b-1\right)^2\Gamma_0+b\left(3-2b\right)\Gamma_1\right]\right]\left(\frac{\hat{\omega}_{di}}{2\omega_{*e}}\right)|\phi|^2\frac{dl}{B}$
- $c_2 \equiv b_3\left[1+\eta_e\right] \rightarrow \frac{1}{2}\int_{\frac{1}{B_{max}}}^{\frac{1}{B_{min}}}\int_{-\infty}^{\infty}\frac{dl}{\sqrt{1-\lambda B}}\left(\frac{3}{2}\frac{F_e\overline{G(\lambda)}}{\omega_{*e}}\left[1+\eta_e\right]\right)|\overline{\phi}|^2 d\lambda$

This allows us to rewrite Eqn. 5.101 in the following concise form:

$$\frac{\omega^2}{\omega_{*e}^2}\underbrace{\left\{a_1-a_2\right\}}_{A}=\frac{\omega}{\omega_{*e}}\underbrace{\left\{b_1+b_2-a_2+b_3\right\}}_{B}+\underbrace{\left\{c_1-c_2\right\}}_{C} \tag{5.102}$$

We will abbreviate this even further to give:

$$A\frac{\omega^2}{\omega_{*e}^2}-B\frac{\omega}{\omega_{*e}}-C=0 \tag{5.103}$$

such that we can use the standard quadratic formula:

$$\begin{aligned} &\rightarrow ax^2 + bx + c = 0 \\ &\rightarrow x = \frac{-b \pm \sqrt{b^2 - 4ac}}{2a} \end{aligned} \tag{5.104}$$

to obtain

$$\frac{\omega}{\omega_{*e}} = \frac{B \pm \sqrt{B^2 + 4AC}}{2A} \tag{5.105}$$

It is important to note that only the positive and real quadratic solution here corresponds to the physically relevant results. This solution can be numerically calculated in a straightforward manner to obtain results for $\frac{\omega}{\omega_{*e}}$, and thus, for the mode frequency ω. In fact, to be more accurate, we are only calculating the real part of the mode frequency ω_r. We can then use these results when evaluating our proxy for the critical density gradient.

Chapter 6

The Critical-Density-Gradient proxy

In this chapter, we analytically derive a proxy for the critical density gradient. We will follow a procedure similar to that found in [12], but with some modifications due to the fact that we are considering geometries more general than quasi-isodynamic configurations. This analysis looks at how resonance can occur in the system, and both ions and electrons will be considered as co-contributors to this resonance.

6.1 Developing the Critical-Density-Gradient Proxy

In this section, we derive our analytical proxy for the critical density gradient of the TEM. The procedure carried out here shares a common starting point as our mode frequency proxy derivation in section 5.2. The primary difference between these two derivations involves the ordering of the magnetic drift frequency ω_{da}. In order to be able to carry out our variational principle approach in section 5.2, we needed to assume a small ordering of this drift frequency compared to the mode frequency ($\omega_{da} \ll \omega$), so as to avoid encountering resonance when $\omega_{da} \sim \omega$ in the denominator of our integral expression. In this section, however, we directly account for resonances between ω_{da} and ω, with the hope that this will allow us to calculate the critical density gradient when this resonance becomes manifest.

As with our mode frequency proxy derivation, we begin by inserting the bounce-averaged solution of the gyrokinetic equation, given by the following expression for g_a,

$$\boxed{g_{a(Trapped)} = \frac{e_a}{T_a}\overline{J_0\phi}\frac{(\omega - \omega_{*a}^T)}{(\omega - \overline{\omega}_{da})}f_{a0}} \tag{6.1}$$

into the QN equation, given by

$$\boxed{\sum_{a=i,e} \frac{n_a e_a^2}{T_a}\phi = \sum_{a=i,e} e_a \int g_a(\mathbf{R},\mathcal{E},\mu) J_0 \left(\frac{k_\perp v_\perp}{\omega_a}\right) d\mathbf{v}} \tag{6.2}$$

This substitution results in

$$\sum_{a=i,e} \frac{n_a e_a^2}{T_a}\phi = \sum_{a=i,e} e_a \int \left(\frac{e_a}{T_a}\overline{J_0\phi}\frac{(\omega-\omega_{*a}^T)}{(\omega-\overline{\omega}_{da})} f_{a0}\right) J_0 d\mathbf{v} \tag{6.3}$$

where once again, the Bessel function J_0 for trapped particles can be set equal to one [12]. In order to obtain a purely real left-hand side, we multiply across by ϕ^* and subsequently integrate along the field line. This gives us

$$\begin{aligned}
\sum_a \frac{n_a e_a^2}{T_a}\int_{-\infty}^{\infty}|\phi|^2\frac{dl}{B} &= \sum_a \sum_{\text{wells}} e_a \oint \frac{dl}{B}\int \frac{e_a}{T_a}\overline{\phi}\phi^*\frac{(\omega-\omega_{*a}^T)}{(\omega-\overline{\omega}_{da})} f_{a0} d\mathbf{v} \\
&= \sum_a \sum_{\text{wells}} e_a \oint \frac{dl}{B}\int_{trapped} \frac{e_a}{T_a}\overline{\phi}\phi^*\frac{(\omega-\omega_{*a}^T)}{(\omega-\overline{\omega}_{da})} f_{a0}\frac{2\pi B v^3 dv d\lambda}{|v_\parallel|} \\
&= \sum_a \sum_{\text{wells}} e_a \int_{\frac{1}{B_{max}}}^{\frac{1}{B_{min}}} d\lambda \int_0^\infty 2\pi v^3 dv \oint \frac{dl}{|v_\parallel|}\frac{e_a}{T_a}\overline{\phi}\phi^*\frac{(\omega-\omega_{*a}^T)}{(\omega-\overline{\omega}_{da})} f_{a0} \\
&= \sum_a \sum_{\text{wells}} e_a \int_{\frac{1}{B_{max}}}^{\frac{1}{B_{min}}} d\lambda \int_0^\infty 2\pi v^3 dv \frac{e_a}{T_a}(\overline{\phi})(\overline{\phi^*})\tau_{ba}(\lambda)\frac{(\omega-\omega_{*a}^T)}{(\omega-\overline{\omega}_{da})} f_{a0} \\
&= \sum_a \sum_{\text{wells}} \int_{\frac{1}{B_{max}}}^{\frac{1}{B_{min}}} d\lambda \int_0^\infty 2\pi v^3 dv \frac{e_a^2}{T_a}|\overline{\phi}|^2\tau_{ba}(\lambda)\frac{(\omega-\omega_{*a}^T)}{(\omega-\overline{\omega}_{da})} f_{a0}
\end{aligned} \tag{6.4}$$

where we have used

$$\begin{aligned}
\int_{-\infty}^{\infty} &\equiv \sum_{\text{wells}} \oint \\
\oint \frac{dl}{|v_\parallel|}\phi^* &= \overline{\phi^*}\tau_{ba} \\
\tau_{ba}(\lambda) &= \oint \frac{dl}{|v_\parallel|} = \oint \frac{dl}{x v_{Ta}\sqrt{1-\lambda B}}
\end{aligned} \tag{6.5}$$

as well as

$$d\mathbf{v} = 2\pi v_\perp dv_\perp dv_\parallel = \sum_\sigma \frac{B\pi v^3 dv d\lambda}{|v_\parallel|} \tag{6.6}$$

with

$$\begin{aligned}
\lambda &= \frac{v_\perp^2}{v^2 B} = \frac{\mu}{\mathcal{E}} \\
\sigma &= \frac{v_\parallel}{|v_\parallel|}
\end{aligned} \tag{6.7}$$

The left-hand side of Eqn. 6.4 is purely real and the right-hand side consequently has to be purely real as well. We now use the normalised velocity coordinate $x = \frac{v}{v_{Ta}}$ and express the

bounce-averaged magnetic drift in terms of this normalised velocity and a factor that depends on the pitch angle λ and the particle species a,

$$\begin{aligned}\overline{\omega}_{da} &= \overline{\mathbf{k}_\perp \cdot \left[\hat{\mathbf{b}} \times \left(\frac{v_\perp^2}{2}\nabla \ln B + v_\parallel^2 \vec{\kappa}\right)\frac{1}{\Omega_a}\right]} \\ &= \overline{\mathbf{k}_\perp \cdot \left[\hat{\mathbf{b}} \times \left(\frac{\lambda B v^2}{2}\nabla \ln B + v^2(1-\lambda B)\vec{\kappa}\right)\frac{1}{\Omega_a}\right]} \\ &= \left(x^2 v_{Ta}^2\right)\overline{\mathbf{k}_\perp \cdot \left[\hat{\mathbf{b}} \times \left(\frac{\lambda B}{2}\nabla \ln B + (1-\lambda B)\vec{\kappa}\right)\frac{1}{\Omega_a}\right]} \\ &= x^2 D_a(\lambda)\end{aligned} \tag{6.8}$$

such that $D_a(\lambda)$ is defined as

$$D_a(\lambda) \equiv v_{Ta}^2 \overline{\mathbf{k}_\perp \cdot \left[\hat{\mathbf{b}} \times \left(\frac{\lambda B}{2}\nabla \ln B + (1-\lambda B)\vec{\kappa}\right)\frac{1}{\Omega_a}\right]} \tag{6.9}$$

where $\vec{\kappa} = \hat{\mathbf{b}} \cdot \nabla \hat{\mathbf{b}}$. In the following aside, Eqn. 6.9 is parsed further such that its species-dependent and λ-dependent components can be defined separately.

Aside

Looking more closely at Eqn. 6.9, let's expand our species-dependent terms as follows

$$\begin{aligned} v_{Ta} &= \sqrt{\frac{2T_a}{m_a}} \\ \overline{\Omega_a} &= \overline{\left(\frac{e_a B}{m_a}\right)} = \frac{e_a \overline{B}}{m_a} \end{aligned} \tag{6.10}$$

Now, going back to our expression for $D_a(\lambda)$

$$D_a(\lambda) \equiv v_{Ta}^2 \overline{\mathbf{k}_\perp \cdot \left[\hat{\mathbf{b}} \times \left(\frac{\lambda B}{2}\nabla \ln B + (1-\lambda B)\vec{\kappa}\right)\frac{1}{\Omega_a}\right]} \tag{6.11}$$

we can insert our expressions from Eqn. 6.10 to obtain

$$\begin{aligned} D_a(\lambda) &= \left(\frac{2T_a}{m_a}\right)\overline{\mathbf{k}_\perp \cdot \left[\hat{\mathbf{b}} \times \left(\frac{\lambda B}{2}\nabla \ln B + (1-\lambda B)\vec{\kappa}\right)\frac{m_a}{e_a B}\right]} \\ &= \left(\frac{2T_a}{m_a}\right)\left(\frac{m_a}{e_a}\right)\overline{\mathbf{k}_\perp \cdot \left[\hat{\mathbf{b}} \times \left(\frac{\lambda B}{2}\nabla \ln B + (1-\lambda B)\vec{\kappa}\right)\frac{1}{B}\right]} \\ &= \left(\frac{2T_a}{e_a}\right)\overline{\mathbf{k}_\perp \cdot \left[\hat{\mathbf{b}} \times \left(\frac{\lambda B}{2}\nabla \ln B + (1-\lambda B)\vec{\kappa}\right)\frac{1}{B}\right]} \\ &= F_a \overline{G(\lambda)} \end{aligned} \tag{6.12}$$

where in the final step, we have split $D_a(\lambda)$ into a species-dependent part F_a, and a λ-dependent part $\overline{G(\lambda)}$.

Let's take a moment to discuss a crucial point in our derivation. Reminding ourselves of where we left off:

$$\sum_a \frac{n_a e_a^2}{T_a} \int_{-\infty}^{\infty} |\phi|^2 \frac{dl}{B} = \sum_a \sum_{\text{wells}} \int_{\frac{1}{B_{max}}}^{\frac{1}{B_{min}}} d\lambda \int_0^{\infty} 2\pi v^3 dv \frac{e_a^2}{T_a} |\overline{\phi}|^2 \tau_{ba}(\lambda) \frac{(\omega - \omega_{*a}^T)}{(\omega - \overline{\omega}_{da})} f_{a0} \tag{6.13}$$

we can see that when $\omega = \overline{\omega}_{da}$, we are going to run into a divergence in our integral expression due to the following term:

$$\frac{1}{(\omega - \overline{\omega}_{da})} = \frac{1}{\left(\omega - x^2 F_a \overline{G(\lambda)}\right)} = \frac{1}{F_a \overline{G(\lambda)}} \frac{1}{\left(\frac{\omega}{F_a \overline{G(\lambda)}} - x^2\right)} \tag{6.14}$$

Now, if we approach the point of marginal stability, where $\omega = \omega_r + i\gamma$ with $\gamma \to 0^+$, we can write

$$\lim_{\frac{\gamma}{F_a \overline{G(\lambda)}} \to 0^+} \left[\frac{1}{\frac{\omega_r}{F_a \overline{G(\lambda)}} + \frac{i\gamma}{F_a \overline{G(\lambda)}} - x^2} \right] = -P \left[\frac{1}{x^2 - \frac{\omega_r}{F_a \overline{G(\lambda)}}} \right] + i\pi\delta \left(\frac{\omega_r}{F_a \overline{G(\lambda)}} - x^2 \right) \tag{6.15}$$

where P denotes the principal value of the integral. Therefore, we will have an imaginary part on the right-hand side of Eqn. 6.13 only when ω_r has the same sign as $F_a \overline{G(\lambda)}$, i.e., when there is a resonance between the frequency of the mode and the bounce-averaged magnetic drift. If the opposite was true, and these signs differed, then the argument of the delta function in Eqn. 6.15 would be negative, which would make the imaginary component of this expression zero.

And so, for resonance to be present, we can concisely state our required criterion as

$$(\text{sign})\omega_r \stackrel{!}{=} (\text{sign}) F_a \overline{G(\lambda)} \tag{6.16}$$

or, in terms of the frequencies

$$(\text{sign})\omega_r \stackrel{!}{=} (\text{sign})\overline{\omega}_{da} \tag{6.17}$$

Alternatively, if $\overline{\omega}_{da} = 0$, then resonance cannot occur and so the imaginary component would once again vanish. Eqn. 6.16 and Eqn. 6.17 will become important later when we need to determine which λ-values correspond to resonance occurring.

Before continuing, let's consider what implications this criterion (Eqn. 6.17) has on the particle species in our system. Firstly, it is important to note that the bounce-averaged magnetic drift frequencies have opposite signs for ions and electrons. Next, it is for now assumed (but later confirmed by numerical simulation) that $\overline{G(\lambda)}$ *can* change sign, meaning that it has a role to play in the overall sign of $\overline{\omega}_{da}$. This then implies that a fraction of both species can be in resonance with the mode, as each species has at least some finite number of particles which satisfy 6.16 and Eqn. 6.17. In other words, both species distributions are composed of particles with either positive or negative bounce-averaged magnetic drift frequencies, $\pm\overline{\omega}_{da}$, meaning that there will *always* be some portion of each species which fulfils the resonance criterion, Eqn. 6.17.

Now, we return to our main derivation. Restating Eqn. 6.13

$$\sum_a \frac{n_a e_a^2}{T_a}\int_{-\infty}^{\infty}|\phi|^2\frac{dl}{B} = \sum_a \sum_{\text{wells}} \int_{\frac{1}{B_{max}}}^{\frac{1}{B_{min}}} d\lambda \int_0^{\infty} 2\pi v^3 dv \frac{e_a^2}{T_a}|\overline{\phi}|^2 \tau_{ba}(\lambda)\frac{(\omega-\omega_{*a}^T)}{(\omega-\overline{\omega}_{da})}f_{a0} \tag{6.18}$$

we will focus on the following part of our main expression for now

$$\int_0^{\infty} 2\pi v^3 dv \frac{e_a^2}{T_a}|\overline{\phi}|^2 \tau_{ba}(\lambda)\frac{(\omega-\omega_{*a}^T)}{(\omega-\overline{\omega}_{da})}f_{a0}$$

which can be rewritten as

$$\int_0^{\infty} 2\pi \left(v_{Ta}^3 x^3\right)(v_{Ta}dx)\frac{e_a^2}{T_a}|\overline{\phi}|^2\tau_{ba}(\lambda)\frac{(\omega-\omega_{*a}^T)}{(\omega-x^2F_a\overline{G(\lambda)})}\left[n_a\left(\frac{1}{\pi v_{Ta}^2}\right)^{\frac{3}{2}}e^{-x^2}\right]$$

where we have made use of the normalised velocity $x = \frac{v}{v_{Ta}}$.

Simplifying further gives

$$\frac{n_a v_{Ta}}{\sqrt{\pi}}\int_0^{\infty}\frac{\tau_{ba}(\lambda)e_a^2}{T_a}|\overline{\phi}|^2\frac{(\omega-\omega_{*a}^T)}{(\omega-x^2F_a\overline{G(\lambda)})}\left(2x^3dx\right)e^{-x^2} \tag{6.19}$$

For reasons that will become clear in a moment, let's briefly relabel $x^2 = y$, such that

$$\frac{d}{dy}(x^2) = \frac{d}{dy}(y) \implies 2x\frac{dx}{dy} = 1 \implies 2xdx = dy \tag{6.20}$$

and multiplying across by x^2 gives

$$2x^3dx = x^2dy \implies 2x^3dx = x^2d(x^2) \tag{6.21}$$

Inserting this into Eqn. 6.19 then gives

$$\begin{aligned}&\frac{n_a v_{Ta}}{\sqrt{\pi}}\int_0^{\infty}\frac{\tau_{ba}(\lambda)e_a^2}{T_a}|\overline{\phi}|^2\frac{(\omega-\omega_{*a}^T)}{(\omega-x^2F_a\overline{G(\lambda)})}\left(x^2d(x^2)\right)e^{-x^2} = \\ &-\frac{n_a v_{Ta}e_a^2}{\sqrt{\pi}T_aF_a\overline{G(\lambda)}}\int_0^{\infty}|\overline{\phi}|^2\tau_{ba}(\lambda)\frac{(\omega-\omega_{*a}^T)}{\left(x^2-\frac{\omega}{F_a\overline{G(\lambda)}}\right)}e^{-x^2}x^2d(x^2)\end{aligned} \tag{6.22}$$

If we approach marginal stability, such that $\omega = \omega_r + i0^+$, and use the following approach to deal with the pole arising in Eqn. 6.22

$$\begin{aligned}\int_0^{\infty}\frac{f(x^2)}{\left(x^2-\frac{\omega_r}{F_a\overline{G(\lambda)}}\right)}d(x^2) &= \frac{1}{2}\int_{-\infty}^{\infty}\frac{f(x^2)}{\left(x^2-\frac{\omega_r}{F_a\overline{G(\lambda)}}\right)}d(x^2) \\ &= \frac{1}{2}\oint\frac{f(z)}{\left(z-\frac{\omega_r}{F_a\overline{G(\lambda)}}\right)}d(z) \\ &= i\pi f\left(\frac{\omega_r}{F_a\overline{G(\lambda)}}\right) + P\int_0^{\infty}\frac{f(x^2)}{x^2-\frac{\omega_r}{F_a\overline{G(\lambda)}}}d(x^2)\end{aligned} \tag{6.23}$$

we see that we pick up a residue when resonance is present ($\overline{\omega}_{da} = \omega$), giving us an imaginary component in our derivation. However, we know from earlier that the left-hand side of Eqn. 6.18 is real, such that the right-hand has to be real also. We therefore require, for the resonating portion of each species, that the total imaginary part of Eqn. 6.18 vanish

$$\mathrm{Im} \sum_a \sum_{\text{wells}} \int_{\frac{1}{B_{max}}}^{\frac{1}{B_{min}}} d\lambda \int_0^\infty 2\pi v^3 dv \frac{e_a^2}{T_a} |\overline{\phi}|^2 \tau_{ba}(\lambda) \frac{(\omega - \omega_{*a}^T)}{(\omega - \overline{\omega}_{da})} f_{a0} \stackrel{!}{=} 0 \tag{6.24}$$

Utilising Eqn. 6.22 and Eqn. 6.23 in Eqn. 6.24 then gives us

$$\sum_a -\frac{n_a v_{Ta} e_a^2 \sqrt{\pi}}{T_a} \sum_{\text{wells}} \int_{\frac{1}{B_{max}}}^{\frac{1}{B_{min}}} d\lambda |\overline{\phi}|^2 \frac{\tau_{ba}(\lambda)}{F_a \overline{G(\lambda)}} \left(\omega - \omega_{*a}^T\right) e^{-x^2} x^2 |_{x^2 = \frac{\omega}{F_a \overline{G(\lambda)}}} \stackrel{!}{=} 0 \tag{6.25}$$

Note, that although we are approaching marginal stability ($\omega = \omega_r + i0^+$), we are using the full ω in the remainder of our derivation, instead of ω_r. This is done to keep our work clean, but it should be noted that we are only considering the point of marginal stability from here on.

Let's return to our main derivation. If we now use our definition for the bounce time $\tau_{ba}(\lambda)$

$$\begin{aligned} \tau_{ba}(\lambda) &= \oint \frac{dl}{|v_\parallel|} \\ |v_\parallel| &= x v_{Ta} \sqrt{1 - \lambda B} \end{aligned} \tag{6.26}$$

such that

$$\tau_{ba}(\lambda) = \oint \frac{dl}{x v_{Ta} \sqrt{1 - \lambda B}} \tag{6.27}$$

and insert this into Eqn. 6.25, we obtain

$$\sum_a -\frac{n_a v_{Ta} e_a^2 \sqrt{\pi}}{T_a} \sum_{\text{wells}} \int_{\frac{1}{B_{max}}}^{\frac{1}{B_{min}}} d\lambda |\overline{\phi}|^2 \frac{1}{F_a \overline{G(\lambda)}} \left(\oint \frac{dl}{x v_{Ta} \sqrt{1 - \lambda B}} \right) \left(\omega - \omega_{*a}^T\right) e^{-x^2} x^2 |_{x^2 = \frac{\omega}{F_a \overline{G(\lambda)}}} \stackrel{!}{=} 0 \tag{6.28}$$

such that the thermal velocities cancel, giving

$$\sum_a -\frac{n_a e_a^2 \sqrt{\pi}}{T_a} \sum_{\text{wells}} \int_{\frac{1}{B_{max}}}^{\frac{1}{B_{min}}} d\lambda |\overline{\phi}|^2 \frac{1}{F_a \overline{G(\lambda)}} \left(\oint \frac{dl}{\sqrt{1 - \lambda B}} \right) \left(\omega - \omega_{*a}^T\right) e^{-x^2} x |_{x^2 = \frac{\omega}{F_a \overline{G(\lambda)}}} \stackrel{!}{=} 0 \tag{6.29}$$

We can now neaten our work by making use of the following expression for the species-independent bounce time:

$$\tau(\lambda) = \oint \frac{dl}{\sqrt{1 - \lambda B}} \tag{6.30}$$

which makes our expression more concise as follows:

$$\sum_a -\frac{n_a e_a^2 \sqrt{\pi}}{T_a} \sum_{\text{wells}} \int_{\frac{1}{B_{max}}}^{\frac{1}{B_{min}}} d\lambda |\overline{\phi}|^2 \frac{1}{F_a \overline{G(\lambda)}} \tau(\lambda) \left(\omega - \omega_{*a}^T\right) e^{-x^2} x |_{x^2 = \frac{\omega}{F_a \overline{G(\lambda)}}} \stackrel{!}{=} 0 \tag{6.31}$$

Evaluating Eqn. 6.31 using our expression for x^2 now gives us

$$\sum_a -\frac{n_a e_a^2 \sqrt{\pi}}{T_a} \sum_{\text{wells}} \int_{\frac{1}{B_{max}}}^{\frac{1}{B_{min}}} d\lambda |\overline{\phi}|^2 \frac{1}{F_a \overline{G(\lambda)}} \tau(\lambda) \left(\omega - \omega_{*a}^T\right) e^{-\frac{\omega}{F_a \overline{G(\lambda)}}} \left(\frac{\omega}{F_a \overline{G(\lambda)}}\right)^{\frac{1}{2}} \stackrel{!}{=} 0 \tag{6.32}$$

which is then equivalent to

$$\sum_a -\frac{n_a e_a^2 \sqrt{\pi}}{T_a} \sum_{\text{wells}} \int_{\frac{1}{B_{max}}}^{\frac{1}{B_{min}}} d\lambda |\overline{\phi}|^2 \frac{1}{F_a \overline{G(\lambda)}} \left(\frac{\omega}{F_a \overline{G(\lambda)}}\right)^{\frac{1}{2}} \tau(\lambda) \left(\omega - \omega_{*a}^T\right) e^{-\frac{\omega}{F_a \overline{G(\lambda)}}} \stackrel{!}{=} 0 \tag{6.33}$$

We can now expand our sum over the particle species a in Eqn. 6.33, which gives

$$\begin{aligned} &-\frac{n_e e_e^2 \sqrt{\pi}}{T_e} \sum_{\text{wells}} \int_{\frac{1}{B_{max}}}^{\frac{1}{B_{min}}} d\lambda |\overline{\phi}|^2 \frac{1}{F_e \overline{G(\lambda)}} \left(\frac{\omega}{F_e \overline{G(\lambda)}}\right)^{\frac{1}{2}} \tau(\lambda) \left(\omega - \omega_{*e}^T\right) e^{-\frac{\omega}{F_e \overline{G(\lambda)}}} \\ &-\frac{n_i e_i^2 \sqrt{\pi}}{T_i} \sum_{\text{wells}} \int_{\frac{1}{B_{max}}}^{\frac{1}{B_{min}}} d\lambda |\overline{\phi}|^2 \frac{1}{F_i \overline{G(\lambda)}} \left(\frac{\omega}{F_i \overline{G(\lambda)}}\right)^{\frac{1}{2}} \tau(\lambda) \left(\omega - \omega_{*i}^T\right) e^{-\frac{\omega}{F_i \overline{G(\lambda)}}} \stackrel{!}{=} 0 \end{aligned} \tag{6.34}$$

Let's now consider how we can analyse what happens when $\overline{G(\lambda)}$ approaches zero, but doesn't ever equal zero. As we will discuss later, we will not be concerned with what happens when $\overline{G(\lambda)} = 0$, and this conveniently helps us to avoid a divergence occurring in Eqn. 6.34.

Aside

As we have already stated, we are going to allow $\overline{G(\lambda)}$ to change sign in our derivation. This means that it must equal zero at some critical point. For instance, we can say that

$$\overline{G(\lambda_{Crit})} = 0 \tag{6.35}$$

for some λ_{Crit}, which is an intermediate λ-value between its minimum and maximum values. More concisely,

$$\frac{1}{B_{max}} < \lambda_{Crit} < \frac{1}{B_{min}} \tag{6.36}$$

so that we can split the λ integral as follows

$$\int_{\frac{1}{B_{max}}}^{\frac{1}{B_{min}}} d\lambda \simeq \lim_{\delta \to 0} \left[\int_{\frac{1}{B_{max}}}^{\lambda_{Crit} - \delta} d\lambda + \int_{\lambda_{Crit} + \delta}^{\frac{1}{B_{min}}} d\lambda \right] \tag{6.37}$$

where $\delta \ll 1$ is an arbitrarily small non-negative quantity.

This then allows us to split our electron and ion integrals in Eqn. 6.34 as follows

$$\begin{aligned}
&-\frac{n_e e_e^2\sqrt{\pi}}{T_e}\lim_{\delta\to 0}\left(\sum_{\text{wells}}\int_{\frac{1}{B_{max}}}^{\lambda_{Crit}-\delta} d\lambda|\overline{\phi}|^2\frac{1}{F_e\overline{G(\lambda)}}\left(\frac{\omega}{F_e\overline{G(\lambda)}}\right)^{\frac{1}{2}}\tau(\lambda)\left(\omega-\omega_{*e}^T\right)e^{-\frac{\omega}{F_e\overline{G(\lambda)}}}\right)\\
&-\frac{n_e e_e^2\sqrt{\pi}}{T_e}\lim_{\delta\to 0}\left(\sum_{\text{wells}}\int_{\lambda_{Crit}+\delta}^{\frac{1}{B_{min}}} d\lambda|\overline{\phi}|^2\frac{1}{F_e\overline{G(\lambda)}}\left(\frac{\omega}{F_e\overline{G(\lambda)}}\right)^{\frac{1}{2}}\tau(\lambda)\left(\omega-\omega_{*e}^T\right)e^{-\frac{\omega}{F_e\overline{G(\lambda)}}}\right)\\
&-\frac{n_i e_i^2\sqrt{\pi}}{T_i}\lim_{\delta\to 0}\left(\sum_{\text{wells}}\int_{\frac{1}{B_{max}}}^{\lambda_{Crit}-\delta} d\lambda|\overline{\phi}|^2\frac{1}{F_i\overline{G(\lambda)}}\left(\frac{\omega}{F_i\overline{G(\lambda)}}\right)^{\frac{1}{2}}\tau(\lambda)\left(\omega-\omega_{*i}^T\right)e^{-\frac{\omega}{F_i\overline{G(\lambda)}}}\right)\\
&-\frac{n_i e_i^2\sqrt{\pi}}{T_i}\lim_{\delta\to 0}\left(\sum_{\text{wells}}\int_{\lambda_{Crit}+\delta}^{\frac{1}{B_{min}}} d\lambda|\overline{\phi}|^2\frac{1}{F_i\overline{G(\lambda)}}\left(\frac{\omega}{F_i\overline{G(\lambda)}}\right)^{\frac{1}{2}}\tau(\lambda)\left(\omega-\omega_{*i}^T\right)e^{-\frac{\omega}{F_i\overline{G(\lambda)}}}\right)\overset{!}{=}0
\end{aligned}\tag{6.38}$$

Let's now make some stronger assumptions to simplify our expression slightly. Firstly, noting the definition of the temperature-dependent diamagnetic drift frequency

$$\omega_{*a}^T=\omega_{*a}\left[1+\eta_a\left(\frac{\mathcal{E}_a}{T_a}-\frac{3}{2}\right)\right]\tag{6.39}$$

we can see that if we make the assumption that the temperature gradient is flat, such that

$$\eta_a=\frac{d\ln T_a}{d\psi}\Big/\frac{d\ln n_a}{d\psi}=0\tag{6.40}$$

then we can see that

$$\omega_{*a}^T=\omega_{*a}\tag{6.41}$$

Making the further assumption that the species temperatures are equal, and also that the species densities are equal

$$\begin{aligned}
T_e&=T_i\\
n_e&=n_i
\end{aligned}\tag{6.42}$$

and using the definition of the temperature-independent diamagnetic drift frequency

$$\omega_{*a}=\frac{T_a k_\alpha}{e_a}\frac{d\ln n_a}{d\psi}\tag{6.43}$$

then we can also see that

$$\omega_{*e}=-\omega_{*i}\tag{6.44}$$

A further consequence of the equal species temperature assumption is that

$$\begin{aligned}
F_e&=\frac{2T_e}{e_e}=-\frac{2T_e}{e}\\
F_i&=\frac{2T_i}{e_i}=\frac{2T_e}{e}
\end{aligned}\tag{6.45}$$

such that

$$F_e = -F_i \tag{6.46}$$

Implementing this into Eqn. 6.38 gives

$$\begin{aligned}
&-\frac{n_e e^2\sqrt{\pi}}{T_e}\lim_{\delta\to 0}\left(\sum_{\text{wells}}\int_{\frac{1}{B_{max}}}^{\lambda_{Crit}-\delta} d\lambda|\overline{\phi}|^2\left(\frac{1}{F_e\overline{G(\lambda)}}\right)\left(\frac{\omega}{F_e\overline{G(\lambda)}}\right)^{\frac{1}{2}}\tau(\lambda)\,(\omega-\omega_{*e})\,e^{-\frac{\omega}{F_e\overline{G(\lambda)}}}\right)\\
&-\frac{n_e e^2\sqrt{\pi}}{T_e}\lim_{\delta\to 0}\left(\sum_{\text{wells}}\int_{\lambda_{Crit}+\delta}^{\frac{1}{B_{min}}} d\lambda|\overline{\phi}|^2\left(\frac{1}{F_e\overline{G(\lambda)}}\right)\left(\frac{\omega}{F_e\overline{G(\lambda)}}\right)^{\frac{1}{2}}\tau(\lambda)\,(\omega-\omega_{*e})\,e^{-\frac{\omega}{F_e\overline{G(\lambda)}}}\right)\\
&-\frac{n_e e^2\sqrt{\pi}}{T_e}\lim_{\delta\to 0}\left(\sum_{\text{wells}}\int_{\frac{1}{B_{max}}}^{\lambda_{Crit}-\delta} d\lambda|\overline{\phi}|^2\left(\frac{1}{-F_e\overline{G(\lambda)}}\right)\left(\frac{\omega}{-F_e\overline{G(\lambda)}}\right)^{\frac{1}{2}}\tau(\lambda)\,(\omega+\omega_{*e})\,e^{-\frac{\omega}{-F_e\overline{G(\lambda)}}}\right)\\
&-\frac{n_e e^2\sqrt{\pi}}{T_e}\lim_{\delta\to 0}\left(\sum_{\text{wells}}\int_{\lambda_{Crit}+\delta}^{\frac{1}{B_{min}}} d\lambda|\overline{\phi}|^2\left(\frac{1}{-F_e\overline{G(\lambda)}}\right)\left(\frac{\omega}{-F_e\overline{G(\lambda)}}\right)^{\frac{1}{2}}\tau(\lambda)\,(\omega+\omega_{*e})\,e^{-\frac{\omega}{-F_e\overline{G(\lambda)}}}\right)\stackrel{!}{=}0
\end{aligned} \tag{6.47}$$

Now that the prefactors are all identical, so we can multiply across by $-\frac{T_e}{n_e e^2\sqrt{\pi}}$, which gives

$$\begin{aligned}
&\lim_{\delta\to 0}\left(\sum_{\text{wells}}\int_{\frac{1}{B_{max}}}^{\lambda_{Crit}-\delta} d\lambda|\overline{\phi}|^2\left(\frac{1}{F_e\overline{G(\lambda)}}\right)\left(\frac{\omega}{F_e\overline{G(\lambda)}}\right)^{\frac{1}{2}}\tau(\lambda)\,(\omega-\omega_{*e})\,e^{-\frac{\omega}{F_e\overline{G(\lambda)}}}\right)+\\
&\lim_{\delta\to 0}\left(\sum_{\text{wells}}\int_{\lambda_{Crit}+\delta}^{\frac{1}{B_{min}}} d\lambda|\overline{\phi}|^2\left(\frac{1}{F_e\overline{G(\lambda)}}\right)\left(\frac{\omega}{F_e\overline{G(\lambda)}}\right)^{\frac{1}{2}}\tau(\lambda)\,(\omega-\omega_{*e})\,e^{-\frac{\omega}{F_e\overline{G(\lambda)}}}\right)+\\
&\lim_{\delta\to 0}\left(\sum_{\text{wells}}\int_{\frac{1}{B_{max}}}^{\lambda_{Crit}-\delta} d\lambda|\overline{\phi}|^2\left(\frac{1}{-F_e\overline{G(\lambda)}}\right)\left(\frac{\omega}{-F_e\overline{G(\lambda)}}\right)^{\frac{1}{2}}\tau(\lambda)\,(\omega+\omega_{*e})\,e^{-\frac{\omega}{-F_e\overline{G(\lambda)}}}\right)+\\
&\lim_{\delta\to 0}\left(\sum_{\text{wells}}\int_{\lambda_{Crit}+\delta}^{\frac{1}{B_{min}}} d\lambda|\overline{\phi}|^2\left(\frac{1}{-F_e\overline{G(\lambda)}}\right)\left(\frac{\omega}{-F_e\overline{G(\lambda)}}\right)^{\frac{1}{2}}\tau(\lambda)\,(\omega+\omega_{*e})\,e^{-\frac{\omega}{-F_e\overline{G(\lambda)}}}\right)\stackrel{!}{=}0
\end{aligned} \tag{6.48}$$

For now, the only behavioural information we have given about $\overline{G(\lambda)}$ is that we have allowed it to change sign, and so it must equal zero at some point. We have already defined the critical λ-value corresponding to this point as follows:

$$\overline{G(\lambda_{Crit})} = 0 \tag{6.49}$$

The λ-range for which $\overline{G(\lambda)}$ is positive or negative has been determined from numerical simulation using Mathematica. As it turns out, for all geometries considered, $\overline{G(\lambda)}$ is > 0 for $\lambda < \lambda_{Crit}$, and $\overline{G(\lambda)}$ is < 0 for $\lambda > \lambda_{Crit}$. By considering the $F_a\overline{G(\lambda)}$ values for different λ-ranges, and for each particle species, we can display these values of interest in the following table:

Species	**λ-Range**		
	$\lambda < \lambda_{Crit}$	$\lambda = \lambda_{Crit}$	$\lambda > \lambda_{Crit}$
Electrons	$F_e\overline{G(\lambda)} < 0$	$F_e\overline{G(\lambda)} = 0$	$F_e\overline{G(\lambda)} > 0$
Ions	$F_i\overline{G(\lambda)} > 0$	$F_i\overline{G(\lambda)} = 0$	$F_i\overline{G(\lambda)} < 0$

Table 6.1: *$F_a\overline{G(\lambda)}$ values for different λ-ranges, for each particle species.*

Now, let's consider a specific case relevant to Table 6.1. Let's assume for now that the sign of ω_r is positive. Then, for resonance to occur, the sign of $\overline{\omega}_{da}$ would need to be positive also. Note that $\overline{\omega}_{da} = x^2 D_a(\lambda)$, and so x^2 is automatically positive. Thus, we require that $D_a(\lambda) = F_a\overline{G(\lambda)} > 0$ for resonance to occur. Thus, for the full range of λ-values, there are always at most two cases where this is satisfied, one for each particle species. Note, the ions and electrons will resonate with ω_r for different λ-values. For example, if the ions resonate for $\lambda < \lambda_{Crit}$, then the electrons will resonate for $\lambda > \lambda_{Crit}$.

When we remind ourselves of our criteria for resonance occurring, given by Eqn. 6.16 and Eqn. 6.17

$$\begin{aligned} (\text{sign})\omega_r &\stackrel{!}{=} (\text{sign})F_a\overline{G(\lambda)} \\ \implies (\text{sign})\omega_r &\stackrel{!}{=} (\text{sign})\overline{\omega}_{da} \end{aligned} \tag{6.50}$$

we can see that $\overline{\omega}_{da} = 0$ violates these conditions, as there would be no finite bounce-averaged magnetic drift frequency present for the finite mode frequency to resonate with. This reasoning will help to simplify our λ-integrals, as only parts of our domain are relevant for resonance occurring. To clarify this, let's consider the following. By splitting our λ-integrals around the λ_{Crit} value, for a given species, we would ignore the λ-integral domain corresponding to

$$(\text{sign})F_a\overline{G(\lambda)} \neq (\text{sign})\omega_r \tag{6.51}$$

such that $\overline{\omega}_{da}$ is not resonating with ω_r. We would also ignore $\overline{\omega}_{da}(\lambda_{Crit}) = 0$, for the aforementioned reasoning. The remaining domains of relevance would differ for electrons and ions, due to $\overline{\omega}_{de} = -\overline{\omega}_{di}$.

Let's now return to our derivation. We will restate Eqn. 6.48 here:

$$\begin{aligned}
&\lim_{\delta\to 0}\left(\sum_{\text{wells}}\int_{\frac{1}{B_{max}}}^{\lambda_{Crit}-\delta} d\lambda|\overline{\phi}|^2\left(\frac{1}{F_e\overline{G(\lambda)}}\right)\left(\frac{\omega}{F_e\overline{G(\lambda)}}\right)^{\frac{1}{2}}\tau(\lambda)\,(\omega-\omega_{*e})\,e^{-\frac{\omega}{F_e\overline{G(\lambda)}}}\right)+\\
&\lim_{\delta\to 0}\left(\sum_{\text{wells}}\int_{\lambda_{Crit}+\delta}^{\frac{1}{B_{min}}} d\lambda|\overline{\phi}|^2\left(\frac{1}{F_e\overline{G(\lambda)}}\right)\left(\frac{\omega}{F_e\overline{G(\lambda)}}\right)^{\frac{1}{2}}\tau(\lambda)\,(\omega-\omega_{*e})\,e^{-\frac{\omega}{F_e\overline{G(\lambda)}}}\right)+\\
&\lim_{\delta\to 0}\left(\sum_{\text{wells}}\int_{\frac{1}{B_{max}}}^{\lambda_{Crit}-\delta} d\lambda|\overline{\phi}|^2\left(\frac{1}{-F_e\overline{G(\lambda)}}\right)\left(\frac{\omega}{-F_e\overline{G(\lambda)}}\right)^{\frac{1}{2}}\tau(\lambda)\,(\omega+\omega_{*e})\,e^{-\frac{\omega}{-F_e\overline{G(\lambda)}}}\right)+\\
&\lim_{\delta\to 0}\left(\sum_{\text{wells}}\int_{\lambda_{Crit}+\delta}^{\frac{1}{B_{min}}} d\lambda|\overline{\phi}|^2\left(\frac{1}{-F_e\overline{G(\lambda)}}\right)\left(\frac{\omega}{-F_e\overline{G(\lambda)}}\right)^{\frac{1}{2}}\tau(\lambda)\,(\omega+\omega_{*e})\,e^{-\frac{\omega}{-F_e\overline{G(\lambda)}}}\right)\stackrel{!}{=}0
\end{aligned}\tag{6.52}$$

We will now modify this result so that it can be used for any given geometry without needing to know in advance what the sign of ω_r will be. We can achieve this by implementing two Heaviside functions, one for each species, which ensure that the integration is being carried out only when the sign of $F_a\overline{G(\lambda)}$ matches the sign of ω_r. We will create these functions as follows:

$$\begin{aligned}
\mathcal{H}_e &\equiv \mathcal{H}\left[\frac{\omega}{F_e\overline{G(\lambda)}}\right]\\
\mathcal{H}_i &\equiv \mathcal{H}\left[\frac{\omega}{F_i\overline{G(\lambda)}}\right]=\mathcal{H}\left[\frac{\omega}{-F_e\overline{G(\lambda)}}\right]
\end{aligned}\tag{6.53}$$

We will insert these Heaviside functions into Eqn. 6.52, giving

$$\begin{aligned}
&\lim_{\delta\to 0}\left(\sum_{\text{wells}}\int_{\frac{1}{B_{max}}}^{\lambda_{Crit}-\delta} d\lambda|\overline{\phi}|^2\left(\frac{1}{F_e\overline{G(\lambda)}}\right)\left(\frac{\omega}{F_e\overline{G(\lambda)}}\right)^{\frac{1}{2}}\tau(\lambda)\,(\omega-\omega_{*e})\,\mathcal{H}_e e^{-\frac{\omega}{F_e\overline{G(\lambda)}}}\right)+\\
&\lim_{\delta\to 0}\left(\sum_{\text{wells}}\int_{\lambda_{Crit}+\delta}^{\frac{1}{B_{min}}} d\lambda|\overline{\phi}|^2\left(\frac{1}{F_e\overline{G(\lambda)}}\right)\left(\frac{\omega}{F_e\overline{G(\lambda)}}\right)^{\frac{1}{2}}\tau(\lambda)\,(\omega-\omega_{*e})\,\mathcal{H}_e e^{-\frac{\omega}{F_e\overline{G(\lambda)}}}\right)+\\
&\lim_{\delta\to 0}\left(\sum_{\text{wells}}\int_{\frac{1}{B_{max}}}^{\lambda_{Crit}-\delta} d\lambda|\overline{\phi}|^2\left(\frac{1}{-F_e\overline{G(\lambda)}}\right)\left(\frac{\omega}{-F_e\overline{G(\lambda)}}\right)^{\frac{1}{2}}\tau(\lambda)\,(\omega+\omega_{*e})\,\mathcal{H}_i e^{-\frac{\omega}{-F_e\overline{G(\lambda)}}}\right)+\\
&\lim_{\delta\to 0}\left(\sum_{\text{wells}}\int_{\lambda_{Crit}+\delta}^{\frac{1}{B_{min}}} d\lambda|\overline{\phi}|^2\left(\frac{1}{-F_e\overline{G(\lambda)}}\right)\left(\frac{\omega}{-F_e\overline{G(\lambda)}}\right)^{\frac{1}{2}}\tau(\lambda)\,(\omega+\omega_{*e})\,\mathcal{H}_i e^{-\frac{\omega}{-F_e\overline{G(\lambda)}}}\right)\stackrel{!}{=}0
\end{aligned}\tag{6.54}$$

The presence of these Heaviside functions prevents the exponential terms from blowing up, as these exponential terms will always decay for $\mathcal{H}_{e/i}=1$, and the given integral vanishes otherwise. These Heaviside functions also ensure that the quantities in parenthesis to the power of $\frac{1}{2}$ are positive, thus making those terms real.

Now, let's expand the $(\omega \pm \omega_{*e})$ terms in Eqn. 6.54 as follows:

$$
\begin{aligned}
&\lim_{\delta\to 0}\left(\sum_{\text{wells}}\int_{\frac{1}{B_{max}}}^{\lambda_{Crit}-\delta} d\lambda|\overline{\phi}|^2\left(\frac{1}{F_e\overline{G(\lambda)}}\right)\left(\frac{\omega}{F_e\overline{G(\lambda)}}\right)^{\frac{1}{2}}\tau(\lambda)\,(\omega)\,\mathcal{H}_e e^{-\frac{\omega}{F_e\overline{G(\lambda)}}}\right) - \\
&\lim_{\delta\to 0}\left(\sum_{\text{wells}}\int_{\frac{1}{B_{max}}}^{\lambda_{Crit}-\delta} d\lambda|\overline{\phi}|^2\left(\frac{1}{F_e\overline{G(\lambda)}}\right)\left(\frac{\omega}{F_e\overline{G(\lambda)}}\right)^{\frac{1}{2}}\tau(\lambda)\,(\omega_{*e})\,\mathcal{H}_e e^{-\frac{\omega}{F_e\overline{G(\lambda)}}}\right) + \\
&\lim_{\delta\to 0}\left(\sum_{\text{wells}}\int_{\lambda_{Crit}+\delta}^{\frac{1}{B_{min}}} d\lambda|\overline{\phi}|^2\left(\frac{1}{F_e\overline{G(\lambda)}}\right)\left(\frac{\omega}{F_e\overline{G(\lambda)}}\right)^{\frac{1}{2}}\tau(\lambda)\,(\omega)\,\mathcal{H}_e e^{-\frac{\omega}{F_e\overline{G(\lambda)}}}\right) - \\
&\lim_{\delta\to 0}\left(\sum_{\text{wells}}\int_{\lambda_{Crit}+\delta}^{\frac{1}{B_{min}}} d\lambda|\overline{\phi}|^2\left(\frac{1}{F_e\overline{G(\lambda)}}\right)\left(\frac{\omega}{F_e\overline{G(\lambda)}}\right)^{\frac{1}{2}}\tau(\lambda)\,(\omega_{*e})\,\mathcal{H}_e e^{-\frac{\omega}{F_e\overline{G(\lambda)}}}\right) + \\
&\lim_{\delta\to 0}\left(\sum_{\text{wells}}\int_{\frac{1}{B_{max}}}^{\lambda_{Crit}-\delta} d\lambda|\overline{\phi}|^2\left(\frac{1}{-F_e\overline{G(\lambda)}}\right)\left(\frac{\omega}{-F_e\overline{G(\lambda)}}\right)^{\frac{1}{2}}\tau(\lambda)\,(\omega)\,\mathcal{H}_i e^{-\frac{\omega}{-F_e\overline{G(\lambda)}}}\right) + \\
&\lim_{\delta\to 0}\left(\sum_{\text{wells}}\int_{\frac{1}{B_{max}}}^{\lambda_{Crit}-\delta} d\lambda|\overline{\phi}|^2\left(\frac{1}{-F_e\overline{G(\lambda)}}\right)\left(\frac{\omega}{-F_e\overline{G(\lambda)}}\right)^{\frac{1}{2}}\tau(\lambda)\,(\omega_{*e})\,\mathcal{H}_i e^{-\frac{\omega}{-F_e\overline{G(\lambda)}}}\right) + \\
&\lim_{\delta\to 0}\left(\sum_{\text{wells}}\int_{\lambda_{Crit}+\delta}^{\frac{1}{B_{min}}} d\lambda|\overline{\phi}|^2\left(\frac{1}{-F_e\overline{G(\lambda)}}\right)\left(\frac{\omega}{-F_e\overline{G(\lambda)}}\right)^{\frac{1}{2}}\tau(\lambda)\,(\omega)\,\mathcal{H}_i e^{-\frac{\omega}{-F_e\overline{G(\lambda)}}}\right) + \\
&\lim_{\delta\to 0}\left(\sum_{\text{wells}}\int_{\lambda_{Crit}+\delta}^{\frac{1}{B_{min}}} d\lambda|\overline{\phi}|^2\left(\frac{1}{-F_e\overline{G(\lambda)}}\right)\left(\frac{\omega}{-F_e\overline{G(\lambda)}}\right)^{\frac{1}{2}}\tau(\lambda)\,(\omega_{*e})\,\mathcal{H}_i e^{-\frac{\omega}{-F_e\overline{G(\lambda)}}}\right) \stackrel{!}{=} 0
\end{aligned}
\tag{6.55}
$$

We can also pull out the remaining ω and ω_{*e} terms to reorganise our result as follows:

$$\begin{aligned}
&\omega\Bigg\{\lim_{\delta\to 0}\left(\sum_{\text{wells}}\int_{\frac{1}{B_{max}}}^{\lambda_{Crit}-\delta} d\lambda|\overline{\phi}|^2\left(\frac{1}{F_e\overline{G(\lambda)}}\right)\left(\frac{\omega}{F_e\overline{G(\lambda)}}\right)^{\frac{1}{2}}\tau(\lambda)\mathcal{H}_e e^{-\frac{\omega}{F_e\overline{G(\lambda)}}}\right)+\\
&\lim_{\delta\to 0}\left(\sum_{\text{wells}}\int_{\lambda_{Crit}+\delta}^{\frac{1}{B_{min}}} d\lambda|\overline{\phi}|^2\left(\frac{1}{F_e\overline{G(\lambda)}}\right)\left(\frac{\omega}{F_e\overline{G(\lambda)}}\right)^{\frac{1}{2}}\tau(\lambda)\mathcal{H}_e e^{-\frac{\omega}{F_e\overline{G(\lambda)}}}\right)+\\
&\lim_{\delta\to 0}\left(\sum_{\text{wells}}\int_{\frac{1}{B_{max}}}^{\lambda_{Crit}-\delta} d\lambda|\overline{\phi}|^2\left(\frac{1}{-F_e\overline{G(\lambda)}}\right)\left(\frac{\omega}{-F_e\overline{G(\lambda)}}\right)^{\frac{1}{2}}\tau(\lambda)\mathcal{H}_i e^{-\frac{\omega}{-F_e\overline{G(\lambda)}}}\right)+\\
&\lim_{\delta\to 0}\left(\sum_{\text{wells}}\int_{\lambda_{Crit}+\delta}^{\frac{1}{B_{min}}} d\lambda|\overline{\phi}|^2\left(\frac{1}{-F_e\overline{G(\lambda)}}\right)\left(\frac{\omega}{-F_e\overline{G(\lambda)}}\right)^{\frac{1}{2}}\tau(\lambda)\mathcal{H}_i e^{-\frac{\omega}{-F_e\overline{G(\lambda)}}}\right)\Bigg\}=\\
&\omega_{*e}\Bigg\{\lim_{\delta\to 0}\left(\sum_{\text{wells}}\int_{\frac{1}{B_{max}}}^{\lambda_{Crit}-\delta} d\lambda|\overline{\phi}|^2\left(\frac{1}{F_e\overline{G(\lambda)}}\right)\left(\frac{\omega}{F_e\overline{G(\lambda)}}\right)^{\frac{1}{2}}\tau(\lambda)\mathcal{H}_e e^{-\frac{\omega}{F_e\overline{G(\lambda)}}}\right)+\\
&\lim_{\delta\to 0}\left(\sum_{\text{wells}}\int_{\lambda_{Crit}+\delta}^{\frac{1}{B_{min}}} d\lambda|\overline{\phi}|^2\left(\frac{1}{F_e\overline{G(\lambda)}}\right)\left(\frac{\omega}{F_e\overline{G(\lambda)}}\right)^{\frac{1}{2}}\tau(\lambda)\mathcal{H}_e e^{-\frac{\omega}{F_e\overline{G(\lambda)}}}\right)-\\
&\lim_{\delta\to 0}\left(\sum_{\text{wells}}\int_{\frac{1}{B_{max}}}^{\lambda_{Crit}-\delta} d\lambda|\overline{\phi}|^2\left(\frac{1}{-F_e\overline{G(\lambda)}}\right)\left(\frac{\omega}{-F_e\overline{G(\lambda)}}\right)^{\frac{1}{2}}\tau(\lambda)\mathcal{H}_i e^{-\frac{\omega}{-F_e\overline{G(\lambda)}}}\right)-\\
&\lim_{\delta\to 0}\left(\sum_{\text{wells}}\int_{\lambda_{Crit}+\delta}^{\frac{1}{B_{min}}} d\lambda|\overline{\phi}|^2\left(\frac{1}{-F_e\overline{G(\lambda)}}\right)\left(\frac{\omega}{-F_e\overline{G(\lambda)}}\right)^{\frac{1}{2}}\tau(\lambda)\mathcal{H}_i e^{-\frac{\omega}{-F_e\overline{G(\lambda)}}}\right)\Bigg\}
\end{aligned}\tag{6.56}$$

If we make the following abbreviations:

$$\begin{aligned}
P &\equiv |\overline{\phi}|^2\left(\frac{1}{F_e\overline{G(\lambda)}}\right)\left(\frac{\omega}{F_e\overline{G(\lambda)}}\right)^{\frac{1}{2}}\tau(\lambda)\mathcal{H}_e e^{-\frac{\omega}{F_e\overline{G(\lambda)}}}\\
M &\equiv |\overline{\phi}|^2\left(\frac{1}{-F_e\overline{G(\lambda)}}\right)\left(\frac{\omega}{-F_e\overline{G(\lambda)}}\right)^{\frac{1}{2}}\tau(\lambda)\mathcal{H}_i e^{-\frac{\omega}{-F_e\overline{G(\lambda)}}}
\end{aligned}\tag{6.57}$$

then we can write our result more concisely as:

$$\begin{aligned}
&\omega\Bigg\{\lim_{\delta\to 0}\left(\sum_{\text{wells}}\int_{\frac{1}{B_{max}}}^{\lambda_{Crit}-\delta} d\lambda P\right)+\lim_{\delta\to 0}\left(\sum_{\text{wells}}\int_{\lambda_{Crit}+\delta}^{\frac{1}{B_{min}}} d\lambda P\right)+\\
&\lim_{\delta\to 0}\left(\sum_{\text{wells}}\int_{\frac{1}{B_{max}}}^{\lambda_{Crit}-\delta} d\lambda M\right)+\lim_{\delta\to 0}\left(\sum_{\text{wells}}\int_{\lambda_{Crit}+\delta}^{\frac{1}{B_{min}}} d\lambda M\right)\Bigg\}\\
&=\omega_{*e}\Bigg\{\lim_{\delta\to 0}\left(\sum_{\text{wells}}\int_{\frac{1}{B_{max}}}^{\lambda_{Crit}-\delta} d\lambda P\right)+\lim_{\delta\to 0}\left(\sum_{\text{wells}}\int_{\lambda_{Crit}+\delta}^{\frac{1}{B_{min}}} d\lambda P\right)-\\
&\lim_{\delta\to 0}\left(\sum_{\text{wells}}\int_{\frac{1}{B_{max}}}^{\lambda_{Crit}-\delta} d\lambda M\right)-\lim_{\delta\to 0}\left(\sum_{\text{wells}}\int_{\lambda_{Crit}+\delta}^{\frac{1}{B_{min}}} d\lambda M\right)\Bigg\}
\end{aligned}\tag{6.58}$$

And rearranging further gives:

$$\frac{\omega}{\omega_{*e}} = \frac{\lim_{\delta\to 0}\sum_{\text{wells}}\left\{\left(\int_{\frac{1}{B_{max}}}^{\lambda_{Crit}-\delta} d\lambda P\right)+\left(\int_{\lambda_{Crit}+\delta}^{\frac{1}{B_{min}}} d\lambda P\right)-\left(\int_{\frac{1}{B_{max}}}^{\lambda_{Crit}-\delta} d\lambda M\right)-\left(\int_{\lambda_{Crit}+\delta}^{\frac{1}{B_{min}}} d\lambda M\right)\right\}}{\lim_{\delta\to 0}\sum_{\text{wells}}\left\{\left(\int_{\frac{1}{B_{max}}}^{\lambda_{Crit}-\delta} d\lambda P\right)+\left(\int_{\lambda_{Crit}+\delta}^{\frac{1}{B_{min}}} d\lambda M\right)+\left(\int_{\frac{1}{B_{max}}}^{\lambda_{Crit}-\delta} d\lambda M\right)+\left(\int_{\lambda_{Crit}+\delta}^{\frac{1}{B_{min}}} d\lambda P\right)\right\}} \tag{6.59}$$

which can be tidied to give:

$$\frac{\omega}{\omega_{*e}} = \frac{\lim_{\delta\to 0}\sum_{\text{wells}}\left\{\left(\int_{\frac{1}{B_{max}}}^{\lambda_{Crit}-\delta} d\lambda [P-M]\right)+\left(\int_{\lambda_{Crit}+\delta}^{\frac{1}{B_{min}}} d\lambda [P-M]\right)\right\}}{\lim_{\delta\to 0}\sum_{\text{wells}}\left\{\left(\int_{\frac{1}{B_{max}}}^{\lambda_{Crit}-\delta} d\lambda [P+M]\right)+\left(\int_{\lambda_{Crit}+\delta}^{\frac{1}{B_{min}}} d\lambda [P+M]\right)\right\}} \tag{6.60}$$

Let's look at how we could further simplify the following terms:

$$\begin{aligned} P &\equiv |\overline{\phi}|^2\tau(\lambda)\left(\frac{1}{F_e\overline{G(\lambda)}}\right)\left(\frac{\omega}{F_e\overline{G(\lambda)}}\right)^{\frac{1}{2}}\mathcal{H}_e e^{-\frac{\omega}{F_e\overline{G(\lambda)}}} \\ M &\equiv |\overline{\phi}|^2\tau(\lambda)\left(\frac{1}{-F_e\overline{G(\lambda)}}\right)\left(\frac{\omega}{-F_e\overline{G(\lambda)}}\right)^{\frac{1}{2}}\mathcal{H}_i e^{-\frac{\omega}{-F_e\overline{G(\lambda)}}} \end{aligned} \tag{6.61}$$

When looking at the full result

$$\frac{\omega}{\omega_{*e}} = \frac{\lim_{\delta\to 0}\sum_{\text{wells}}\left\{\left(\int_{\frac{1}{B_{max}}}^{\lambda_{Crit}-\delta} d\lambda [P-M]\right)+\left(\int_{\lambda_{Crit}+\delta}^{\frac{1}{B_{min}}} d\lambda [P-M]\right)\right\}}{\lim_{\delta\to 0}\sum_{\text{wells}}\left\{\left(\int_{\frac{1}{B_{max}}}^{\lambda_{Crit}-\delta} d\lambda [P+M]\right)+\left(\int_{\lambda_{Crit}+\delta}^{\frac{1}{B_{min}}} d\lambda [P+M]\right)\right\}} \tag{6.62}$$

we can see that all four integrals share a common factor of $\left(\frac{1}{F_e}\right)$, which is unaffected by the integration. Let's simplify our expressions in the following way:

$$\begin{aligned} P &\equiv |\overline{\phi}|^2\tau(\lambda)\left(\frac{1}{F_e\overline{G(\lambda)}}\right)\left(\frac{\omega}{F_e\overline{G(\lambda)}}\right)^{\frac{1}{2}}\mathcal{H}_e e^{-\frac{\omega}{F_e\overline{G(\lambda)}}} = \left(\frac{1}{F_e}\right)P_1 \\ M &\equiv |\overline{\phi}|^2\tau(\lambda)\left(\frac{1}{-F_e\overline{G(\lambda)}}\right)\left(\frac{\omega}{-F_e\overline{G(\lambda)}}\right)^{\frac{1}{2}}\mathcal{H}_i e^{-\frac{\omega}{-F_e\overline{G(\lambda)}}} = \left(\frac{1}{F_e}\right)M_1 \end{aligned} \tag{6.63}$$

where

$$\begin{aligned} P_1 &\equiv |\overline{\phi}|^2\tau(\lambda)\left(\frac{1}{\overline{G(\lambda)}}\right)\left(\frac{\omega}{F_e\overline{G(\lambda)}}\right)^{\frac{1}{2}}\mathcal{H}_e e^{-\frac{\omega}{F_e\overline{G(\lambda)}}} \\ M_1 &\equiv |\overline{\phi}|^2\tau(\lambda)\left(\frac{1}{-\overline{G(\lambda)}}\right)\left(\frac{\omega}{-F_e\overline{G(\lambda)}}\right)^{\frac{1}{2}}\mathcal{H}_i e^{-\frac{\omega}{-F_e\overline{G(\lambda)}}} \end{aligned} \tag{6.64}$$

Thus, we can rewrite our result as follows

$$\frac{\omega}{\omega_{*e}} = \frac{\lim_{\delta\to 0}\sum_{\text{wells}}\left\{\left(\int_{\frac{1}{B_{max}}}^{\lambda_{Crit}-\delta} d\lambda[P_1 - M_1]\right) + \left(\int_{\lambda_{Crit}+\delta}^{\frac{1}{B_{min}}} d\lambda[P_1 - M_1]\right)\right\}}{\lim_{\delta\to 0}\sum_{\text{wells}}\left\{\left(\int_{\frac{1}{B_{max}}}^{\lambda_{Crit}-\delta} d\lambda[P_1 + M_1]\right) + \left(\int_{\lambda_{Crit}+\delta}^{\frac{1}{B_{min}}} d\lambda[P_1 + M_1]\right)\right\}} \tag{6.65}$$

where the $\left(\frac{1}{F_e}\right)$ terms common to the numerator and denominator have been pulled out and cancel.

We can avoid dealing with a vanishing denominator by simply rewriting Eqn. 6.65 as follows:

$$\begin{aligned}\left(\frac{\omega}{\omega_{*e}}\right)\lim_{\delta\to 0}\sum_{\text{wells}}\left\{\left(\int_{\frac{1}{B_{max}}}^{\lambda_{Crit}-\delta} d\lambda[P_1 + M_1]\right) + \left(\int_{\lambda_{Crit}+\delta}^{\frac{1}{B_{min}}} d\lambda[P_1 + M_1]\right)\right\} \\ - \lim_{\delta\to 0}\sum_{\text{wells}}\left\{\left(\int_{\frac{1}{B_{max}}}^{\lambda_{Crit}-\delta} d\lambda[P_1 - M_1]\right) + \left(\int_{\lambda_{Crit}+\delta}^{\frac{1}{B_{min}}} d\lambda[P_1 - M_1]\right)\right\} = 0\end{aligned} \tag{6.66}$$

Before we can evaluate this result numerically, we first need to note how our variational principle result comes into play. For the $\frac{\omega}{\omega_{*e}}$ term in Eqn. 6.66, we insert our analytical expression Eqn. 5.105 directly - which we know is compatible with the variational principle. We also insert a modified form of this result for when we have ω on its own. From here, we can numerically evaluate this quantity on the left-hand side of Eqn. 6.66, and gradually adjust the value of $\frac{a}{L_n}$ (which is found in the ω_{*e} term, and also within our ω proxy expression) until this equation is satisfied, i.e., when the left-hand side equals zero. The lowest value of $\frac{a}{L_n}$ which satisfies this equation is the critical density gradient. The numerical results of this procedure are presented in section 7.2.2 for various geometrical configurations. This will include a discussion on some possible interpretations of the results.

In the next section, we describe an alternative method to deriving an analytical proxy for the critical density gradient. This alternative approach is significantly simpler and shorter than the one derived here, and it was investigated to serve as a potential backup in the event that our results here failed to successfully approximate the critical density gradient.

6.2 Alternative Derivation of the Critical-Density-Gradient Proxy

In this section, we will discuss an alternative approach to obtaining an analytical proxy for the critical density gradient of the TEM. As stated before, this alternative approach is significantly simpler, and much shorter, than the derivation carried out in the previous section. This idea was investigated to serve as a potential backup in the event that our original method failed to produce satisfying results.

If the mode frequency is defined as:

$$\omega = \omega_r + i\gamma \tag{6.67}$$

then we can easily find ω^2

$$\omega^2 = (\omega_r + i\gamma)^2 = \omega_r^2 - \gamma^2 + 2i\omega_r\gamma \tag{6.68}$$

Now, we know from the theory of magneto-hydrodynamic (MHD) instabilities that in the idealised case, ω^2 is always a real expression [1]. However, we are interested in the smaller scale behaviour of plasma micro-instabilities. Nevertheless, ω^2 being real is also ostensibly true for trapped particle micro-instabilities, as seen in [4]. This then implies that

$$\begin{aligned} \omega^2 &\stackrel{!}{=} \omega_r^2 - \gamma^2 \\ 2i\omega_r\gamma &\stackrel{!}{=} 0 \implies \omega_r\gamma = 0 \end{aligned} \tag{6.69}$$

Thus, our expression for ω^2 can be positive, zero, or negative in the following scenarios:

$$\begin{aligned} \omega^2 > 0 &\implies \omega^2 = \omega_r^2 \implies \omega_r = \pm\sqrt{\omega^2} \\ \omega^2 = 0 &\implies \omega_r = \gamma = 0 \\ \omega^2 < 0 &\implies \omega^2 = -\gamma^2 \implies \gamma = \pm\sqrt{-\omega^2} \end{aligned} \tag{6.70}$$

From these different cases, we can ascertain the following information about the stability of the mode:

- When $\omega^2 > 0$, the system is stable since $\gamma = 0$ and $\omega_r = \pm\sqrt{\omega^2}$. The modes are oscillatory, but not growing or decaying.
- When $\omega^2 < 0$ the system is unstable since $\omega_r = 0$ and $\gamma = \pm\sqrt{-\omega^2}$. Thus, there always exists one mode with a positive growth rate.
- The point of marginal stability clearly must then occur for $\omega^2 = 0$, i.e., when $\omega_r = \gamma = 0$.

Thus, the point of marginal stability which corresponds to when $\gamma \to 0^+$ should then also correspond to $\omega_r \to 0$. In reality for a general physical system, the transition to marginal stability can occur at a finite value of the real frequency, i.e., $\omega_r \neq 0$ as $\gamma \to 0$. However, for the ideal MHD system, the transition occurs precisely when $\omega_r = 0$ [1]. Thus, we will make use of this idealised case for our purposes in investigating trapped-particle micro-instabilities also. This theoretical case may then guide us toward finding a suitable proxy for the critical density gradient, which is found at marginal stability.

Given that our variational principle approach is capable of finding a decent approximation for ω_r (which we will refer to as $\omega_{r(VP)}$), we can use our result to investigate what happens when we set:

$$\omega_{r(VP)} \stackrel{!}{=} 0 \tag{6.71}$$

According to our theoretical argument above, this should then occur at the point of marginal stability. Now let's look at how we obtain an expression for the critical density gradient explicitly. Remember that we are only interested in the real part of the plus quadratic solution to $\left(\frac{\omega}{\omega_{*e}}\right)_{VP}$:

$$\mathrm{Re}\left[\left(\frac{\omega}{\omega_{*e}}\right)_{VP}\right] = \mathrm{Re}\left[\frac{B+\sqrt{B^2+4AC}}{2A}\right] \tag{6.72}$$

Where we recall that our full quadratic equation is

$$\frac{\omega^2}{\omega_{*e}^2}\underbrace{\{a_1-a_2\}}_{A} - \frac{\omega}{\omega_{*e}}\underbrace{\{b_1+b_2-a_2+b_3\}}_{B} - \underbrace{\{c_1-c_2\}}_{C} = 0 \tag{6.73}$$

and

- $a_1 \rightarrow \int_{-\infty}^{\infty}\left(1+\tau\left[1-\Gamma_0\right]\right)|\phi|^2\frac{dl}{B}$
- $a_2 \rightarrow \frac{1}{2}\int_{\frac{1}{B_{max}}}^{\frac{1}{B_{min}}}\int_{-\infty}^{\infty}\frac{dl}{\sqrt{1-\lambda B}}|\overline{\phi}|^2 d\lambda$
- $b_1+b_2 \rightarrow \int_{-\infty}^{\infty}\left[\left[\Gamma_0-\eta_i b\left(\Gamma_0-\Gamma_1\right)\right]+\left[2\Gamma_0-b\left(\Gamma_0-\Gamma_1\right)\right]\frac{\hat{\omega}_{di}\tau}{2\omega_{*e}}\right]|\phi|^2\frac{dl}{B}$
- $b_3 \rightarrow \frac{1}{2}\int_{\frac{1}{B_{max}}}^{\frac{1}{B_{min}}}\int_{-\infty}^{\infty}\frac{dl}{\sqrt{1-\lambda B}}\left(\frac{3}{2}\frac{F_e\overline{G(\lambda)}}{\omega_{*e}}\right)|\overline{\phi}|^2 d\lambda$
- $c_1 \rightarrow \int_{-\infty}^{\infty}\left[2\Gamma_0-b\left(\Gamma_0-\Gamma_1\right)+\eta_i\left[2\left(b-1\right)^2\Gamma_0+b\left(3-2b\right)\Gamma_1\right]\right]\left(\frac{\hat{\omega}_{di}}{2\omega_{*e}}\right)|\phi|^2\frac{dl}{B}$
- $c_2 \equiv b_3\left[1+\eta_e\right] \rightarrow \frac{1}{2}\int_{\frac{1}{B_{max}}}^{\frac{1}{B_{min}}}\int_{-\infty}^{\infty}\frac{dl}{\sqrt{1-\lambda B}}\left(\frac{3}{2}\frac{F_e\overline{G(\lambda)}}{\omega_{*e}}\left[1+\eta_e\right]\right)|\overline{\phi}|^2 d\lambda$

To simplify our situation further, we know from our numerical work that the critical density gradient always occurs before the discriminant in Eqn. 6.72 becomes positive. This implies that the square root term is not relevant in the region of parameter space we are considering, as it only contributes an imaginary part. Therefore, since we are only interested in the real part, all we need is the following:

$$\mathrm{Re}\left[\left(\frac{\omega}{\omega_{*e}}\right)_{VP}\right] = \frac{B}{2A} \tag{6.74}$$

Thus, if we want to know where $\omega_r = 0$ we simply set Eqn. 6.74 equal to zero, giving

$$\frac{B}{2A} = 0 \implies B = 0 \tag{6.75}$$

To clarify, we are aiming to find the density gradient value corresponding to $B = 0$, which should be equal to the critical density gradient. We can now use

$$B = (b_1+b_2-a_2+b_3) \tag{6.76}$$

Then $B = 0$ implies

$$\begin{aligned}(b_1 + b_2 - a_2 + b_3) &= 0 \\ \implies b_1 + b_2 + b_3 &= a_2\end{aligned} \tag{6.77}$$

which gives us

$$\begin{aligned}&\int_{-\infty}^{\infty}\left[\left[\Gamma_0 - \eta_i b\left(\Gamma_0 - \Gamma_1\right)\right] + \left[2\Gamma_0 - b\left(\Gamma_0 - \Gamma_1\right)\right]\frac{\hat{\omega}_{di}\tau}{2\omega_{*e}}\right]|\phi|^2\frac{dl}{B} + \\ &\frac{1}{2}\int_{\frac{1}{B_{max}}}^{\frac{1}{B_{min}}}\int_{-\infty}^{\infty}\frac{dl}{\sqrt{1-\lambda B}}\left(\frac{3}{2}\frac{F_e\overline{G(\lambda)}}{\omega_{*e}}\right)|\overline{\phi}|^2 d\lambda \\ &= \frac{1}{2}\int_{\frac{1}{B_{max}}}^{\frac{1}{B_{min}}}\int_{-\infty}^{\infty}\frac{dl}{\sqrt{1-\lambda B}}|\overline{\phi}|^2 d\lambda\end{aligned} \tag{6.78}$$

Using our assumption of equal species temperature then sets $\tau = \frac{T_e}{T_i} = 1$. We can also use our species-independent bounce time expression:

$$\tau(\lambda) = \oint\frac{dl}{\sqrt{1-\lambda B}} \implies \sum_{\text{wells}}\tau(\lambda) = \int_{-\infty}^{\infty}\frac{dl}{\sqrt{1-\lambda B}} \tag{6.79}$$

Rearranging to get the terms containing ω_{*e} on one side of the equals sign gives

$$\begin{aligned}&\frac{1}{\omega_{*e}}\left\{\int_{-\infty}^{\infty}\left[2\Gamma_0 - b\left(\Gamma_0 - \Gamma_1\right)\right]\frac{\hat{\omega}_{di}}{2}|\phi|^2\frac{dl}{B} + \frac{1}{2}\int_{\frac{1}{B_{max}}}^{\frac{1}{B_{min}}}\sum_{\text{wells}}\tau(\lambda)\left(\frac{3}{2}F_e\overline{G(\lambda)}\right)|\overline{\phi}|^2 d\lambda\right\} \\ &= \frac{1}{2}\int_{\frac{1}{B_{max}}}^{\frac{1}{B_{min}}}\sum_{\text{wells}}\tau(\lambda)|\overline{\phi}|^2 d\lambda - \int_{-\infty}^{\infty}\left[\Gamma_0 - \eta_i b\left(\Gamma_0 - \Gamma_1\right)\right]|\phi|^2\frac{dl}{B}\end{aligned} \tag{6.80}$$

Then isolating ω_{*e} gives

$$\omega_{*e} = \frac{\left\{\int_{-\infty}^{\infty}\left[2\Gamma_0 - b\left(\Gamma_0 - \Gamma_1\right)\right]\frac{\hat{\omega}_{di}}{2}|\phi|^2\frac{dl}{B} + \frac{1}{2}\int_{\frac{1}{B_{max}}}^{\frac{1}{B_{min}}}\sum_{\text{wells}}\tau(\lambda)\left(\frac{3}{2}F_e\overline{G(\lambda)}\right)|\overline{\phi}|^2 d\lambda\right\}}{\frac{1}{2}\int_{\frac{1}{B_{max}}}^{\frac{1}{B_{min}}}\sum_{\text{wells}}\tau(\lambda)|\overline{\phi}|^2 d\lambda - \int_{-\infty}^{\infty}\left[\Gamma_0 - \eta_i b\left(\Gamma_0 - \Gamma_1\right)\right]|\phi|^2\frac{dl}{B}} \tag{6.81}$$

Now, if we note the definition for ω_{*e}, we see that it contains the density gradient:

$$\omega_{*e} \equiv -\frac{T_e k_\alpha}{e}\frac{d\ln n_e}{d\psi} = -\frac{T_e}{eB}\frac{d\ln n_e}{dr}\underbrace{\left(\hat{\mathbf{b}}\times\nabla r\right)\cdot\mathbf{k}_\perp}_{k_\alpha} = -\frac{k_\alpha T_e}{eB}\frac{d\ln n_e}{dr} \tag{6.82}$$

We can substitute this into Eqn. 6.81 as follows:

$$-\frac{k_\alpha T_e}{eB}\frac{d\ln n_e}{dr} = \frac{\left\{\int_{-\infty}^{\infty}\left[2\Gamma_0 - b\left(\Gamma_0 - \Gamma_1\right)\right]\frac{\hat{\omega}_{di}}{2}|\phi|^2\frac{dl}{B} + \frac{1}{2}\int_{\frac{1}{B_{max}}}^{\frac{1}{B_{min}}}\sum_{\text{wells}}\tau(\lambda)\left(\frac{3}{2}F_e\overline{G(\lambda)}\right)|\overline{\phi}|^2 d\lambda\right\}}{\frac{1}{2}\int_{\frac{1}{B_{max}}}^{\frac{1}{B_{min}}}\sum_{\text{wells}}\tau(\lambda)|\overline{\phi}|^2 d\lambda - \int_{-\infty}^{\infty}\left[\Gamma_0 - \eta_i b\left(\Gamma_0 - \Gamma_1\right)\right]|\phi|^2\frac{dl}{B}} \tag{6.83}$$

Rearranging to isolate the density gradient leads to

$$-\frac{d\ln n_e}{dr} = \frac{\left(\frac{eB}{k_\alpha T_e}\right)\left\{\int_{-\infty}^{\infty}\left[2\Gamma_0 - b\left(\Gamma_0-\Gamma_1\right)\right]\frac{\hat{\omega}_{di}}{2}|\phi|^2\frac{dl}{B} + \frac{1}{2}\int_{\frac{1}{B_{max}}}^{\frac{1}{B_{min}}}\sum_{\text{wells}}\tau(\lambda)\left(\frac{3}{2}F_e\overline{G(\lambda)}\right)|\overline{\phi}|^2 d\lambda\right\}}{\frac{1}{2}\int_{\frac{1}{B_{max}}}^{\frac{1}{B_{min}}}\sum_{\text{wells}}\tau(\lambda)|\overline{\phi}|^2 d\lambda - \int_{-\infty}^{\infty}\left[\Gamma_0 - \eta_i b\left(\Gamma_0-\Gamma_1\right)\right]|\phi|^2\frac{dl}{B}} \tag{6.84}$$

If we now multiply across by the minor radius coordinate a, and also make use of the definition for the density length scale:

$$L_{n_a} \equiv -\left(\frac{d\ln n_a}{dr}\right)^{-1} \tag{6.85}$$

then our result becomes

$$\frac{a}{L_{n_e}} = \frac{\left(\frac{eBa}{k_\alpha T_e}\right)\left\{\int_{-\infty}^{\infty}\left[2\Gamma_0 - b\left(\Gamma_0-\Gamma_1\right)\right]\frac{\hat{\omega}_{di}}{2}|\phi|^2\frac{dl}{B} + \frac{1}{2}\int_{\frac{1}{B_{max}}}^{\frac{1}{B_{min}}}\sum_{\text{wells}}\tau(\lambda)\left(\frac{3}{2}F_e\overline{G(\lambda)}\right)|\overline{\phi}|^2 d\lambda\right\}}{\frac{1}{2}\int_{\frac{1}{B_{max}}}^{\frac{1}{B_{min}}}\sum_{\text{wells}}\tau(\lambda)|\overline{\phi}|^2 d\lambda - \int_{-\infty}^{\infty}\left[\Gamma_0 - \eta_i b\left(\Gamma_0-\Gamma_1\right)\right]|\phi|^2\frac{dl}{B}} \tag{6.86}$$

This is then our analytical prediction for the critical density gradient:

$$\boxed{\left(\frac{a}{L_{n_e}}\right)_{Crit} = \frac{\left(\frac{eBa}{k_\alpha T_e}\right)\left\{\int_{-\infty}^{\infty}\left[2\Gamma_0 - b\left(\Gamma_0-\Gamma_1\right)\right]\frac{\hat{\omega}_{di}}{2}|\phi|^2\frac{dl}{B} + \frac{1}{2}\int_{\frac{1}{B_{max}}}^{\frac{1}{B_{min}}}\sum_{\text{wells}}\tau(\lambda)\left(\frac{3}{2}F_e\overline{G(\lambda)}\right)|\overline{\phi}|^2 d\lambda\right\}}{\frac{1}{2}\int_{\frac{1}{B_{max}}}^{\frac{1}{B_{min}}}\sum_{\text{wells}}\tau(\lambda)|\overline{\phi}|^2 d\lambda - \int_{-\infty}^{\infty}\left[\Gamma_0 - \eta_i b\left(\Gamma_0-\Gamma_1\right)\right]|\phi|^2\frac{dl}{B}}} \tag{6.87}$$

Note, in the remainder of this report, we simply use $\frac{a}{L_n}$ instead of $\frac{a}{L_{n_e}}$.

Beyond the work of this project, the next steps would be to insert Eqn. 6.87 into an optimiser (STELLOPT), and instruct it to search for a geometry in configuration space such that the left-hand side of Eqn. 6.87 is maximised. This should then delay the onset of the TEM instability, along with the subsequent transport caused by it.

Part III

Results and Conclusion

Chapter 7

Results and Findings

In this chapter, we discuss the numerical results and findings of this project. All numerical work and analysis was carried out using Mathematica and Python.

We begin by looking at the ω_r proxy results obtained using the variational principle in Chapter 5, in comparison with GENE simulation output. As already discussed, the ω_r proxy corresponding to trapped ions and trapped electrons is not modelled in this report, but is left for future investigation (see Appendix A for the derivation of this alternative proxy). Instead, the ω_r proxy corresponding to passing ions and trapped electrons was modelled here. This choice was made for the following reason. The latter ω_r proxy has already been shown to work when applied to the simpler case of a tokamak [12, 18]. However, it was not known before this project whether this ω_r proxy would be applicable to the more complicated stellarator geometries. Thus, a contingency plan was developed in the event that this ω_r proxy failed to model the stellarator case to a sufficient standard. This is what led to the development of the ω_r proxy dealing with trapped particles only (see Appendix A). This particular choice was made because destabilising resonance from the TEM instability is predicted to be caused solely by trapped-particle behaviour, so only trapped particles were considered. As it turned out, the ω_r proxy developed to model passing ions and trapped electrons turned out to work sufficiently well in most stellarator geometries considered, and so, only it was used throughout the remainder of the project when developing the proxy outlined in Chapter 6.

For the ω_r proxy component of the results, two separate methods were undertaken for the simulations. Each method considered a different level of dependency on preexisting data output from GENE. Firstly, the ω_r proxy obtained using the variational principle was simulated using geometrical inputs and GENE data inputs. The geometrical inputs included the magnetic field strength profile and the curvature profile, whilst the GENE inputs consisted of mode structure data for the ϕ-profiles. The results of these simulations were then compared with the ω_r output given purely by GENE, which acts as our most accurate control case. This allowed us to see

whether or not the variational principle approach was indeed suitable for stellarator geometries. Once this was proven to work, the second level of investigation to be carried out involved relying only on the geometrical information as an input. In this second case, the magnetic field strength profile and the curvature profile for a given geometry were used directly as before, but they were also utilised in predicting the mode structure ϕ. The motivation behind investigating whether such an approach works lies in the following fact. If the mode structure can be predicted successfully based purely on geometrical information, then this would mitigate the need to procure data from costly and time-consuming 5D gyrokinetic supercomputer simulations. Of course, use of a predicted mode structure is not ideal and was never expected to be as accurate as using GENE simulation data. However, if a proof-of-principle can be presented successfully here, then it would act as a preliminary - but promising - sign that this method could be further refined and improved in future for more accurate results.

For the critical-density-gradient proxy component of the results, a similar procedure was undertaken as described for modelling the ω_r proxy. In this procedure, however, the ω_r proxy results from before were inserted into this critical-density-gradient proxy as an input. Following this, the predicted mode structure was then inserted into both of these nested proxies where necessary. No GENE data was used for this part of numerical work, as it did not make sense to use data pertaining to the mode's behaviour *beyond* the point of marginal stability. Our analytical work underlying this part of the project is predicated on what happens precisely at the point of marginal stability - not before or beyond this point. Thus, we were heavily reliant on the efficacy of our analytical prediction of ϕ.

Before presenting the results, we must first briefly describe what the simulation data - and therefore, our proxy - is actually modelling. As discussed in section 3.2, the plasma structure can be understood as comprising concentric layers of constant pressure [1]. These 2D surfaces of constant plasma pressure are known as flux surfaces. We can think of these flux surfaces as being composed of magnetic field lines confined to the surface. In this work, we consider a field line within a flux surface that has a normalised toroidal flux given by $s = \frac{\psi}{\psi_0} = 0.5$, where ψ_0 is the toroidal flux at full plasma radius. The simulation domain in our results is that of a flux-tube [25, 34], which corresponds to a small annulus around one given field line - where the field line is considered as a one-dimensional structure [34]. This annulus moves along the path taken by the field line and forms a tube. The relevant physical information contained within this tube is simulated, and the background density and temperature profiles are assumed to remain constant over the simulation domain. In fact, in our cases here, we simplify matters by assuming a constant background temperature gradient for all simulations, such that for both particle species, we have:

$$\eta_a = \frac{d \ln T_a}{d\psi} \Big/ \frac{d \ln n_a}{d\psi} = 0 \tag{7.1}$$

Using flux-tube simulations greatly reduces the computational cost compared with simulating

the full 2D flux surface [12]. When carrying out such simulations in an axisymmetric geometry, such as a tokamak, all flux-tubes are equivalent. However, in the non-axisymmetric geometries of stellarators, this luxury is lost. Thus, we must take care to specify which type of flux-tube simulation we are utilising. For this report, only one type of simulation will be considered. These are known as "bean" flux-tube simulations. This type of simulation gave the clearest results for our proxy output, so only these will be discussed here to exhibit the proof-of-principle of our technique. These bean flux-tubes are those with their center located in the outboard midplane of the so-called bean-shaped plane. These bean-shaped planes can be seen from the poloidal cross-sections displayed for each stellarator geometry (see Figures 7.7, 7.13, 7.19, 7.25 and 7.31). Although other flux-tube simulations will not be presented here, they can be investigated using precisely the same methods in this report. These may be of more interest in future after further improvements have been made to other components of this work, such as our procedure for predicting the mode structure. For the qualitative approach taken in this project, which aims to simply prove the principle of our methods, using only the bean flux-tube simulations will suffice.

We must also note some important conventions used in our results, regarding the perpendicular wavevector $\mathbf{k}_\perp$, and the units of certain GENE outputs. Firstly, we recall the definition of $\mathbf{k}_\perp$:

$$\mathbf{k}_\perp = k_\psi \nabla\psi + k_\alpha \nabla\alpha \tag{7.2}$$

For reasons we will not go into here, the nature of our flux-tube simulations allows us to set $k_\psi = 0$ [12]. Therefore, we only end up working with k_α. As a reminder, α is known as the binormal coordinate, or the field line labelling coordinate. The binormal wavenumber can be expressed as $k_\alpha = qk_y a$, where q is the safety factor defined in Chapter 3, and a is the minor radius of the torus being considered [12]. In our numerical results, the simulations are carried out using the poloidal wavenumber normalised by the ion-sound gyro radius, $k_y\rho_s$ [12]. From here on, this normalised wavenumber is simply denoted by $k_y\rho$. Other quantities being plotted here, such as the real mode frequency ω_r and the growth rate γ, are given in terms of the gyro-Bohm units used by GENE, $\left[\frac{c_s}{a}\right]$, where $c_s = \sqrt{\frac{T_e}{m_i}}$ is the ion sound speed and a is once again the minor radius.

7.1 Proxy for the Mode Frequency

In this section, we present the numerical results and findings for our proxy of the mode frequency ω. More accurately, our proxy solely models the real part of the mode frequency ω_r. Our proxy will be calculated using different levels of dependency on GENE data. The analytical work that led to this proxy can be found in section 5.2.

In the first case - dependent on GENE data - we show how the ω_r proxy performs using our

variational principle result (Eqn. 5.101 and 5.105), and inputting GENE data for our mode structure ϕ. We will compare the results of this approach with the direct GENE output of ω_r in section 7.1.1. In the second case - independent of GENE data - we once again utilise our variational principle result (Eqn. 5.101 and 5.105), however, we no longer rely on GENE data for ϕ. Instead, we use a prediction for ϕ, which is developed using geometrical information only. We will discuss the development of this ϕ prediction separately in section 7.1.2, before we present the results of the ω_r proxy which relies on this predicted mode structure.

As is expected, a heavier reliance on GENE data yields a stronger agreement between our ω_r proxy and the GENE output for ω_r. This validates the function of our proxy, even though we would prefer to have less dependency on such GENE data. This is why we have our second case which relies on a predicted mode structure in place of GENE data. By showing, at least in principle, that we can approximately predict the mode structure by using geometrical information only, we are freeing ourselves of the dependency on preexisting GENE data. This GENE data is not simple or quick to obtain, as it requires the computation of complicated 5D gyrokinetic supercomputer simulations [13]. Avoiding such a requirement would mean that optimisation of stellarator geometry could, in principle, be achieved more quickly and conveniently.

7.1.1 Using Variational Principle and GENE Data

We now present the results of our mode frequency proxy for various toroidal configurations. For our trial function ϕ, we insert preexisting GENE simulation data, whereby distinct profiles are used for every pair of $(k_y\rho, \frac{a}{L_n})$ values, in each geometric configuration. We start with the simplest geometry of the DIII-D tokamak, before considering the more complex stellarator geometries of the NCSX (National Compact Stellarator Experiment), the W7-X (Wendelstein 7 Experiment) and the HSX (Helically Symmetric Experiment). For W7-X, we have three distinct variants of its geometry. These are known as the standard configuration (SC), the high mirror (HM) configuration, and the low mirror (LM) configuration. Each variant has its own magnetic field profile, the form of which dictates the 'high/low mirror' in its name. For all toroidal configurations, we show the 3D geometry under consideration, whereby we look at a poloidal cut in each case (see Figures 7.7, 7.13, 7.19, 7.25 and 7.31). These colour coded images indicate the strength of the magnetic field in different regions of the geometry. Blue represents the minimum of the magnetic field strength, whilst red represents the maximum. For the stellarator cases, we are solely considering results of the bean flux-tube simulations. For all geometries, we also present a plot of the geometric profiles (see Figures 7.2, 7.8, 7.14, 7.20, 7.26 and 7.32). This consists of the magnetic field strength and the curvature experienced by the field line for the journey of the flux-tube simulation. We follow this up with presenting the mode frequency results, where we compare the output of our proxy in comparison with GENE simulation data. In these plots, our proxy is denoted by VP(ϕ_{DATA}), which is shorthand for: variational principle result, with

ϕ-data as the trial function input.

DIII-D Tokamak

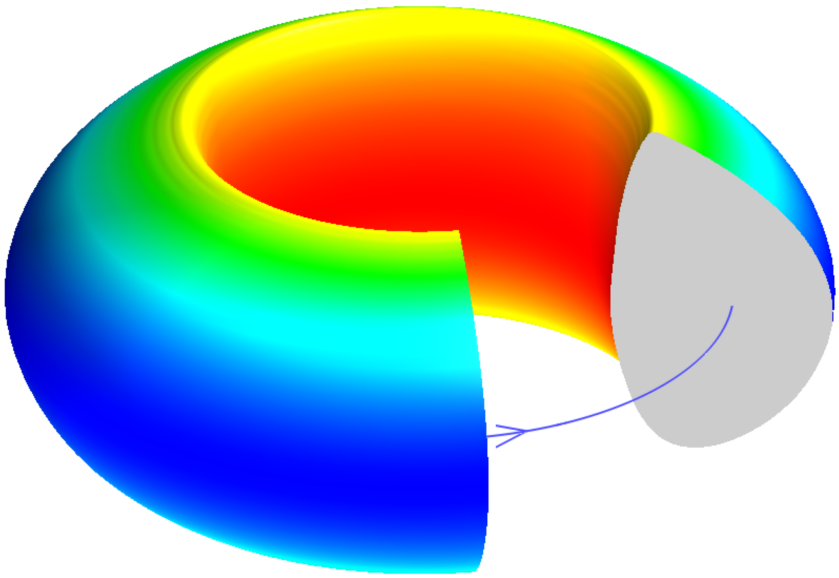

Figure 7.1: *Magnetic field strength B of the DIII-D tokamak, where red indicates the maximum of the field, and blue indicates the minimum. the Source: [12]*

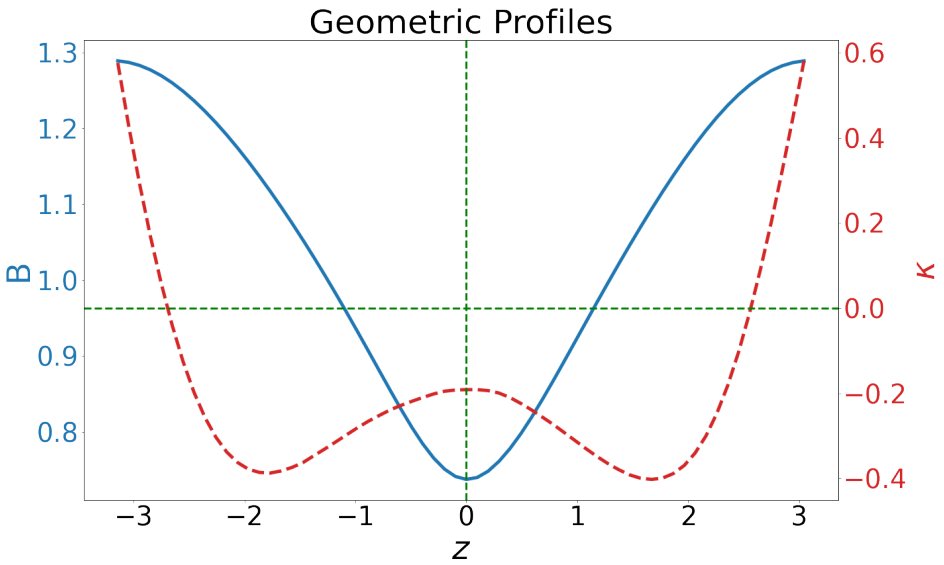

Figure 7.2: *Magnetic field strength B and curvature κ along the magnetic field line in the DIII-D tokamak. Source: GIST data from [12]*

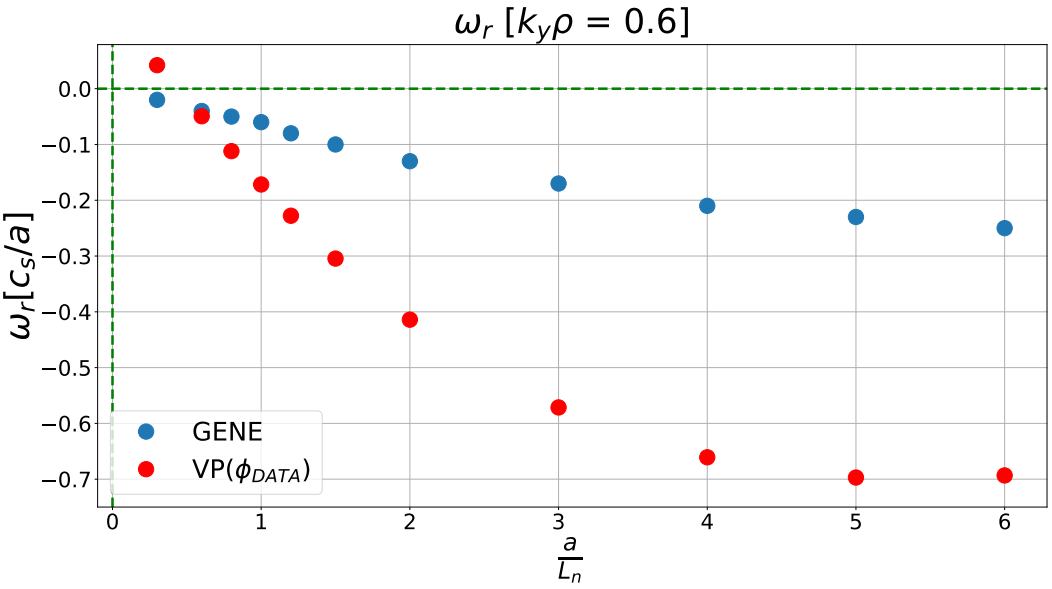

Figure 7.3: *Real mode frequency versus density gradient in the DIII-D tokamak. GENE simulation data in blue and variational principle proxy in red. Source: GENE data from [12]*

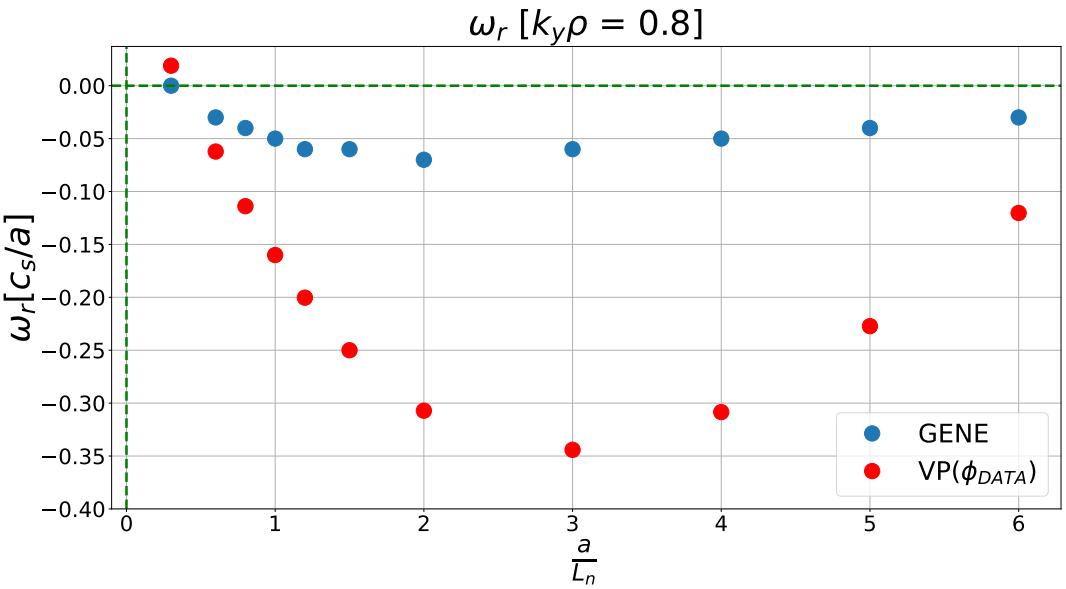

Figure 7.4: *Real mode frequency versus density gradient in the DIII-D tokamak. GENE simulation data in blue and variational principle proxy in red. Source: GENE data from [12]*

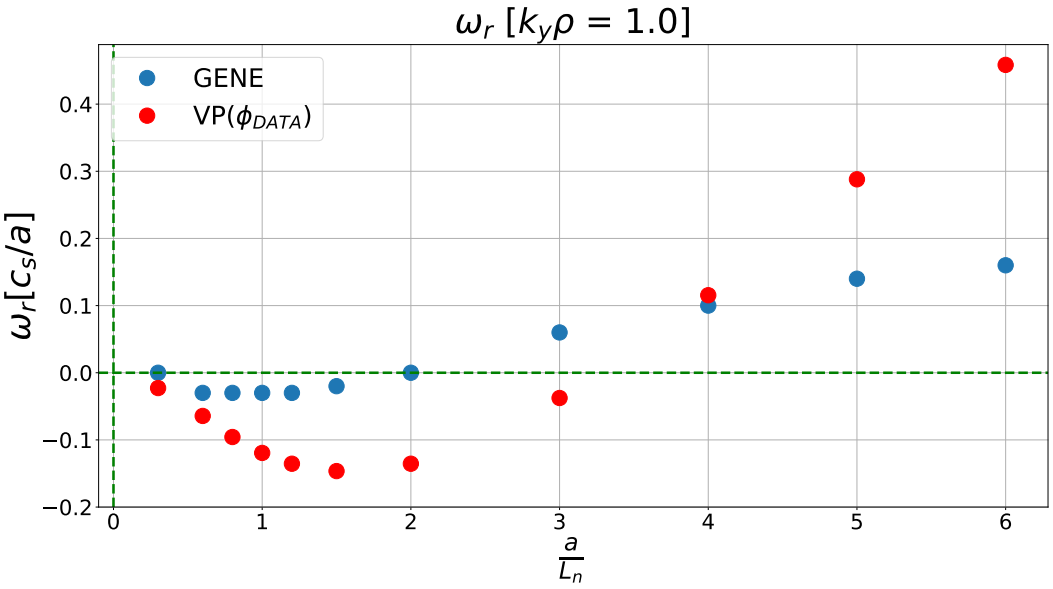

Figure 7.5: *Real mode frequency versus density gradient in the DIII-D tokamak. GENE simulation data in blue and variational principle proxy in red. Source: GENE data from [12]*

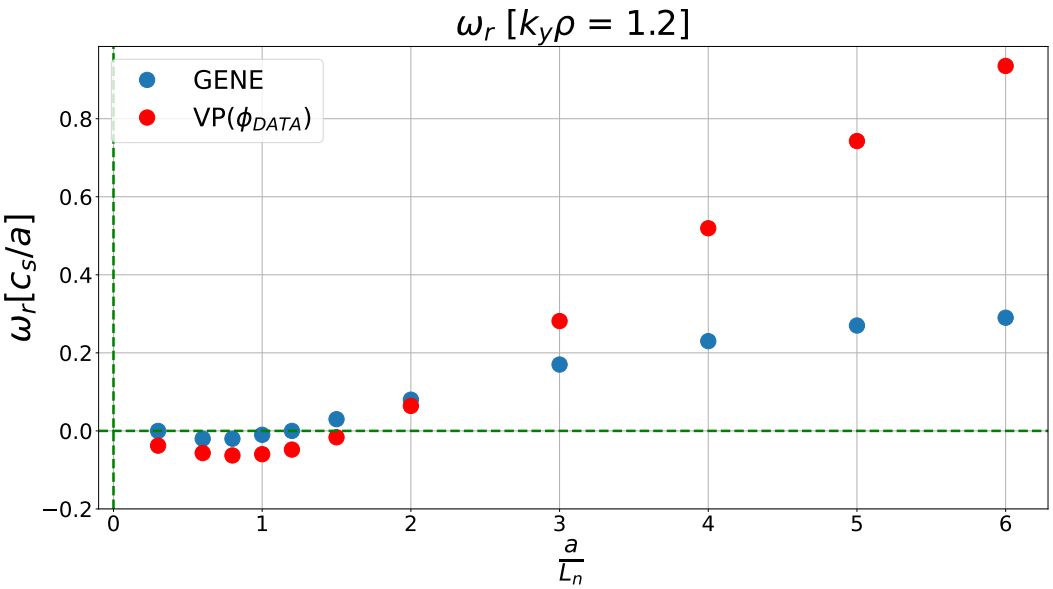

Figure 7.6: *Real mode frequency versus density gradient in the DIII-D tokamak. GENE simulation data in blue and variational principle proxy in red. Source: GENE data from [12]*

NCSX

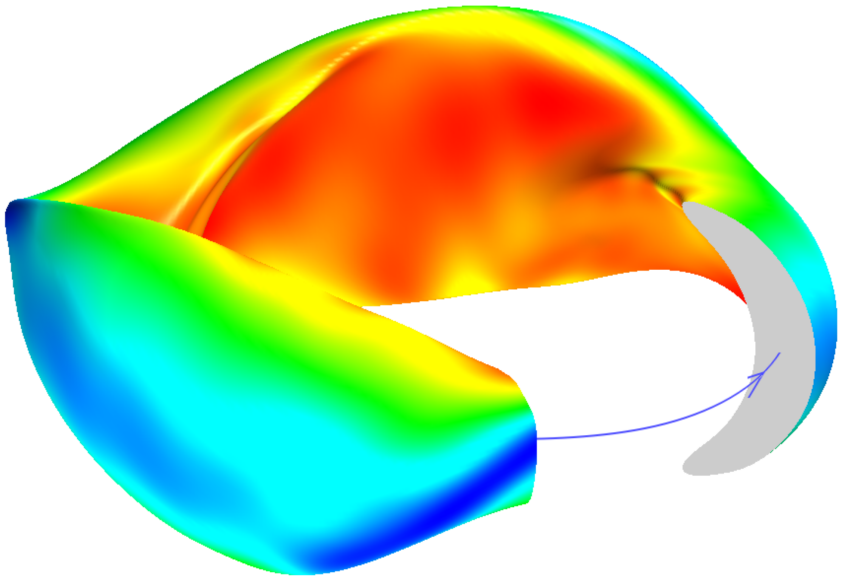

Figure 7.7: *Magnetic field strength B of NCSX, where red indicates the maximum of the field, and blue the minimum. The open slice shows the bean-shaped poloidal cross-section. Source: [12]*

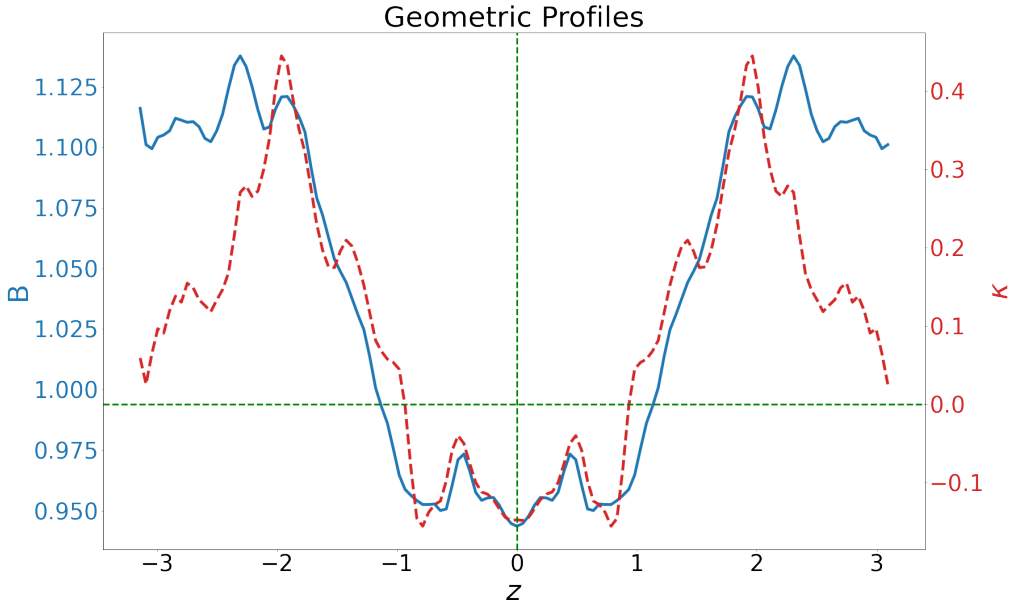

Figure 7.8: *Magnetic field strength B and curvature κ along the magnetic field line in NCSX. Source: GIST data from [12]*

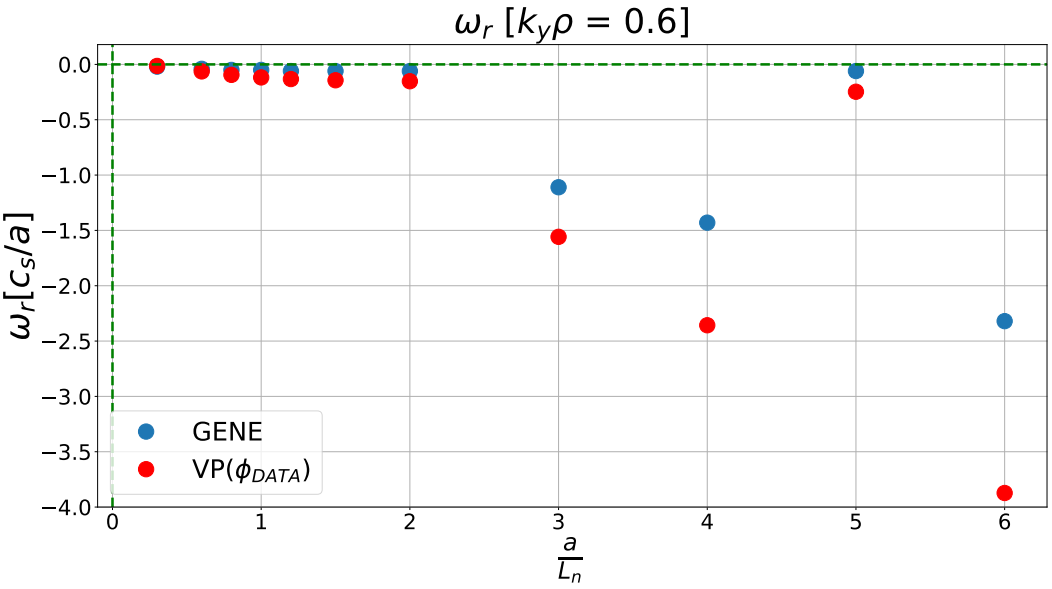

Figure 7.9: *Real mode frequency versus density gradient in NCSX. GENE simulation data in blue and variational principle proxy in red. Source: GENE data from [12]*

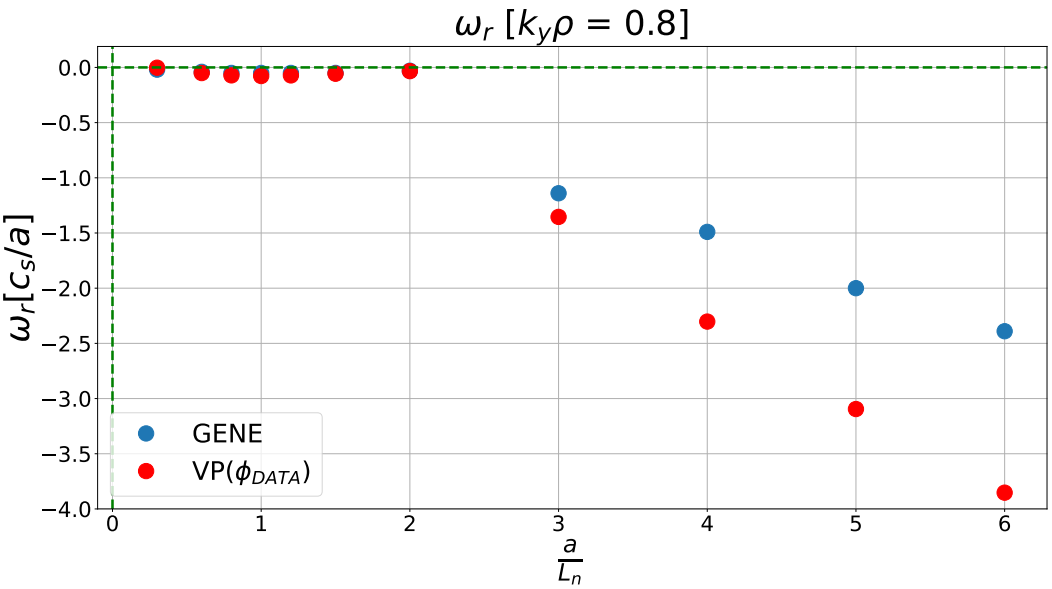

Figure 7.10: *Real mode frequency versus density gradient in NCSX. GENE simulation data in blue and variational principle proxy in red. Source: GENE data from [12]*

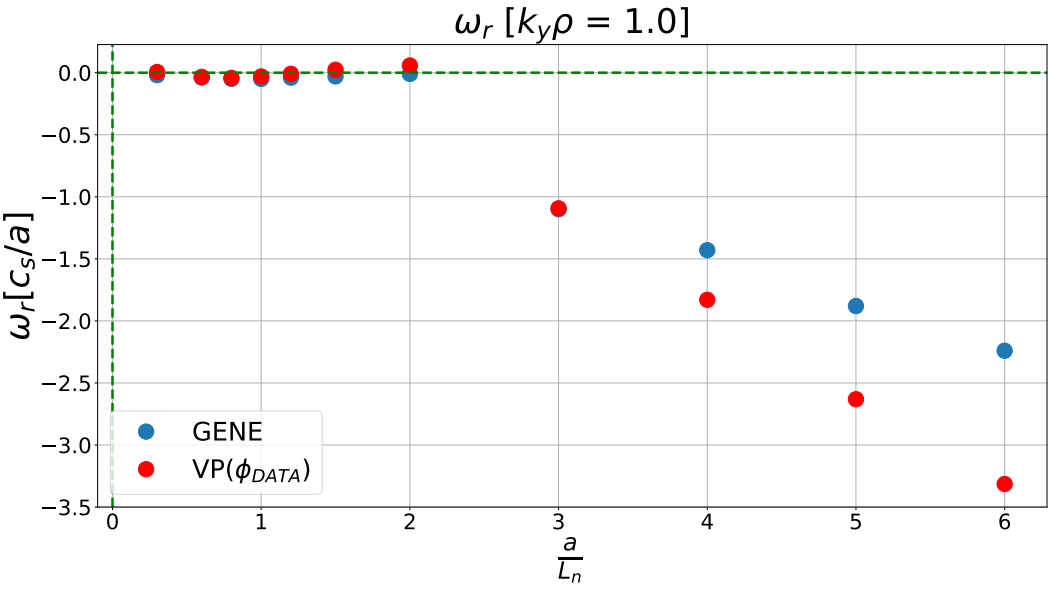

Figure 7.11: *Real mode frequency versus density gradient in NCSX. GENE simulation data in blue and variational principle proxy in red. Source: GENE data from [12]*

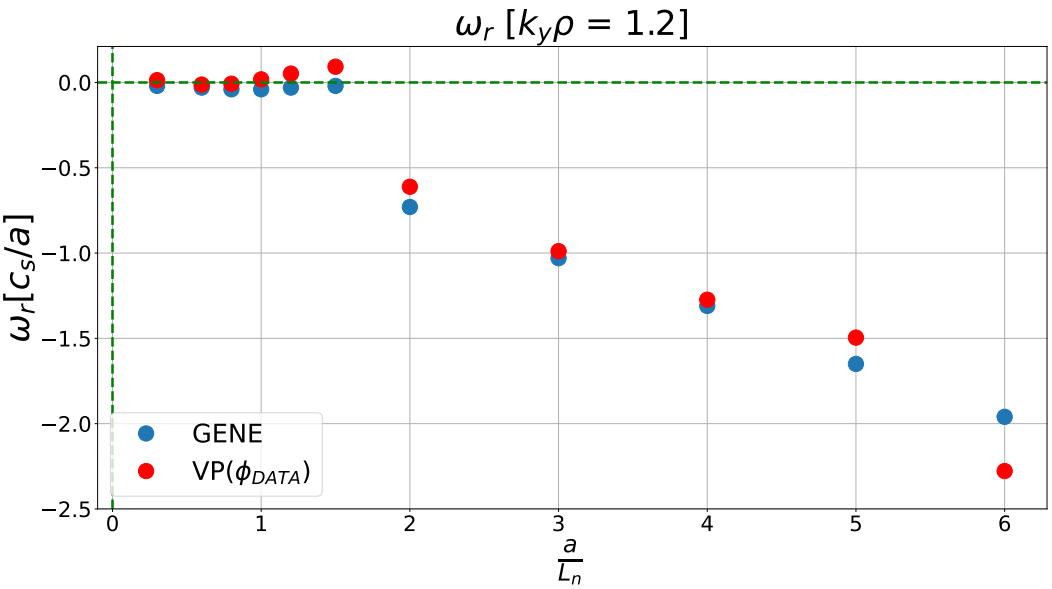

Figure 7.12: *Real mode frequency versus density gradient in NCSX. GENE simulation data in blue and variational principle proxy in red. Source: GENE data from [12]*

W7-X (SC)

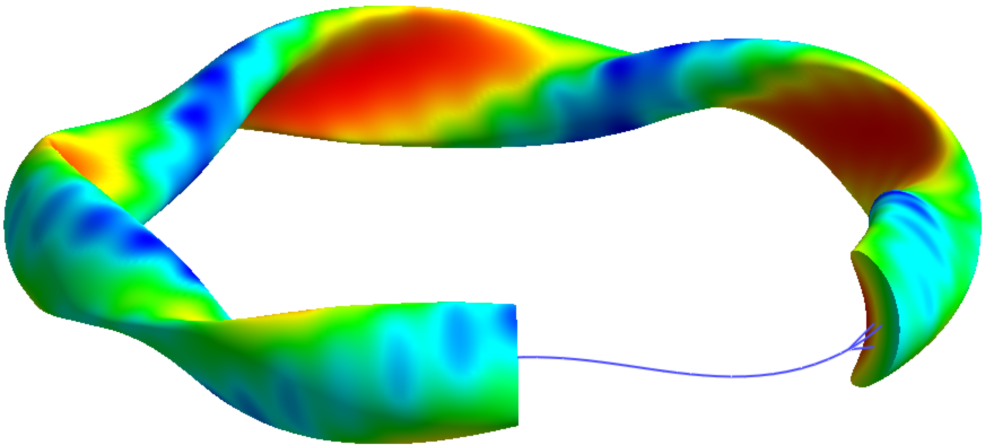

Figure 7.13: *Magnetic field strength B of W7-X (SC), where red indicates the maximum of the field, and blue indicates the minimum. The open slice shows the bean-shaped poloidal cross-section. Source: [53]*

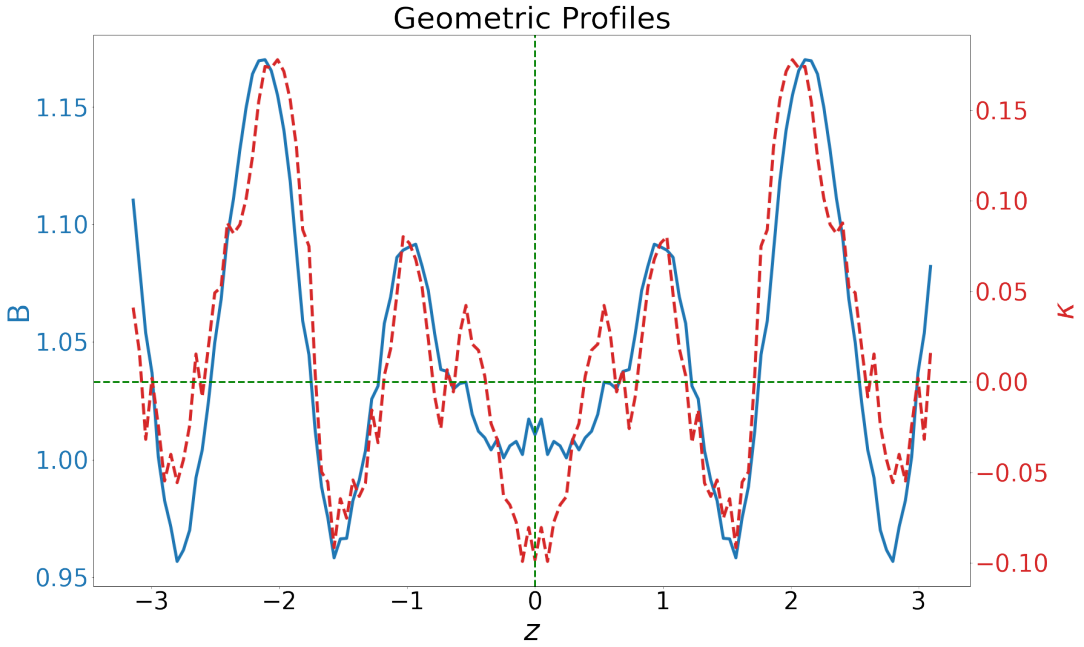

Figure 7.14: *Magnetic field strength B and curvature κ along the magnetic field line in W7-X (SC). Source: GIST data from [12]*

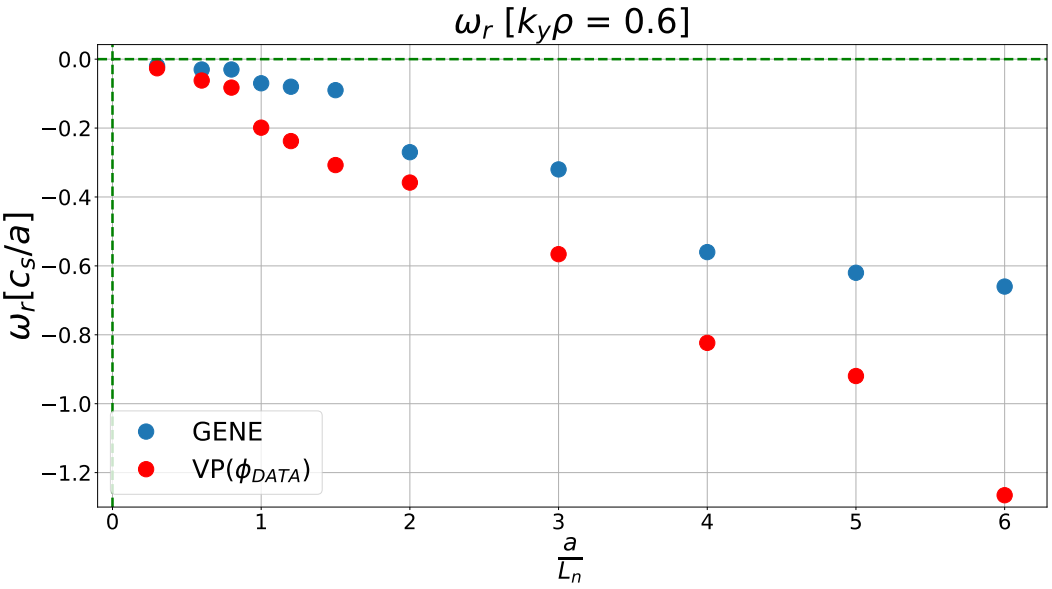

Figure 7.15: *Real mode frequency versus density gradient in W7-X (SC). GENE simulation data in blue and variational principle proxy in red. Source: GENE data from [12]*

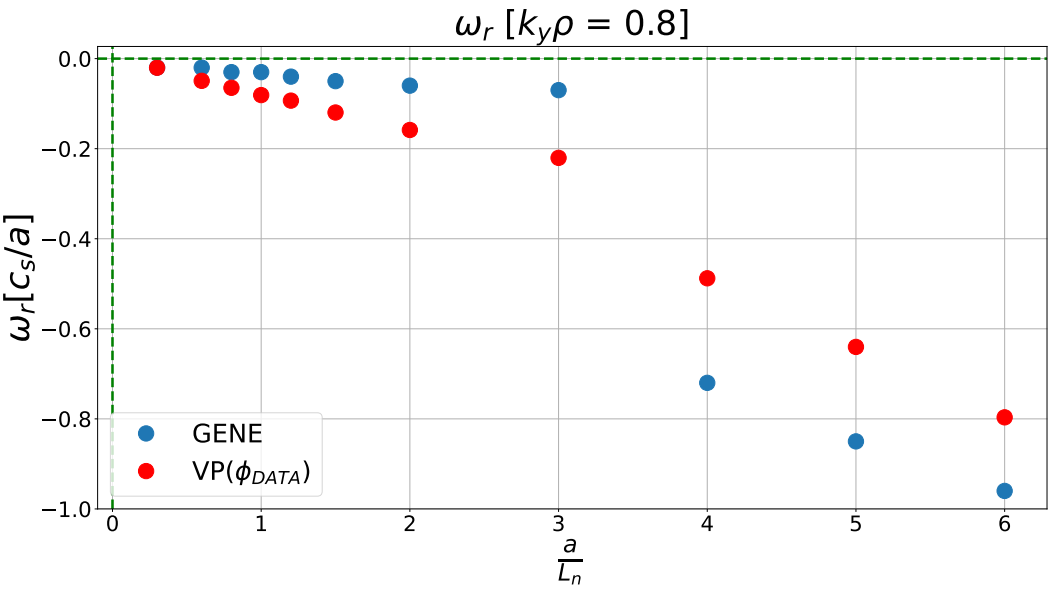

Figure 7.16: *Real mode frequency versus density gradient in W7-X (SC). GENE simulation data in blue and variational principle proxy in red. Source: GENE data from [12]*

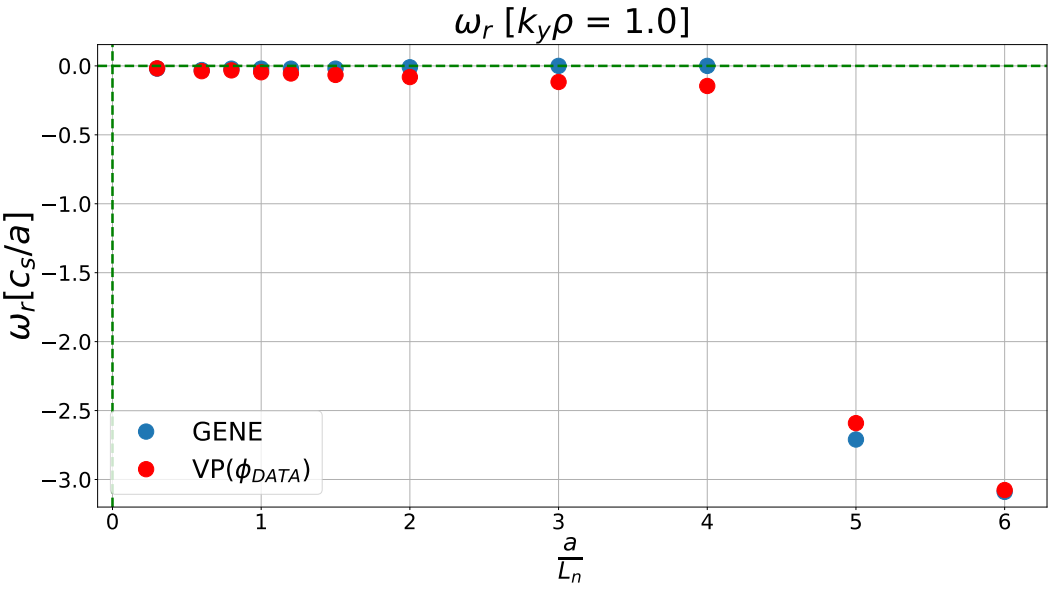

Figure 7.17: *Real mode frequency versus density gradient in W7-X (SC). GENE simulation data in blue and variational principle proxy in red. Source: GENE data from [12]*

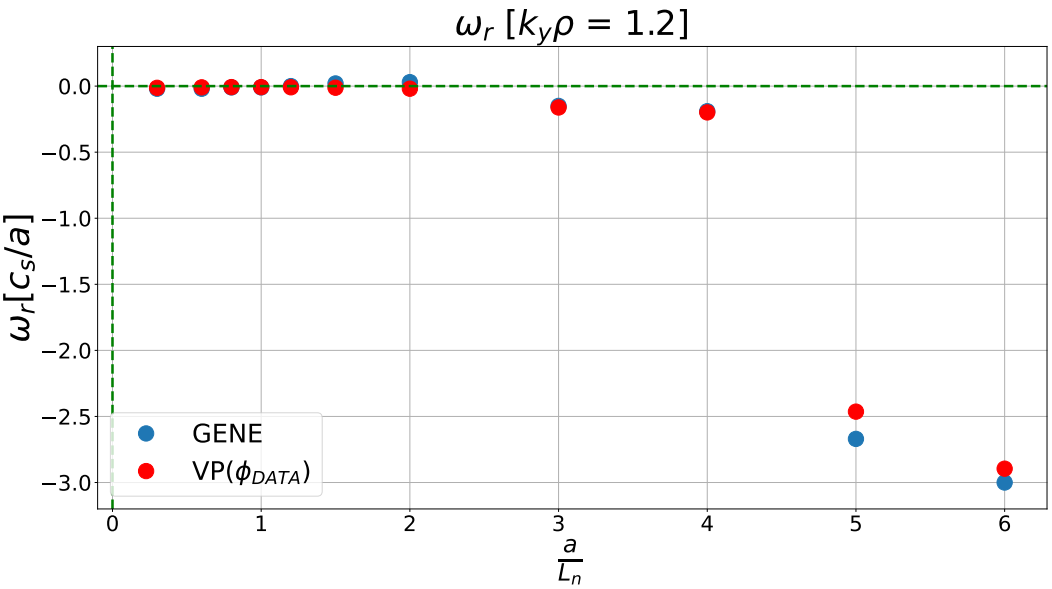

Figure 7.18: *Real mode frequency versus density gradient in W7-X (SC). GENE simulation data in blue and variational principle proxy in red. Source: GENE data from [12]*

W7-X (HM)

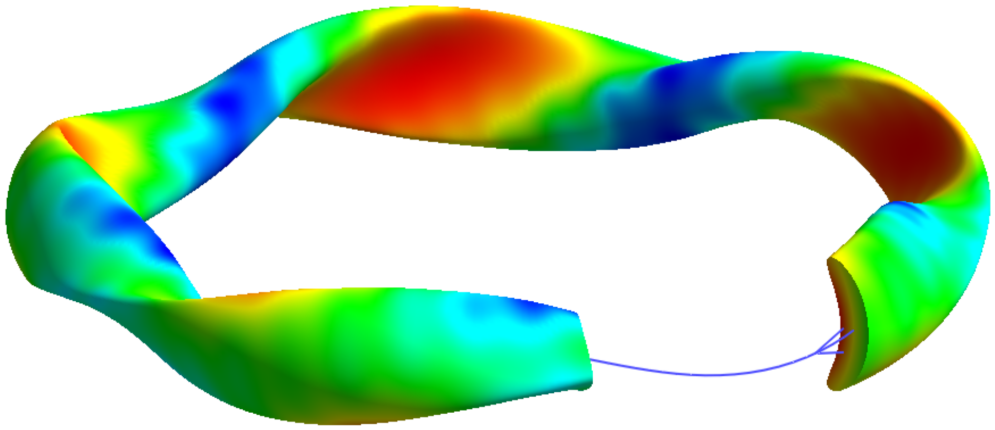

Figure 7.19: *Magnetic field strength B of W7-X (HM), where red indicates the maximum of the field, and blue indicates the minimum. The open slice shows the bean-shaped poloidal cross-section. Source: [53]*

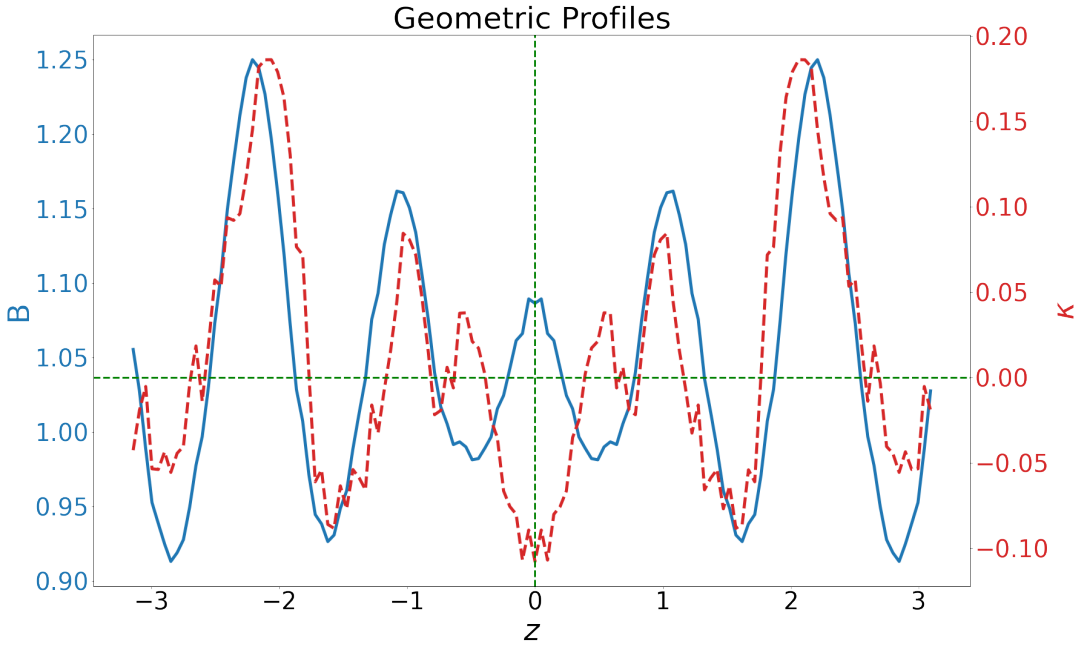

Figure 7.20: *Magnetic field strength B and curvature κ along the magnetic field line in W7-X (HM). Source: GIST data from [12]*

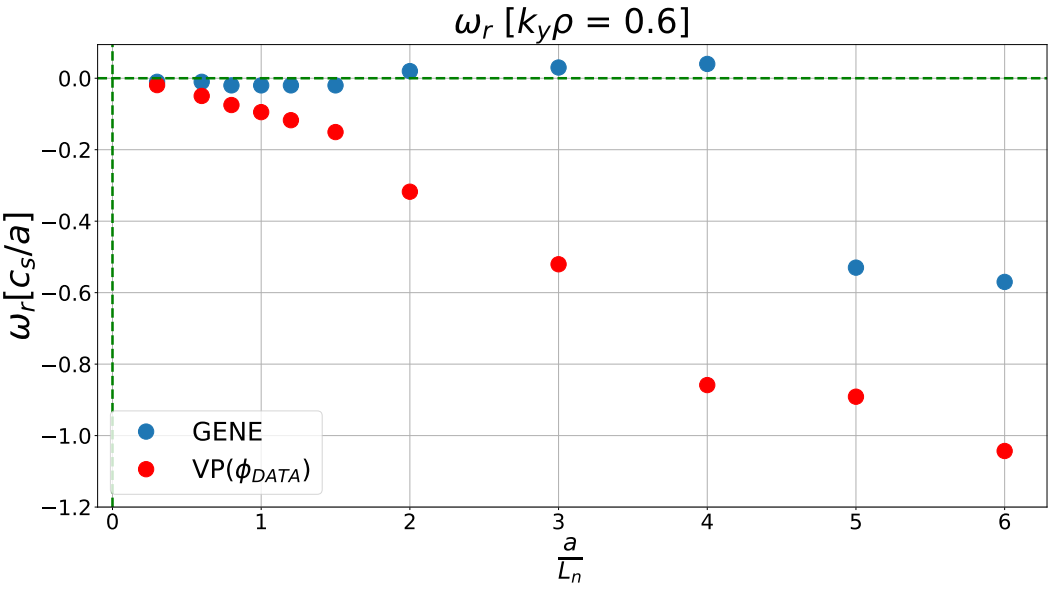

Figure 7.21: *Real mode frequency versus density gradient in W7-X (HM). GENE simulation data in blue and variational principle proxy in red. Source: GENE data from [12]*

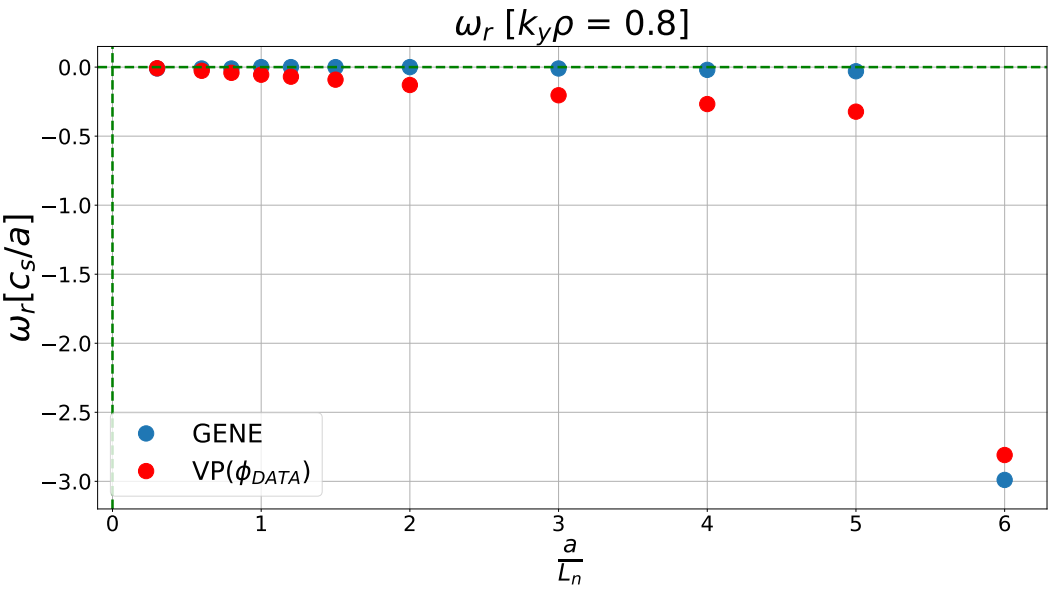

Figure 7.22: *Real mode frequency versus density gradient in W7-X (HM). GENE simulation data in blue and variational principle proxy in red. Source: GENE data from [12]*

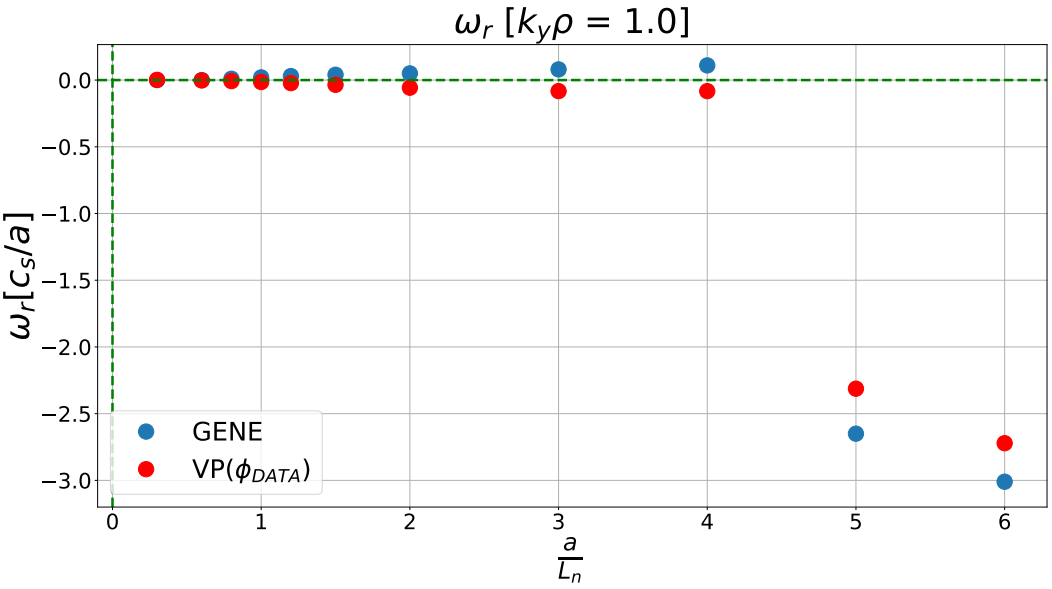

Figure 7.23: *Real mode frequency versus density gradient in W7-X (HM). GENE simulation data in blue and variational principle proxy in red. Source: GENE data from [12]*

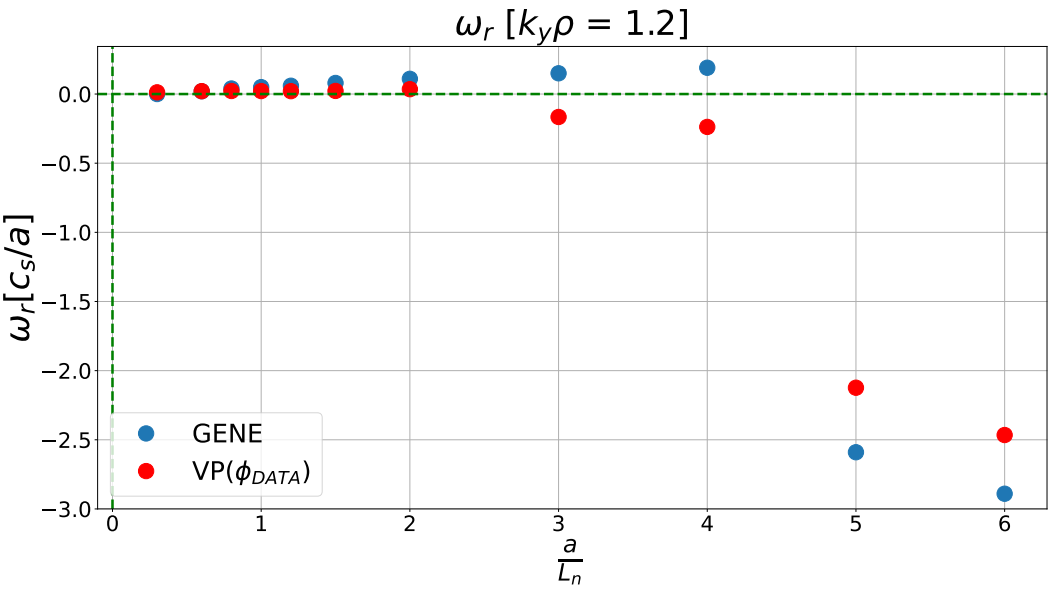

Figure 7.24: *Real mode frequency versus density gradient in W7-X (HM). GENE simulation data in blue and variational principle proxy in red. Source: GENE data from [12]*

W7-X (LM)

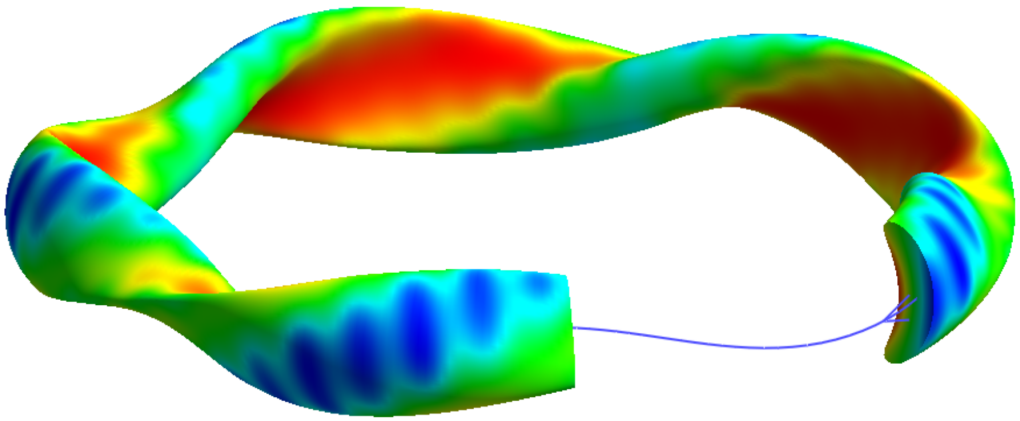

Figure 7.25: *Magnetic field strength B of W7-X (LM), where red indicates the maximum of the field, and blue indicates the minimum. The open slice shows the bean-shaped poloidal cross-section. Source: [53]*

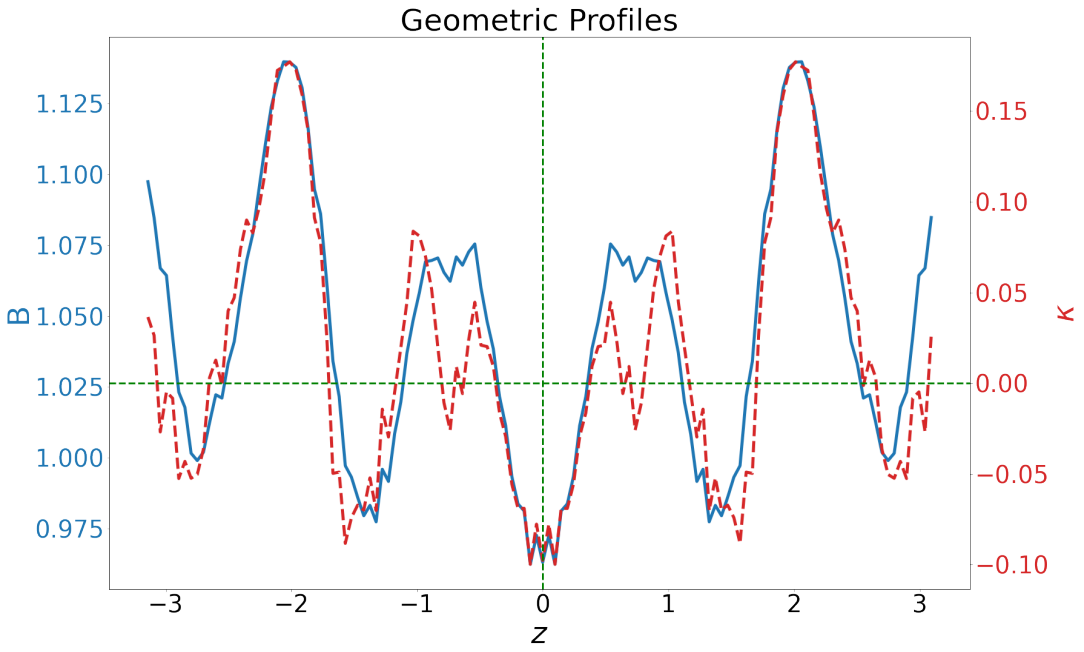

Figure 7.26: *Magnetic field strength B and curvature κ along the magnetic field line in W7-X (LM). Source: GIST data from [12]*

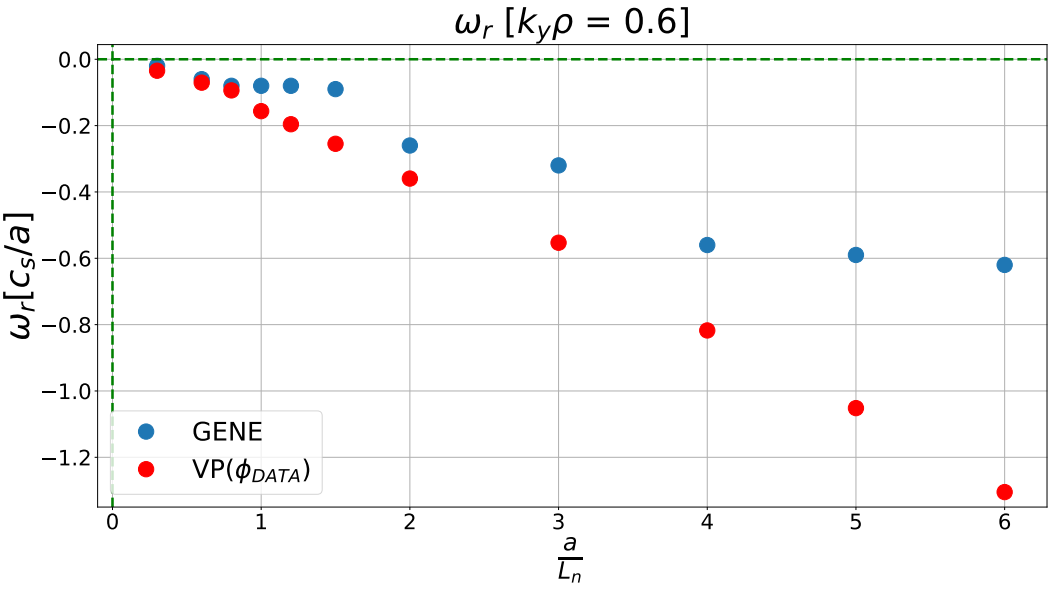

Figure 7.27: *Real mode frequency versus density gradient in W7-X (LM). GENE simulation data in blue and variational principle proxy in red. Source: GENE data from [12]*

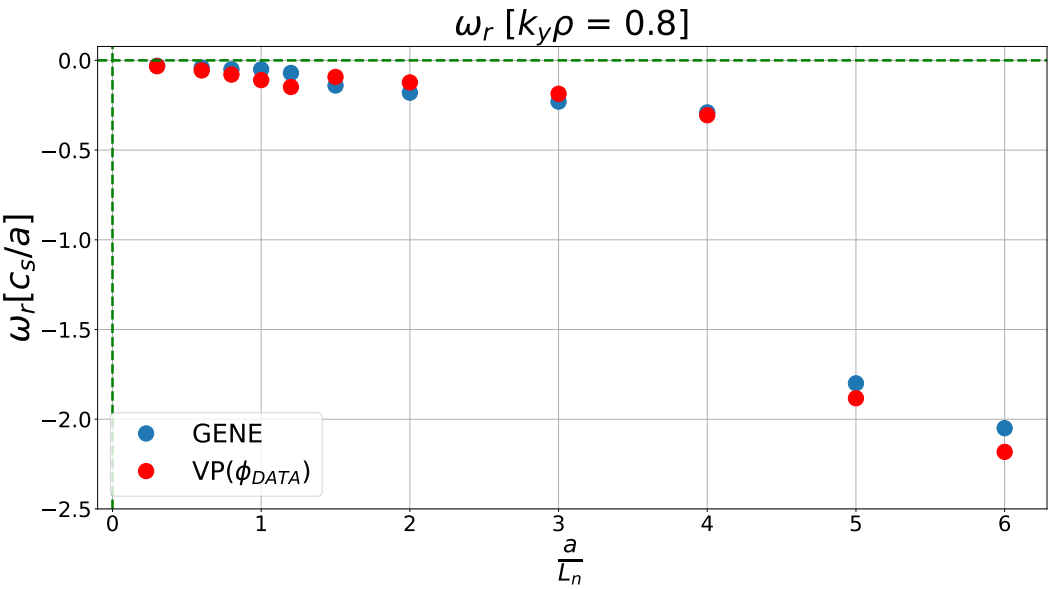

Figure 7.28: *Real mode frequency versus density gradient in W7-X (LM). GENE simulation data in blue and variational principle proxy in red. Source: GENE data from [12]*

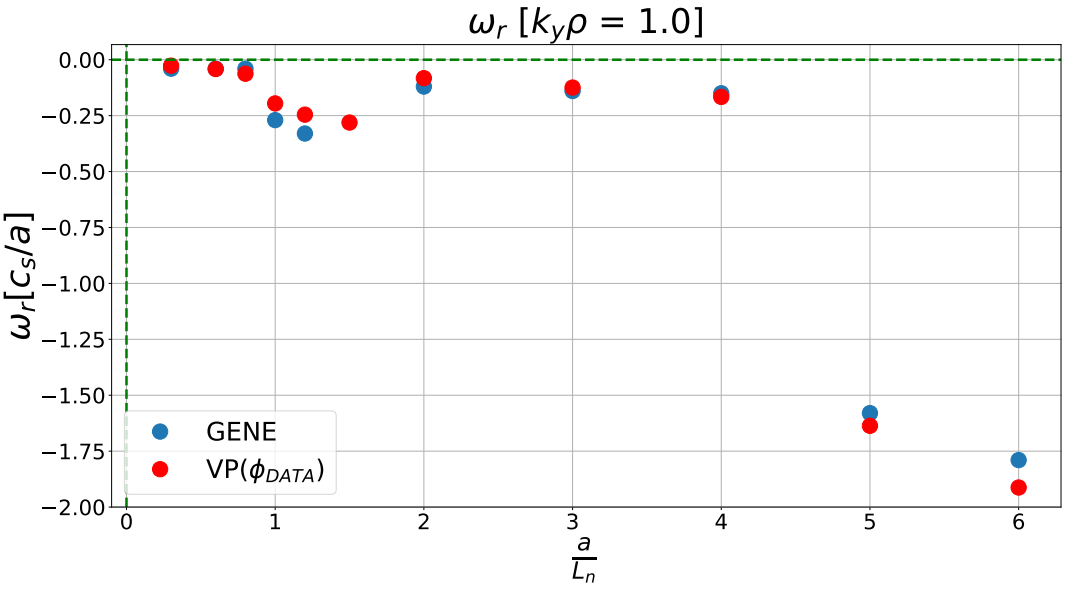

Figure 7.29: *Real mode frequency versus density gradient in W7-X (LM). GENE simulation data in blue and variational principle proxy in red. Source: GENE data from [12]*

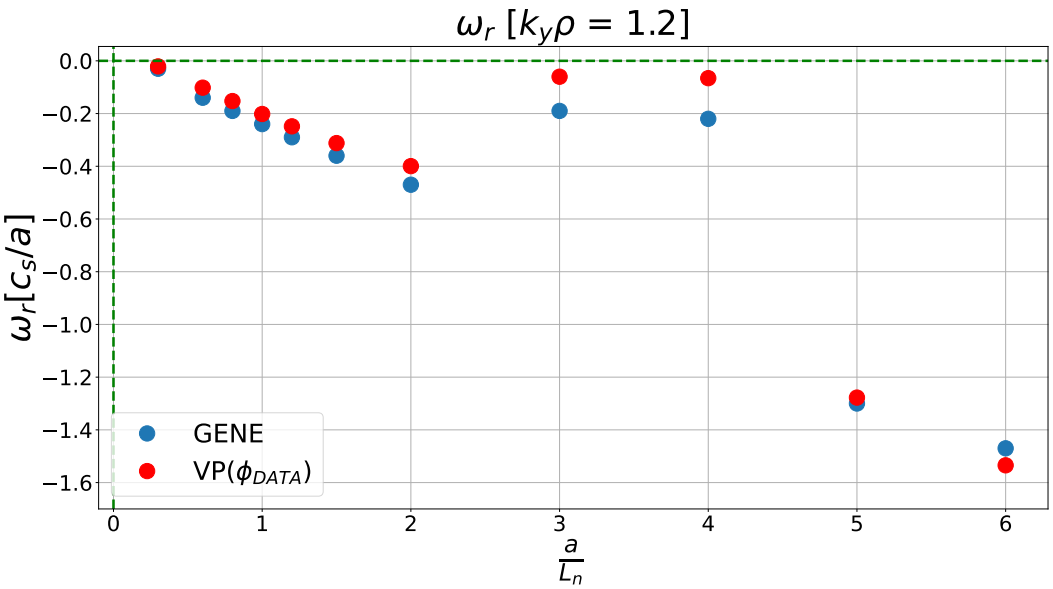

Figure 7.30: *Real mode frequency versus density gradient in W7-X (LM). GENE simulation data in blue and variational principle proxy in red. Source: GENE data from [12]*

HSX

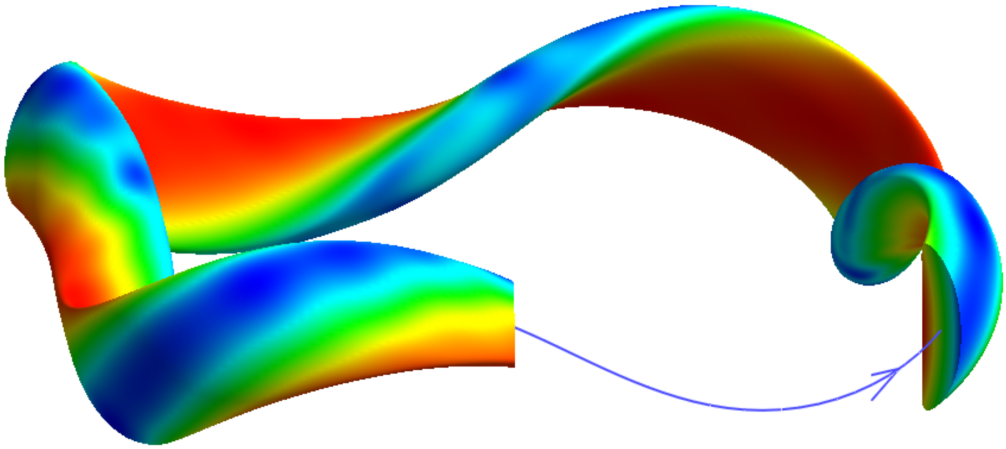

Figure 7.31: *Magnetic field strength B of HSX, where red indicates the maximum of the field, and blue indicates the minimum. The open slice shows the bean-shaped poloidal cross-section. Source: [54]*

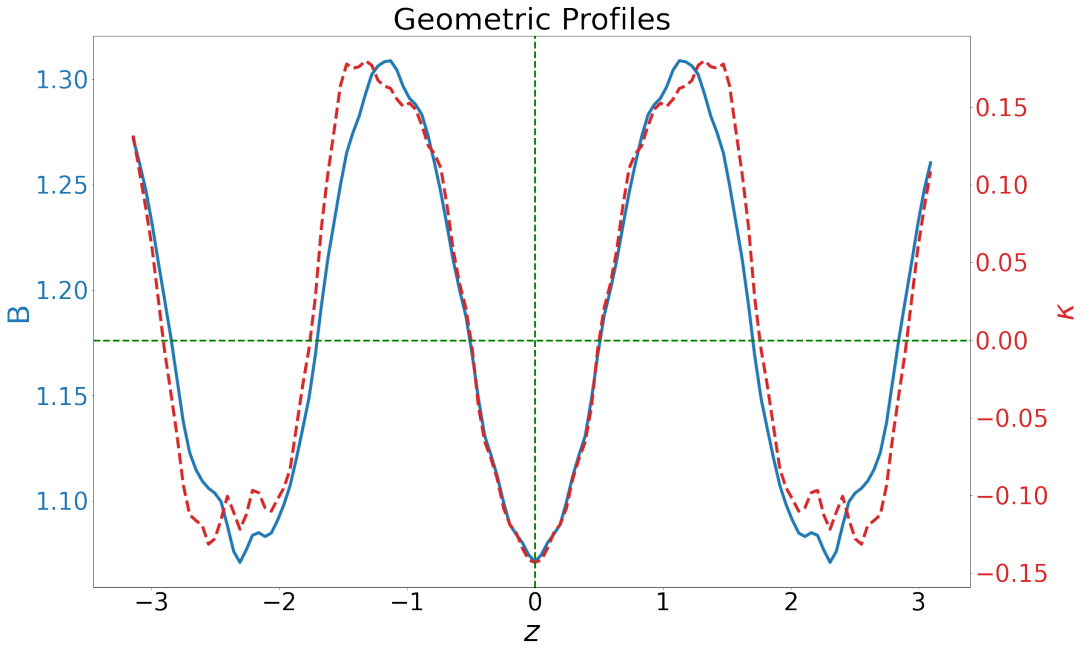

Figure 7.32: *Magnetic field strength B and curvature κ along the magnetic field line in HSX. Source: GIST data from [12]*

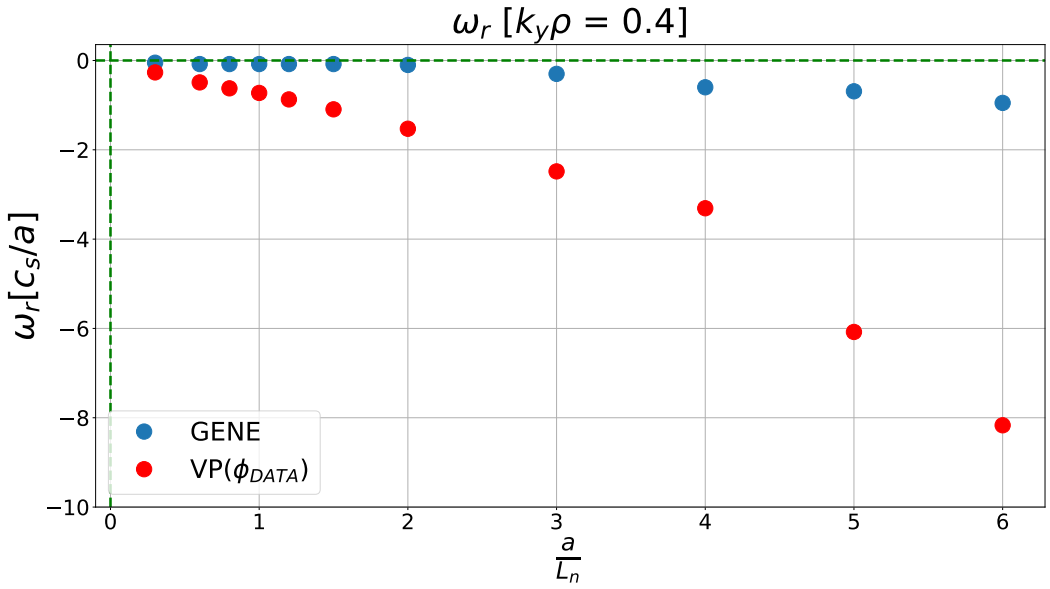

Figure 7.33: *Real mode frequency versus density gradient in HSX. GENE simulation data in blue and variational principle proxy in red. Source: GENE data from [12]*

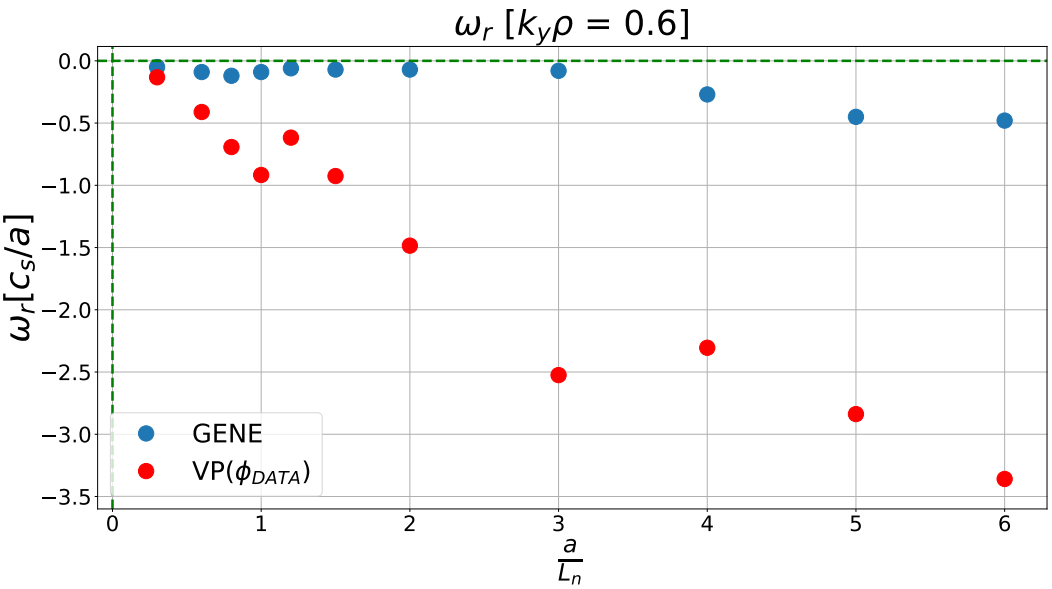

Figure 7.34: *Real mode frequency versus density gradient in HSX. GENE simulation data in blue and variational principle proxy in red. Source: GENE data from [12]*

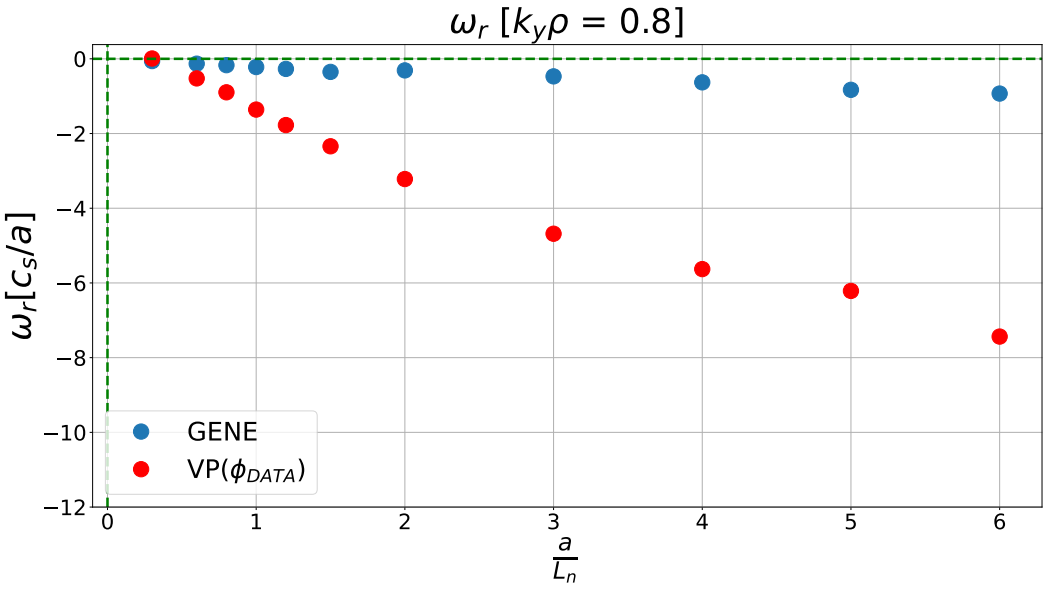

Figure 7.35: *Real mode frequency versus density gradient in HSX. GENE simulation data in blue and variational principle proxy in red. Source: GENE data from [12]*

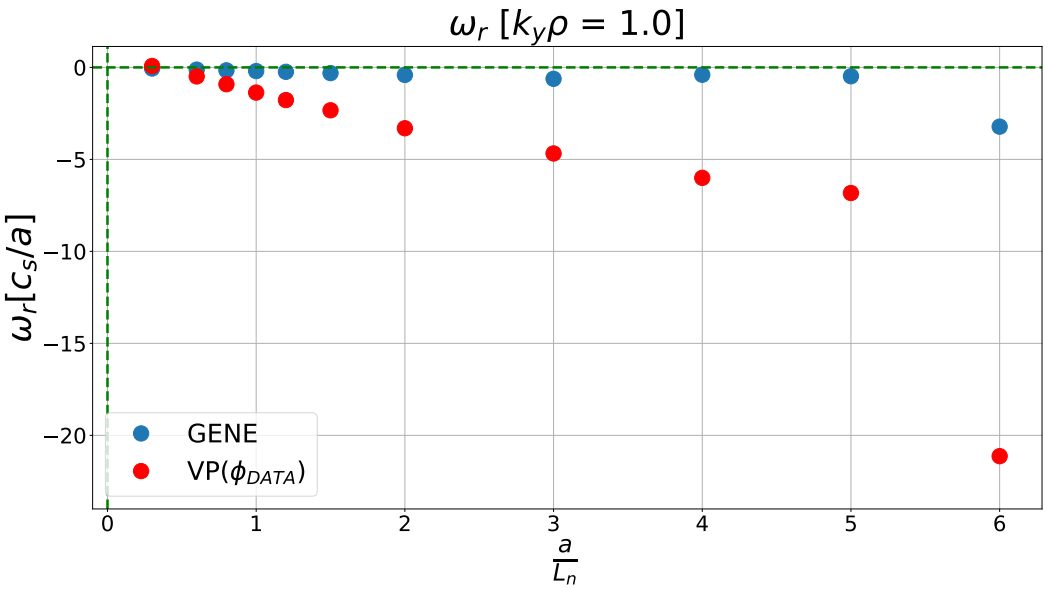

Figure 7.36: *Real mode frequency versus density gradient in HSX. GENE simulation data in blue and variational principle proxy in red. Source: GENE data from [12]*

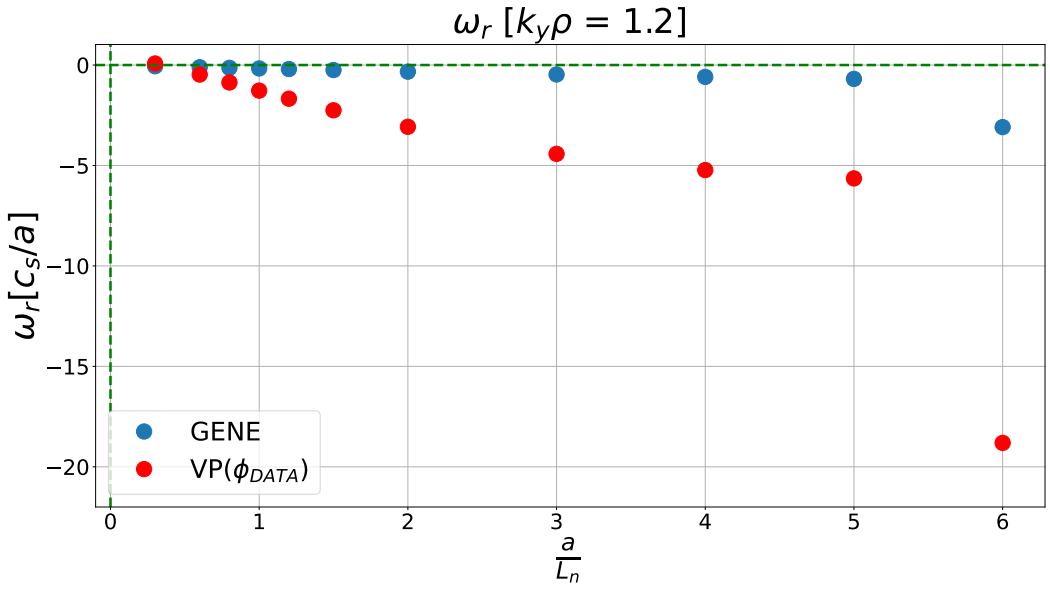

Figure 7.37: *Real mode frequency versus density gradient in HSX. GENE simulation data in blue and variational principle proxy in red. Source: GENE data from [12]*

Discussion

We now discuss these results, which arose from utilising a variational principle technique to approximate the real mode frequency ω_r of the TEM. The trial function input for the variational principle technique is the mode structure ϕ. In this case, this input took the form of GENE simulation data. This is the idealised case, as we are relying heavily on simulation data to know the nature of the mode structure. Regardless, this idealised case allows us to validate our approach by showing how we can accurately model the TEM behaviour, given that the trial function input sufficiently approximates the actual mode structure ϕ.

As can be seen from the plots of the real mode frequency, there are varying levels of agreement depending on the geometry under consideration. The strongest agreement between the GENE simulation data and our proxy is manifest in NCSX, and in each of the W7-X configurations. In these cases, for most wavenumber values (perhaps excluding $k_y\rho = 0.6$ for each W7-X configuration), sudden drops and jumps in the GENE data are tracked quite accurately by the proxy.
In DIII-D, the general trend and magnitude of the GENE data is mirrored somewhat well by the proxy, but is less compelling than the aforementioned stellarator cases. This is quite an interesting observation, given that the DIII-D tokamak is by far the simplest geometry, with the smoothest geometric profiles. This may indicate that geometrical complexity does not play a significant role in the efficacy of our variational principle technique for predicting the mode frequency. Other underlying factors may be at play which have a greater effect on the outcome of our model's predictions.
The weakest agreement between simulation and proxy is found in the HSX case. Here, it looks as if the proxy amplifies subtle inflections in the GENE data, such that the magnitudes are over-exaggerated. Examples of this can be seen in the final data points of Figures 7.36 and 7.37. A potential reason for this weaker agreement in HSX could be due to the presence of more subdominant modes, which could be interacting with the TEM we are modelling [55].

It is also worth noting that in most of the stellarator cases - in particular, in NCSX, W7-X (SC) and W7-X (HM) - we notice that the GENE data for ω_r has a distinct drop-off after some density gradient value. In these cases, the magnitude of ω_r seems to remain close to zero for lower density gradients before suddenly dropping to a relatively larger negative value. According to [56], which investigated the ITGM, such a discontinuity in the mode frequency may indicate a transition between two different branches of micro-instabilities. Our data may then indicate that such a transition between two trapped-electron modes is taking place in these stellarators. It is mentioned in [56] that such behaviour may manifest itself in axisymmetric configurations also, but only in the long wavelength limit.

As mentioned earlier in this report, previous research has shown that this mode frequency proxy procedure works quite successfully in the simpler DIII-D tokamak geometry [18, 12]. However,

the efficacy of this method in stellarator geometries had not been investigated prior to this project. Thus, the proxy procedure has been replicated here in the tokamak case, and subsequently expanded to the more complex stellarator geometries. As we have now seen, the proxy procedure does successfully model the instability behaviour in various stellarator geometries, with varying degrees of agreement. This indicates that the level of geometric complexity is not a pressing issue for approximately modelling the TEM behaviour. However, as posited in the HSX case, the presence of subdominant modes may threaten the validity of our analysis of the TEM.

Another potential explanation for the discrepancies between our proxy prediction and the GENE output could be due to an ordering assumption made during our analytical derivation. This was in regard to the magnetic drift frequency ω_{da} and the mode frequency ω. In order to be able to carry out our variational principle approach in section 5.2, we needed to assume a small ordering of this drift frequency compared to the mode frequency ($\omega_{da} \ll \omega$), so as to avoid encountering resonance when $\omega_{da} \sim \omega$ in the denominator of our integral expression. This is ultimately because our variational principle procedure is only known to work in cases where the integral expression is fully real. Thus, we had to avoid the manifestation of a pole in our calculation in order to successfully implement this variational principle procedure. Despite this assumption, our procedure here still managed to yield very promising results in almost all cases.

7.1.2 Using Variational Principle and Predicted Mode Structure

Once again, we present the results of our mode frequency proxy for various toroidal configurations. For our trial function ϕ in this case, we insert our prediction of the mode structure, whereby only one profile is used for each geometric configuration and is held constant for varying wavenumber ($k_y\rho$) and density gradient $\left(\frac{a}{L_n}\right)$ values. The procedure for calculating this predicted mode structure will be explained before presenting the mode frequency proxy results. As before, we start with the simplest geometry of the DIII-D tokamak, before considering the more complex stellarator geometries of the NCSX (National Compact Stellarator Experiment), the W7-X (Wendelstein 7 Experiment) and the HSX (Helically Symmetric Experiment). For each geometric configuration, we first show the predicted mode structure profile (see Figures 7.40, 7.46, 7.52, 7.58, 7.64, 7.70), which relies upon the geometric profiles only (see Figures 7.41, 7.47, 7.53, 7.59, 7.65 and 7.71). We follow this up with presenting the mode frequency results, where we compare the output of our proxy in comparison with GENE simulation data. In these plots, our proxy is denoted by VP(ϕ_{Pred}), which is shorthand for: variational principle result, with $\phi_{(Pred)}$ as the trial function input.

Predicting the Mode Structure

Here, we show how the mode structure ϕ can be very roughly predicted using only geometrical information. The inputs used here are the magnetic field strength profile B, and the curvature profile κ. As already mentioned, the benefit of being able to successfully predict the mode structure is that we can circumvent the need to run costly and time-consuming 5D GENE simulations [13]. The method carried out here is only a first approximation toward achieving the mode structure, but it serves to prove the principle of this technique. Further investigation and refinement of this prediction procedure is recommended for future work.

In order to predict the mode structure, we first need to know the relationship between the mode itself and the geometry it exists in. We are, of course, concerned with the nature of the trapped-electron mode, so it is helpful to remind ourselves of trapped particle behaviour in toroidal geometry. This was discussed in some detail in section 3.2, but we will reiterate some of the relevant details here for convenience. Trapped particles are those that are periodically reflected between regions of high magnetic field with a characteristic frequency, known as the bounce frequency. This occurs when particles enter a region of low magnetic field strength, and do not have sufficient parallel velocity (parallel to the magnetic field line) to escape the region. Such a region can be thought of as a magnetic-field well, bounded by regions of higher magnetic field. Due to the intrinsic toroidal nature of our geometrical configurations, the magnetic coils that create the plasma's magnetic cage are inevitably closer together at the centre of the torii than on the outboard side. Thus, this leads to a magnetic field strength gradient ∇B, which points toward the central toroidal axis. The magnetic field is then weakest at the outboard side, and so this is where trapped particles primarily reside. This outboard side is also where the curvature is negative, and this is known as a "bad curvature" region. More specifically, bad or negative curvature occurs where the equilibrium plasma pressure gradient (∇p_0) and the magnetic field strength gradient (∇B) are aligned. In this region, free energy can be released when a field line is exchanged between two flux tubes [13]. Micro-instabilities feed from this supply of free energy and grow as a result.

With this information at hand, we now know that our mode of interest is dependent on the geometry in a two-fold manner. Firstly, the TEM must occur in regions of low magnetic field, so the mode ought to peak where the magnetic field has a minimum. We also know that free energy is supplied to the mode in regions of bad curvature, i.e., negative curvature ($\kappa < 0$). Using this information, we can impose that the mode structure is required to peak where the magnetic field has a minimum, and where the curvature is negative (bad curvature region). We can then use these requirements to approximate the mode structure. We will use the simplest case of the DIII-D tokamak as an example to demonstrate how this can be done. We can start by simply combining the the magnetic field strength profile with the curvature profile, giving us the second plot seen in Fig. 7.38. It is worth noting that we are not concerned by the magnitude of the our result, only the shape.

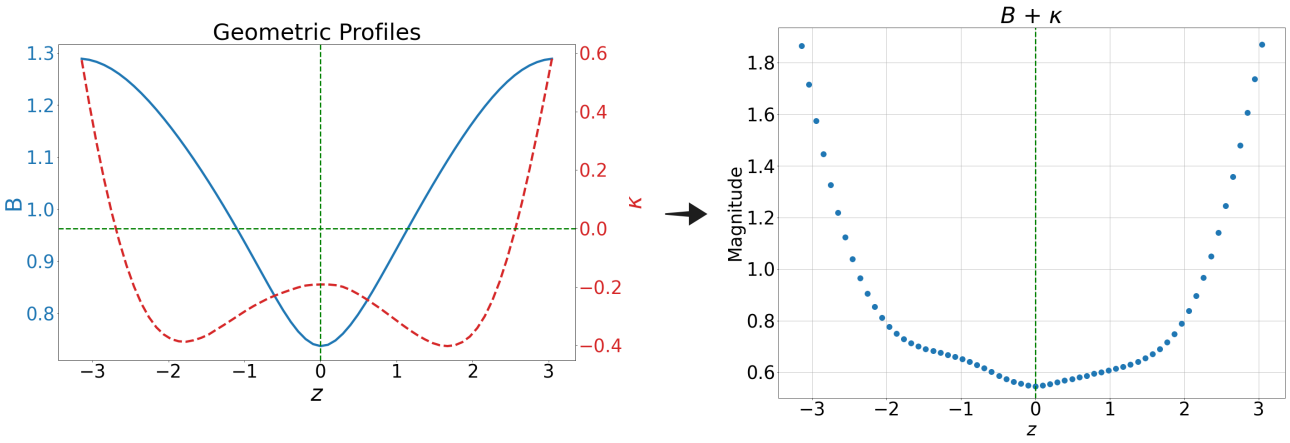

Figure 7.38: *Magnetic field strength B and curvature κ along the magnetic field line in the DIII-D tokamak, and the combination of these two profiles, $B + \kappa$. Source: GIST data from [12]*

After combining the magnetic field strength with the curvature, the next step is to invert this result. We do this because we know our mode should have its maximum where these geometric quantities both have their lowest values. We also normalise our result, due to the fact that we are only interested in the mode shape, not its magnitude. Inverting and normalising the $B + \kappa$ plot in Fig. 7.38 then gives us our final result for the predicted mode structure in Fig. 7.39. Clearly, our approach is extremely simple and straightforward, but by no means rigorous. There is plenty of room for improvement and refinement, and so some suggestions for how to go about doing this will be mentioned in the discussion to follow later. With our method for predicting the mode structure now described, we can present the results of this procedure in our geometric configurations of interest, as well as the results of the mode frequency proxy which relied on the accuracy of these predicted ϕ profiles.

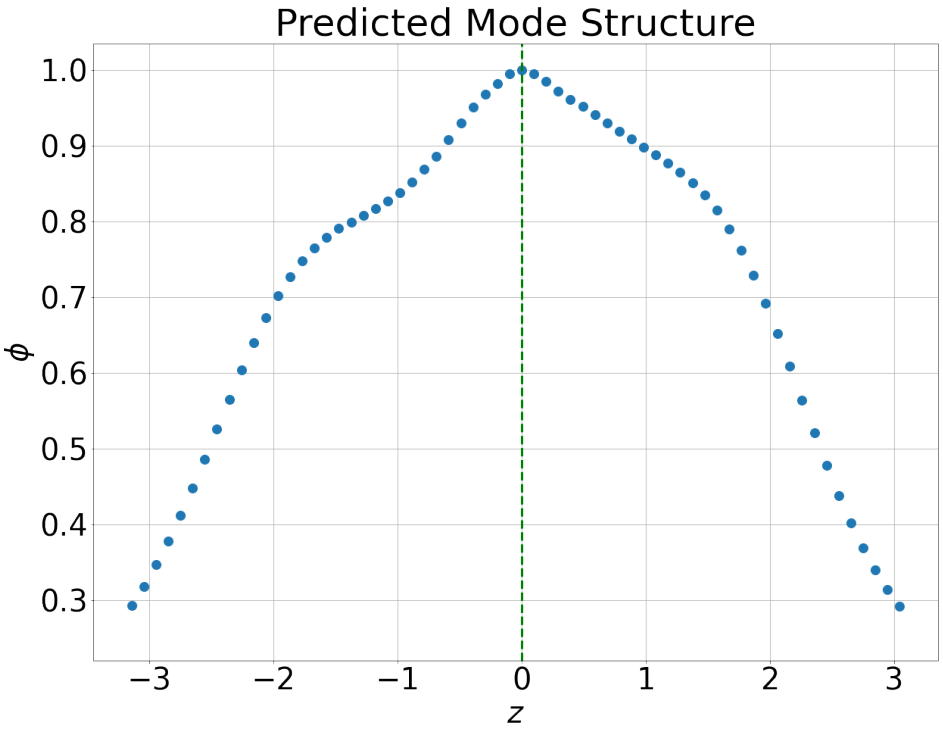

Figure 7.39: *The predicted mode structure profile $\phi_{(Pred)}$ along the magnetic field line for the DIII-D tokamak.*

DIII-D Tokamak

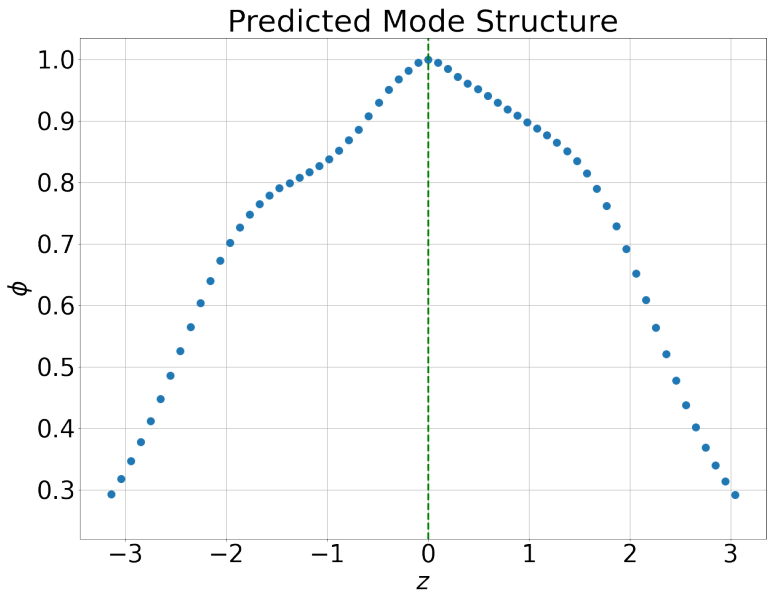

Figure 7.40: *The predicted mode structure profile $\phi_{(Pred)}$ along the magnetic field line for the DIII-D tokamak.*

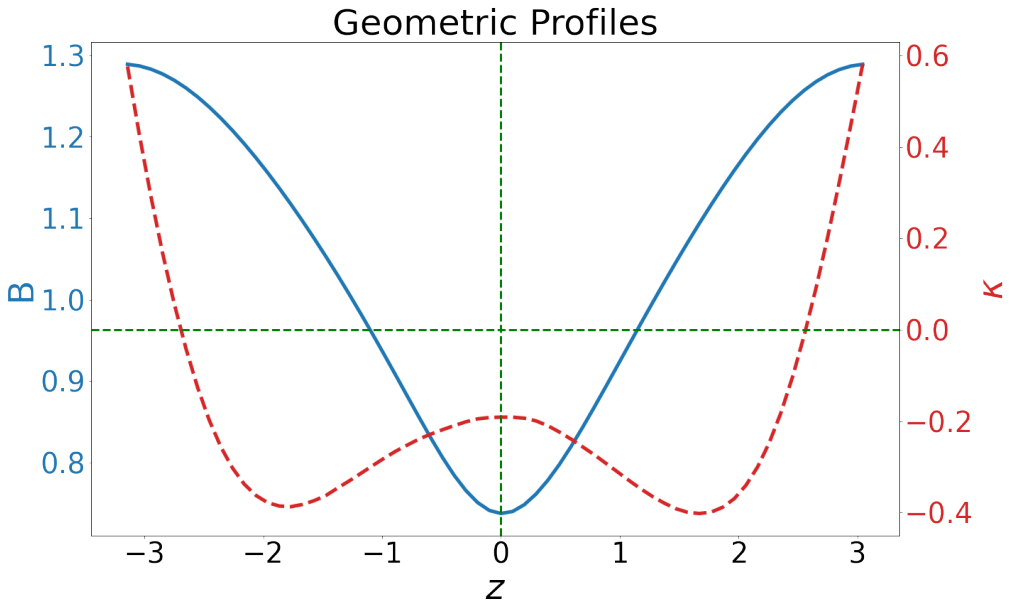

Figure 7.41: *Magnetic field strength B and curvature κ along the magnetic field line in the DIII-D tokamak. Source: GIST data from [12]*

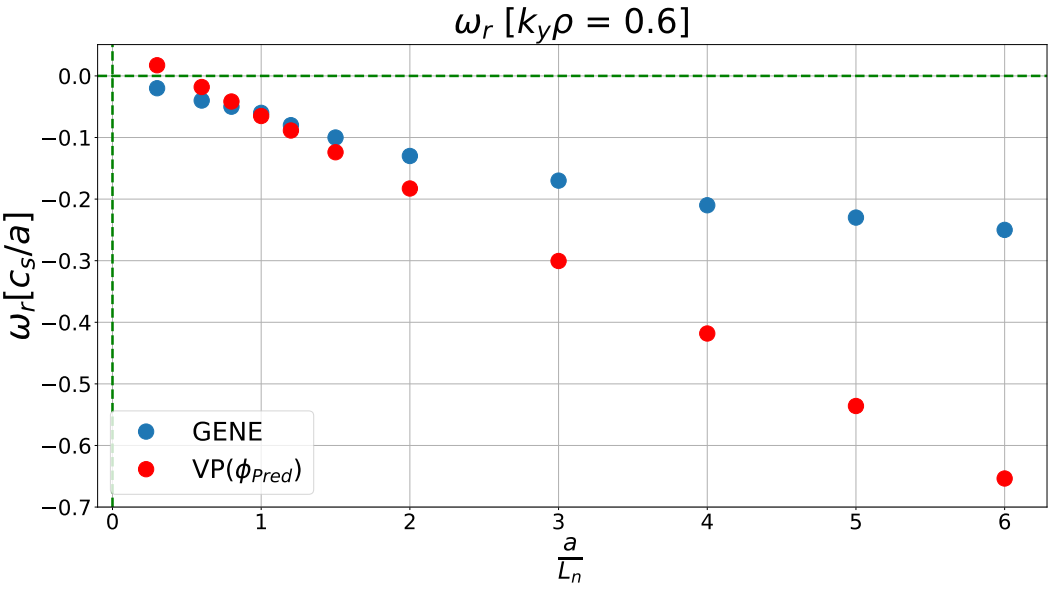

Figure 7.42: *Real mode frequency versus density gradient in the DIII-D tokamak. GENE simulation data in blue and variational principle proxy in red. Source: GENE data from [12]*

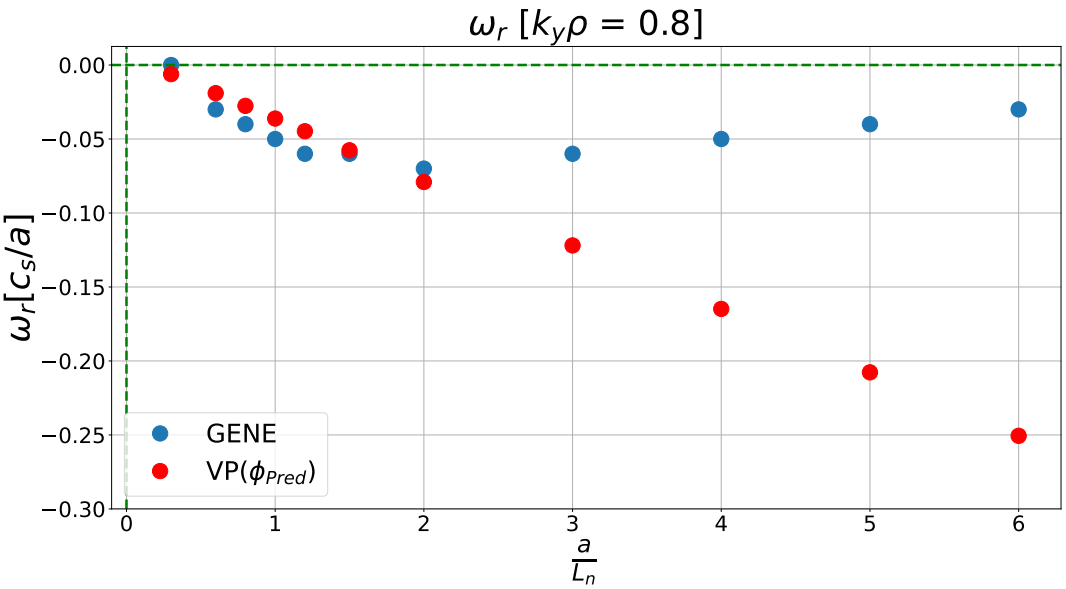

Figure 7.43: *Real mode frequency versus density gradient in the DIII-D tokamak. GENE simulation data in blue and variational principle proxy in red. Source: GENE data from [12]*

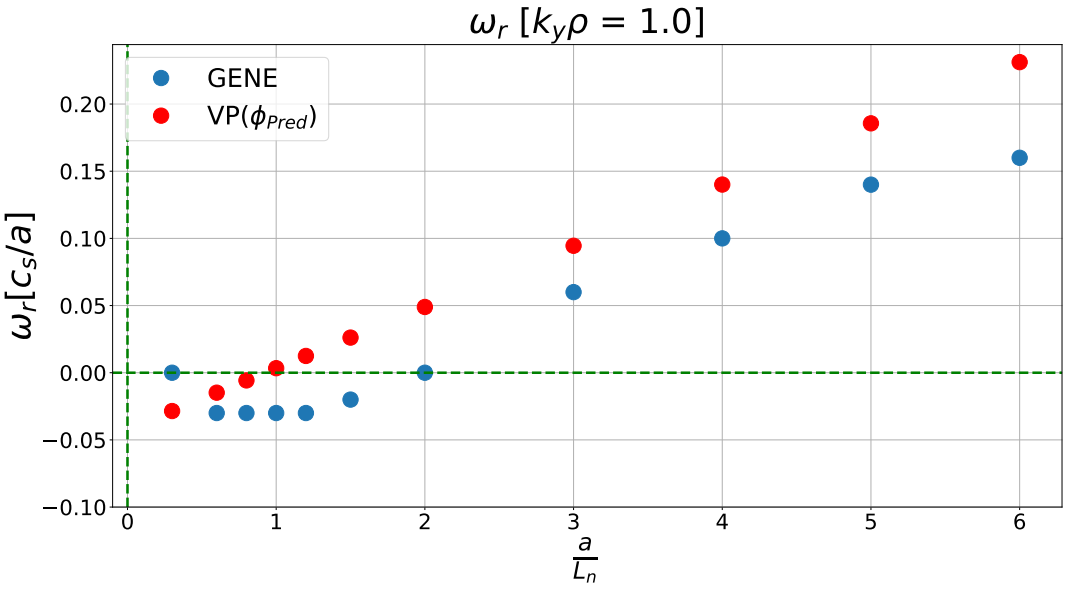

Figure 7.44: *Real mode frequency versus density gradient in the DIII-D tokamak. GENE simulation data in blue and variational principle proxy in red. Source: GENE data from [12]*

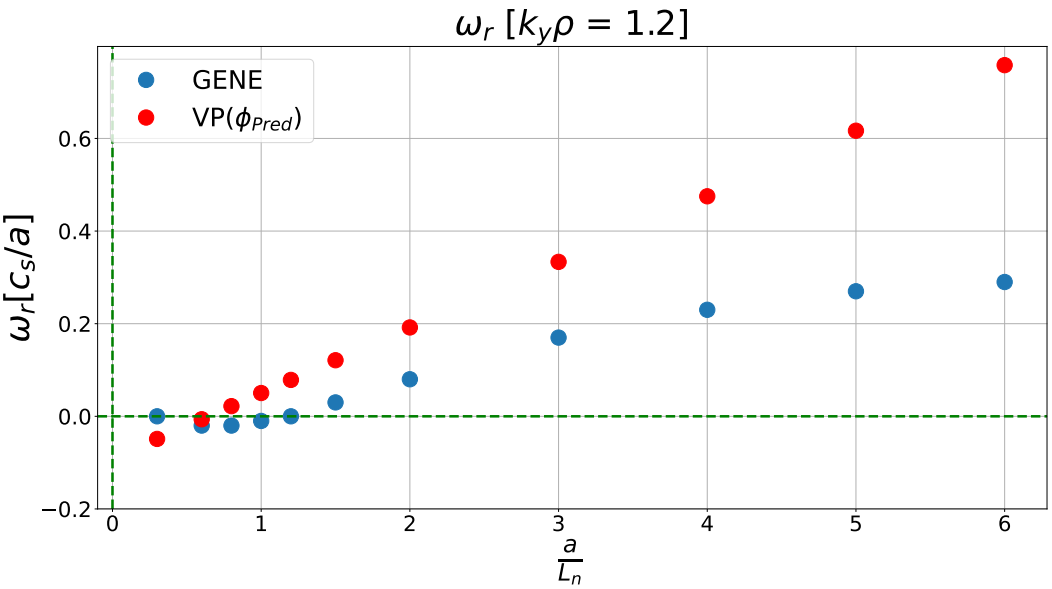

Figure 7.45: *Real mode frequency versus density gradient in the DIII-D tokamak. GENE simulation data in blue and variational principle proxy in red. Source: GENE data from [12]*

NCSX

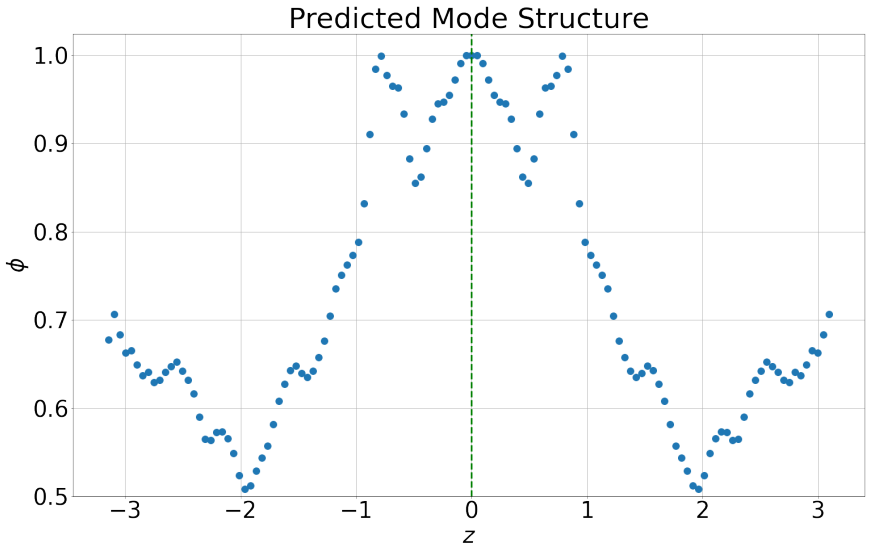

Figure 7.46: *The predicted mode structure profile $\phi_{(Pred)}$ along the magnetic field line for NCSX.*

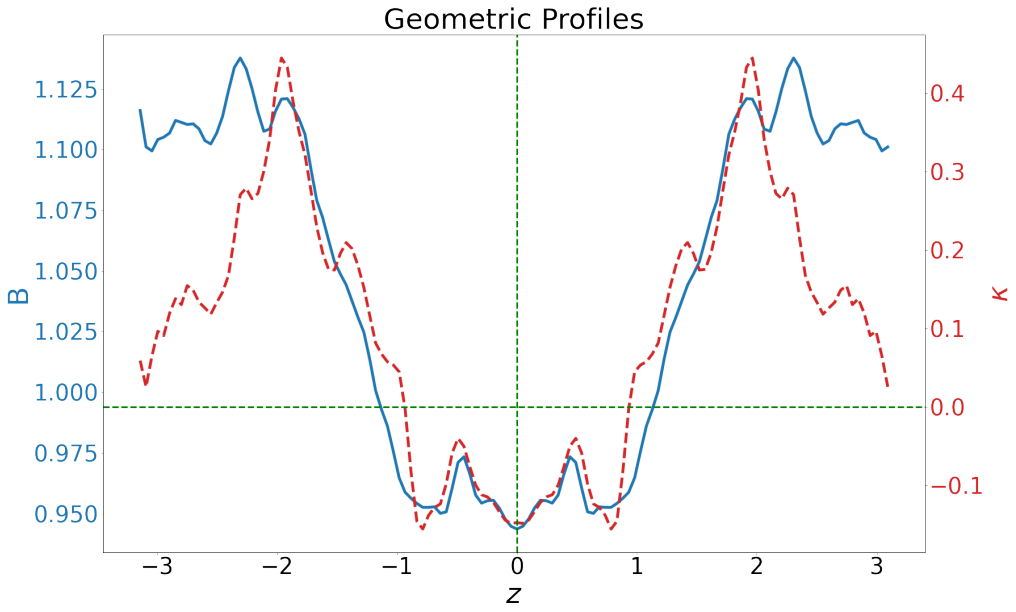

Figure 7.47: *Magnetic field strength B and curvature κ along the magnetic field line in NCSX. Source: GIST data from [12]*

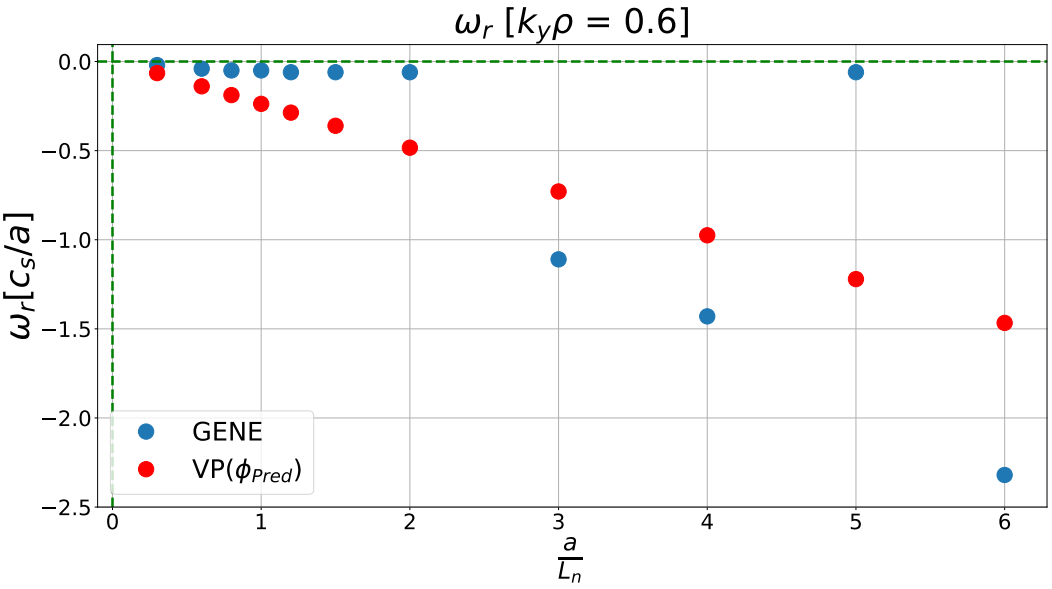

Figure 7.48: *Real mode frequency versus density gradient in the NCSX. GENE simulation data in blue and variational principle proxy in red. Source: GENE data from [12]*

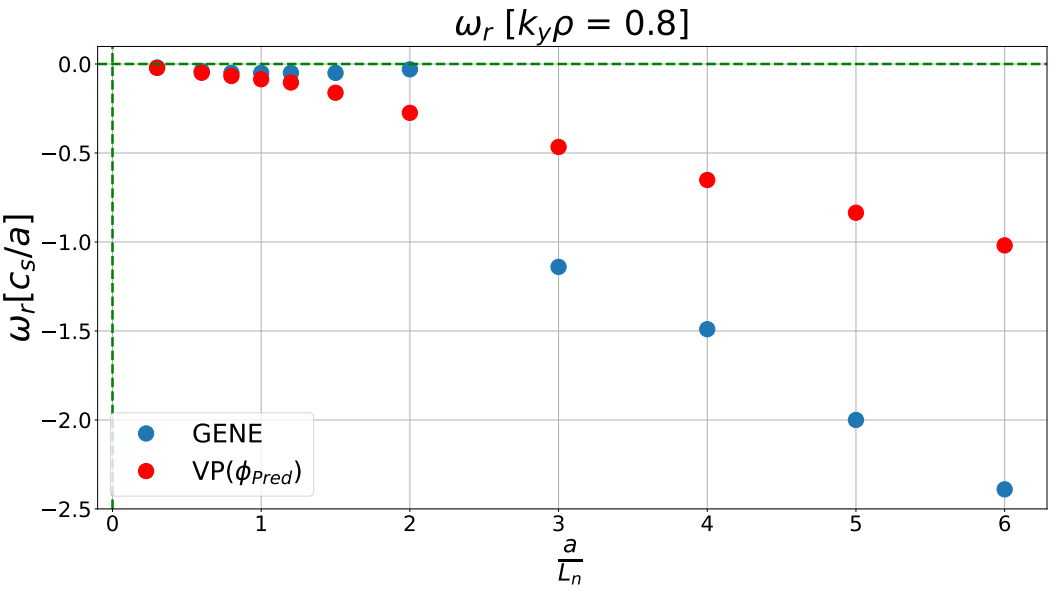

Figure 7.49: *Real mode frequency versus density gradient in the NCSX. GENE simulation data in blue and variational principle proxy in red. Source: GENE data from [12]*

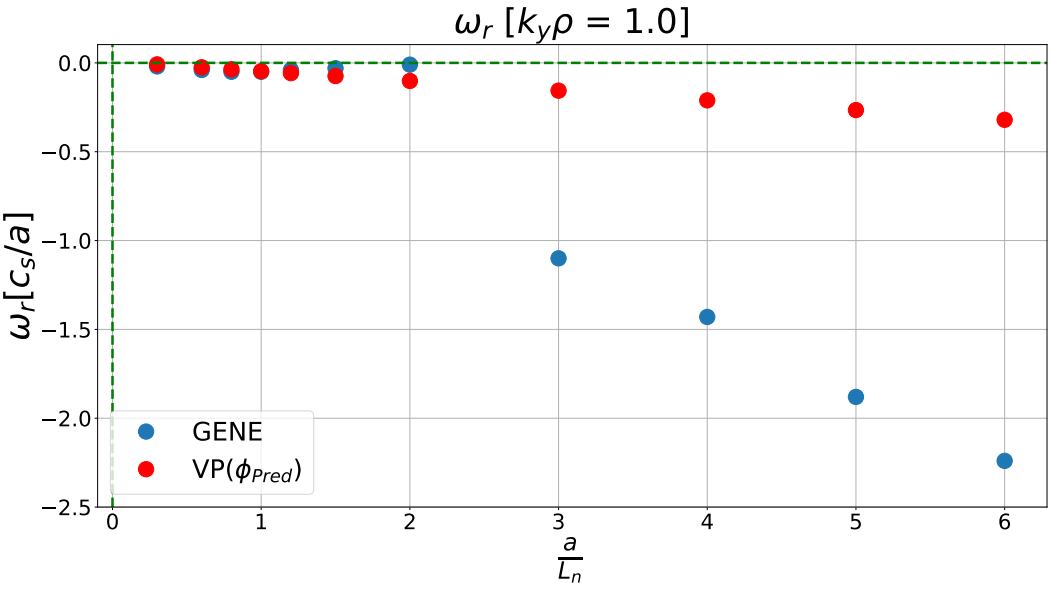

Figure 7.50: *Real mode frequency versus density gradient in the NCSX. GENE simulation data in blue and variational principle proxy in red. Source: GENE data from [12]*

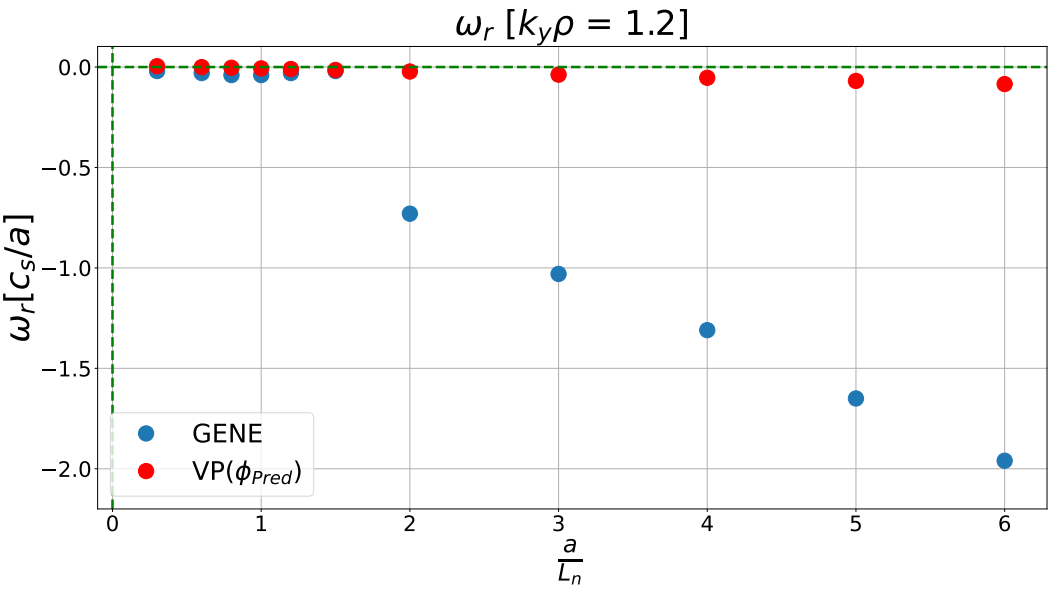

Figure 7.51: *Real mode frequency versus density gradient in the NCSX. GENE simulation data in blue and variational principle proxy in red. Source: GENE data from [12]*

W7-X (SC)

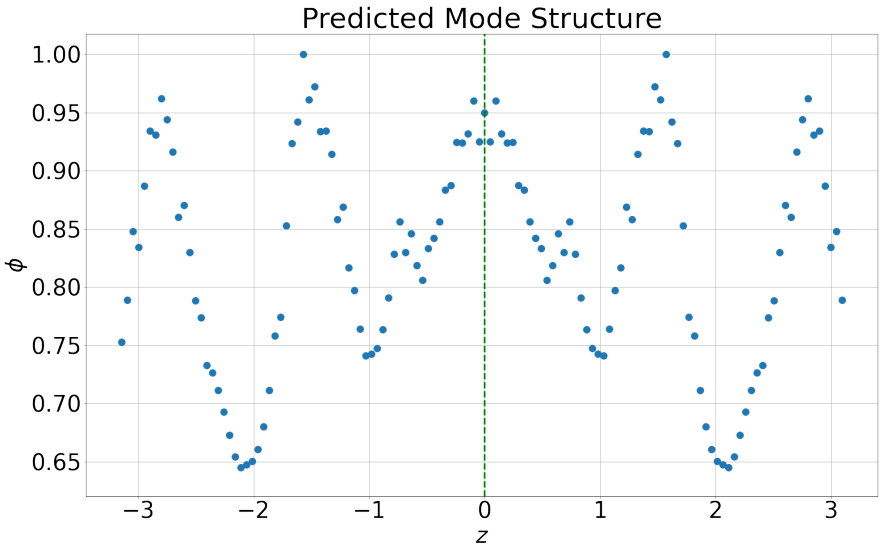

Figure 7.52: *The predicted mode structure profile $\phi_{(Pred)}$ along the magnetic field line for W7-X (SC).*

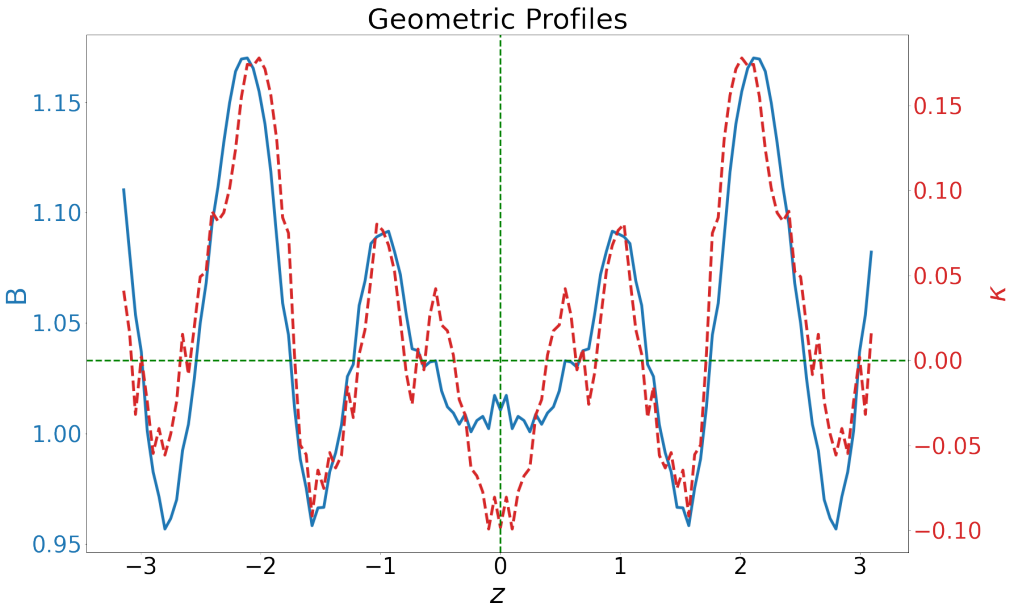

Figure 7.53: *Magnetic field strength B and curvature κ along the magnetic field line in W7-X (SC). Source: GIST data from [12]*

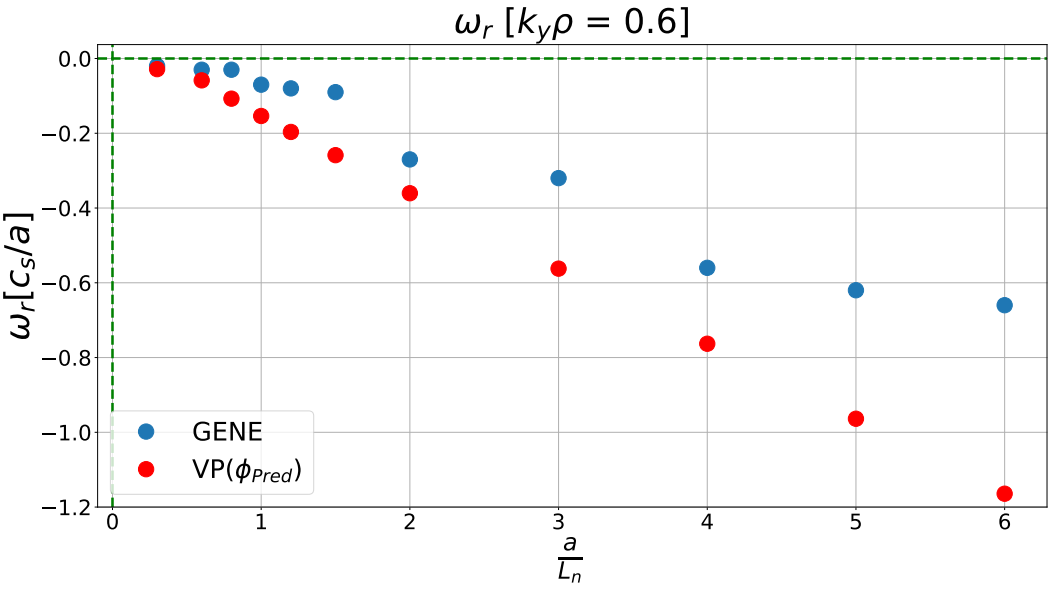

Figure 7.54: *Real mode frequency versus density gradient in the W7-X (SC). GENE simulation data in blue and variational principle proxy in red. Source: GENE data from [12]*

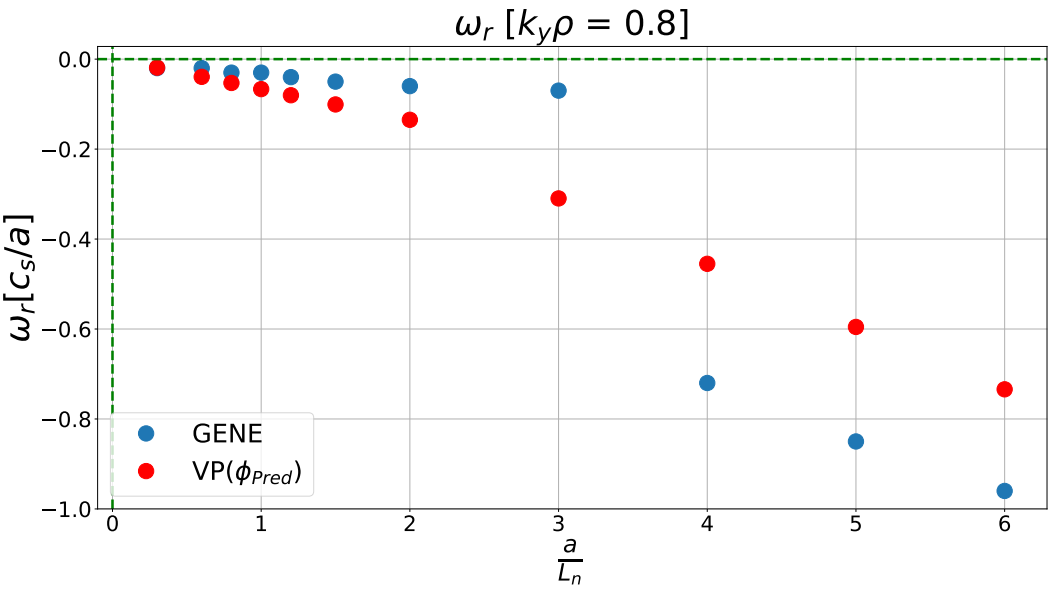

Figure 7.55: *Real mode frequency versus density gradient in the W7-X (SC). GENE simulation data in blue and variational principle proxy in red. Source: GENE data from [12]*

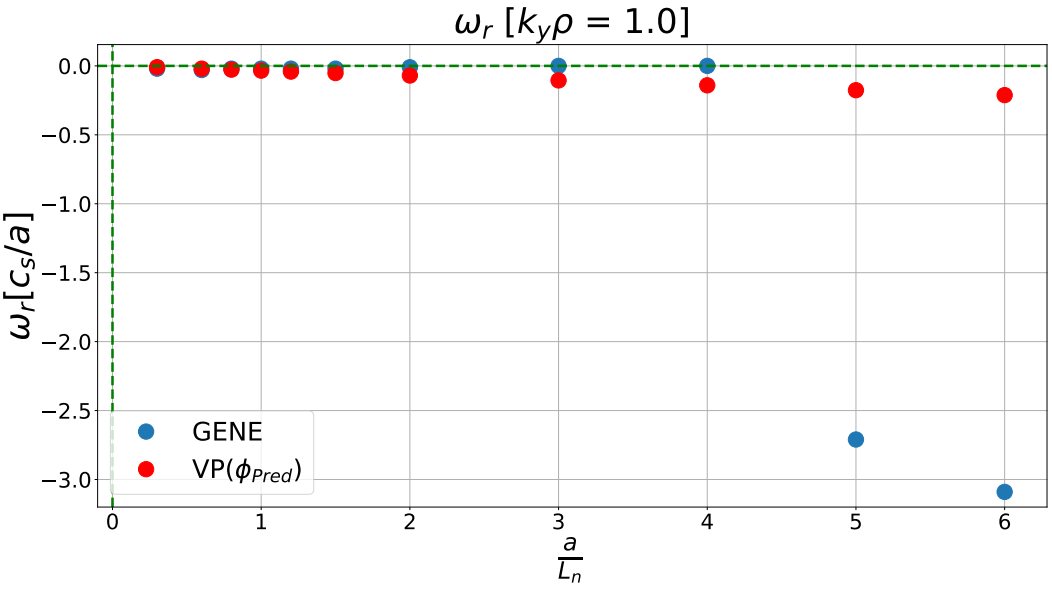

Figure 7.56: *Real mode frequency versus density gradient in the W7-X (SC). GENE simulation data in blue and variational principle proxy in red. Source: GENE data from [12]*

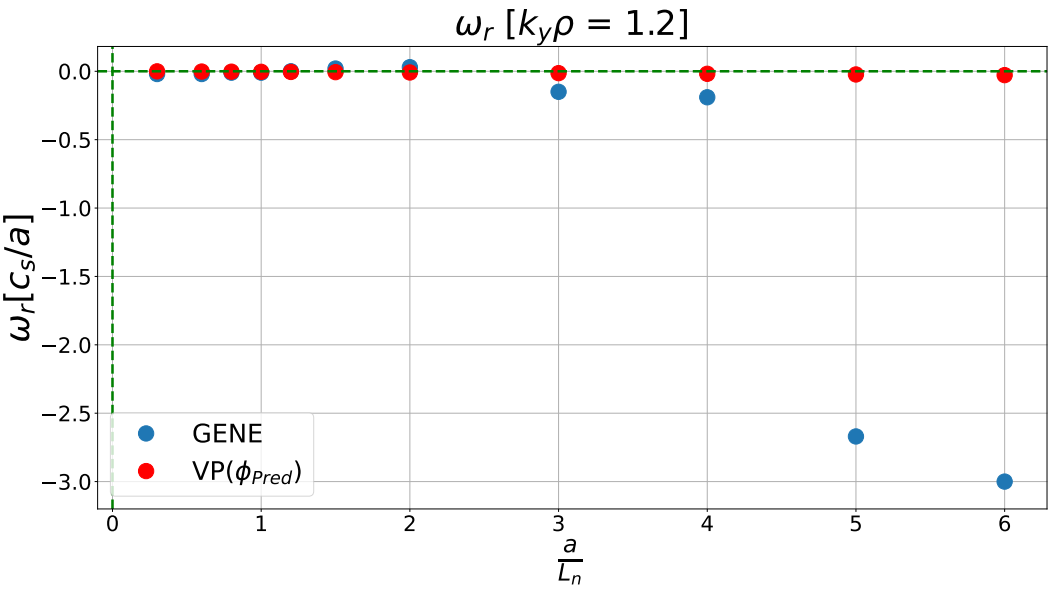

Figure 7.57: *Real mode frequency versus density gradient in the W7-X (SC). GENE simulation data in blue and variational principle proxy in red. Source: GENE data from [12]*

W7-X (HM)

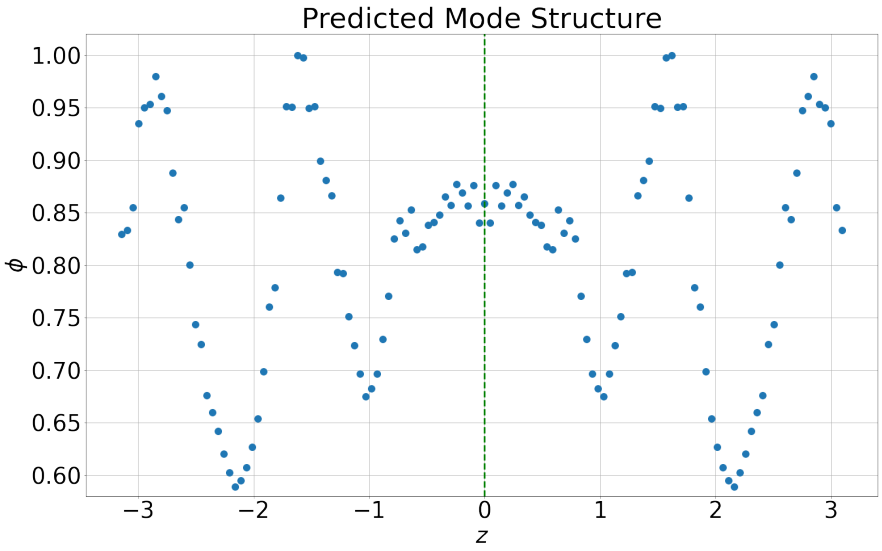

Figure 7.58: *The predicted mode structure profile $\phi_{(Pred)}$ along the magnetic field line for W7-X (HM).*

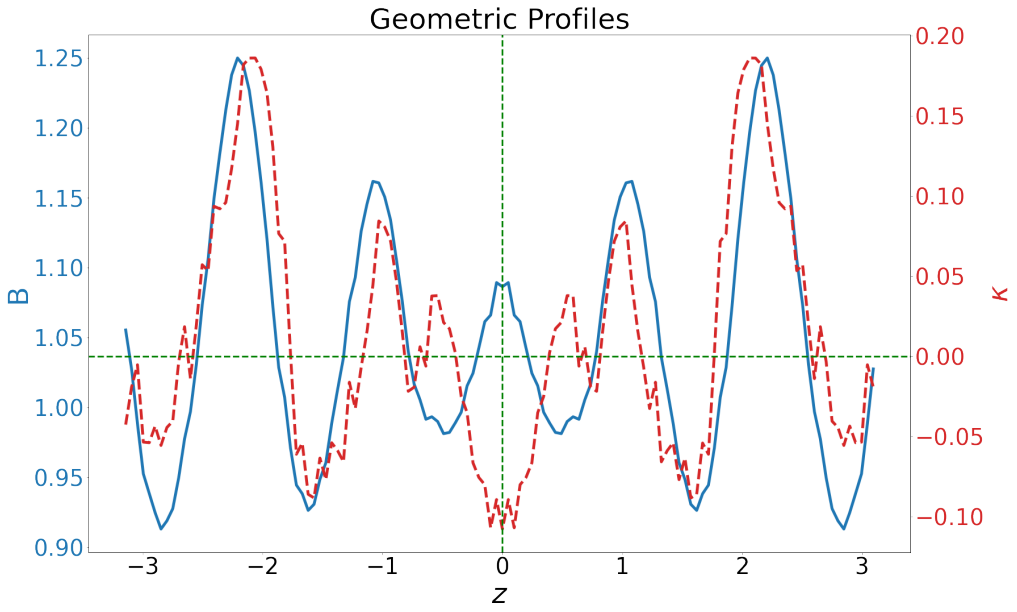

Figure 7.59: *Magnetic field strength B and curvature κ along the magnetic field line in W7-X (HM). Source: GIST data from [12]*

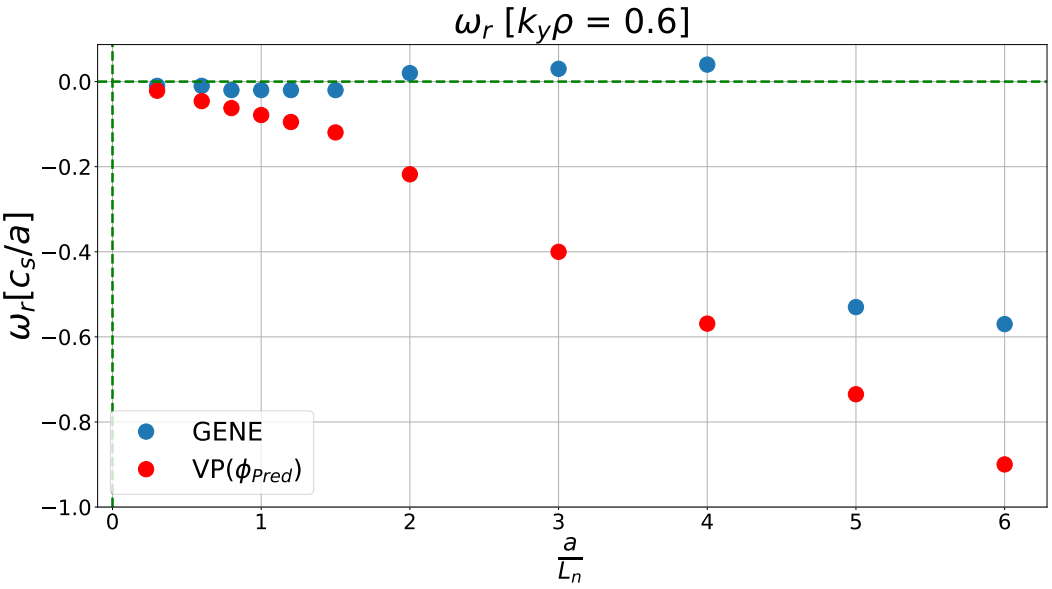

Figure 7.60: *Real mode frequency versus density gradient in the W7-X (HM). GENE simulation data in blue and variational principle proxy in red. Source: GENE data from [12]*

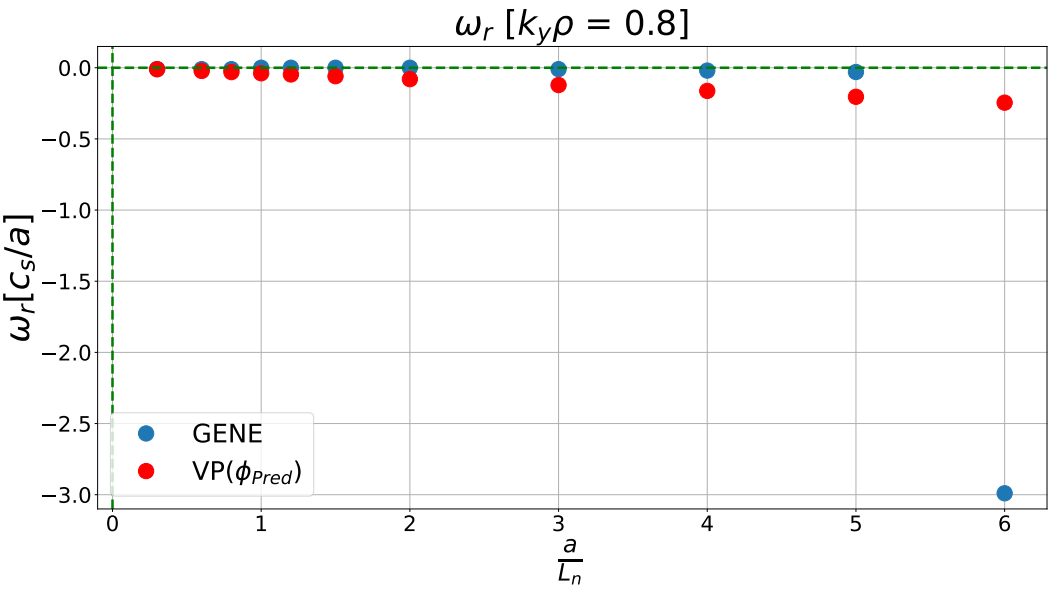

Figure 7.61: *Real mode frequency versus density gradient in the W7-X (HM). GENE simulation data in blue and variational principle proxy in red. Source: GENE data from [12]*

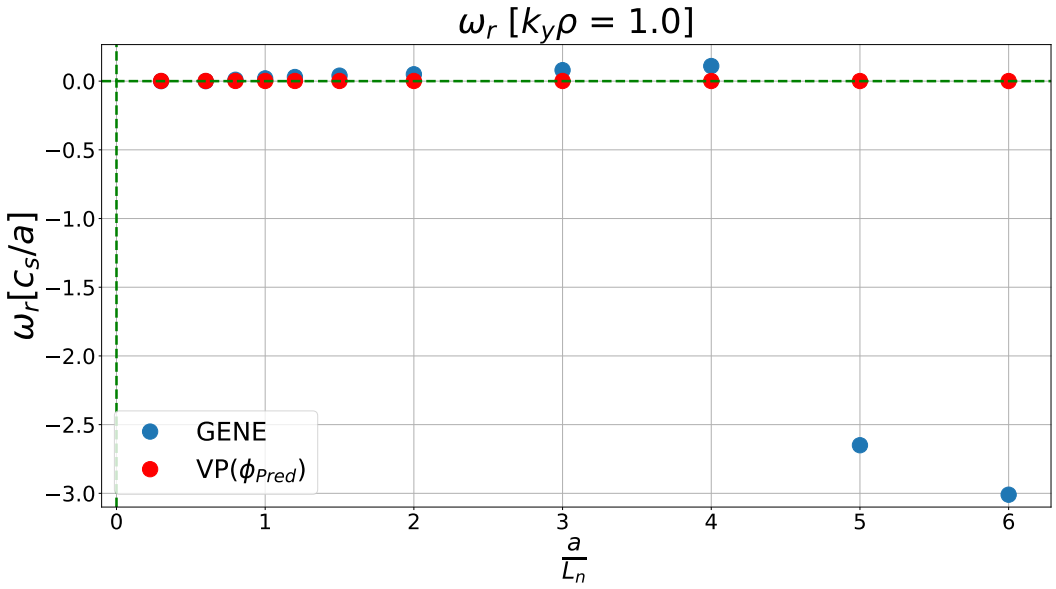

Figure 7.62: *Real mode frequency versus density gradient in the W7-X (HM). GENE simulation data in blue and variational principle proxy in red. Source: GENE data from [12]*

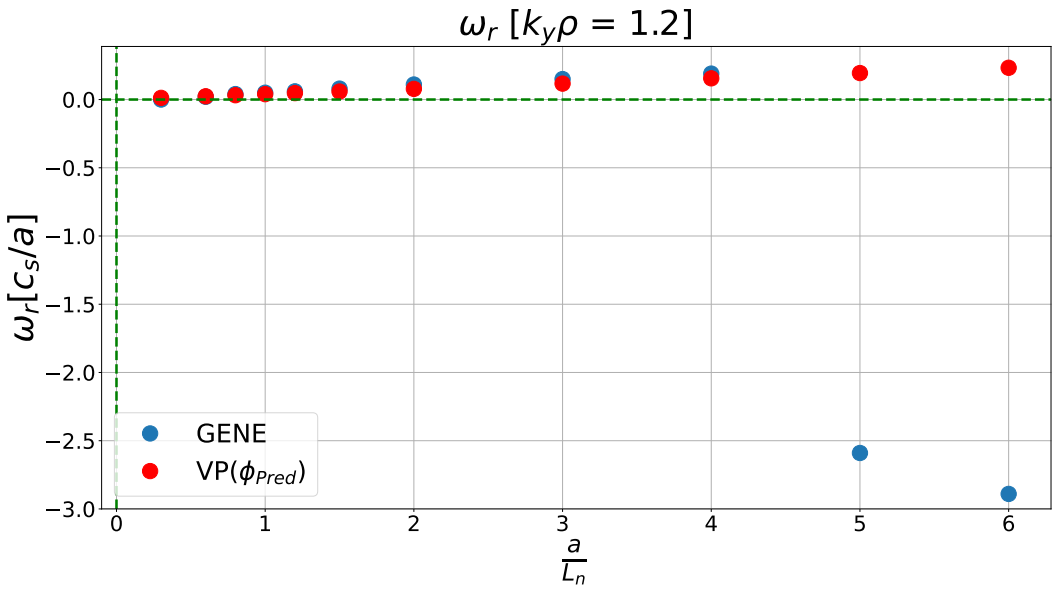

Figure 7.63: *Real mode frequency versus density gradient in the W7-X (HM). GENE simulation data in blue and variational principle proxy in red. Source: GENE data from [12]*

W7-X (LM)

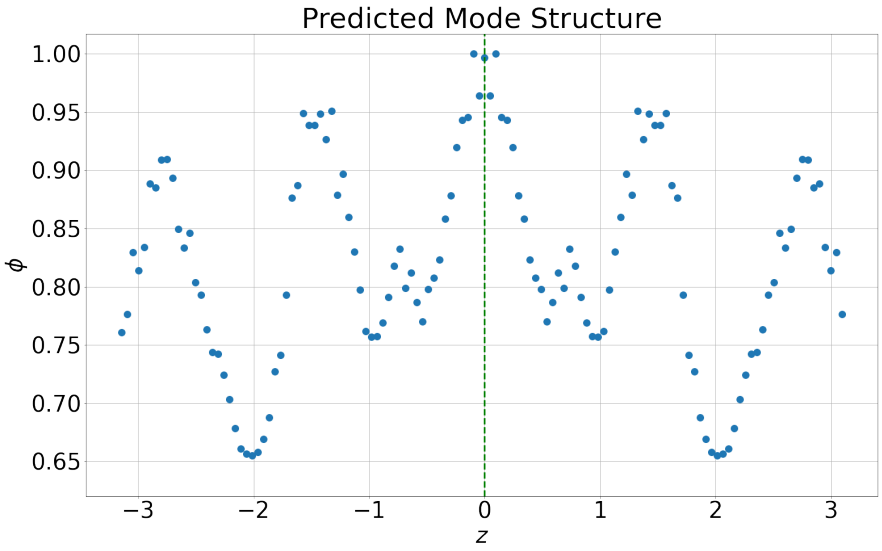

Figure 7.64: *The predicted mode structure profile $\phi_{(Pred)}$ along the magnetic field line for W7-X (LM).*

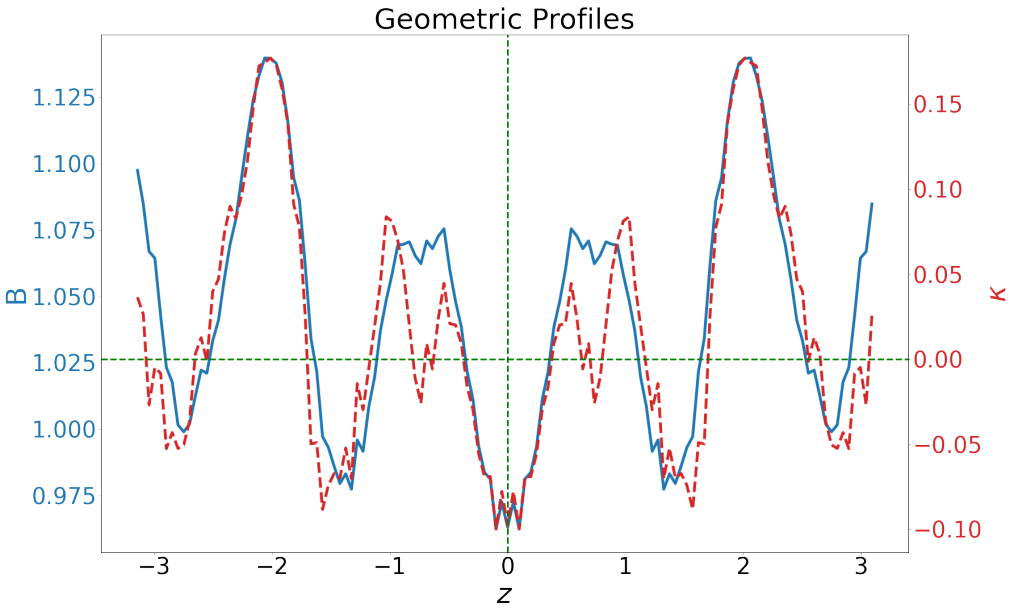

Figure 7.65: *Magnetic field strength B and curvature κ along the magnetic field line in W7-X (LM). Source: GIST data from [12]*

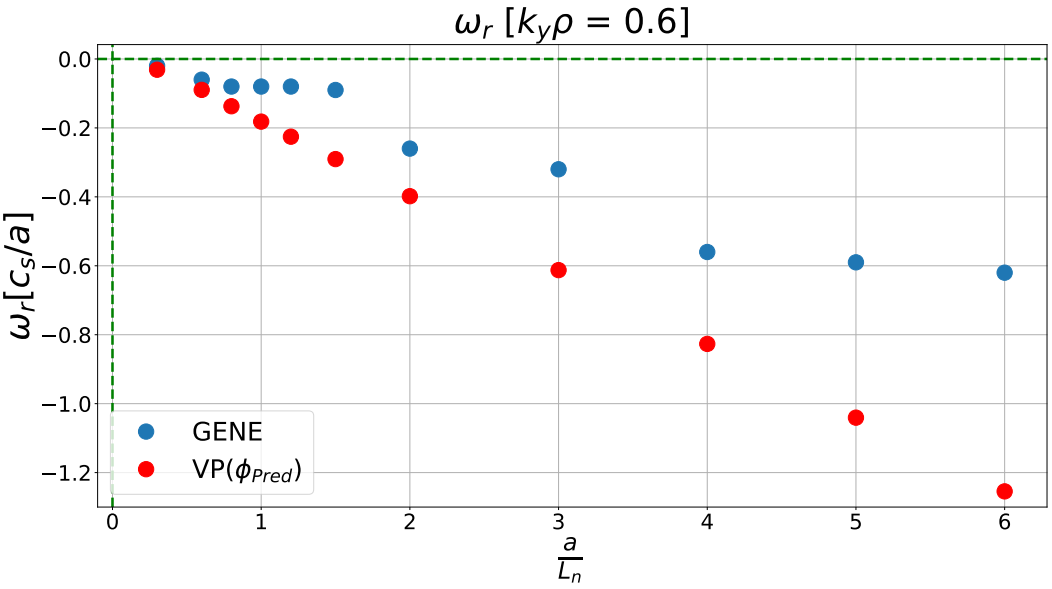

Figure 7.66: *Real mode frequency versus density gradient in the W7-X (LM). GENE simulation data in blue and variational principle proxy in red. Source: GENE data from [12]*

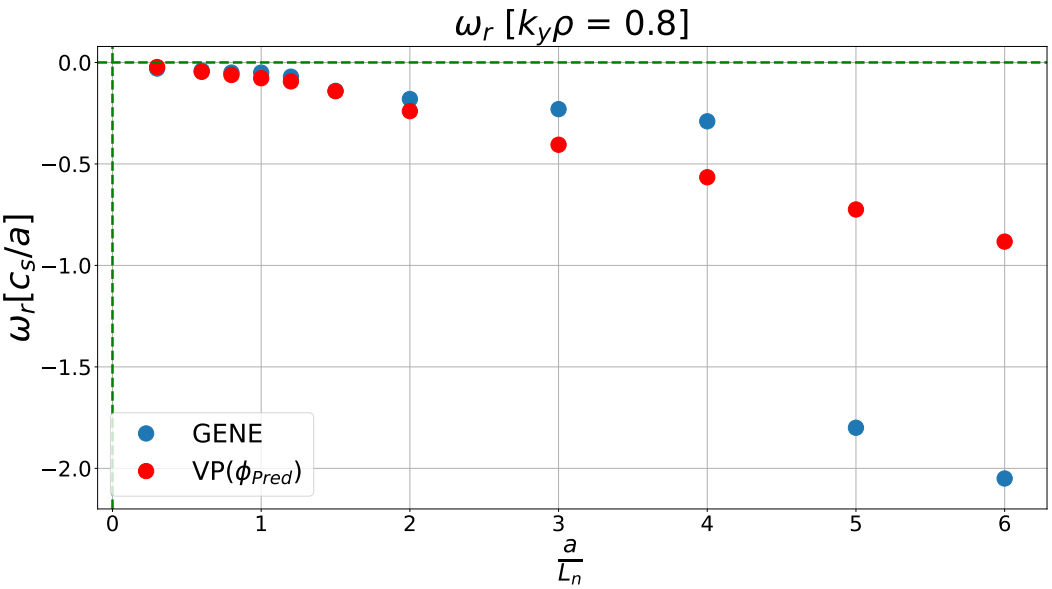

Figure 7.67: *Real mode frequency versus density gradient in the W7-X (LM). GENE simulation data in blue and variational principle proxy in red. Source: GENE data from [12]*

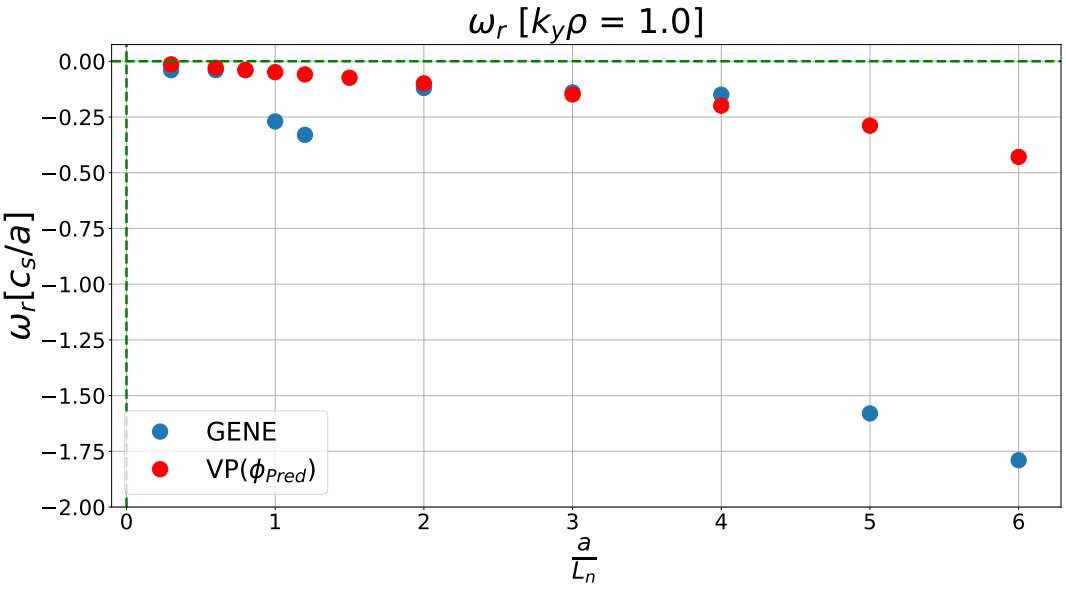

Figure 7.68: *Real mode frequency versus density gradient in the W7-X (LM). GENE simulation data in blue and variational principle proxy in red. Source: GENE data from [12]*

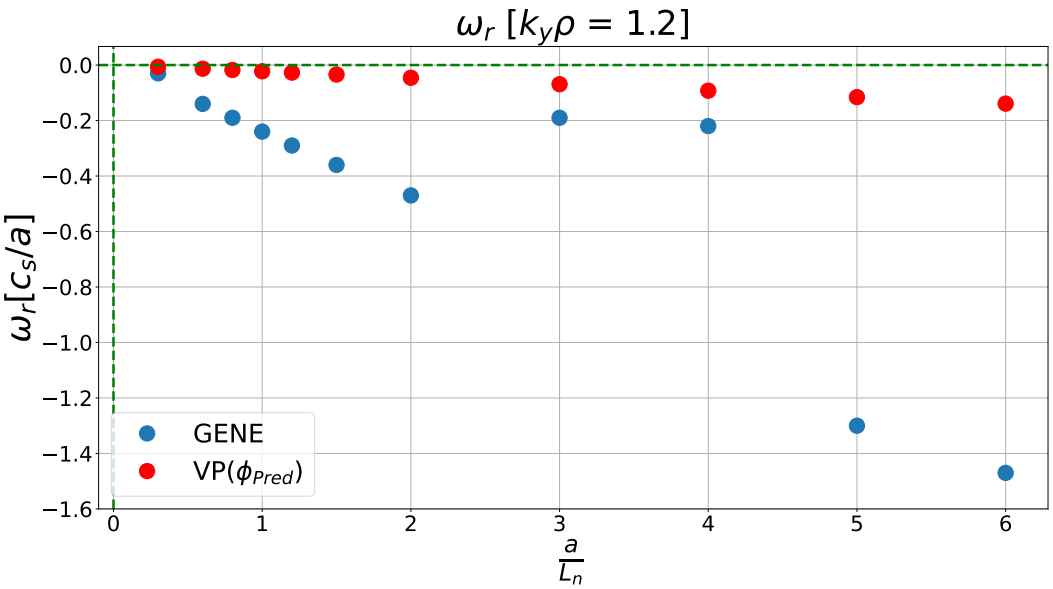

Figure 7.69: *Real mode frequency versus density gradient in the W7-X (LM). GENE simulation data in blue and variational principle proxy in red. Source: GENE data from [12]*

HSX

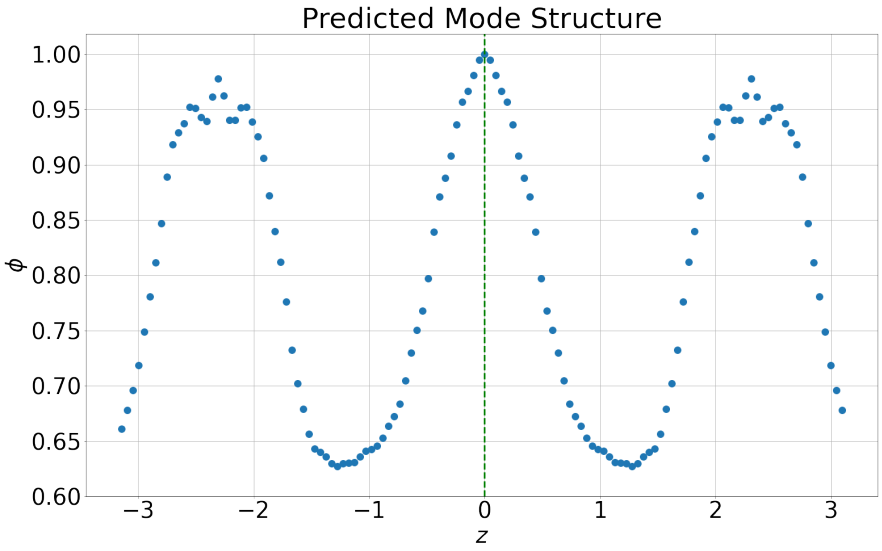

Figure 7.70: *The predicted mode structure profile $\phi_{(Pred)}$ along the magnetic field line for HSX.*

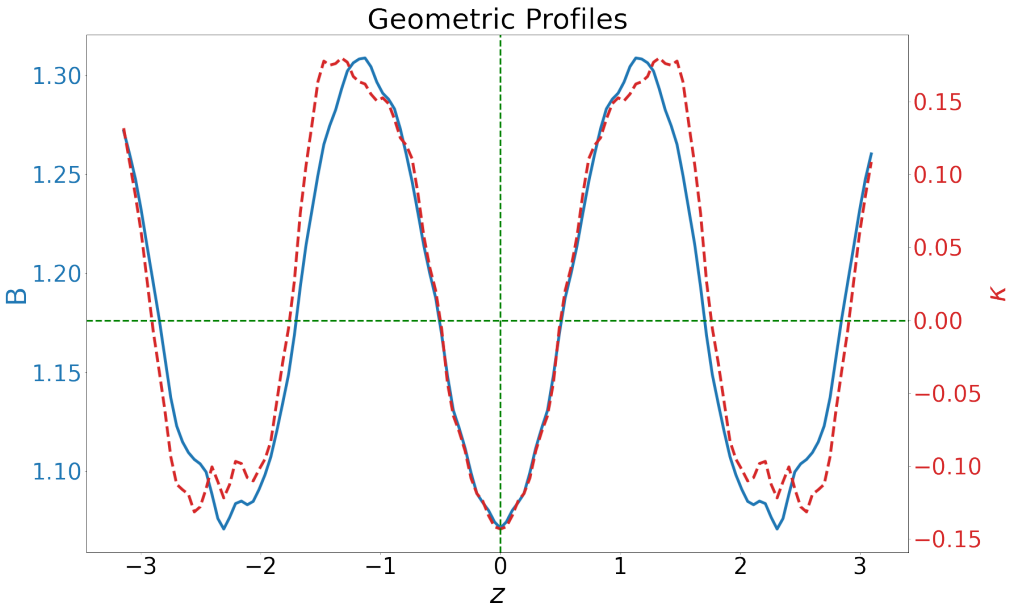

Figure 7.71: *Magnetic field strength B and curvature κ along the magnetic field line in HSX. Source: GIST data from [12]*

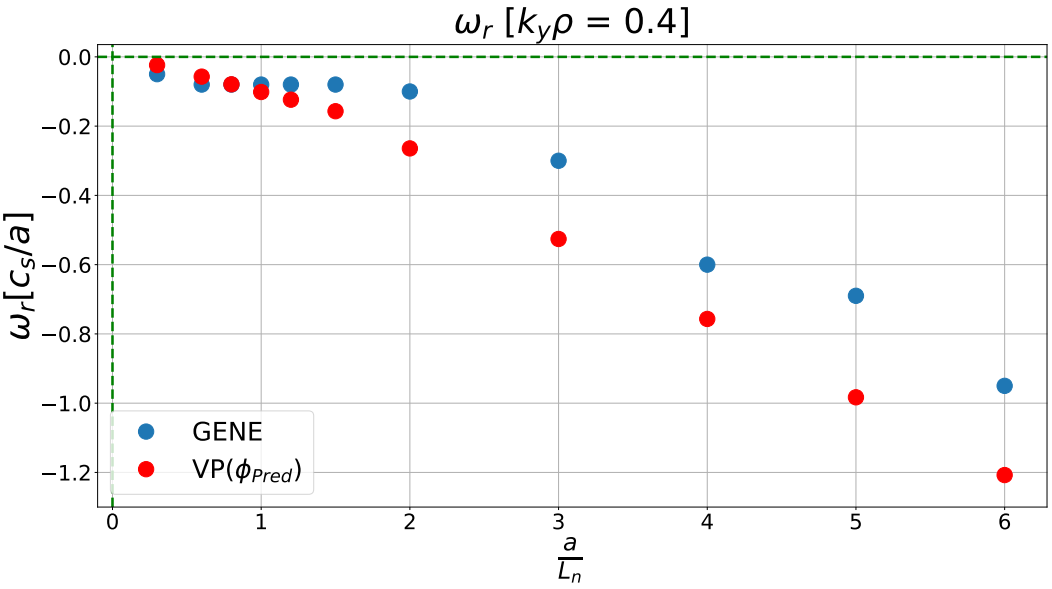

Figure 7.72: *Real mode frequency versus density gradient in the HSX. GENE simulation data in blue and variational principle proxy in red. Source: GENE data from [12]*

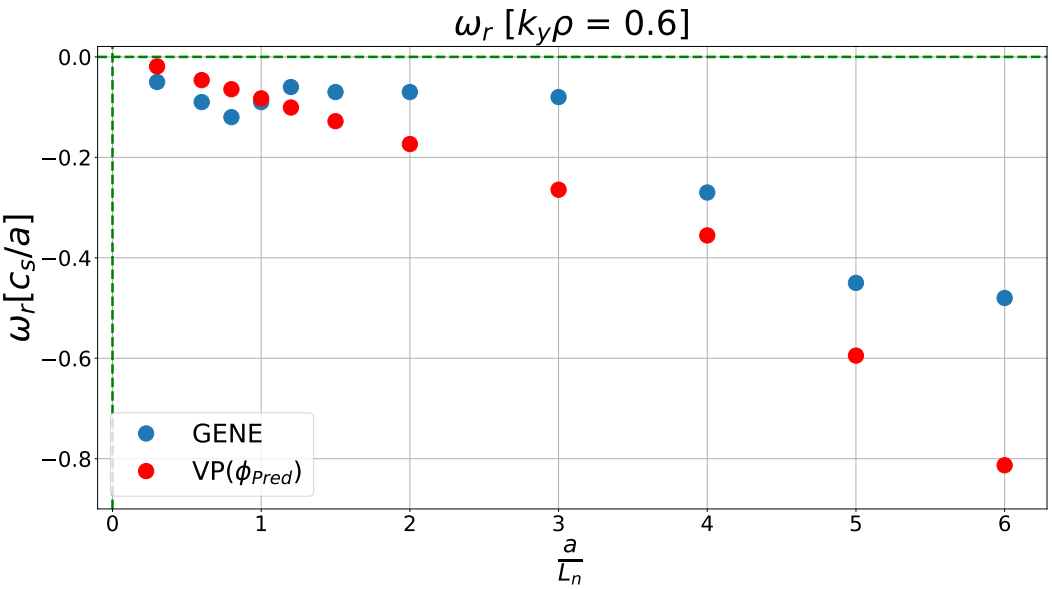

Figure 7.73: *Real mode frequency versus density gradient in the HSX. GENE simulation data in blue and variational principle proxy in red. Source: GENE data from [12]*

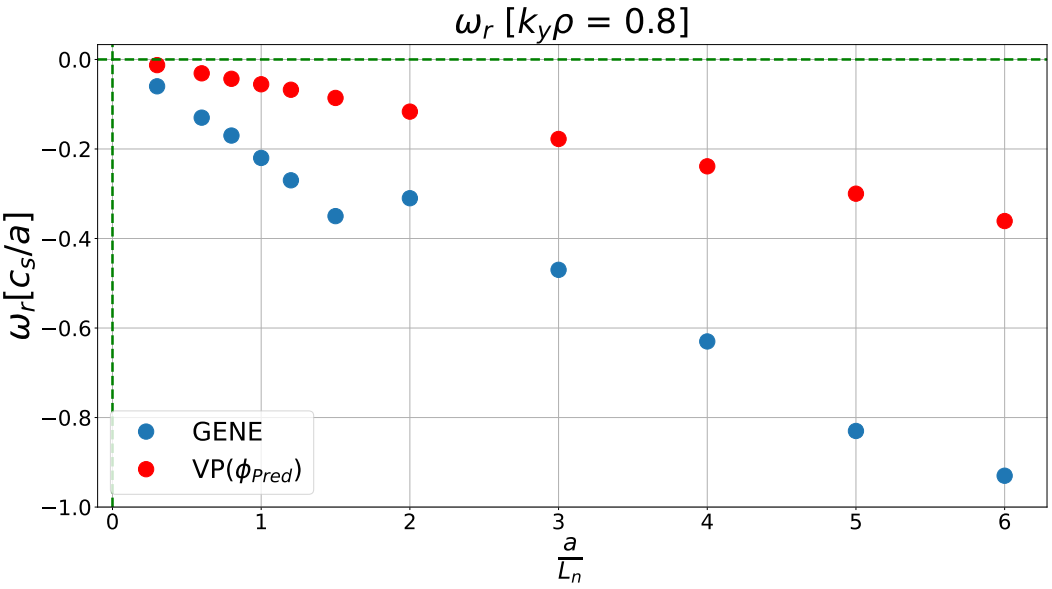

Figure 7.74: *Real mode frequency versus density gradient in the HSX. GENE simulation data in blue and variational principle proxy in red. Source: GENE data from [12]*

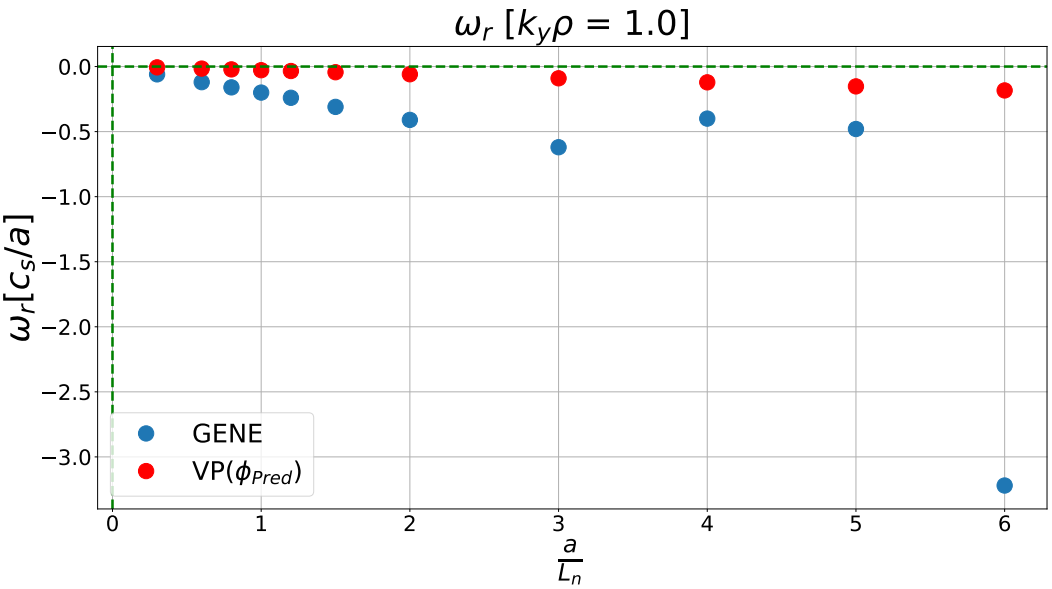

Figure 7.75: *Real mode frequency versus density gradient in the HSX. GENE simulation data in blue and variational principle proxy in red. Source: GENE data from [12]*

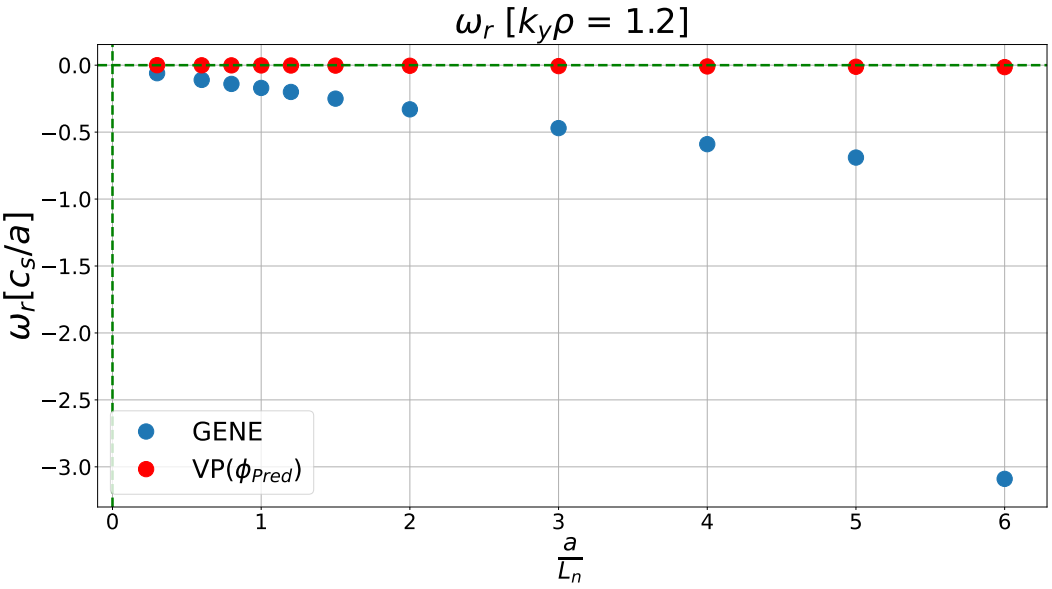

Figure 7.76: *Real mode frequency versus density gradient in the HSX. GENE simulation data in blue and variational principle proxy in red. Source: GENE data from [12]*

Discussion

We now discuss these results, which once again arose from utilising a variational principle technique to approximate the real mode frequency ω_r of the TEM. As before, the trial function input for the variational principle technique is the mode structure ϕ. In this case, however, this input took the form of a single predicted ϕ profile, which depended on the geometric information of the configuration at hand (magnetic field strength B and curvature κ). This approach no longer relies on any simulation data from GENE, and so one expects a weaker agreement between the proxy prediction and the GENE output for the real mode frequency. Nonetheless, our method for predicting the mode structure was extremely simple, and serves only to prove the principle of the procedure, which has much room for improvement. With this in mind, we first briefly discuss the results shown in this section, followed by suggesting some means to improving our prediction procedure, which may be implemented in future work.

Our mode frequency results here, which relied upon the accuracy of our ϕ prediction, predictably showed a weaker agreement with GENE output in comparison to our previous set of results which utilised ϕ-data from GENE. In most configurations, there appears to be stronger agreement between our proxy and GENE simulation for lower density gradient values, and increasingly weaker agreement as the density gradient increases. This can be explained by the ϕ prediction used in the proxy. When comparing our ϕ prediction with the ϕ-data profiles from GENE (which are not included in this report), it was found that the best agreement occurred when considering the lowest density gradient values. The mode structure profiles from GENE change as $\frac{a}{L_n}$ increases, and this may be due to the presence of subdominant modes at these higher gradients. Our ϕ prediction is solely dependent on the geometry of the configuration, so this behaviour is not captured when $\frac{a}{L_n}$ increases. This inevitably degrades the reliability of the mode frequency proxy in these higher regions of parameter space. Thus, the overall trend of ω_r is captured quite well by the proxy for low $\frac{a}{L_n}$ values, but sudden drops and jumps in the GENE data are not tracked by the proxy. As mentioned in the previous section, these sharp drops in the GENE data may indicate the transition to a new TEM [56]. Sudden changes in the simulation data such as these are expected to be replicated by the proxy if the ϕ prediction is improved. We can be confident of this as we have already seen that this variational procedure has the capability to mirror such sudden changes when the idealised trial function is used, i.e., inserting GENE data for ϕ directly.

We can now propose some potential improvements to be made to our mode structure prediction technique. Firstly, more care could be taken when combining the magnetic field and curvature profiles, which are the only inputs used to generate our prediction. This could take the form of giving each quantity a certain weight corresponding to their level of influence on the mode. In our approach here, we brutally added these quantities together without giving much consideration for how significantly each one influences the mode on its own. It might be worth experimenting with this linear combination by giving each geometric quantity a weighted coefficient, which can

be varied to find the optimal value. This may look as follows:

$$c_1 B + c_2 \kappa \tag{7.3}$$

where c_1 and c_2 are the adjustable weighted coefficients.
Secondly, we know that the mode structure varies with wavenumber and density gradient, and not only with the geometric information (B and κ). Thus, realistically, there ought to be a distinct ϕ profile for each pairing $\left(k_y\rho, \frac{a}{L_n}\right)$, for every geometric configuration considered. However, in our procedure, we only use a first approximation for the ϕ profile prediction, and assume it is not dependent on these plasma quantities. Our current prediction for ϕ can be thought of as follows:

$$\phi_{(Pred)} = \phi(B, \kappa) \tag{7.4}$$

Therefore, an immediate improvement to be made to this procedure in future work would be to find a prediction for the mode structure that functions as follows:

$$\phi_{(Pred)} = \phi\left(B, \kappa, k_y\rho, \frac{a}{L_n}\right) \tag{7.5}$$

In the end, despite our very rough method here, our results exhibit a clear proof of principle for this technique. Our work indicates that with sufficient knowledge of the mode structure's dependence on geometric and plasma quantities, one can approximately predict the ϕ profile to a reliable level.

7.2 Proxy for the Critical Density Gradient

In this section, we first present the values of the critical density gradient for the TEM - as obtained from GENE data - in the various geometrical configurations considered. This provides our benchmark, to which we compare the results of our proxy procedures in order to determine their performance. Following this, we then look at the results of two separate approaches to developing a proxy for the critical density gradient. We first consider our original approach, pertaining to the analytical work carried out in section 6.1. We then consider a simpler alternative approach, pertaining to the analytical work from section 6.2. Each set of results will be followed by a discussion of their interpretation.

7.2.1 Critical Density Gradient from GENE Growth Rate

Here, we look at how to calculate the critical density gradient values from GENE data for each geometrical configuration. We achieve this by looking at the growth rate γ for each configuration and wavenumber, and seeing where it approximately equals zero. Our procedure involves

analysing GENE output data for γ and fitting a polynomial to this data in order to find the root ($\gamma = 0$). The $\frac{a}{L_n}$ value found where $\gamma = 0$ should then correspond to the critical density gradient. The results of this section are displayed in Table 7.1.

It is worth noting that these values have been obtained using a limited amount of data, and the polynomial fitting procedure is done by hand. The degree of this polynomial fit is manually adjusted until the best possible match is found by eye. Therefore, this method is only able to *approximate* the trend of the given data set. It is from this approximate polynomial that a root was found, which gives us our supposed critical density gradient values. Therefore, we are more concerned with the approximate *neighbourhood* of values obtained from GENE, and not the precise values shown.

DIII-D Tokamak

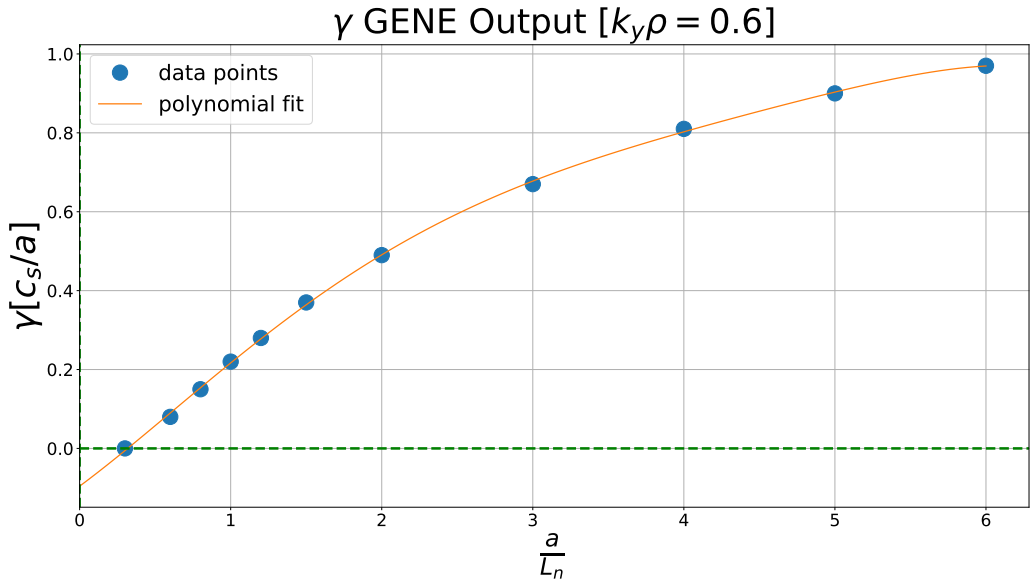

Figure 7.77: *Growth rate γ in the DIII-D tokamak.*

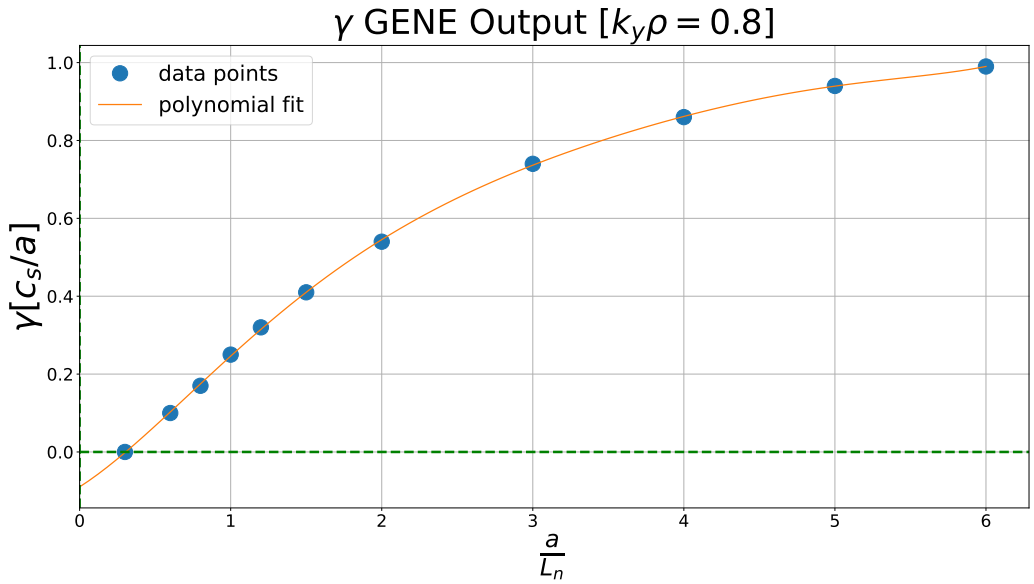

Figure 7.78: *Growth rate γ in the DIII-D tokamak.*

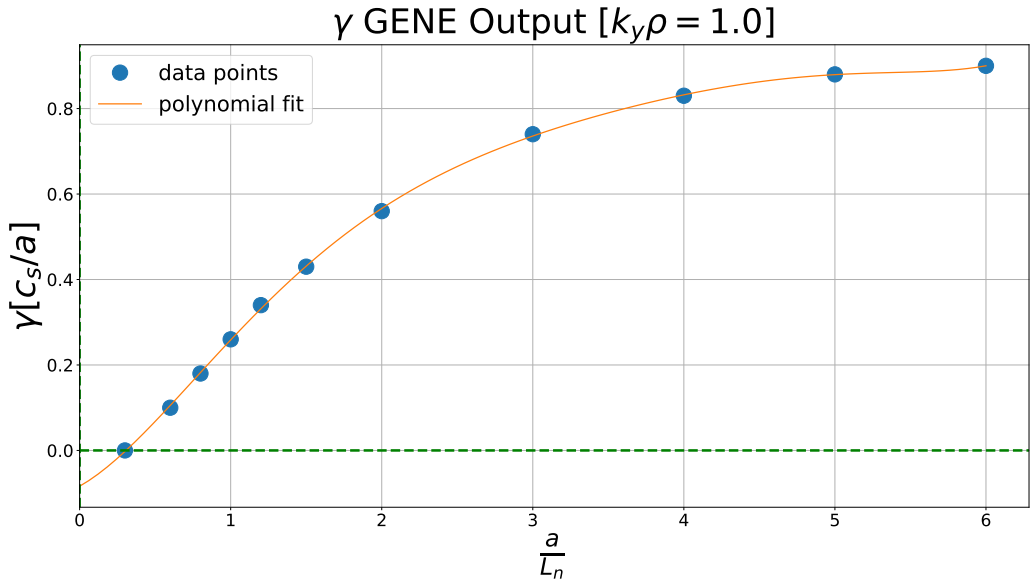

Figure 7.79: *Growth rate γ in the DIII-D tokamak.*

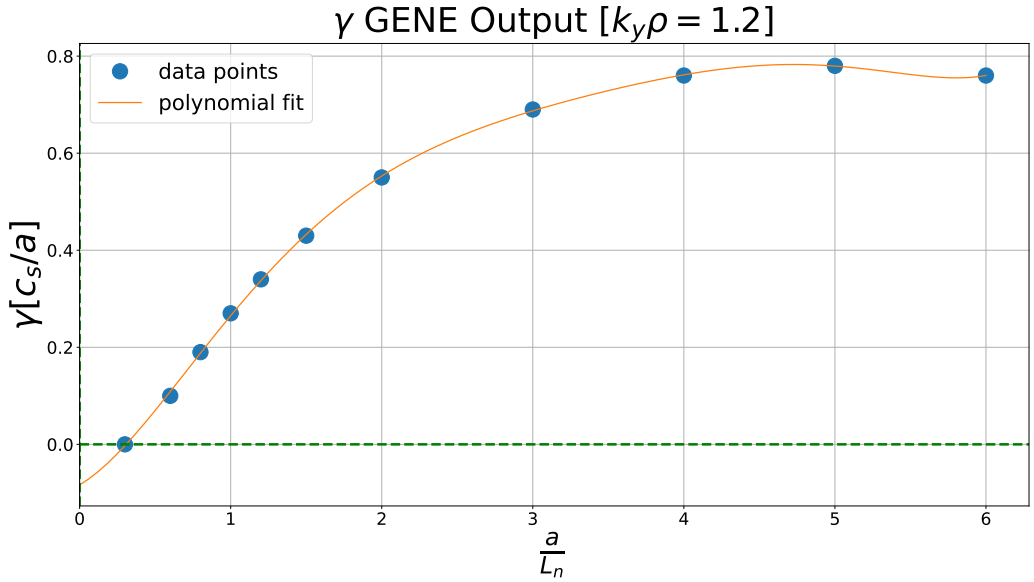

Figure 7.80: *Growth rate γ in the DIII-D tokamak.*

NCSX

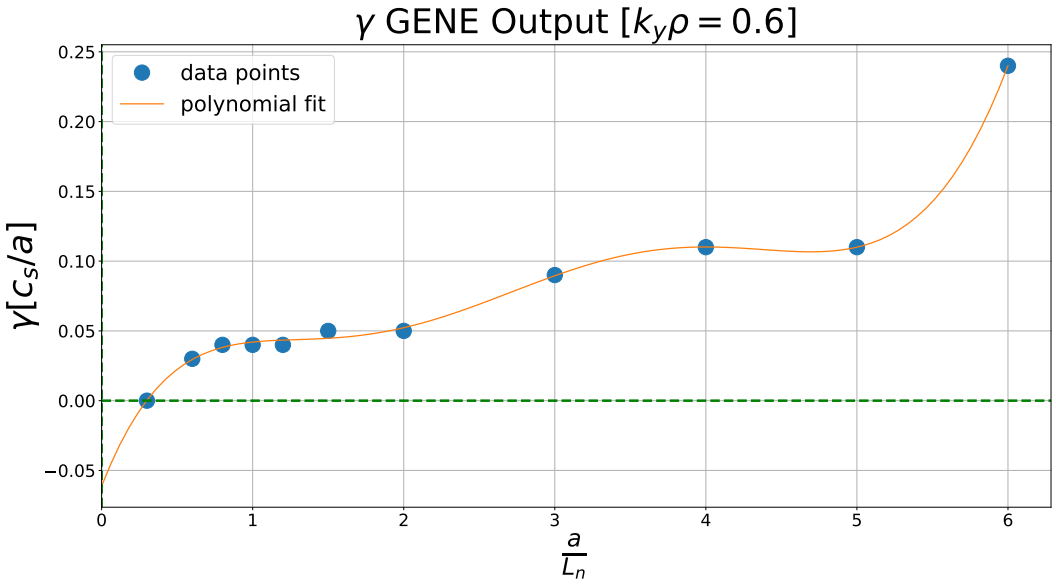

Figure 7.81: *Growth rate γ in NCSX.*

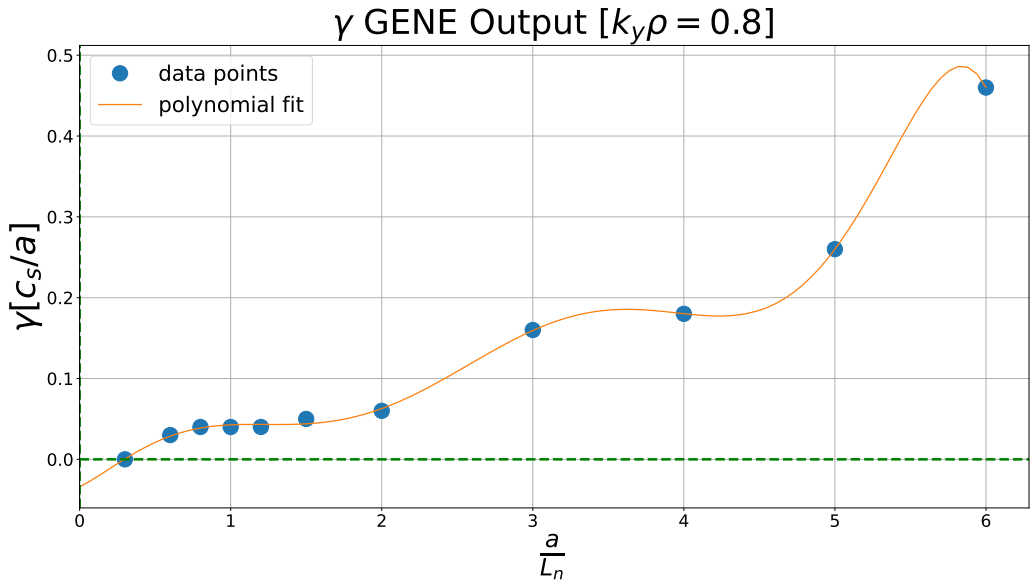

Figure 7.82: *Growth rate γ in NCSX.*

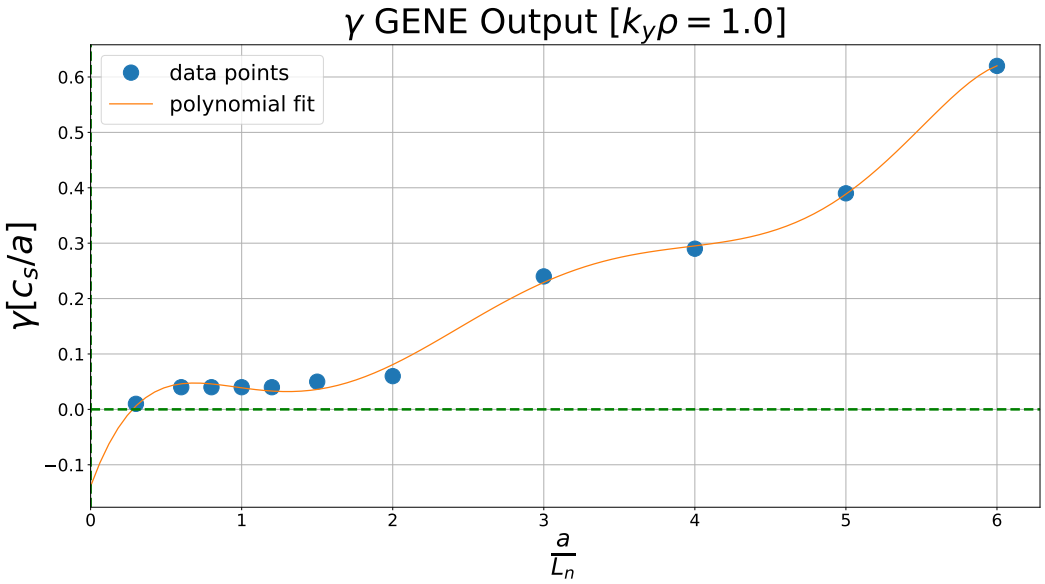

Figure 7.83: *Growth rate γ in NCSX.*

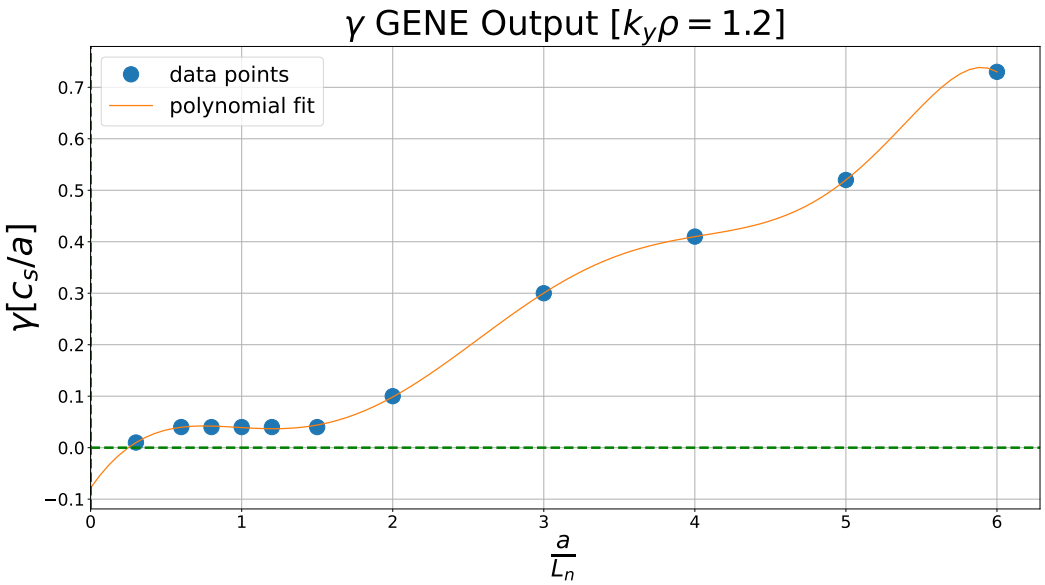

Figure 7.84: *Growth rate γ in NCSX.*

W7-X (SC)

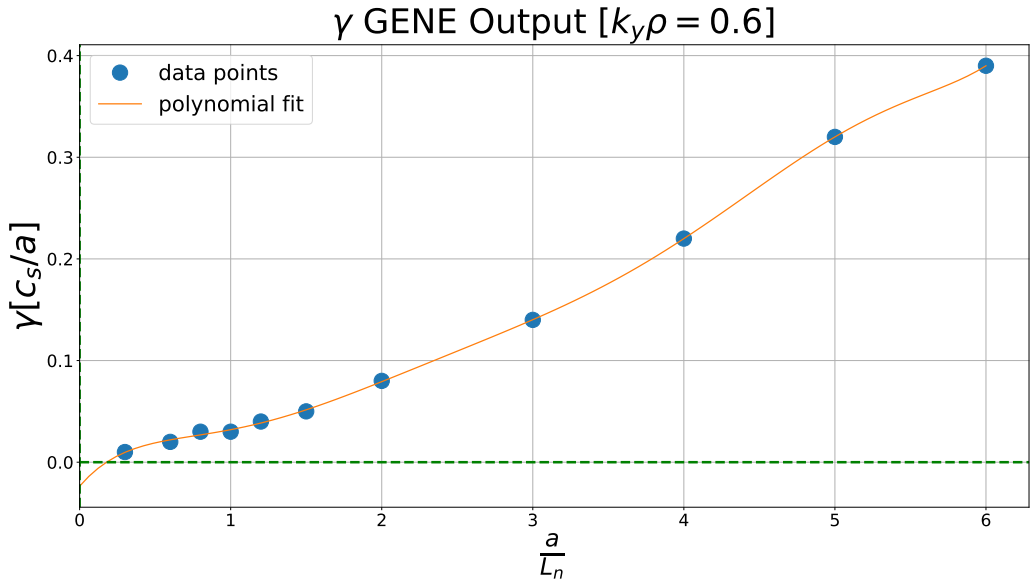

Figure 7.85: *Growth rate γ in W7-X (SC).*

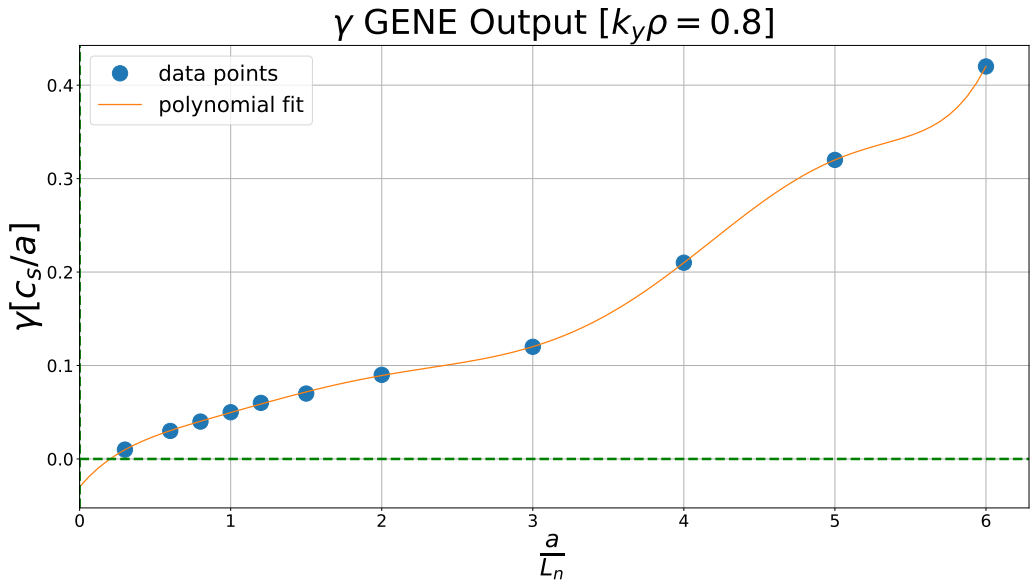

Figure 7.86: *Growth rate γ in W7-X (SC).*

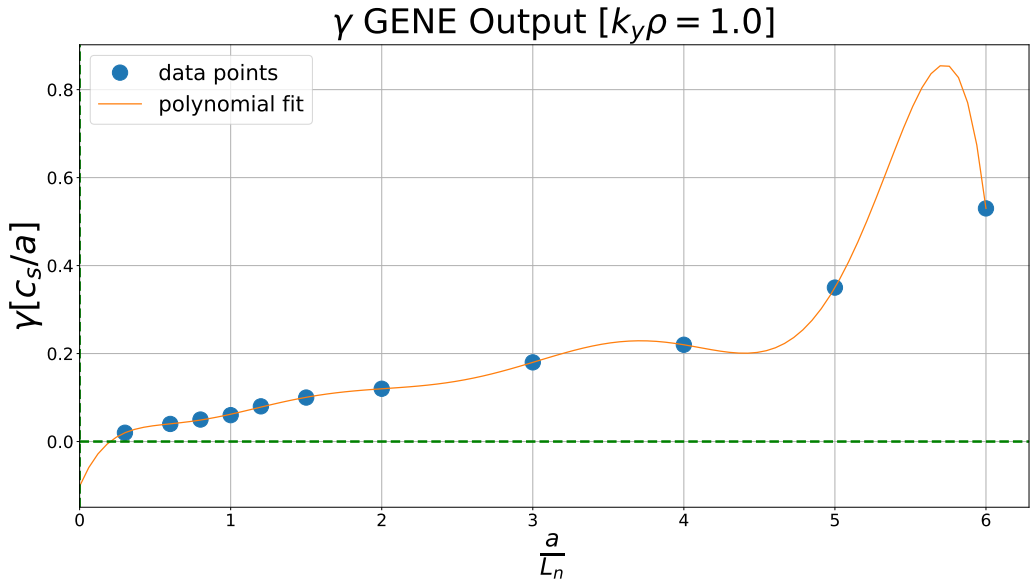

Figure 7.87: *Growth rate γ in W7-X (SC).*

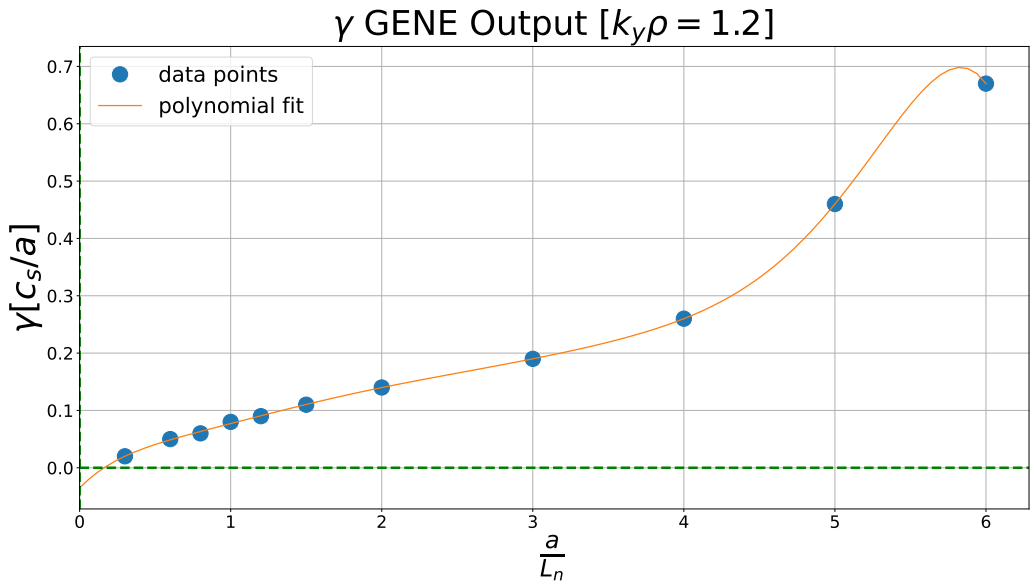

Figure 7.88: *Growth rate γ in W7-X (SC).*

W7-X (HM)

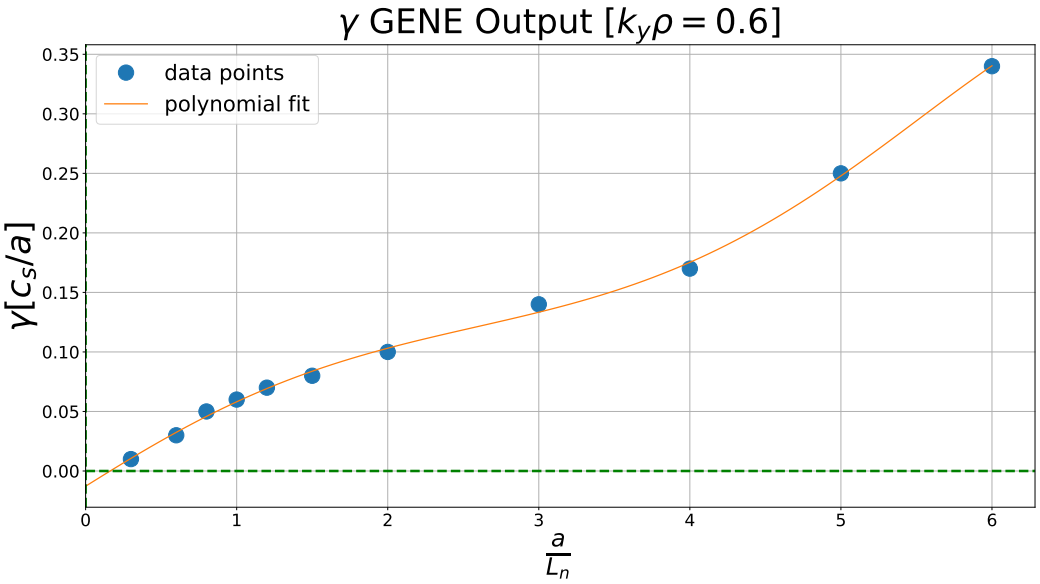

Figure 7.89: *Growth rate γ in W7-X (HM).*

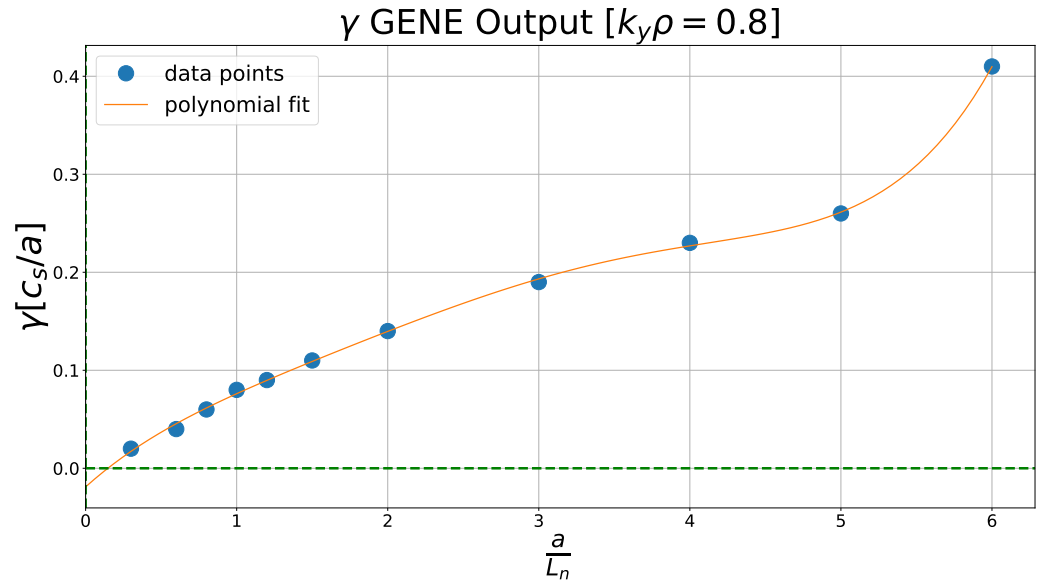

Figure 7.90: *Growth rate γ in W7-X (HM).*

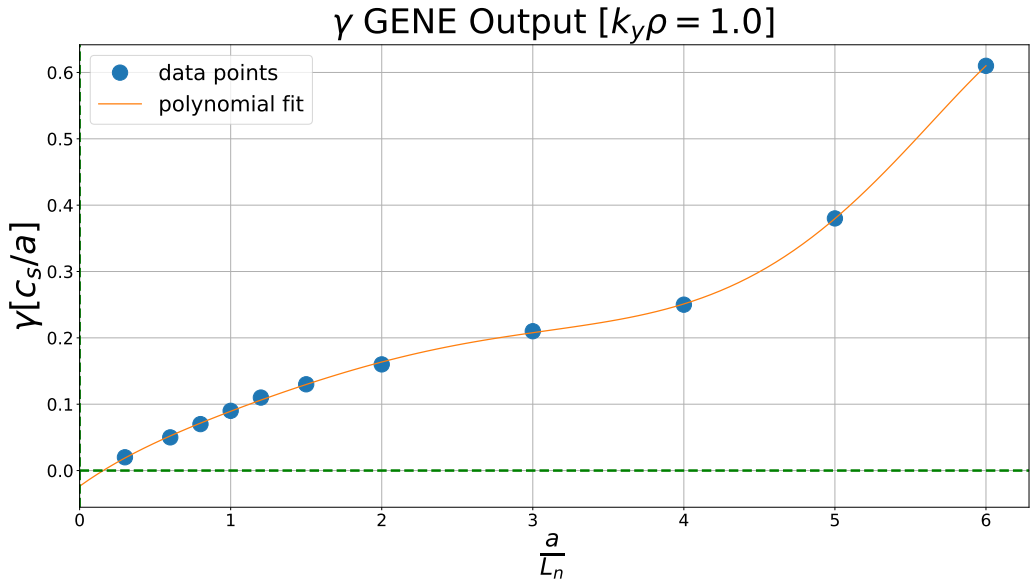

Figure 7.91: *Growth rate γ in W7-X (HM).*

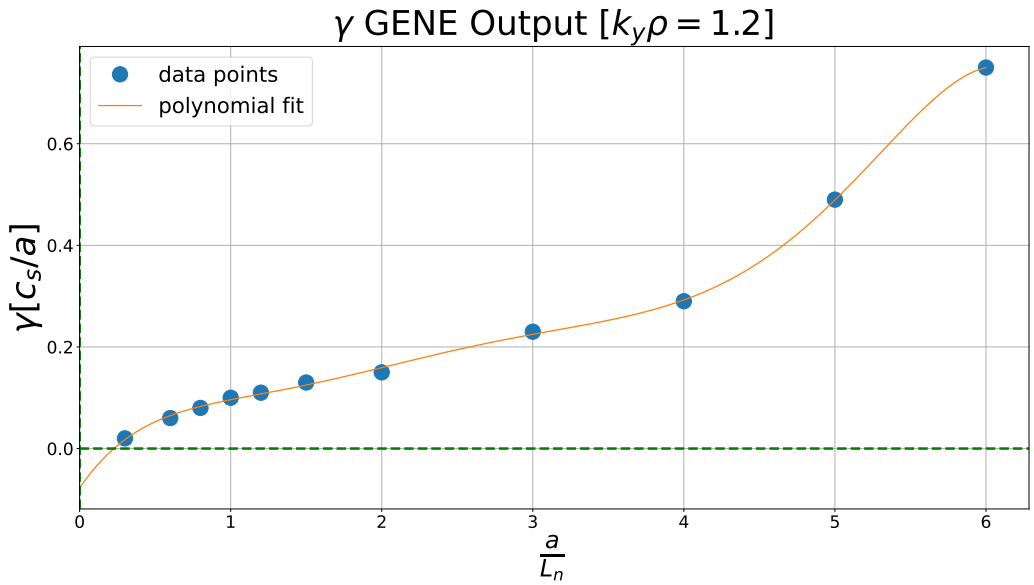

Figure 7.92: *Growth rate γ in W7-X (HM).*

W7-X (LM)

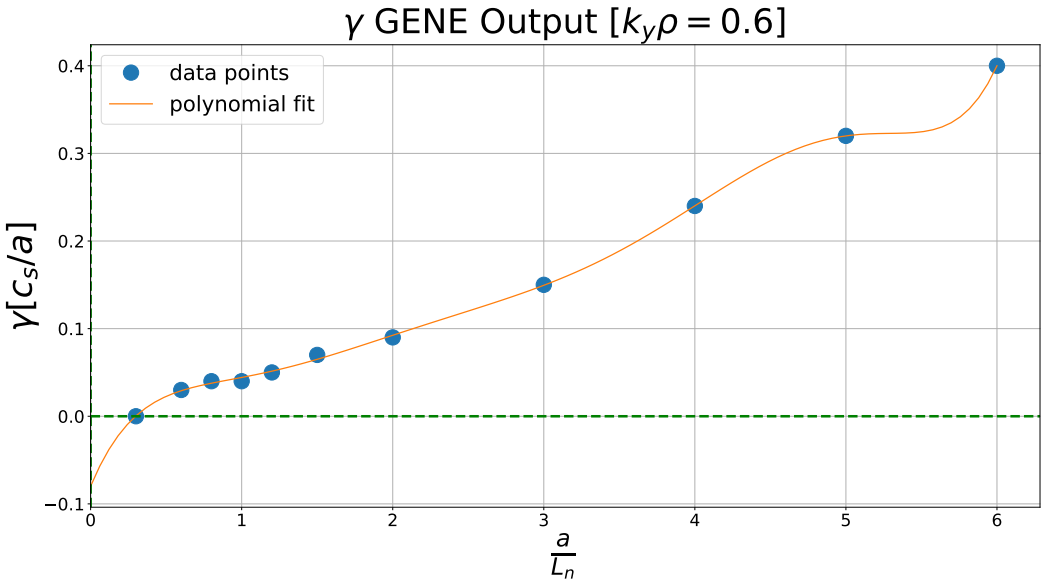

Figure 7.93: *Growth rate γ in W7-X (LM).*

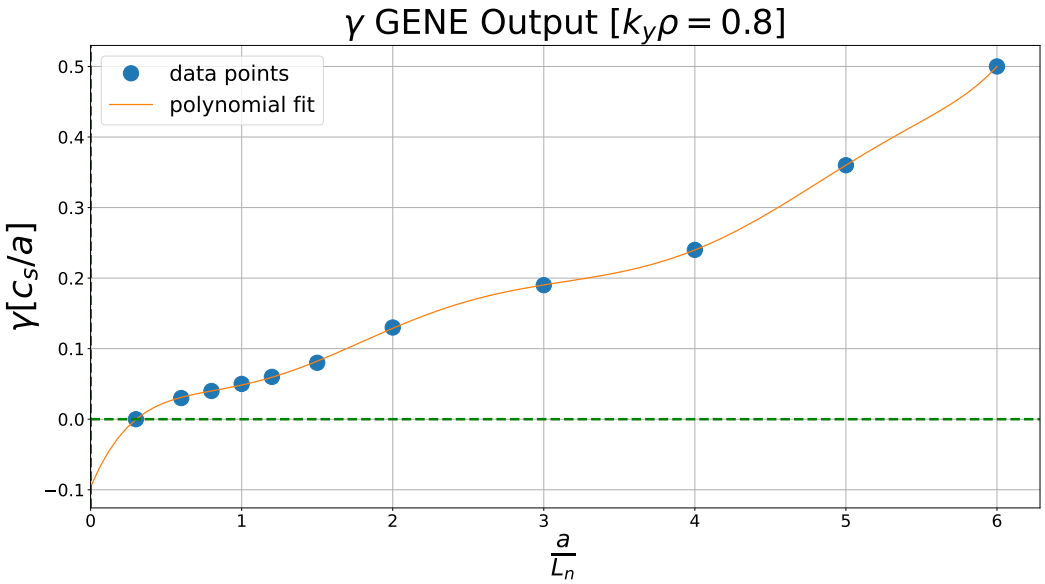

Figure 7.94: *Growth rate γ in W7-X (LM).*

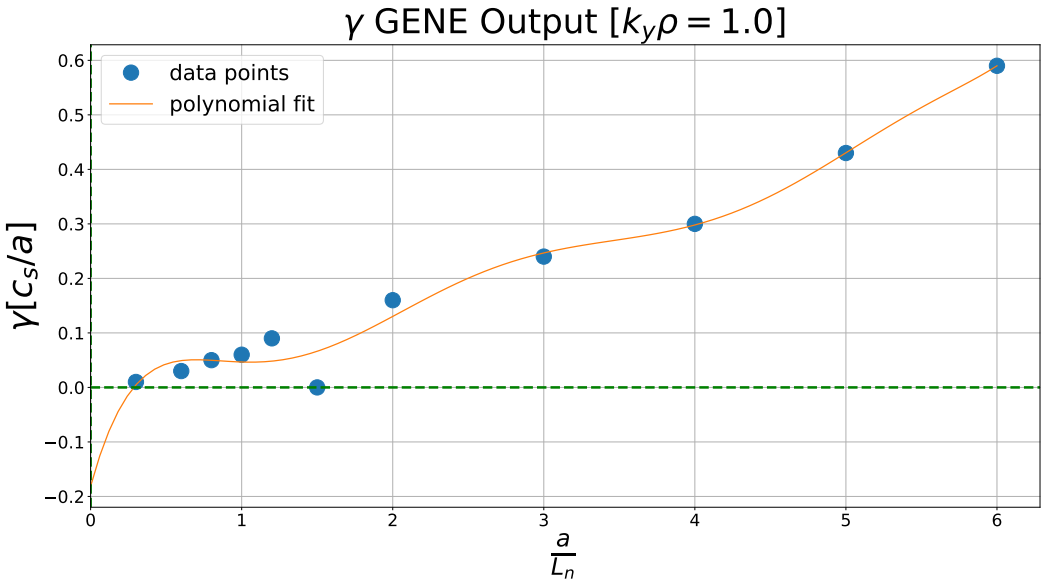

Figure 7.95: *Growth rate γ in W7-X (LM).*

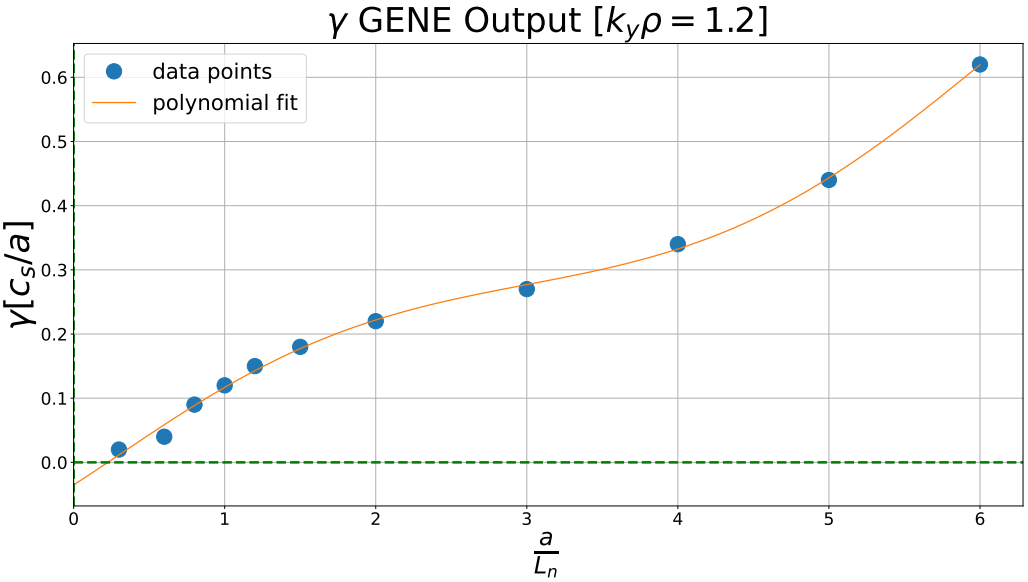

Figure 7.96: *Growth rate γ in W7-X (LM).*

HSX

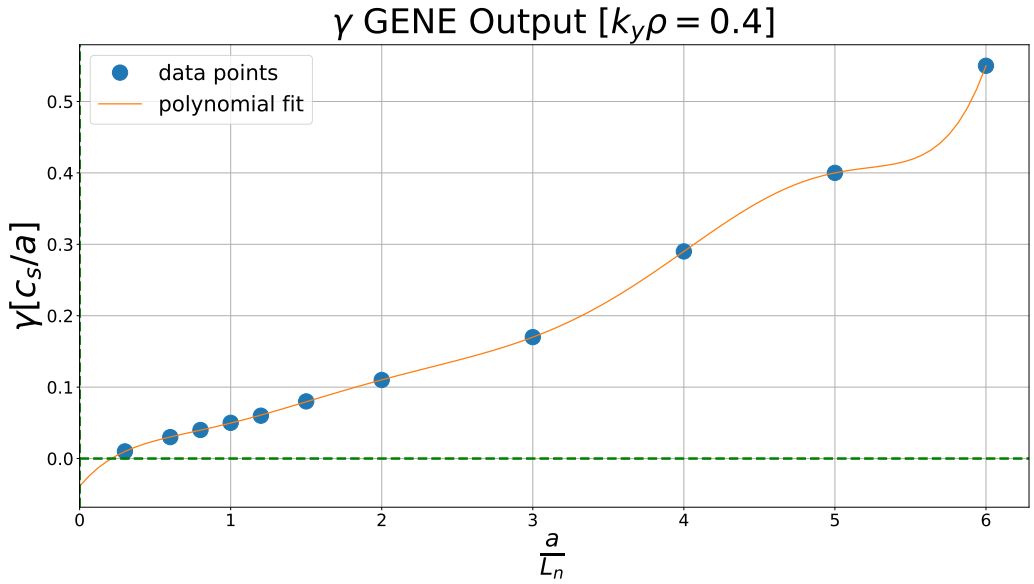

Figure 7.97: *Growth rate γ in HSX.*

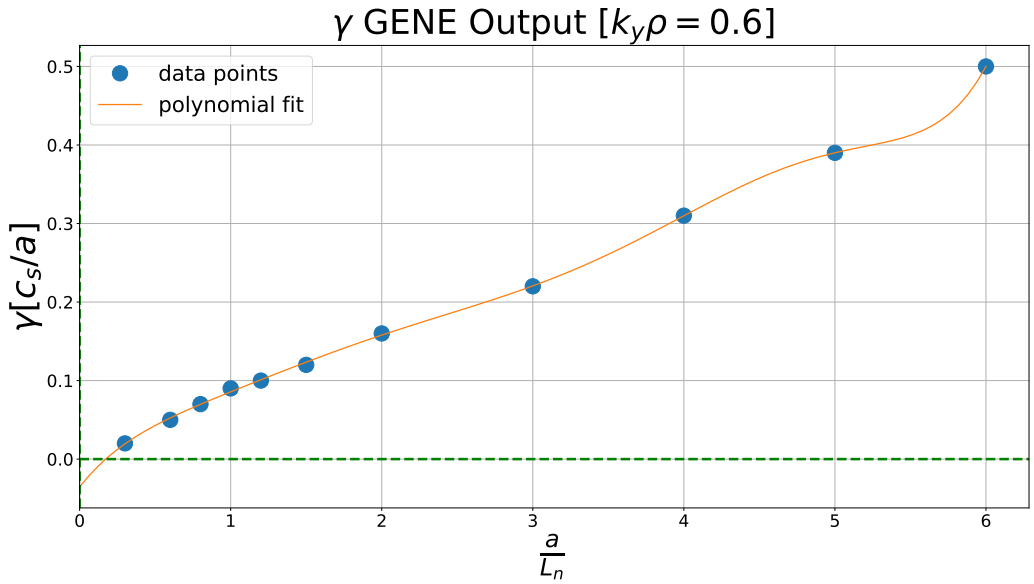

Figure 7.98: *Growth rate γ in HSX.*

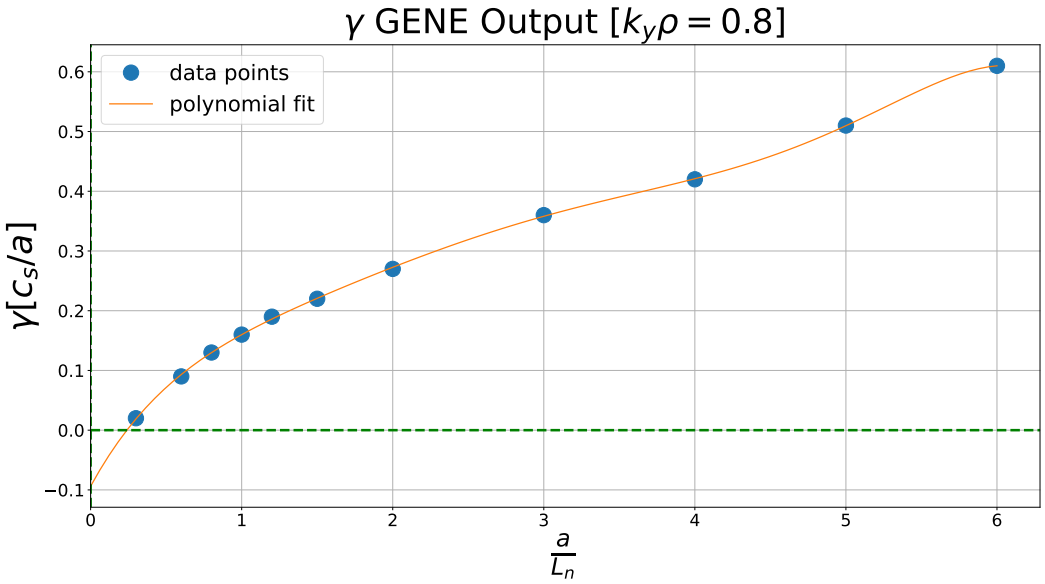

Figure 7.99: *Growth rate γ in HSX.*

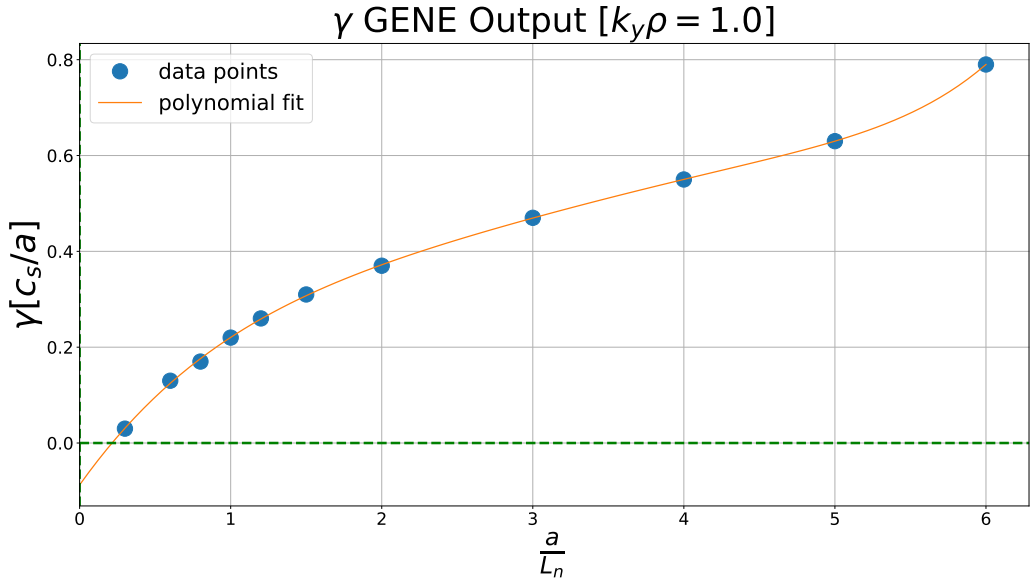

Figure 7.100: *Growth rate γ in HSX.*

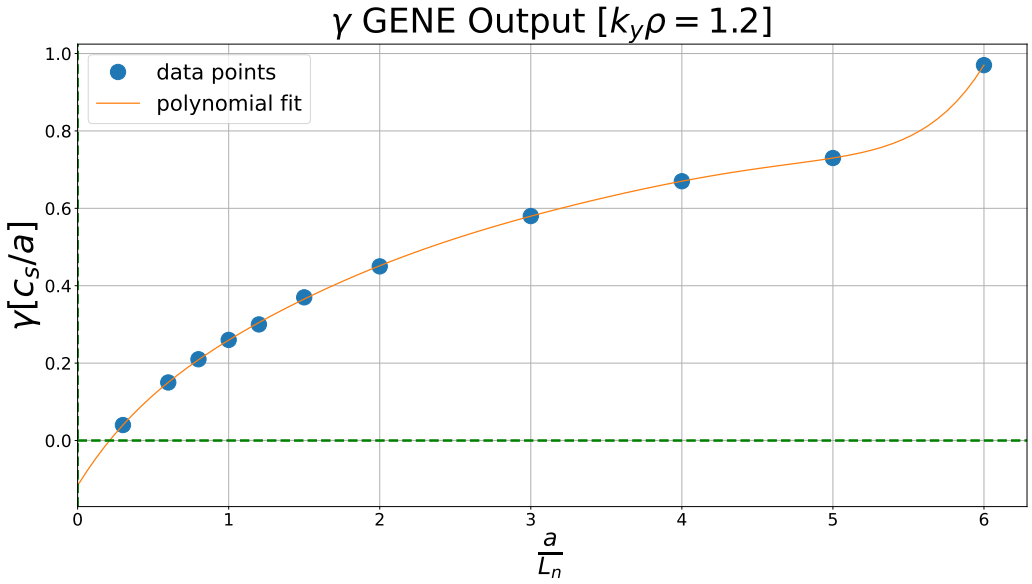

Figure 7.101: *Growth rate γ in HSX.*

7.2.2 Original Approach

Here, we will present the results of our original approach to finding a proxy for the critical density gradient. The analytical work that produced these results can be found in section 6.1. The final analytical result from that procedure, Eqn. 6.66 will be restated here:

$$\begin{aligned}\left(\frac{\omega}{\omega_{*e}}\right)\lim_{\delta\to 0}\sum_{\text{wells}}\left\{\left(\int_{\frac{1}{B_{max}}}^{\lambda_{Crit}-\delta} d\lambda[P_1+M_1]\right)+\left(\int_{\lambda_{Crit}+\delta}^{\frac{1}{B_{min}}} d\lambda[P_1+M_1]\right)\right\}\\ -\lim_{\delta\to 0}\sum_{\text{wells}}\left\{\left(\int_{\frac{1}{B_{max}}}^{\lambda_{Crit}-\delta} d\lambda[P_1-M_1]\right)+\left(\int_{\lambda_{Crit}+\delta}^{\frac{1}{B_{min}}} d\lambda[P_1-M_1]\right)\right\}=0\end{aligned} \tag{7.6}$$

where

$$\begin{aligned}P_1 &\equiv |\overline{\phi}|^2\tau(\lambda)\left(\frac{1}{\overline{G(\lambda)}}\right)\left(\frac{\omega}{F_e\overline{G(\lambda)}}\right)^{\frac{1}{2}}\mathcal{H}_e e^{-\frac{\omega}{F_e\overline{G(\lambda)}}}\\ M_1 &\equiv |\overline{\phi}|^2\tau(\lambda)\left(\frac{1}{-\overline{G(\lambda)}}\right)\left(\frac{\omega}{-F_e\overline{G(\lambda)}}\right)^{\frac{1}{2}}\mathcal{H}_i e^{-\frac{\omega}{-F_e\overline{G(\lambda)}}}\end{aligned} \tag{7.7}$$

For the $\frac{\omega}{\omega_{*e}}$ term in Eqn. 7.6, we insert our analytical expression Eqn. 5.105 directly - which we know is compatible with the variational principle. We also insert a modified form of this result for when we have ω on its own, which is necessary for both expressions in Eqn. 7.7. The input for ϕ here is $\phi_{(Pred)}$. We only use this predicted mode structure here as it does not make sense to insert GENE data, which solely corresponds to the characteristics of the mode *beyond* the point of marginal stability. This is not the region of parameter space we are concerned with here, as we only want to find the point at which the mode first exists. This is precisely at the point of marginal stability, which is where Eqn. 7.6 should be satisfied. Hence, we are not concerned with the subsequent behaviour of the mode, which is precisely what GENE models.

The plots we are presenting here represent the left-hand side of Eqn. 7.6, such that we are interested in where this result is approaching zero. The density gradient value corresponding to where our result is approximately zero should then be our proxy for the critical density gradient. Note, we are not concerned by the magnitude of our results - we are only interested in finding the roots of our plotted functions. Note, for each plot, we only show the relevant section of parameter space where a root was to be found. In some cases, no root was found in a realistic region of parameter space, but an explanation for these outliers will be provided in our discussion to follow. Also, our plots use the shorthand CDG for critical density gradient.

DIII-D Tokamak

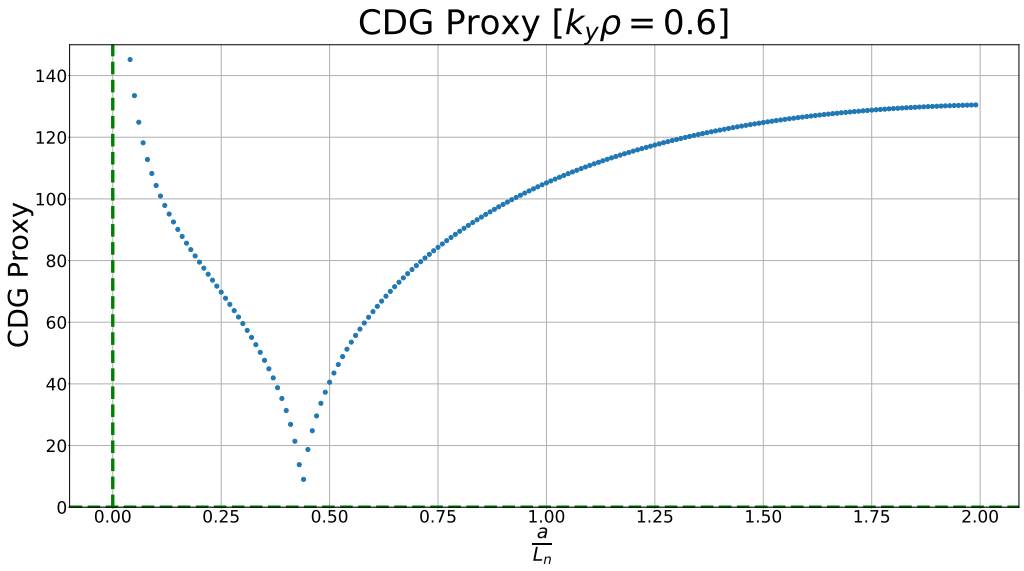

Figure 7.102: *Critical-density-gradient proxy in the DIII-D tokamak.*

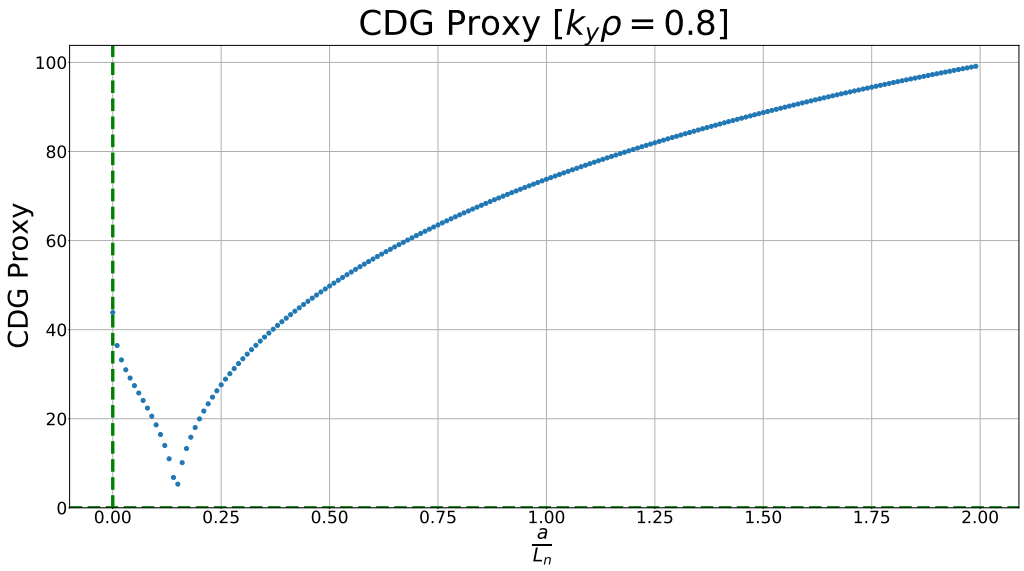

Figure 7.103: *Critical-density-gradient proxy in the DIII-D tokamak.*

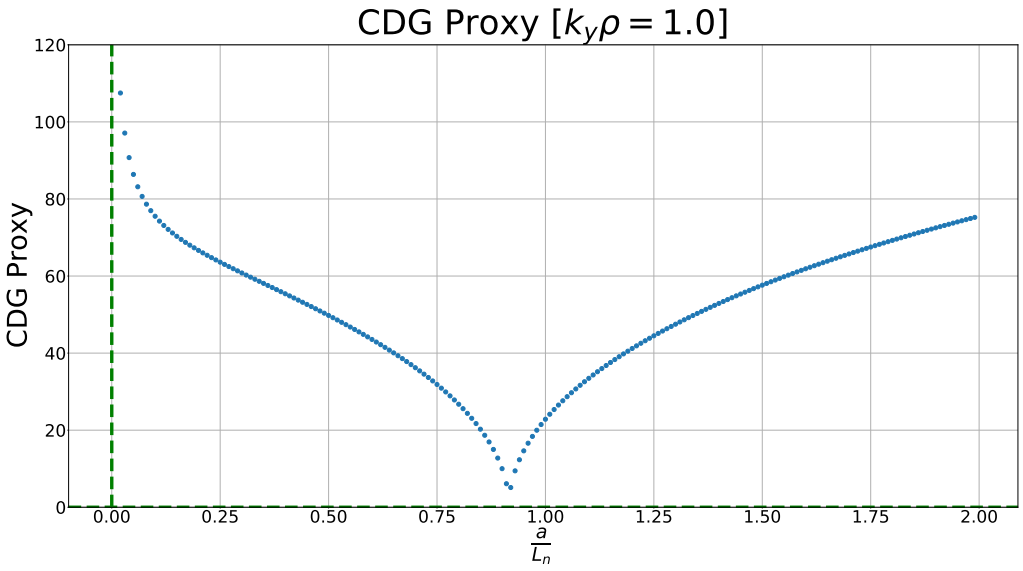

Figure 7.104: *Critical-density-gradient proxy in the DIII-D tokamak.*

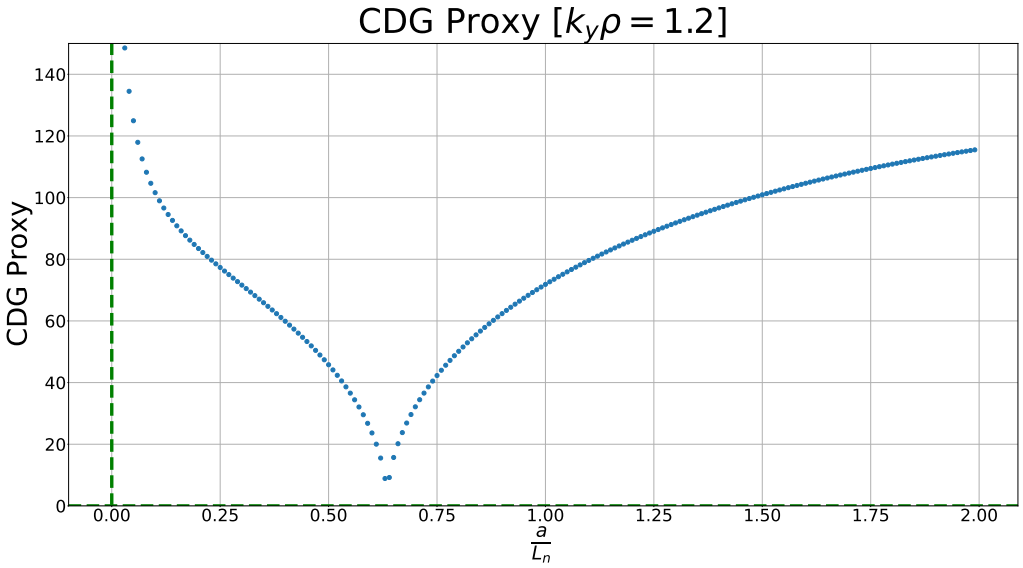

Figure 7.105: *Critical-density-gradient proxy in the DIII-D tokamak.*

NCSX

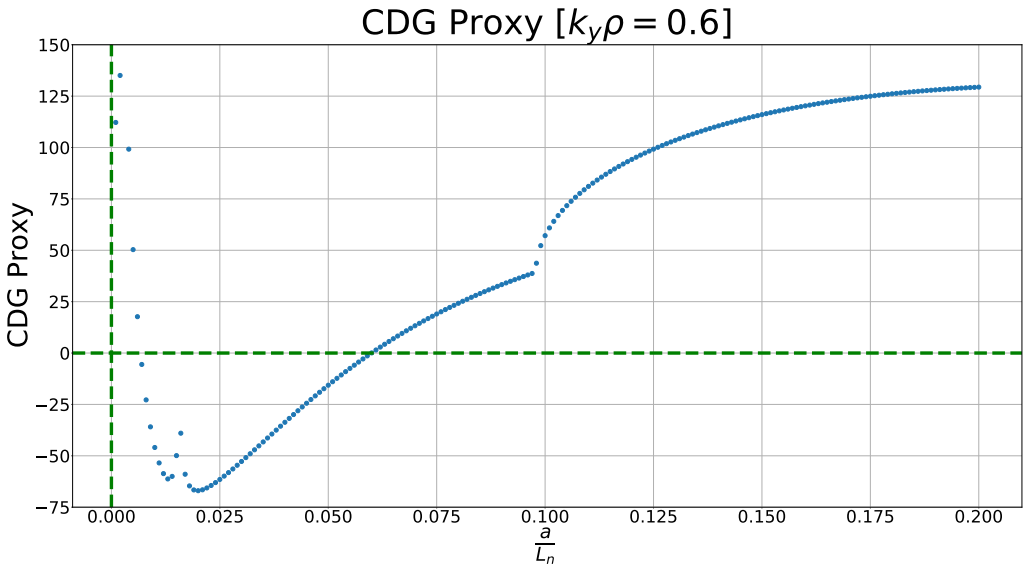

Figure 7.106: *Critical-density-gradient proxy in NCSX.*

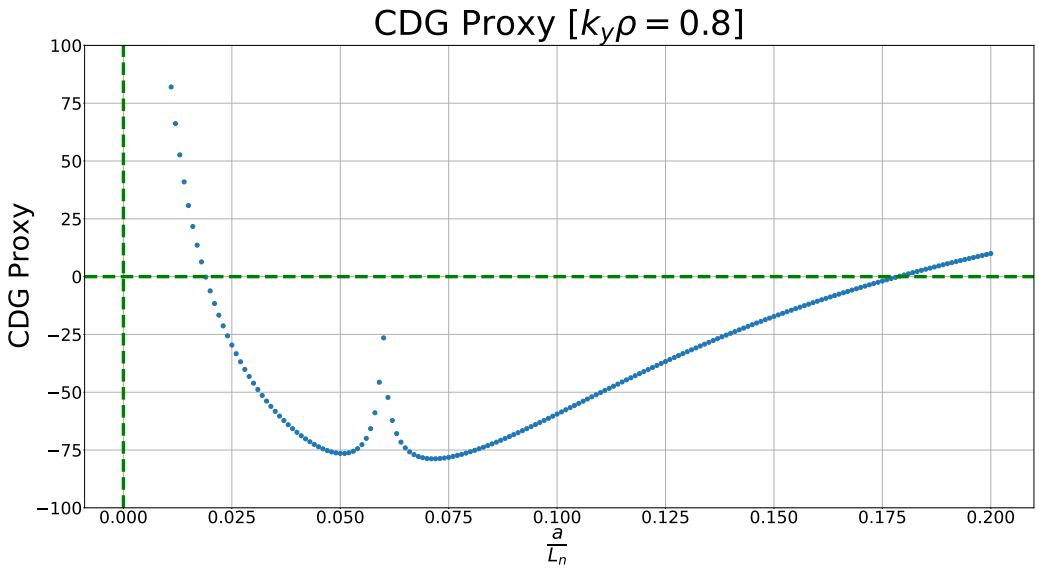

Figure 7.107: *Critical-density-gradient proxy in NCSX.*

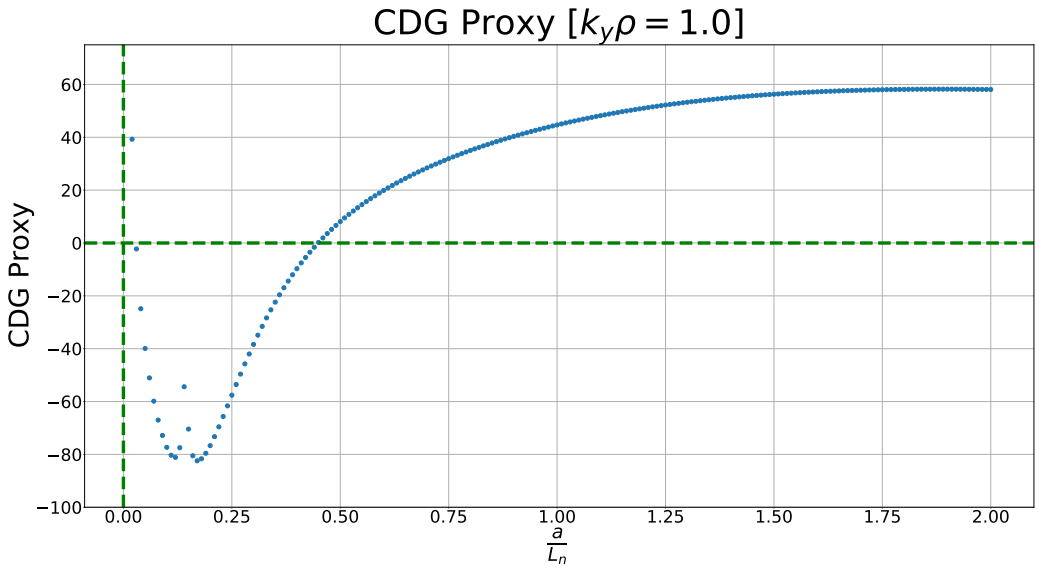

Figure 7.108: *Critical-density-gradient proxy in NCSX.*

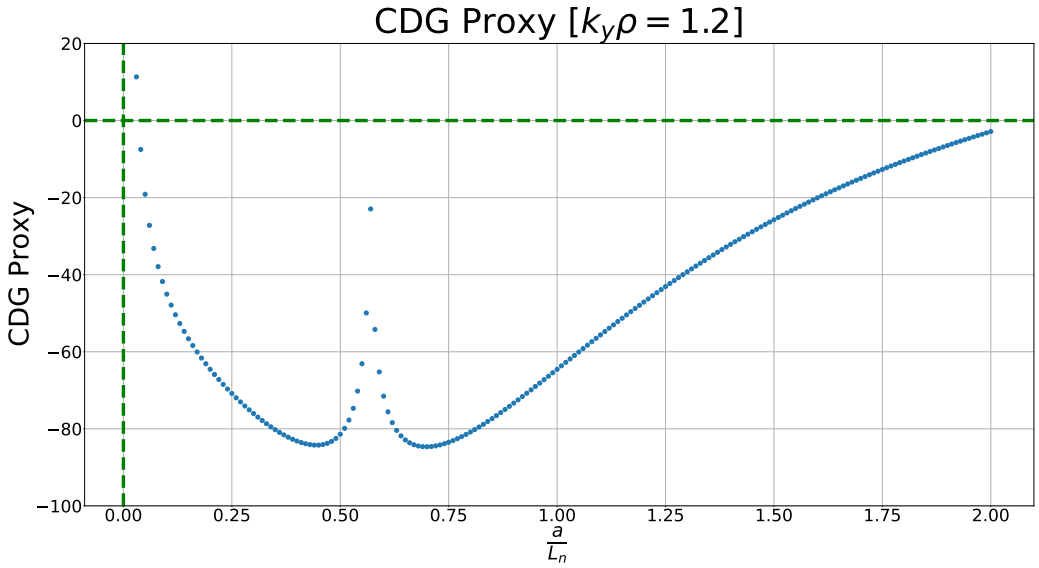

Figure 7.109: *Critical-density-gradient proxy in NCSX.*

W7-X (SC)

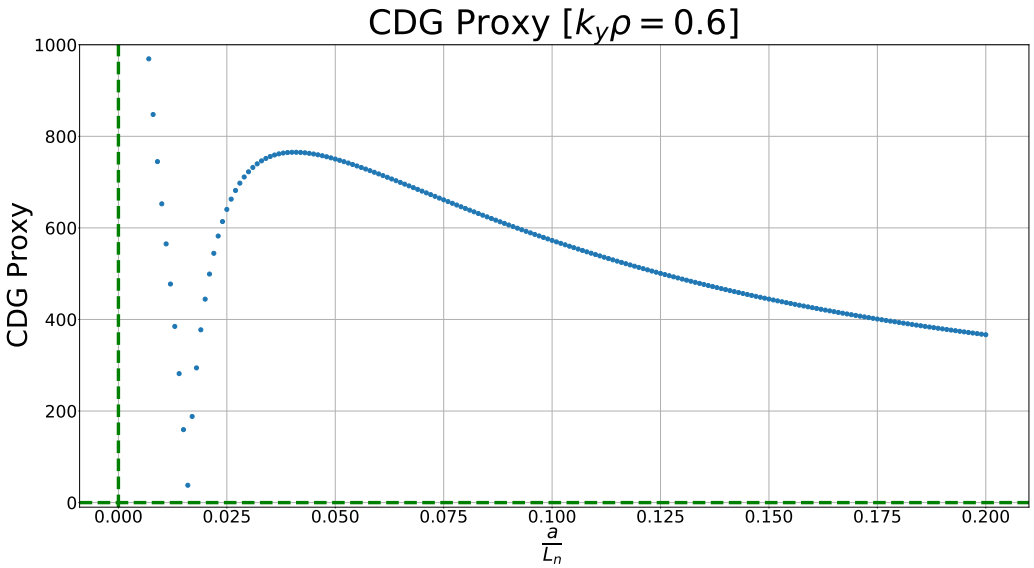

Figure 7.110: *Critical-density-gradient proxy in W7-X (SC).*

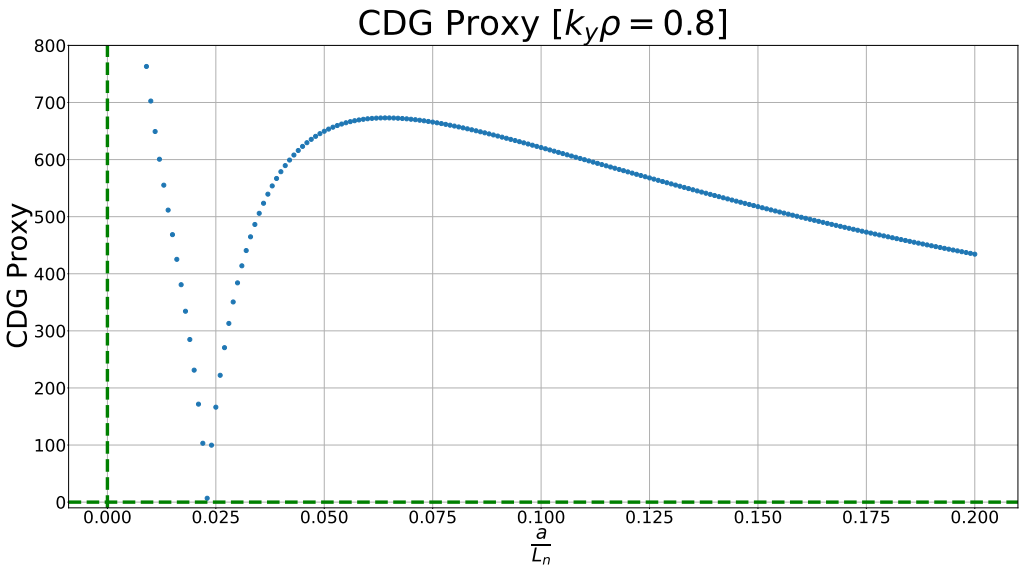

Figure 7.111: *Critical-density-gradient proxy in W7-X (SC).*

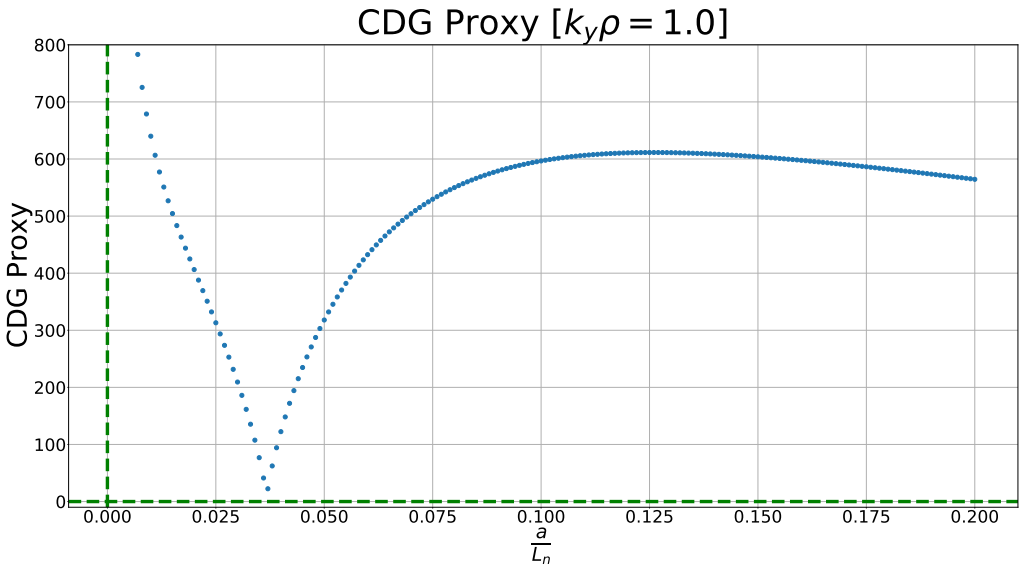

Figure 7.112: *Critical-density-gradient proxy in W7-X (SC).*

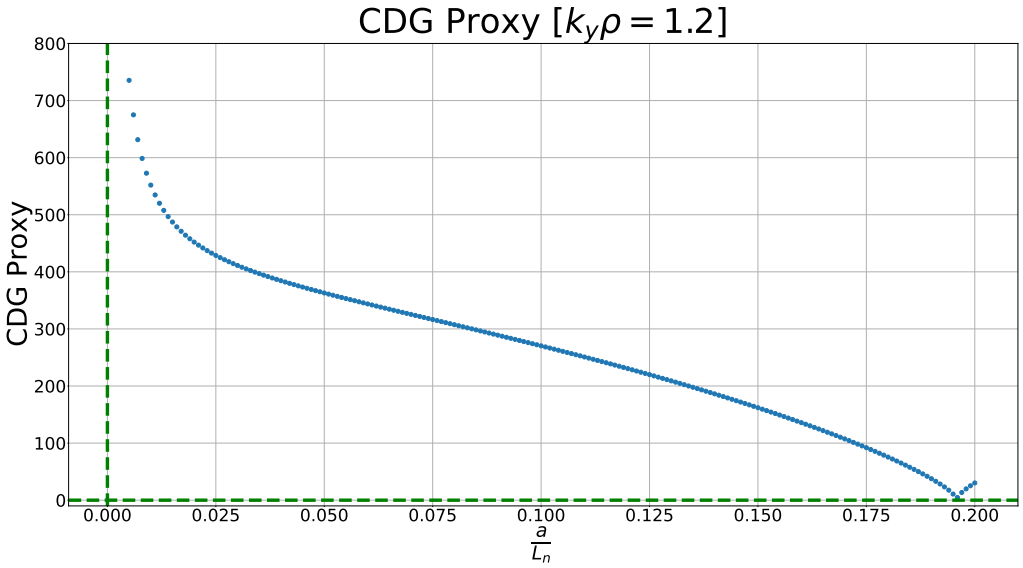

Figure 7.113: *Critical-density-gradient proxy in W7-X (SC).*

W7-X (HM)

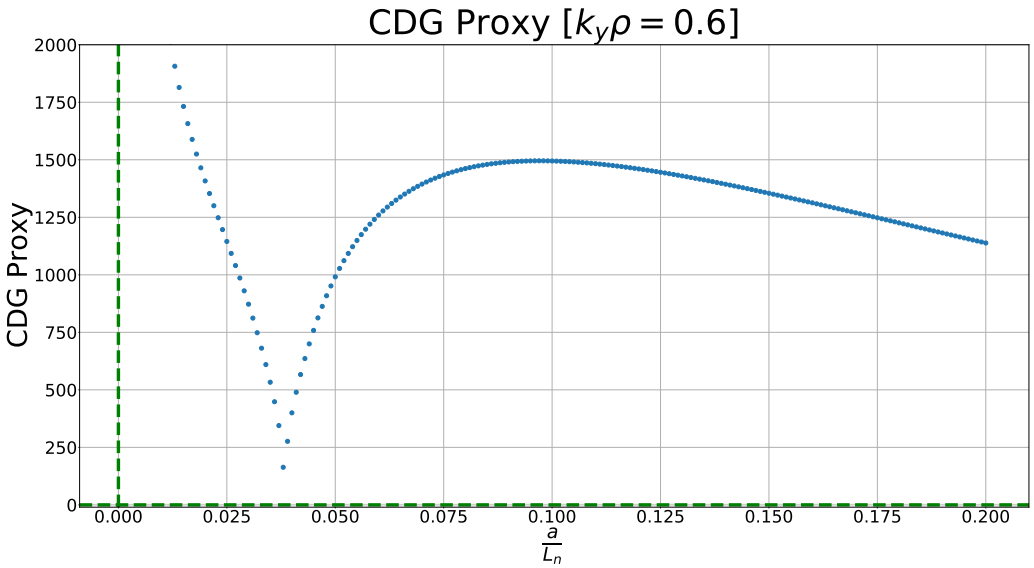

Figure 7.114: *Critical-density-gradient proxy in W7-X (HM).*

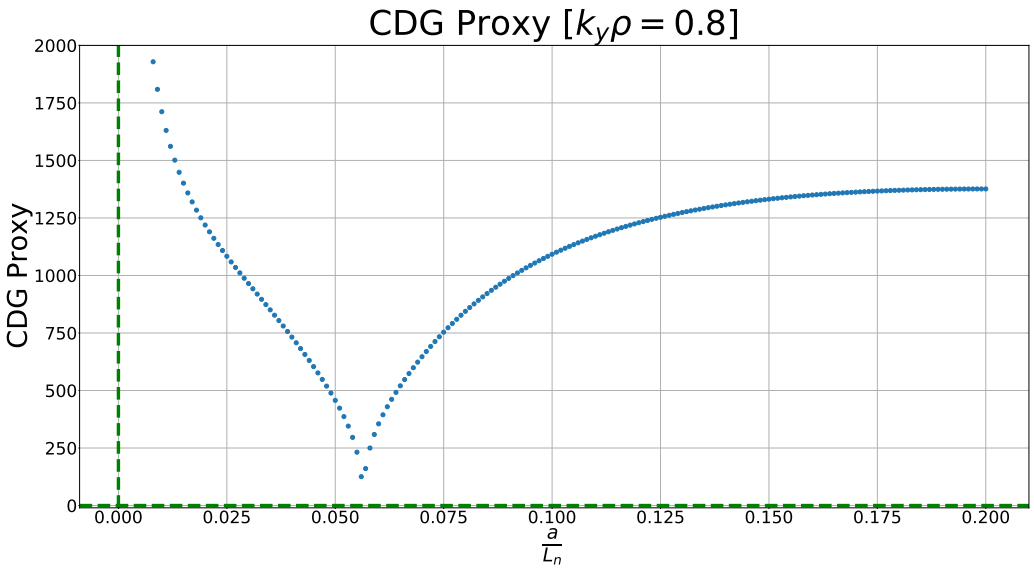

Figure 7.115: *Critical-density-gradient proxy in W7-X (HM).*

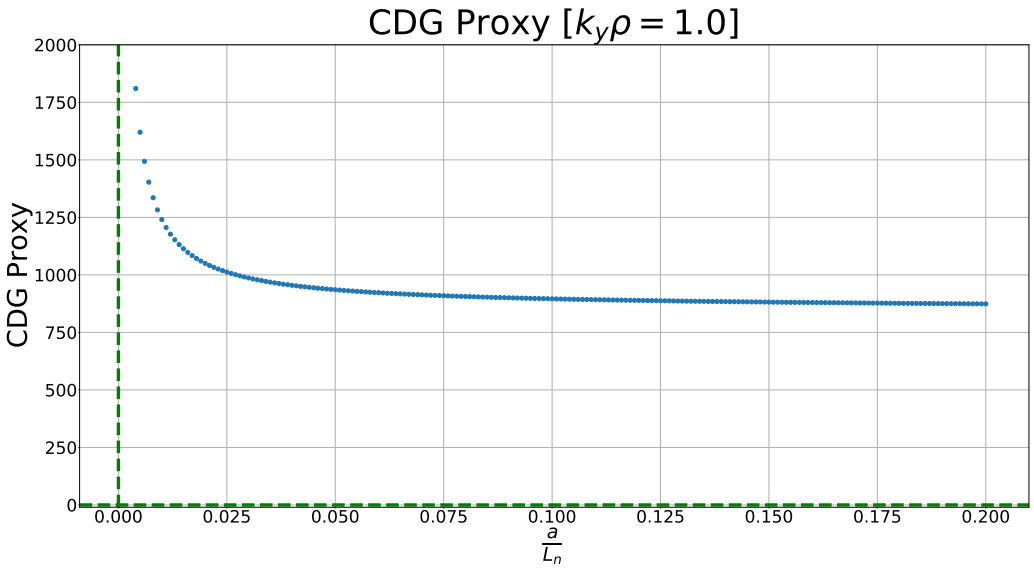

Figure 7.116: *Critical-density-gradient proxy in W7-X (HM).*

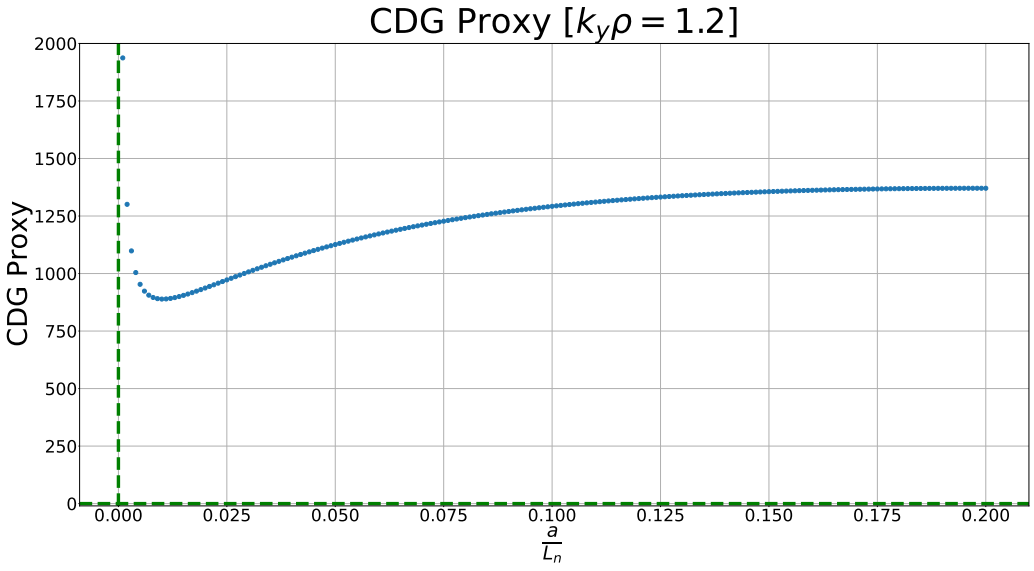

Figure 7.117: *Critical-density-gradient proxy in W7-X (HM).*

W7-X (LM)

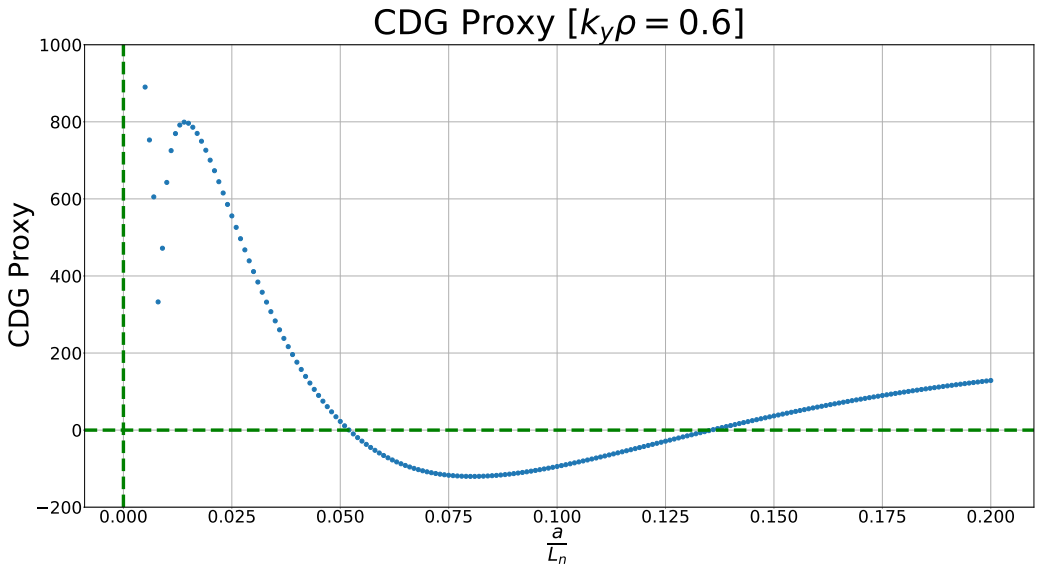

Figure 7.118: *Critical-density-gradient proxy in W7-X (LM).*

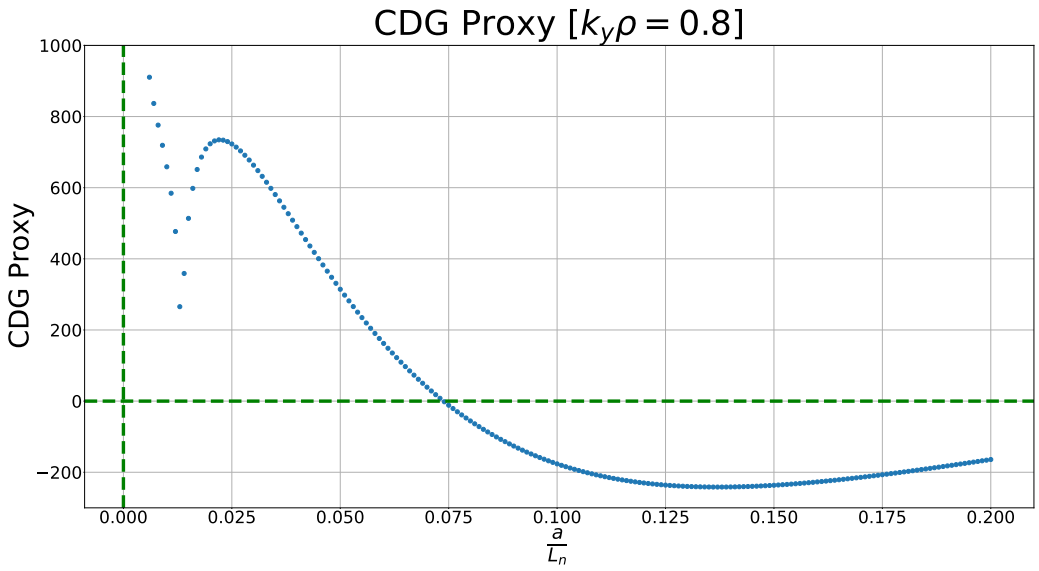

Figure 7.119: *Critical-density-gradient proxy in W7-X (LM).*

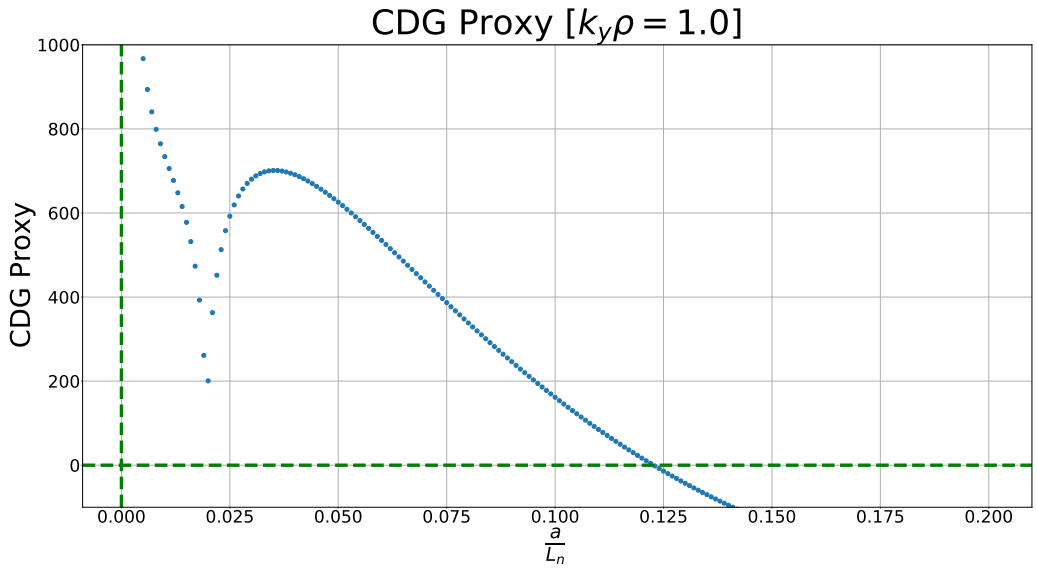

Figure 7.120: *Critical-density-gradient proxy in W7-X (LM).*

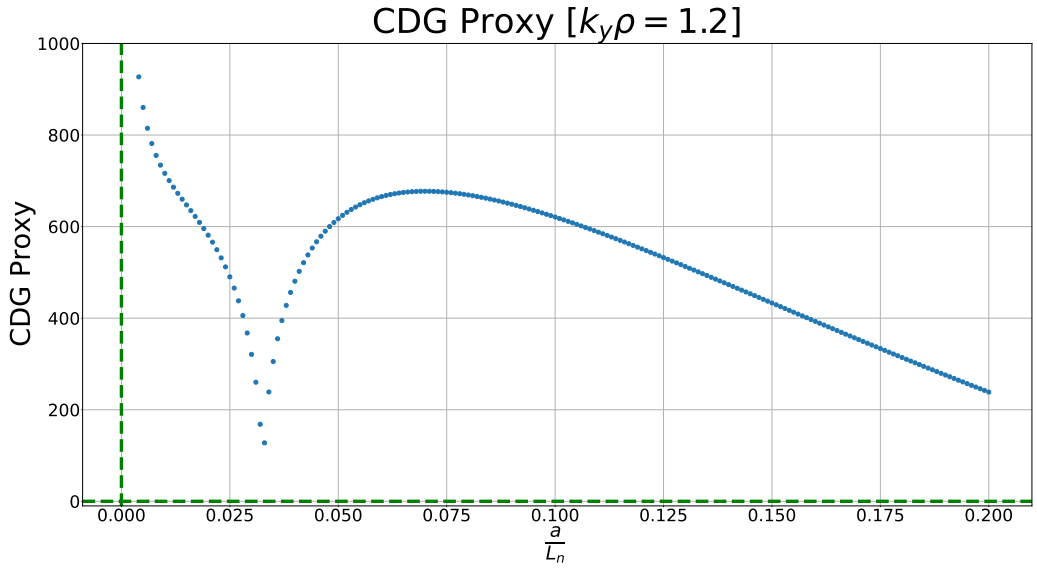

Figure 7.121: *Critical-density-gradient proxy in W7-X (LM).*

HSX

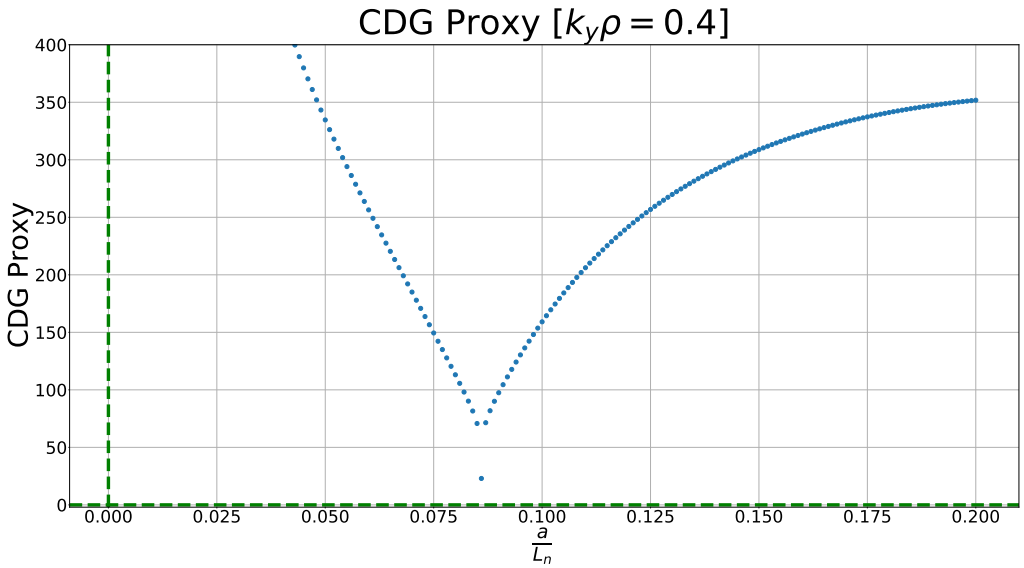

Figure 7.122: *Critical-density-gradient proxy in HSX.*

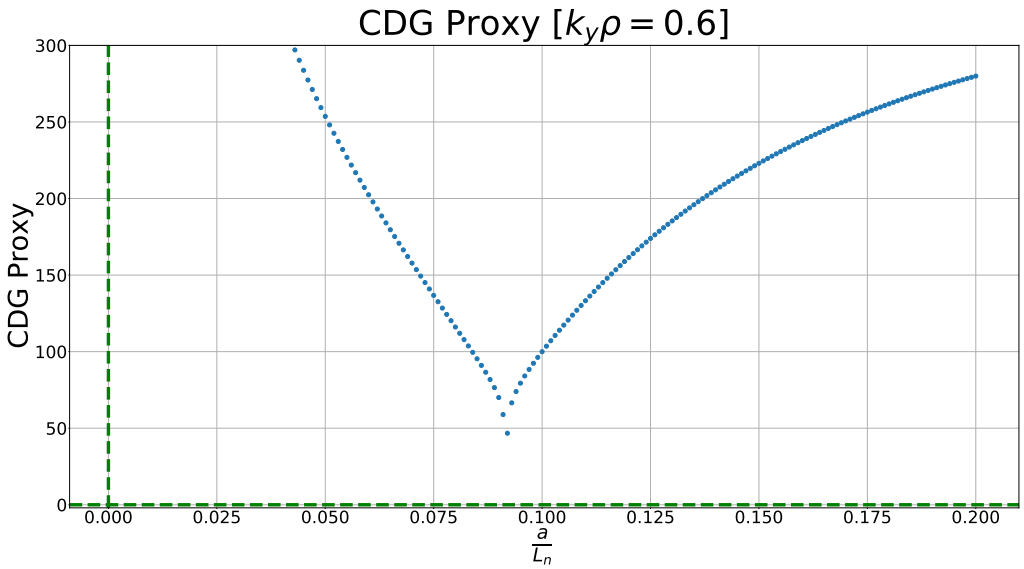

Figure 7.123: *Critical-density-gradient proxy in HSX.*

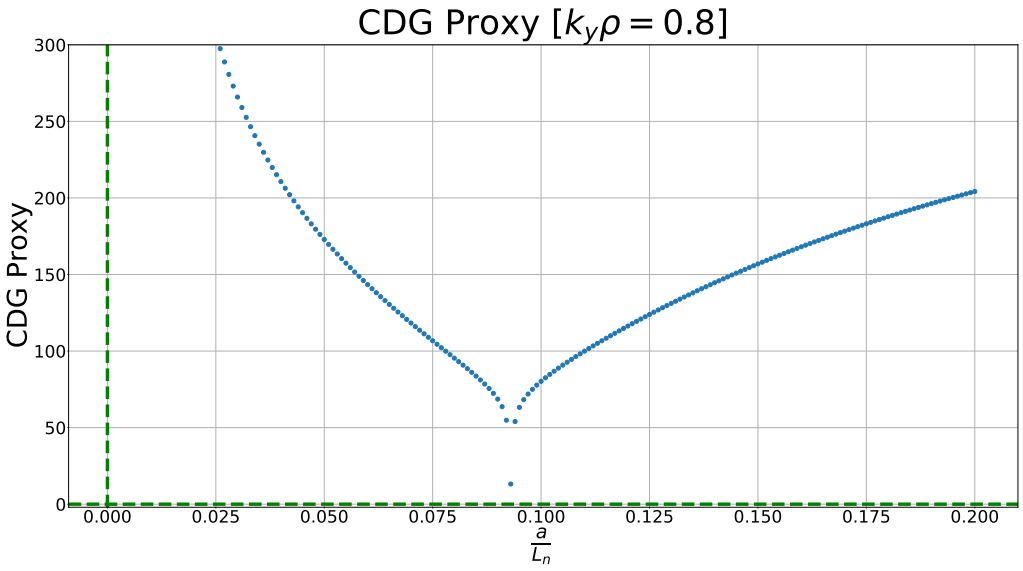

Figure 7.124: *Critical-density-gradient proxy in HSX.*

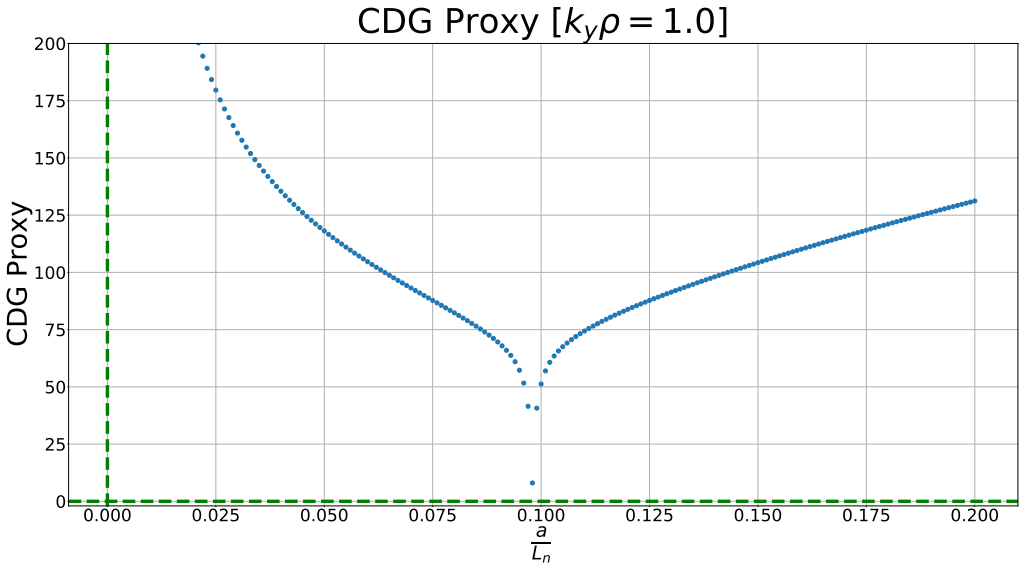

Figure 7.125: *Critical-density-gradient proxy in HSX.*

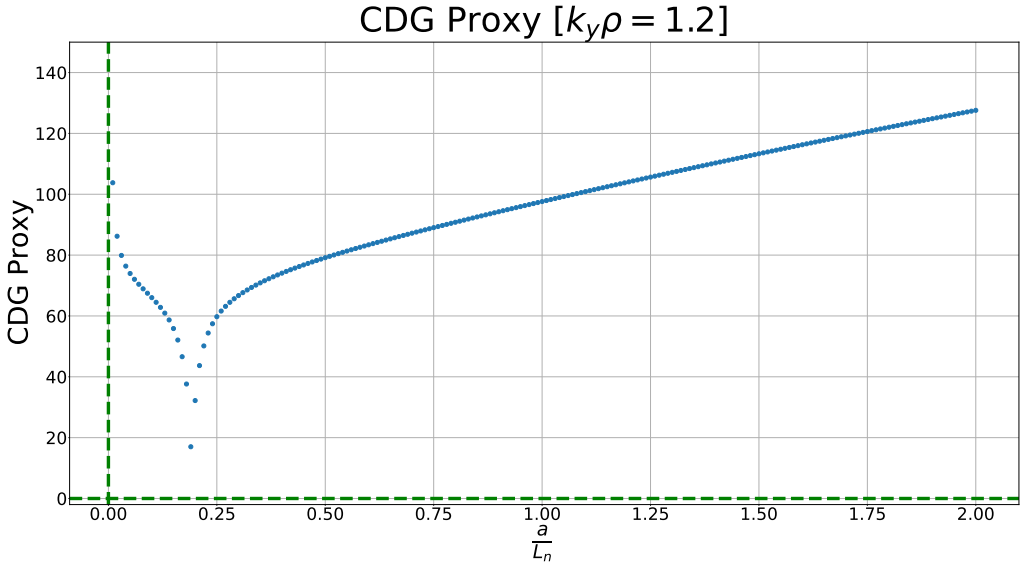

Figure 7.126: *Critical-density-gradient proxy in HSX.*

Discussion of Original Approach

We now discuss the results of this original approach to finding the critical density gradient. The results show that there is sometimes one clear solitary root found in the region of parameter space we are concerned with, but there is also sometimes multiple roots, or even no roots found. Some explanation will be provided here to explain this behaviour, but it ought to be noted that the discussion here will be somewhat trepidatious, and we will thus not draw any absolute or concrete conclusions. We will, however, provide our most solid interpretation of these findings.

Starting with the simplest case of the DIII-D tokamak, we see that there is only a single root to be found in the parameter space considered, for each wavenumber shown. At these points, there is a sharp turning point in our curves, which may be indicative of a discontinuity. This point corresponds to where $\omega_r = 0$, as our proxy expression given in Eqn. 7.6 has an ω_r in all terms. Thus, the proxy is automatically satisfied when the real mode frequency vanishes. For higher density gradients, there are no other roots found for this configuration. Therefore, we will assume that this solitary root, which occurs at the point of discontinuity in each of our curves, corresponds to the point of marginal stability. If we assume this to be true in all of our remaining geometries, then we need only focus on the roots corresponding to a discontinuity in our curves. Following from this, we find that each of these roots are also due to where $\omega_r = 0$. Interestingly, this is precisely the requirement found in our alternative proxy approach described in section 6.2. Thus, as we will see in the next section when we present the results of this alternative method, we find that the numerical results of these root values (where a discontinuity occurs) are sometimes in exact agreement (depending on the wavenumber) with the density gradient values found by our alternative method, which simply considers where $\omega_r = 0$.

We have some outliers in our results, whereby no root is found in the region of parameter space considered. The two cases where this occurred were both for the W7-X (HM) configuration (see Figures 7.116 and 7.117). This can be explained by a poor performance on the part of the predicted mode structure. More specifically, the mode frequency proxy - which depended on this predicted mode structure - was unable to adequately predict the behaviour of the actual mode frequency. This is most clearly evident in the next section (see the lower plots in Figures 7.145 and 7.146). In these two instances, the critical density gradient is predicted to be approximately 12.1527 and -0.0159, respectively. The expected value is somewhere between 0 and 1. Thus, we disregard these results as explainable outliers, which would not have occurred had our mode structure prediction been more rigorous.

We shall now present and discuss the numerical results of this critical-density-gradient proxy in Table 7.1. Here, we compare these proxy results with those found using GENE data. These results are also presented more visually using scatter-correlation plots (see Figures 7.127, 7.128, 7.129 and 7.130). When considering the critical-density-gradient proxy plots presented earlier in this section, it should be noted that the precise values of the roots are in exact agreement with

evaluating our analytical expression, Eqn. 6.87. This should make sense, as both our proxy-plots and Eqn. 6.87 have a solution for $\omega_r = 0$, and both procedures rely on our predicted mode structure $\phi_{(Pred)}$ as in input. Thus, this is how our proxy values were calculated in Table 7.1. We can see from this table of results and the corresponding scatter-correlation plots that we do not have a strong agreement between our proxy's prediction and the results obtained from GENE. In our scatter-correlation plots, perfect agreement between our proxy and GENE would be indicated by having a one-to-one correlation, such that the line of best fit would have a slope equal to 1 with a y-intercept at the origin, and all data points would fall on this line. This is, of course, the idealised case, and is never expected realistically. Our scatter-correlation plots all show a weak-positive correlation, with the strongest result being at wavenumber $k_y\rho = 1.2$. Although this may seem like a disappointing outcome, some potential reasons for these discrepancies in values (and weak correlations) are important to keep in mind.

Firstly, the values obtained from the GENE growth rate data are by no means infallible or without error. These values have been obtained using a limited amount of data, which has then been fitted with a polynomial. The degree of this polynomial fit is manually adjusted until the best possible match is found by eye. This method is only able to *approximate* the trend of the given data set. It is from this approximate polynomial that a root was found, which gives us our supposed critical density gradient values. Therefore, we are more concerned with the approximate *neighbourhood* of values obtained from GENE, and not the precise values shown.

Secondly, it is important to remember that our proxy is reliant on the efficacy of the mode frequency proxy, and thus, on the accuracy of the predicted mode structure. Therefore, there is an inevitable propagation of error manifest here due to this heavy dependence on earlier steps. And so, we may expect a better agreement between the proxy and the GENE output when these earlier procedures have been further improved. If this is the case, then our analytical work carried out for the critical-density-gradient proxy is still valid and potentially useful. Thus, we may only need to improve the accuracy of our inputs for this proxy to yield more accurate results.

In relation to this second point, there is another potential explanation for the discrepancies between our proxy prediction and the GENE values, which arises from the analytical work underlying these results. As already mentioned in section 7.1, where we discussed the results of the mode frequency proxy, an important ordering assumption had to be made in order to be able to carry out our variational principle approach in section 5.2. Specifically, we needed to assume a small ordering of the magnetic drift frequency compared to the mode frequency ($\omega_{da} \ll \omega$), so as to avoid encountering resonance when $\omega_{da} \sim \omega$ in the denominator of our integral expression. This is ultimately because our variational principle procedure is only known to work in cases where the integral expression is fully real. Thus, we had to avoid the manifestation of a pole in our calculation in order to successfully implement this variational principle procedure. However, in our analytical derivation for the critical-density-gradient proxy (see section 6.1), we do not implement this assumption. Instead, we directly address this presence of a pole by assuming an ordering of $\omega_{da} \sim \omega$ in our derivation. This was necessary because the presence of a pole

corresponds to the manifestation of our instability mode (the TEM in this case). Once our final result from this procedure was obtained, we inserted our mode frequency proxy result into this critical-density-gradient proxy expression. Thus, we end up calculating a single expression which relied on a particular ordering scheme ($\omega_{da} \sim \omega$), but whose input relied upon a different ordering scheme ($\omega_{da} \ll \omega$). This was an unfortunate, but ultimately necessary, course of action for this very particular procedure. For future work, it may be worth investigating whether a similar procedure can be carried out whereby there is greater consistency of assumption made throughout the full analytical derivation.

Despite the aforementioned discrepancies and weak correlations in our results, we are still seeing a positive correlation for all wavenumbers considered. This may indicate that our proxy is working *sufficiently well* for optimisation purposes. In other words, our proxy seems to be correctly indicating the approximate *direction of optimisation*, i.e., where a new stellarator geometry should fall in these plots such that it possess a higher critical density gradient. Therefore, a perfect one-to-one correlation may not be necessary for finding a stellarator geometry with increased critical density gradient, and our proxy would provide a relatively fast means to achieving this, which is totally independent of costly GENE simulation data.

Geometry	Critical Density Gradient Values	
	γ GENE	CDG Proxy
DIII-D ($k_y\rho = 0.6$)	0.3182	0.4470
DIII-D ($k_y\rho = 0.8$)	0.3051	0.1562
DIII-D ($k_y\rho = 1.0$)	0.3073	0.9259
DIII-D ($k_y\rho = 1.2$)	0.3080	0.6448
NCSX ($k_y\rho = 0.6$)	0.2980	0.0157
NCSX ($k_y\rho = 0.8$)	0.2961	0.0598
NCSX ($k_y\rho = 1.0$)	0.2776	0.1428
NCSX ($k_y\rho = 1.2$)	0.2495	0.5688
W7-X (SC) ($k_y\rho = 0.6$)	0.1783	0.0159
W7-X (SC) ($k_y\rho = 0.8$)	0.2014	0.0230
W7-X (SC) ($k_y\rho = 1.0$)	0.2021	0.0367
W7-X (SC) ($k_y\rho = 1.2$)	0.1617	0.1958
W7-X (HM) ($k_y\rho = 0.6$)	0.1624	0.0382
W7-X (HM) ($k_y\rho = 0.8$)	0.1472	0.0564
W7-X (HM) ($k_y\rho = 1.0$)	0.1559	12.1527
W7-X (HM) ($k_y\rho = 1.2$)	0.2265	-0.0159
W7-X (LM) ($k_y\rho = 0.6$)	0.2975	0.0083
W7-X (LM) ($k_y\rho = 0.8$)	0.3015	0.0133
W7-X (LM) ($k_y\rho = 1.0$)	0.2858	0.0196
W7-X (LM) ($k_y\rho = 1.2$)	0.2264	0.0326
HSX ($k_y\rho = 0.4$)	0.2106	0.0860
HSX ($k_y\rho = 0.6$)	0.1725	0.0917
HSX ($k_y\rho = 0.8$)	0.2401	0.0930
HSX ($k_y\rho = 1.0$)	0.2146	0.0980
HSX ($k_y\rho = 1.2$)	0.2115	0.1919

Table 7.1: *Critical density gradient values from GENE data and from our proxy.*

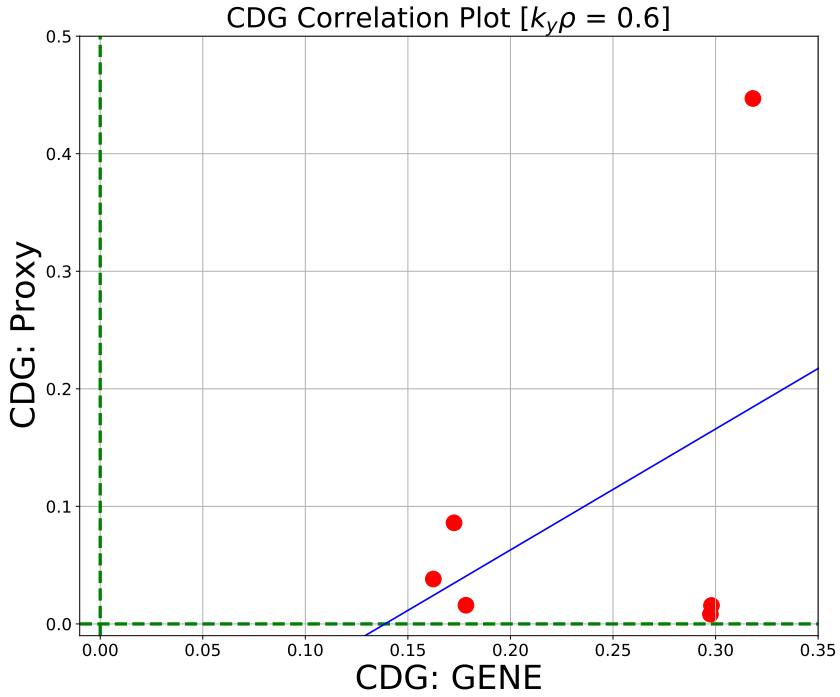

Figure 7.127: *Scatter-correlation plot comparing our critical-density-gradient proxy results with GENE.*

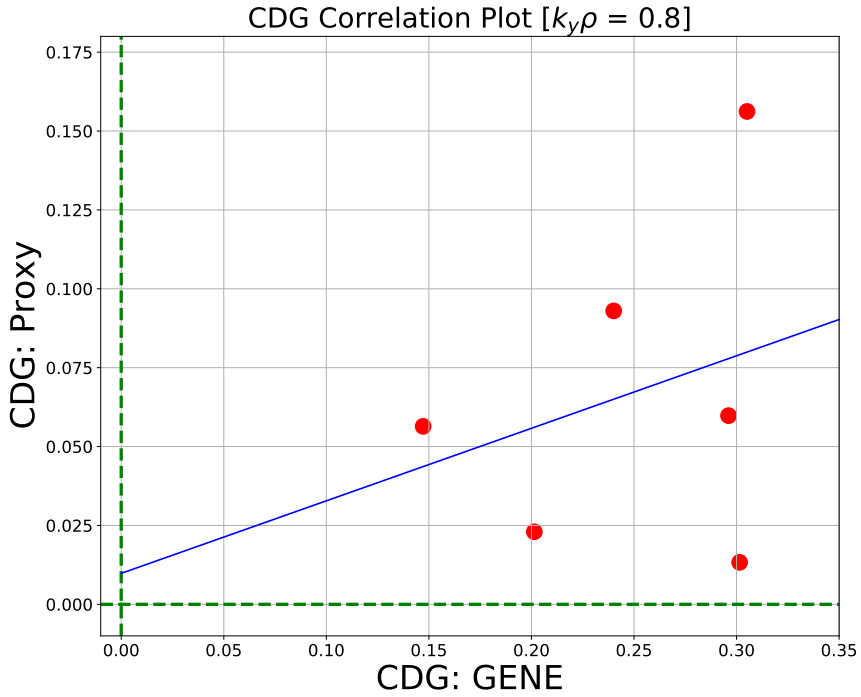

Figure 7.128: *Scatter-correlation plot comparing our critical-density-gradient proxy results with GENE.*

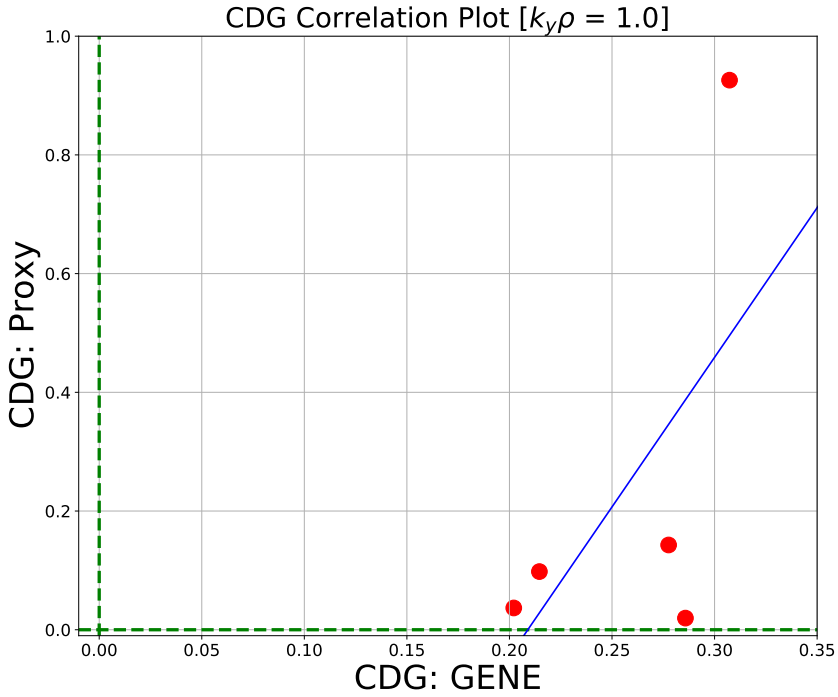

Figure 7.129: *Scatter-correlation plot comparing our critical-density-gradient proxy results with GENE.*

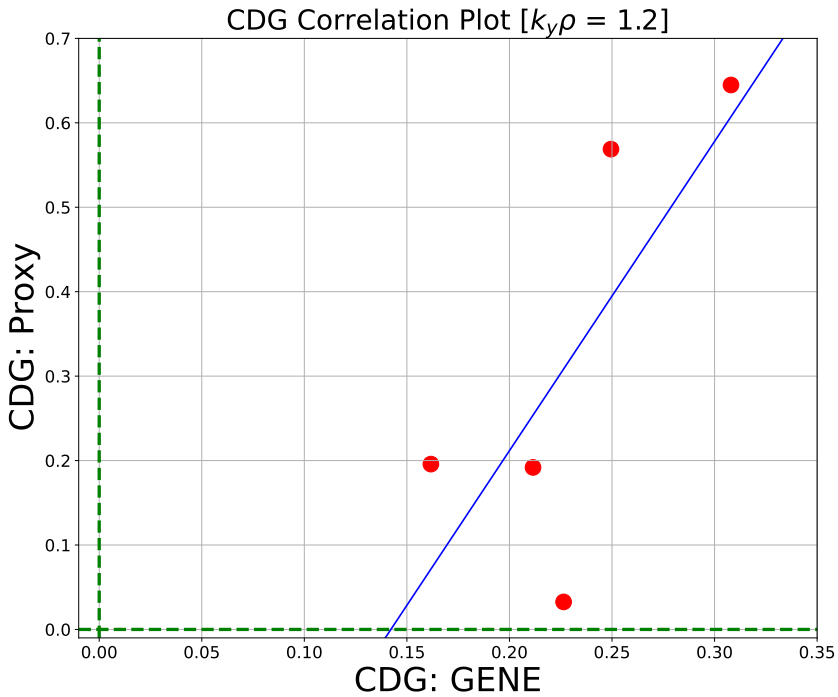

Figure 7.130: *Scatter-correlation plot comparing our critical-density-gradient proxy results with GENE.*

7.2.3 Alternative Approach

Here, we will present the results of our alternative approach to finding a proxy for the critical density gradient. The analytical work that produced these results can be found in section 6.2. Very simply stated, this procedure indicated that the critical density gradient is that which corresponds to:

$$\omega_r \stackrel{!}{=} \gamma \stackrel{!}{=} 0 \tag{7.8}$$

This implies that we can use our variational principle proxy for ω_r to approximate the critical density gradient as follows:

$$\omega_{r(VP)} \stackrel{!}{=} 0 \tag{7.9}$$

The plots presented in this section are thus the real mode frequency results from various methods. These methods are as follows: ω_r directly from GENE data; ω_r from our variational principle proxy, where ϕ-data from GENE was used as our input; ω_r from our variational principle proxy, where the predicted mode structure $\phi_{(Pred)}$ was used as our input. The critical density gradient is then found from calculating the first root of these plotted functions, where $\omega_r = 0$. The results of this procedure are displayed in Table 7.2.

For the final case stated here, whereby we use the variational principle and the predicted mode structure, the critical density gradient can also be calculated directly using the the final analytical result from section 6.2 - Eqn. 6.87. This will be restated here:

$$\left(\frac{a}{L_{n_e}}\right)_{Crit} = \frac{\left(\frac{eBa}{k_\alpha T_e}\right)\left\{\int_{-\infty}^{\infty}\left[2\Gamma_0 - b\left(\Gamma_0 - \Gamma_1\right)\right]\frac{\hat{\omega}_{di}}{2}|\phi|^2\frac{dl}{B} + \frac{1}{2}\int_{\frac{1}{B_{max}}}^{\frac{1}{B_{min}}}\sum_{\text{wells}}\tau(\lambda)\left(\frac{3}{2}F_e\overline{G(\lambda)}\right)|\overline{\phi}|^2 d\lambda\right\}}{\frac{1}{2}\int_{\frac{1}{B_{max}}}^{\frac{1}{B_{min}}}\sum_{\text{wells}}\tau(\lambda)|\overline{\phi}|^2 d\lambda - \int_{-\infty}^{\infty}\left[\Gamma_0 - \eta_i b\left(\Gamma_0 - \Gamma_1\right)\right]|\phi|^2\frac{dl}{B}} \tag{7.10}$$

The input for ϕ here is $\phi_{(Pred)}$, which is the same input used for our original proxy approach. Once again, we only use this predicted mode structure here as it does not make sense to insert GENE data, which solely corresponds to the characteristics of the mode *beyond* the point of marginal stability. This is not the region of parameter space we are concerned with, as we only want to find the point at which the mode first exists. This is precisely at the point of marginal stability. Hence, we are not concerned with the subsequent behaviour of the mode, which is precisely what GENE models.

DIII-D Tokamak

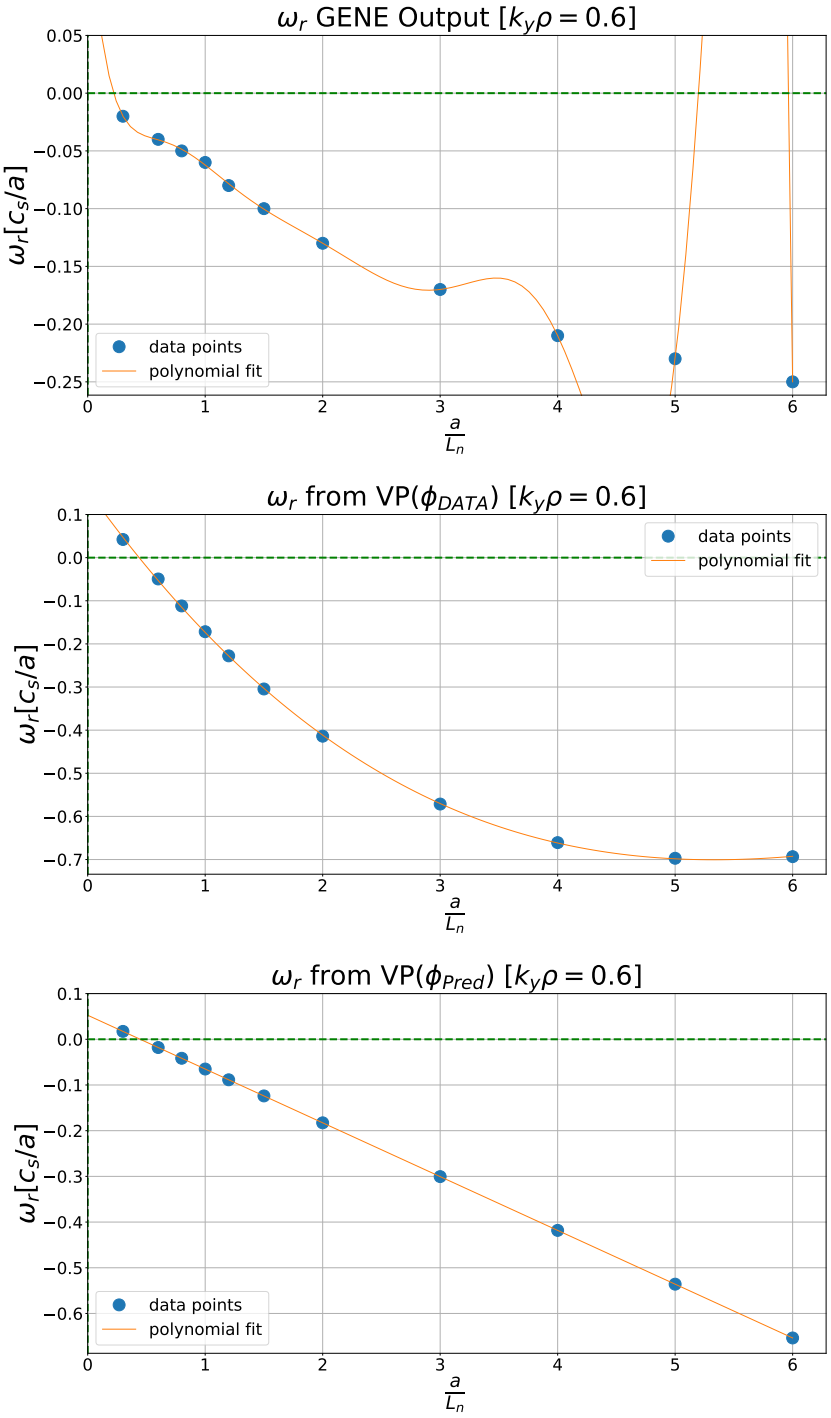

Figure 7.131: *Plots of the real mode frequency ω_r in the DIII-D tokamak from: (i) GENE, (ii) the variational principle using ϕ-data, and (iii) the variational principle using $\phi_{(Pred)}$.*

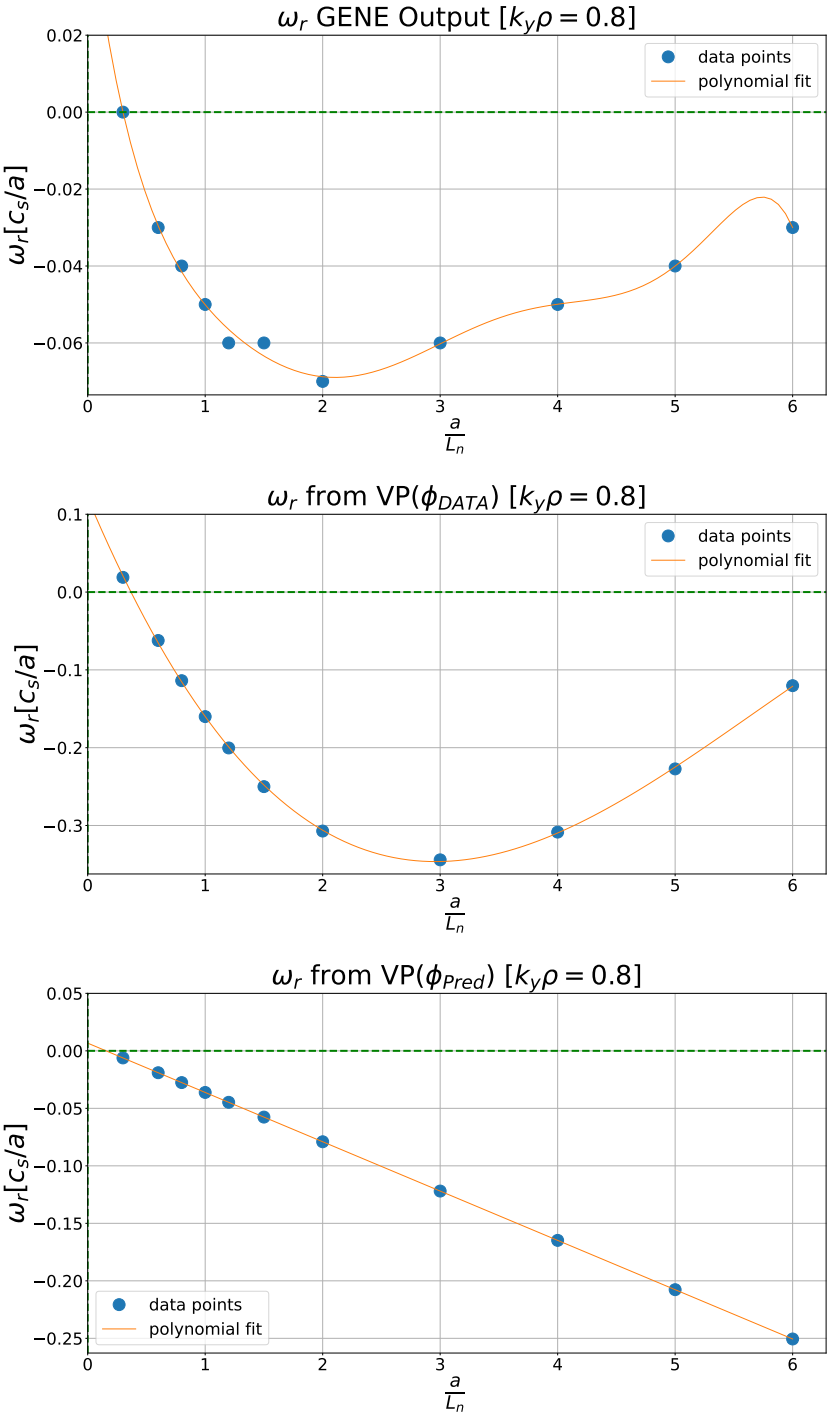

Figure 7.132: *Plots of the real mode frequency ω_r in the DIII-D tokamak from: (i) GENE, (ii) the variational principle using ϕ-data, and (iii) the variational principle using $\phi_{(Pred)}$.*

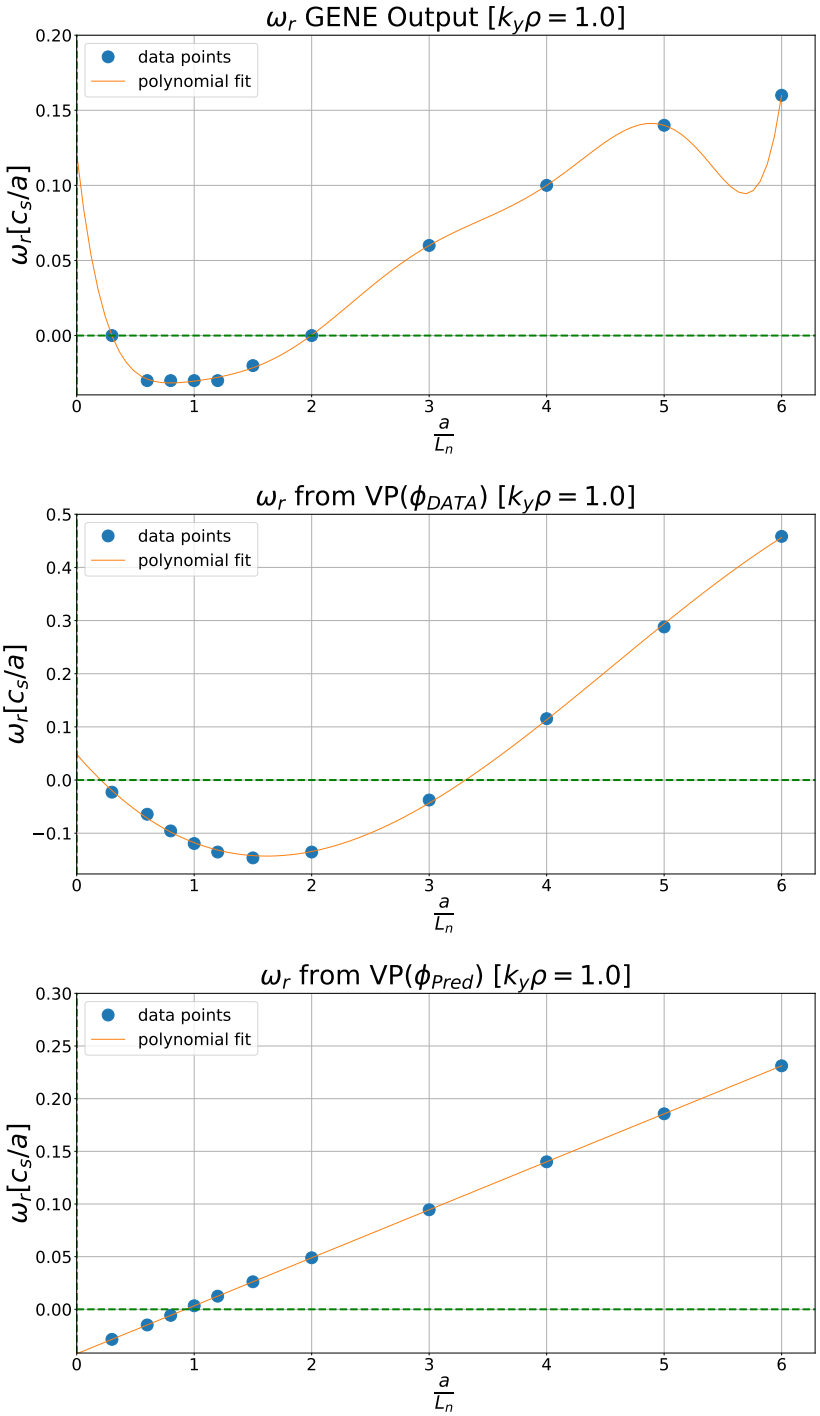

Figure 7.133: *Plots of the real mode frequency ω_r in the DIII-D tokamak from: (i) GENE, (ii) the variational principle using ϕ-data, and (iii) the variational principle using $\phi_{(Pred)}$.*

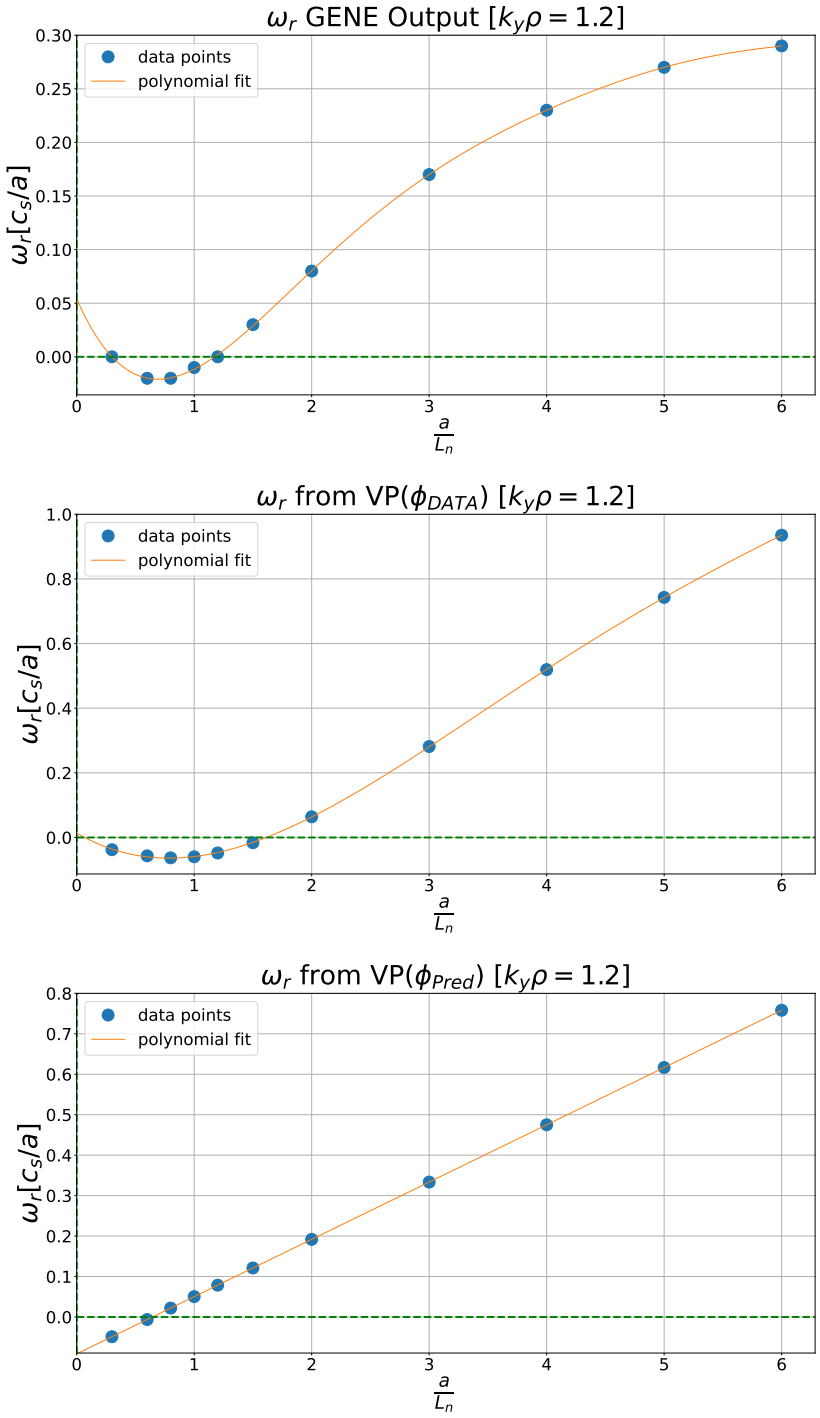

Figure 7.134: *Plots of the real mode frequency ω_r in the DIII-D tokamak from: (i) GENE, (ii) the variational principle using ϕ-data, and (iii) the variational principle using $\phi_{(Pred)}$.*

NCSX

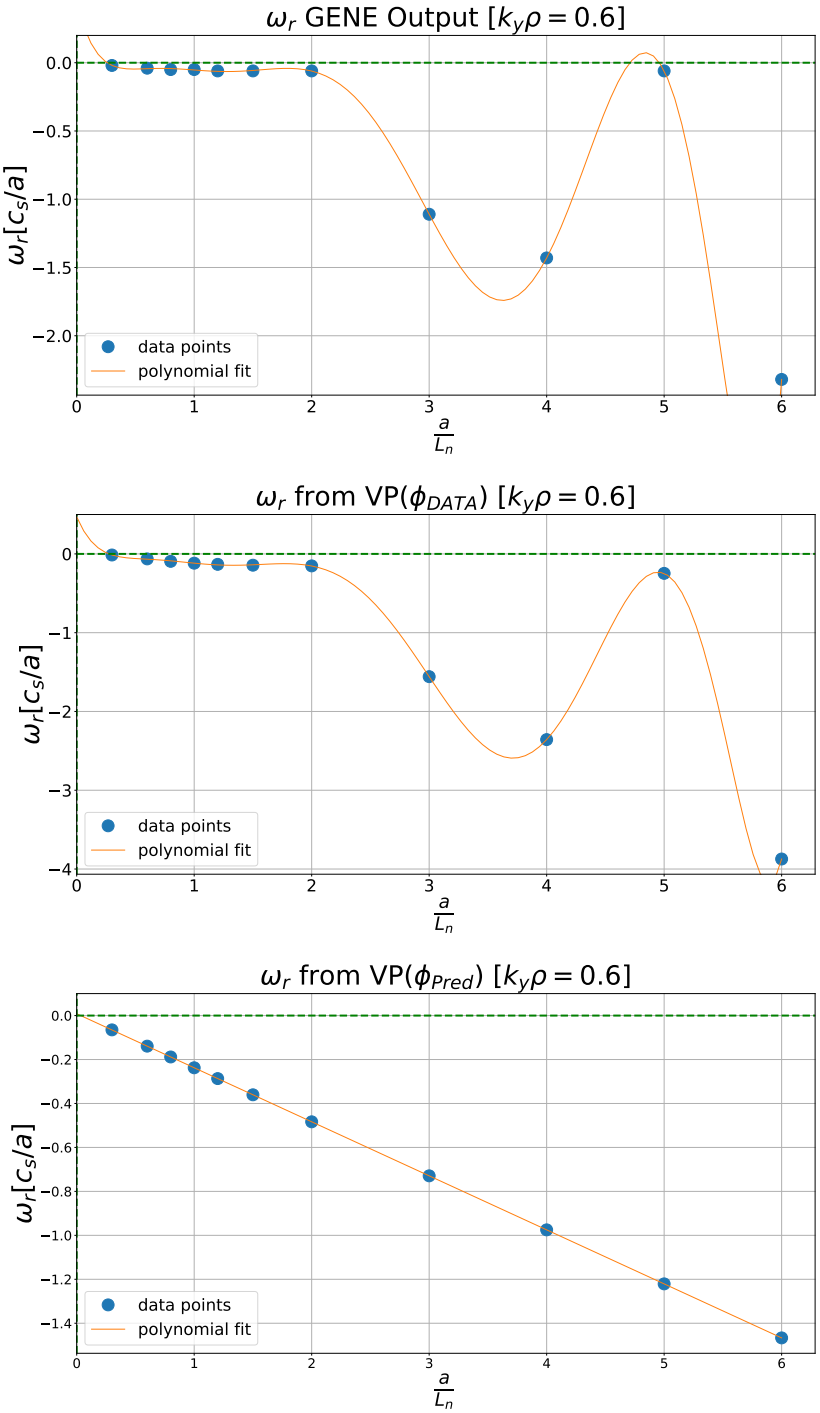

Figure 7.135: *Plots of the real mode frequency ω_r in NCSX from: (i) GENE, (ii) the variational principle using ϕ-data, and (iii) the variational principle using $\phi_{(Pred)}$.*

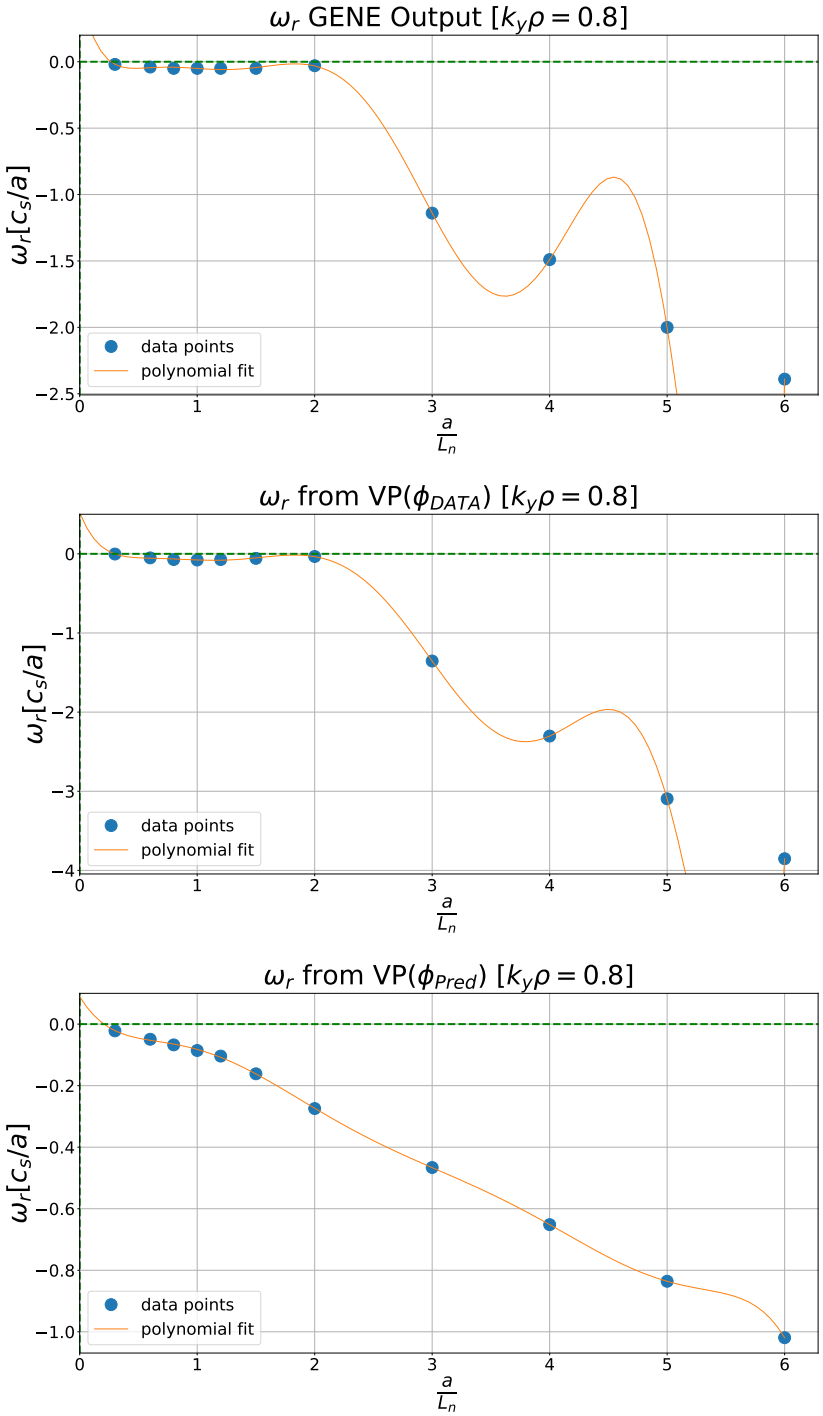

Figure 7.136: *Plots of the real mode frequency ω_r in NCSX from: (i) GENE, (ii) the variational principle using ϕ-data, and (iii) the variational principle using $\phi_{(Pred)}$.*

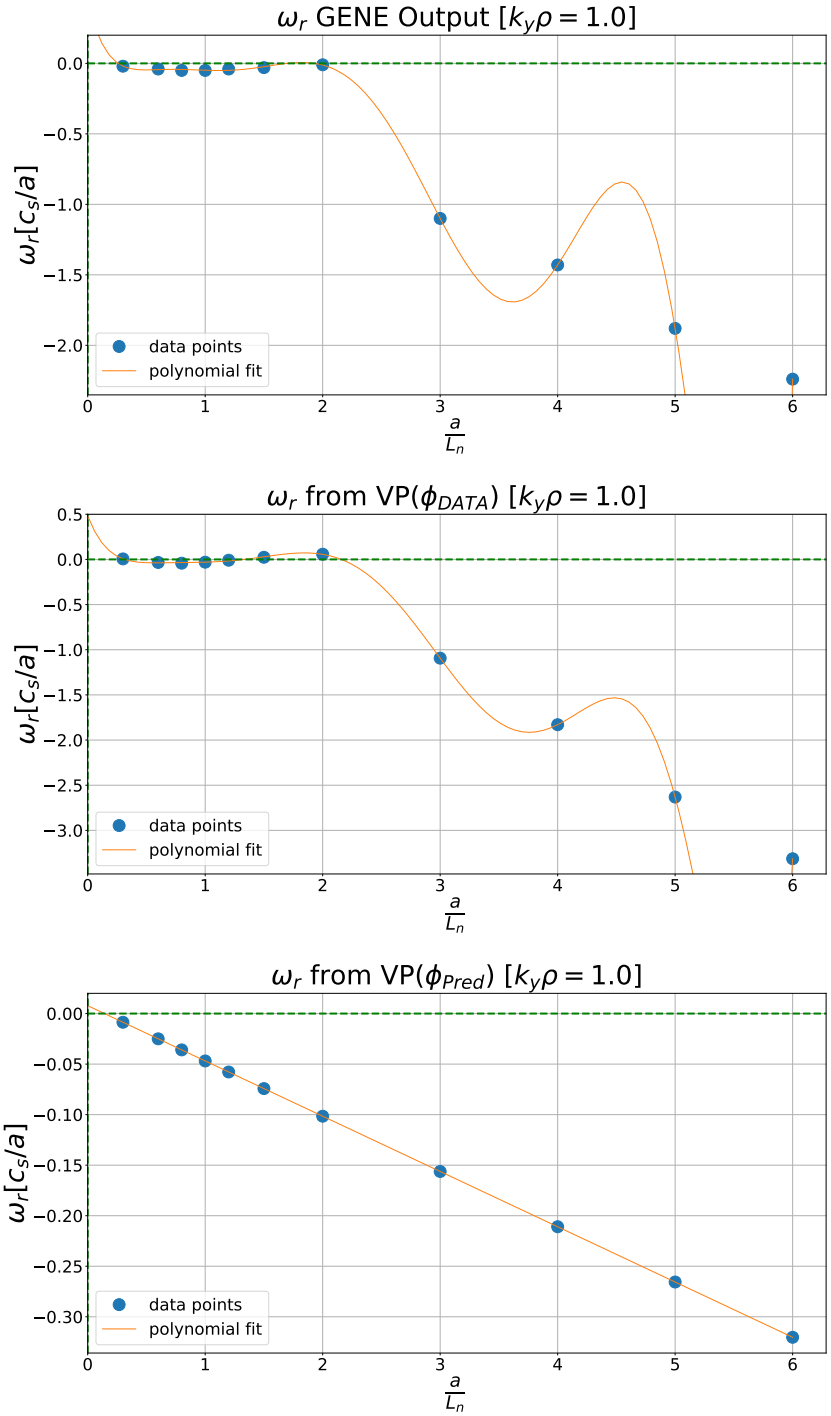

Figure 7.137: *Plots of the real mode frequency ω_r in NCSX from: (i) GENE, (ii) the variational principle using ϕ-data, and (iii) the variational principle using $\phi_{(Pred)}$.*

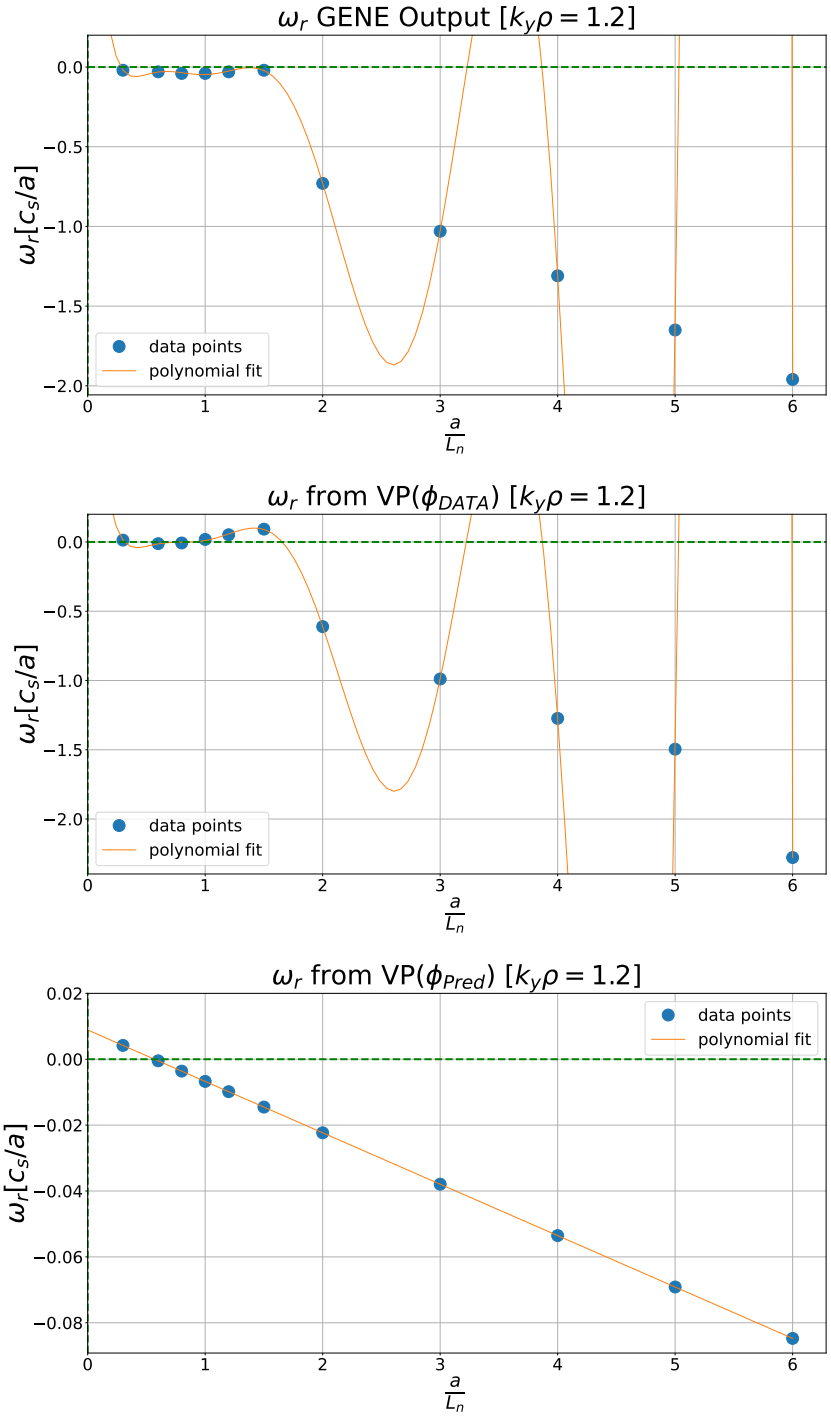

Figure 7.138: *Plots of the real mode frequency ω_r in NCSX from: (i) GENE, (ii) the variational principle using ϕ-data, and (iii) the variational principle using $\phi_{(Pred)}$.*

W7-X (SC)

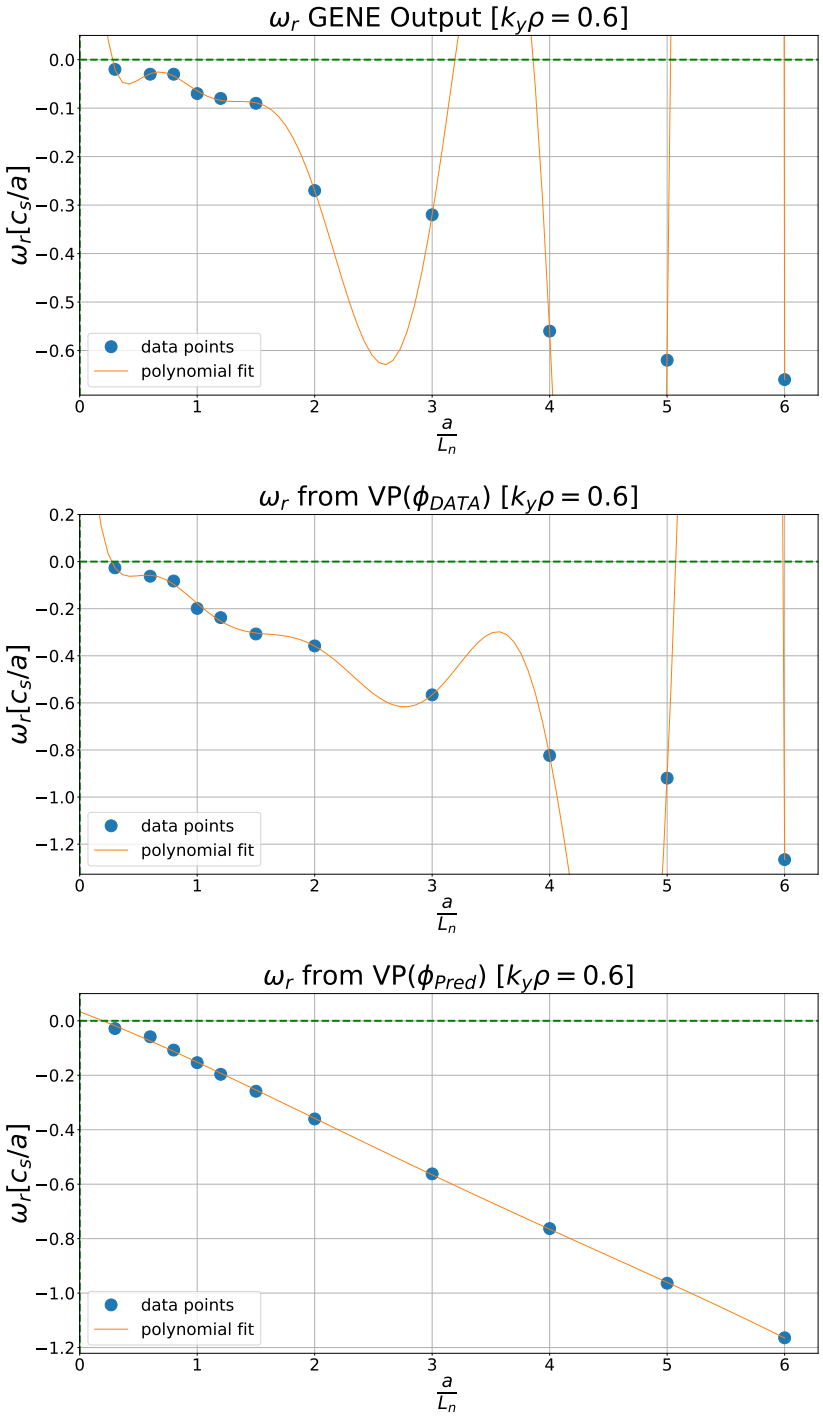

Figure 7.139: *Plots of the real mode frequency ω_r in W7-X (SC) from: (i) GENE, (ii) the variational principle using ϕ-data, and (iii) the variational principle using $\phi_{(Pred)}$.*

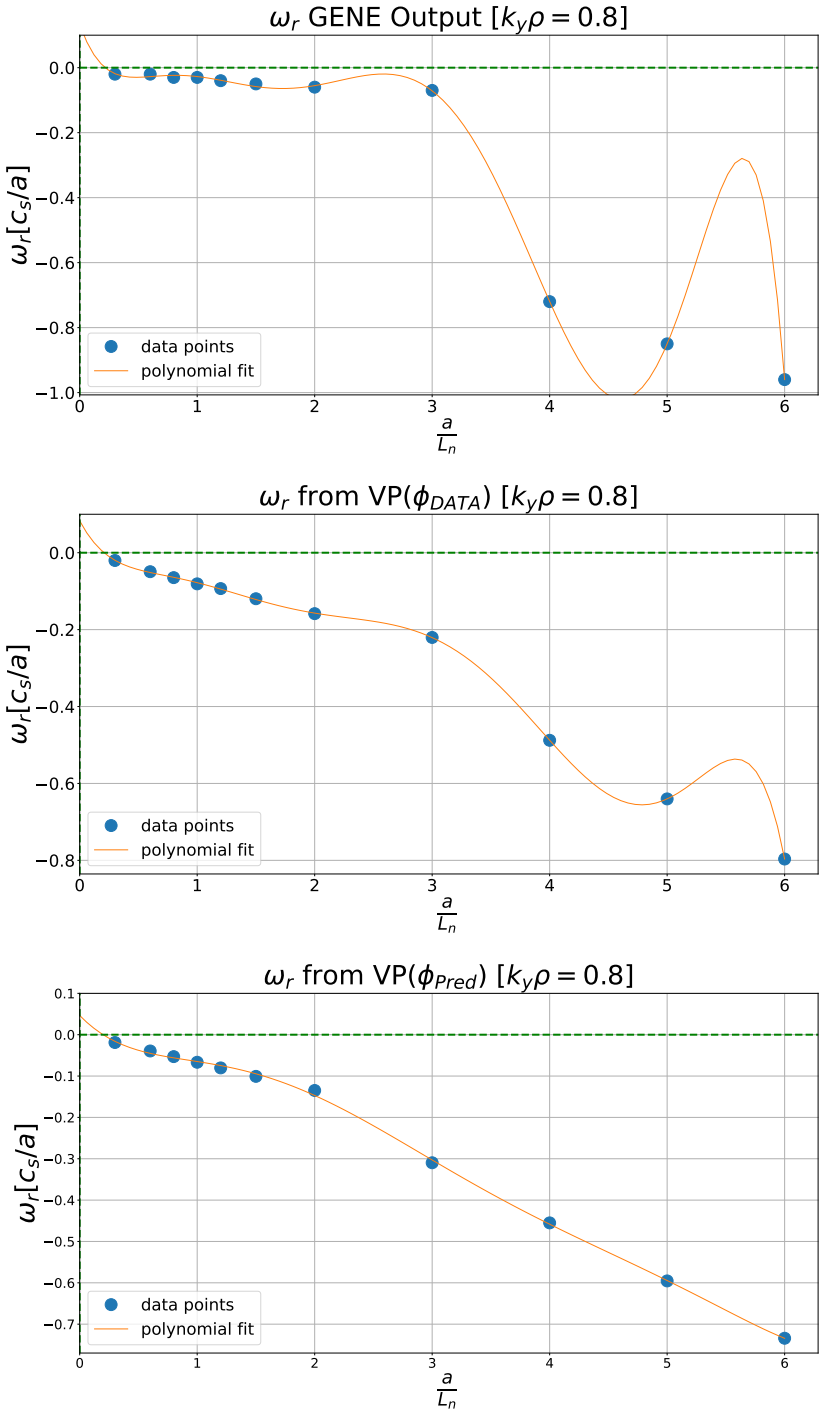

Figure 7.140: *Plots of the real mode frequency ω_r in W7-X (SC) from: GENE, the variational principle using ϕ-data, and the variational principle using $\phi_{(Pred)}$.*

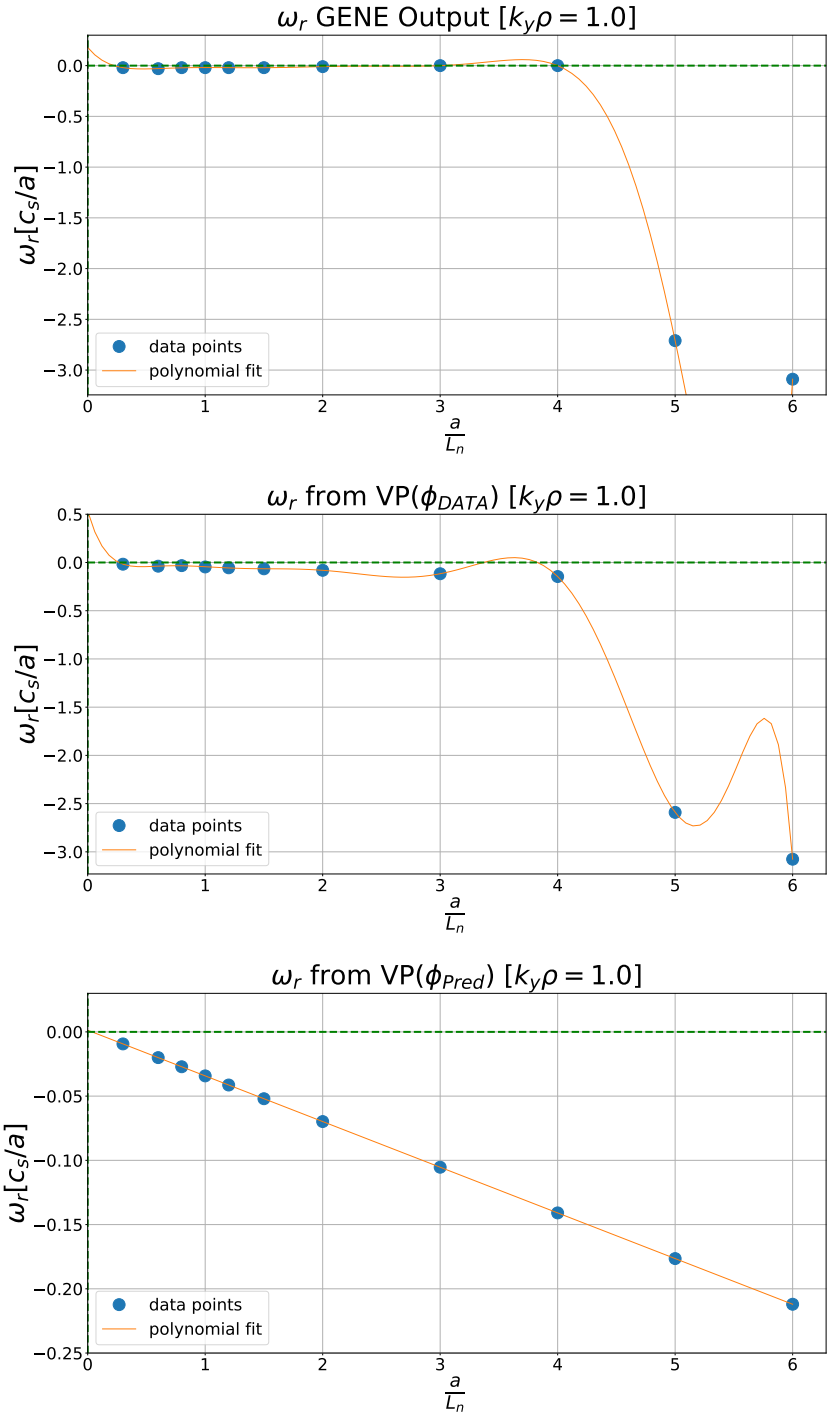

Figure 7.141: *Plots of the real mode frequency ω_r in W7-X (SC) from: (i) GENE, (ii) the variational principle using ϕ-data, and (iii) the variational principle using $\phi_{(Pred)}$.*

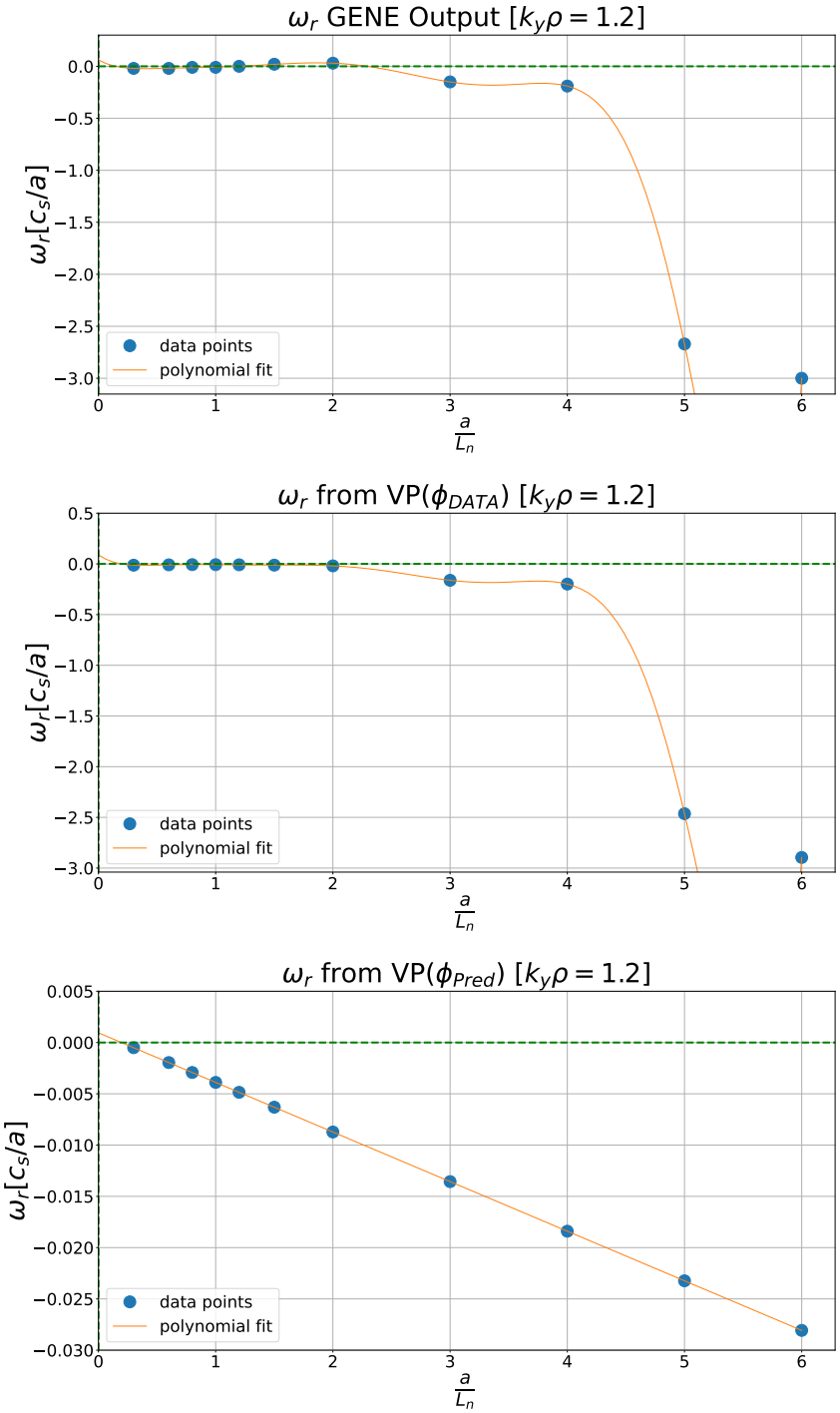

Figure 7.142: *Plots of the real mode frequency ω_r in W7-X (SC) from: (i) GENE, (ii) the variational principle using ϕ-data, and (iii) the variational principle using $\phi_{(Pred)}$.*

W7-X (HM)

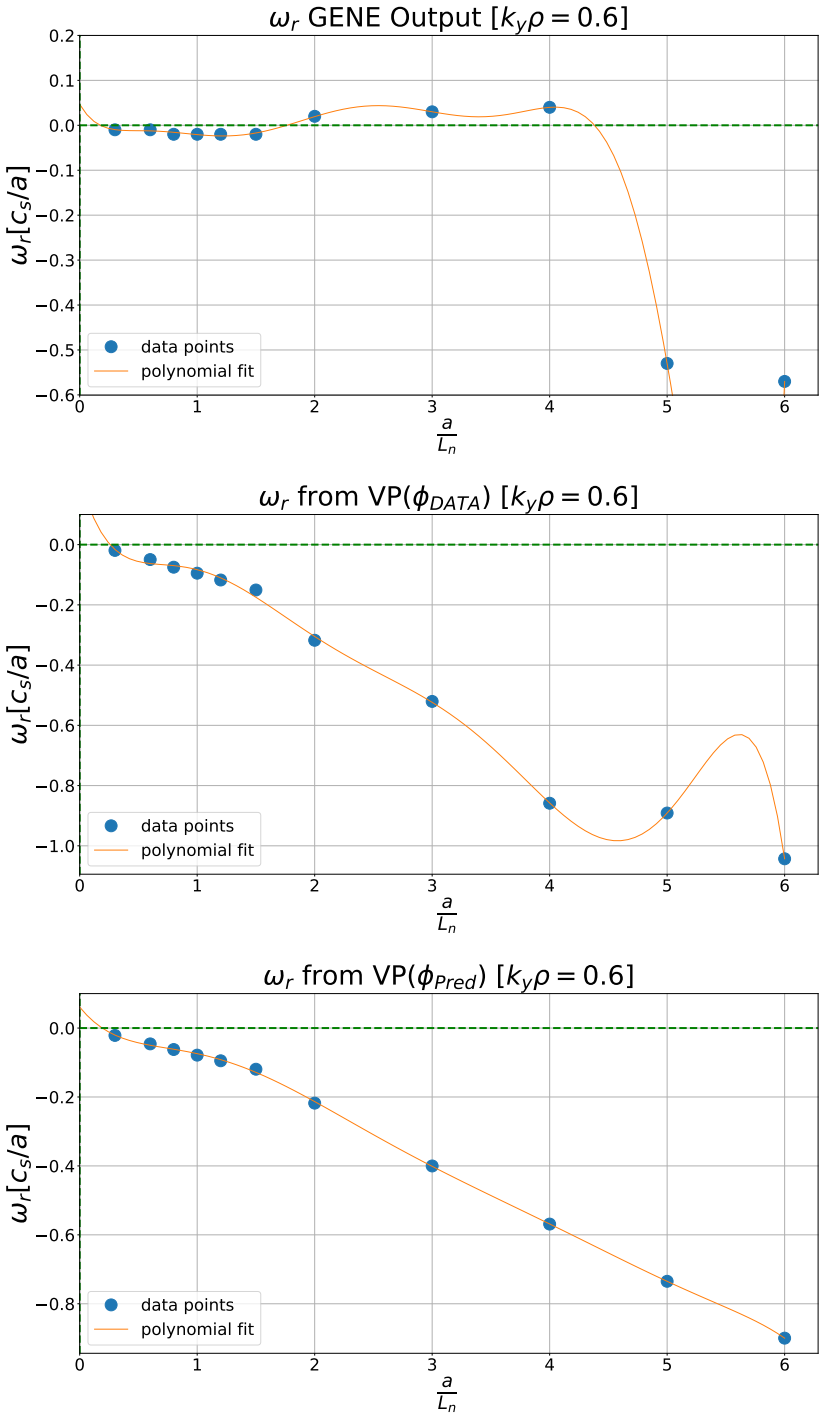

Figure 7.143: *Plots of the real mode frequency ω_r in W7-X (HM) from: (i) GENE, (ii) the variational principle using ϕ-data, and (iii) the variational principle using $\phi_{(Pred)}$.*

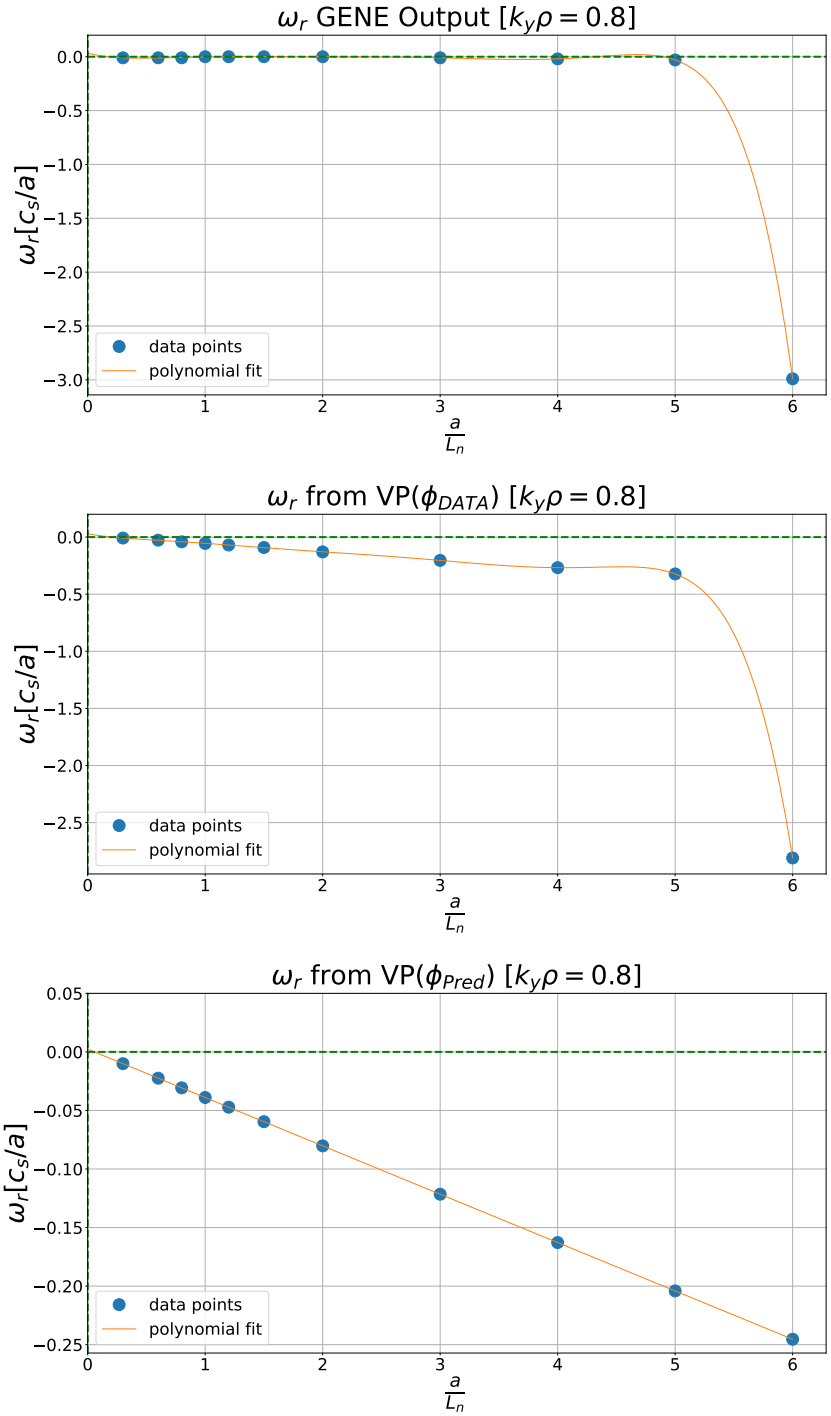

Figure 7.144: *Plots of the real mode frequency ω_r in W7-X (HM) from: (i) GENE, (ii) the variational principle using ϕ-data, and (iii) the variational principle using $\phi_{(Pred)}$.*

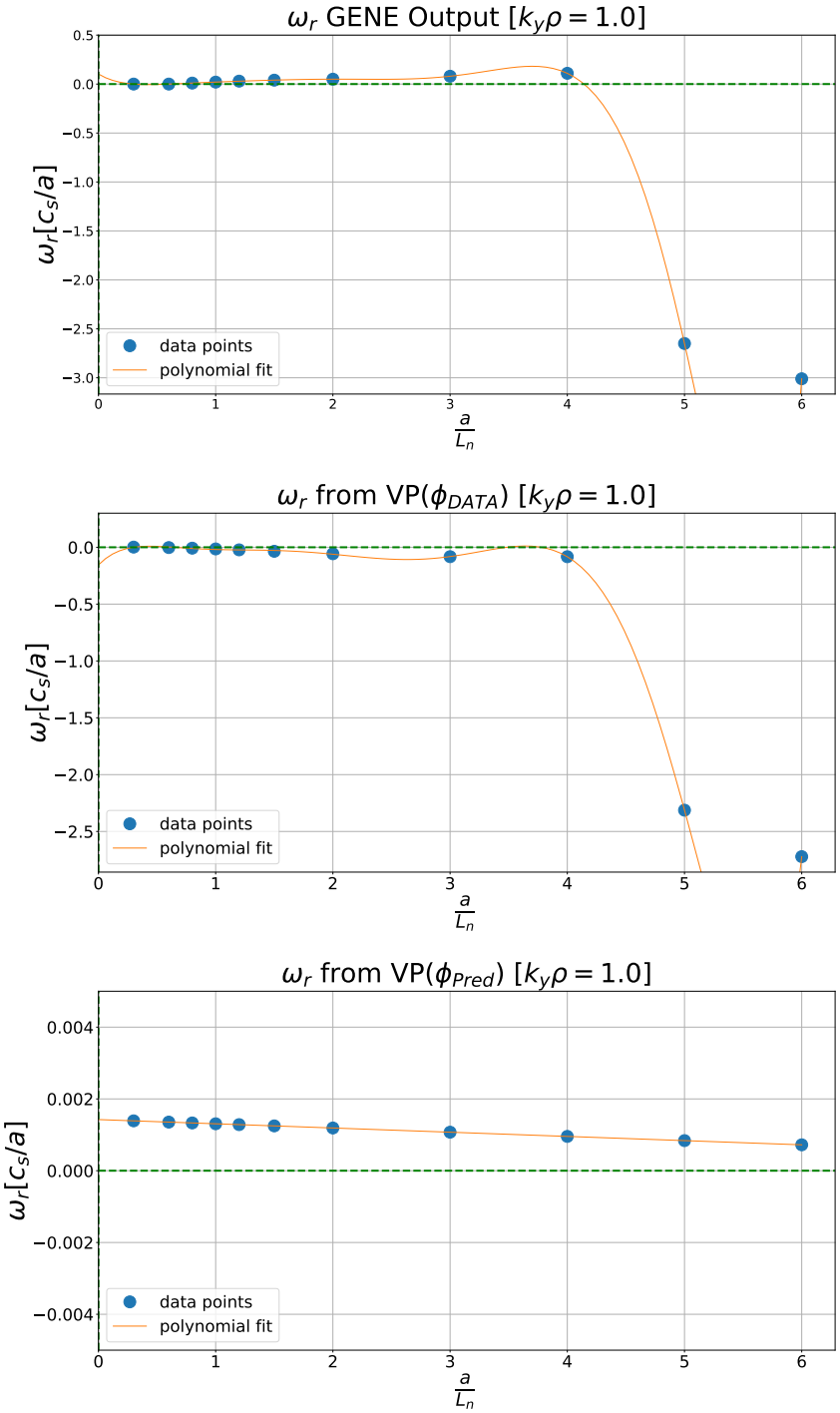

Figure 7.145: *Plots of the real mode frequency ω_r in W7-X (HM) from: (i) GENE, (ii) the variational principle using ϕ-data, and (iii) the variational principle using $\phi_{(Pred)}$.*

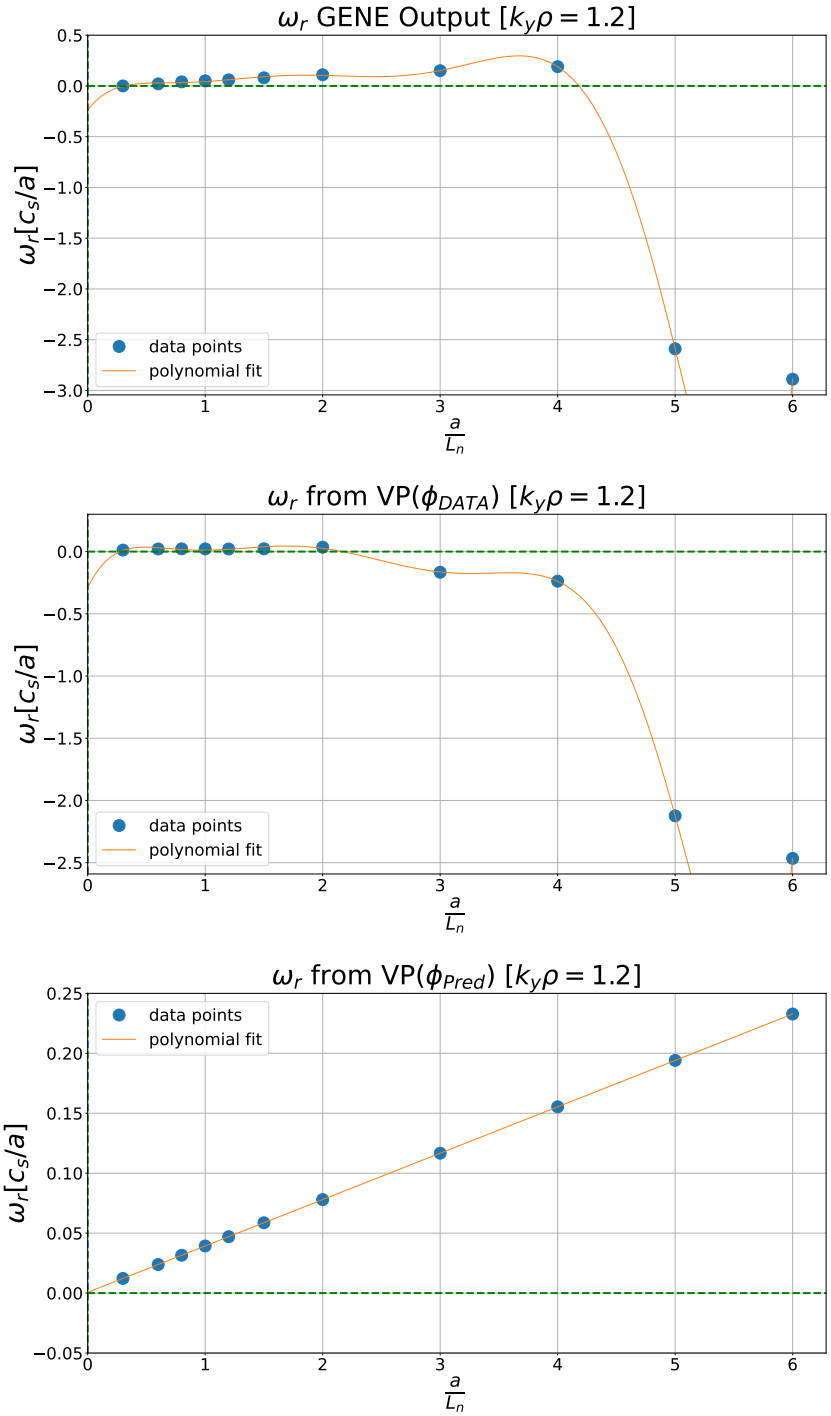

Figure 7.146: *Plots of the real mode frequency ω_r in W7-X (HM) from: (i) GENE, (ii) the variational principle using ϕ-data, and (iii) the variational principle using $\phi_{(Pred)}$.*

W7-X (LM)

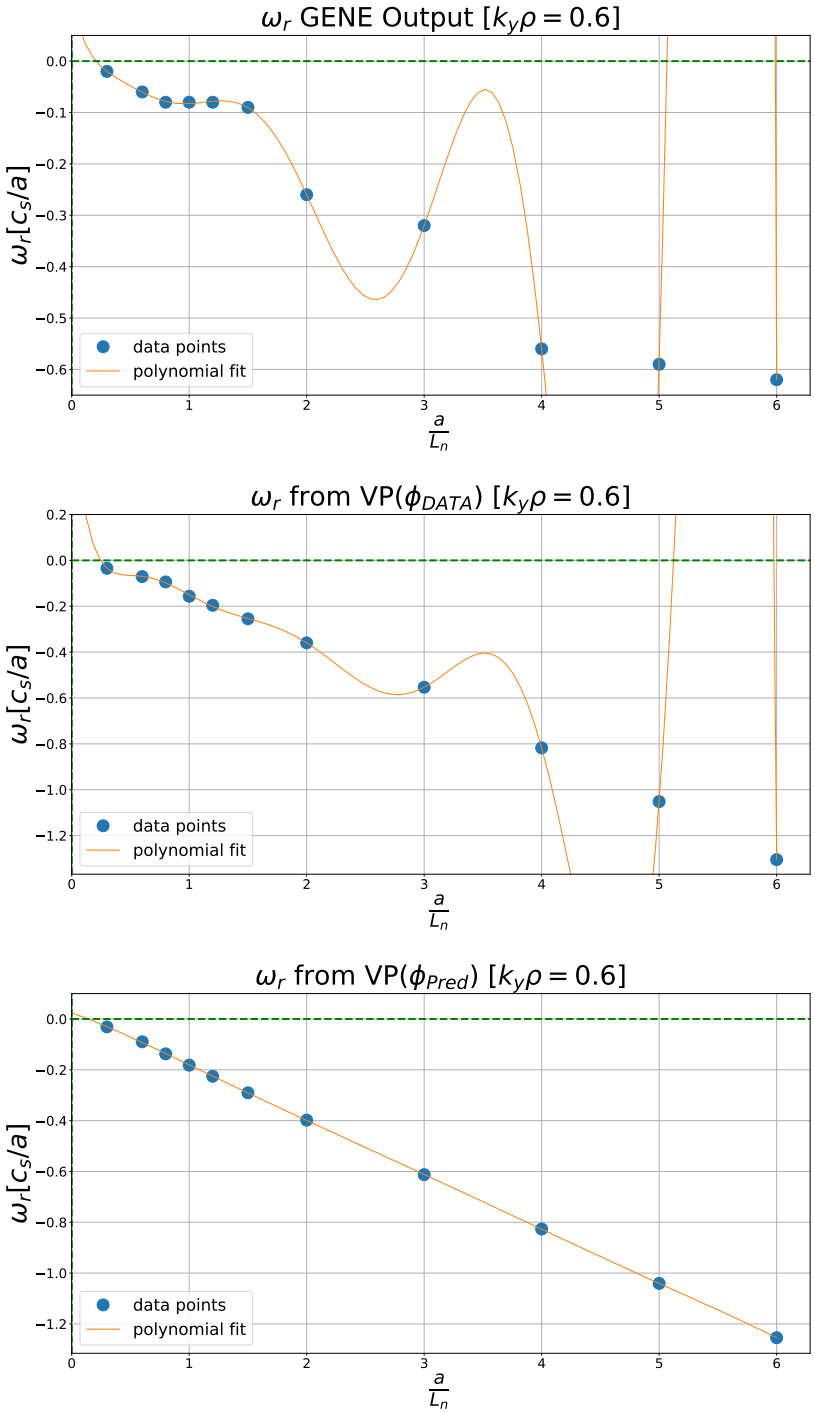

Figure 7.147: *Plots of the real mode frequency ω_r in W7-X (LM) from: (i) GENE, (ii) the variational principle using ϕ-data, and (iii) the variational principle using $\phi_{(Pred)}$.*

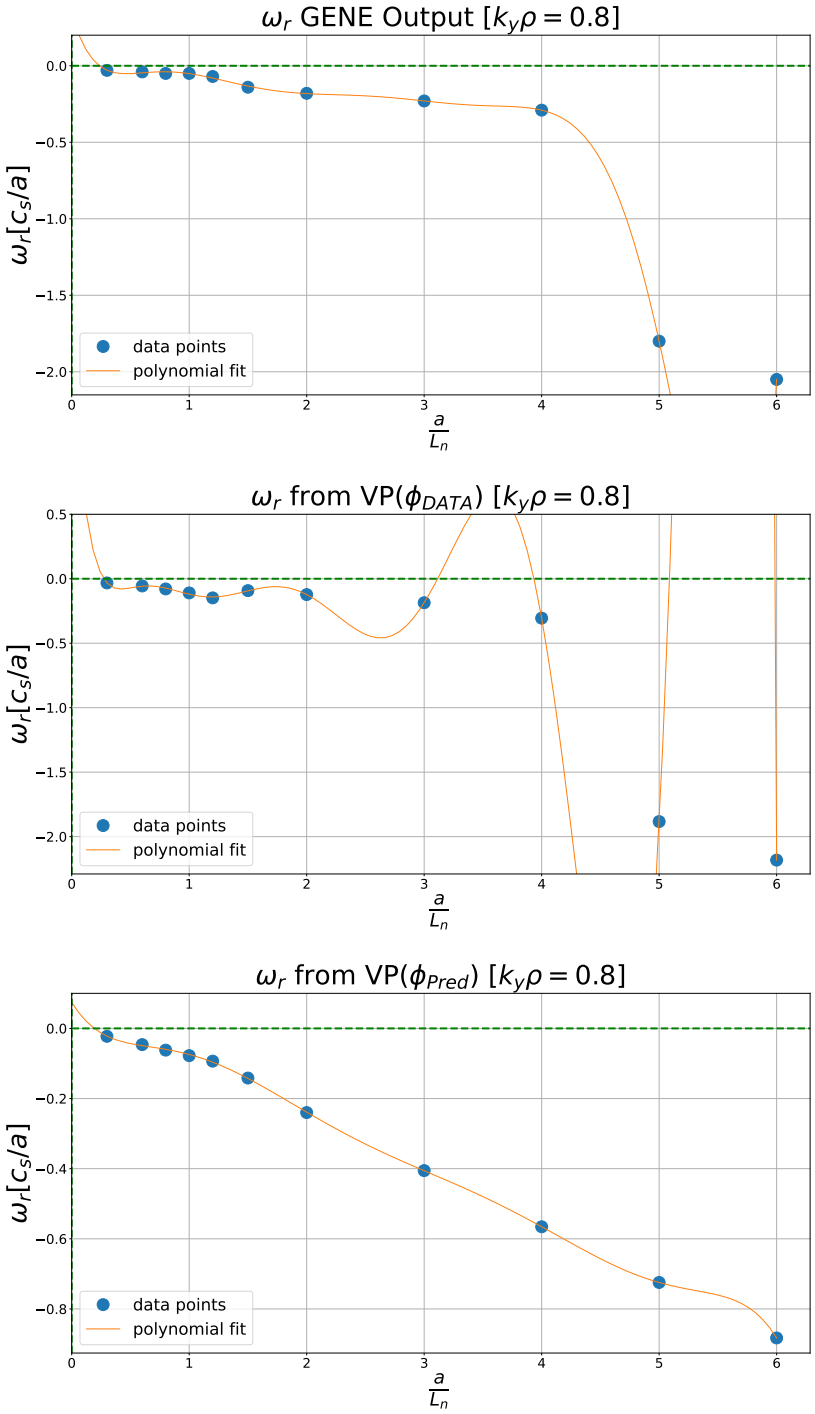

Figure 7.148: *Plots of the real mode frequency ω_r in W7-X (LM) from: (i) GENE, (ii) the variational principle using ϕ-data, and (iii) the variational principle using $\phi_{(Pred)}$.*

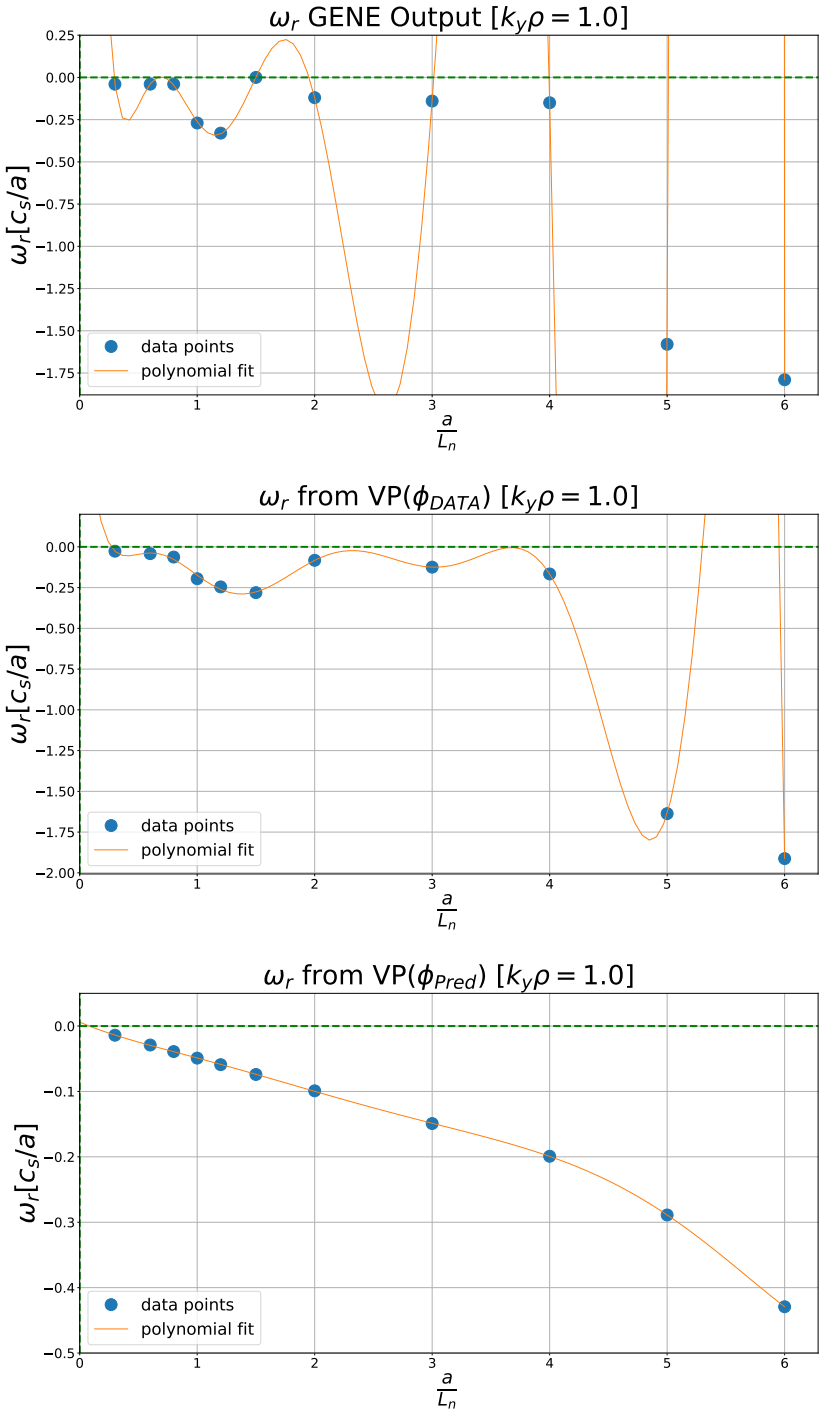

Figure 7.149: *Plots of the real mode frequency ω_r in W7-X (LM) from: (i) GENE, (ii) the variational principle using ϕ-data, and (iii) the variational principle using $\phi_{(Pred)}$.*

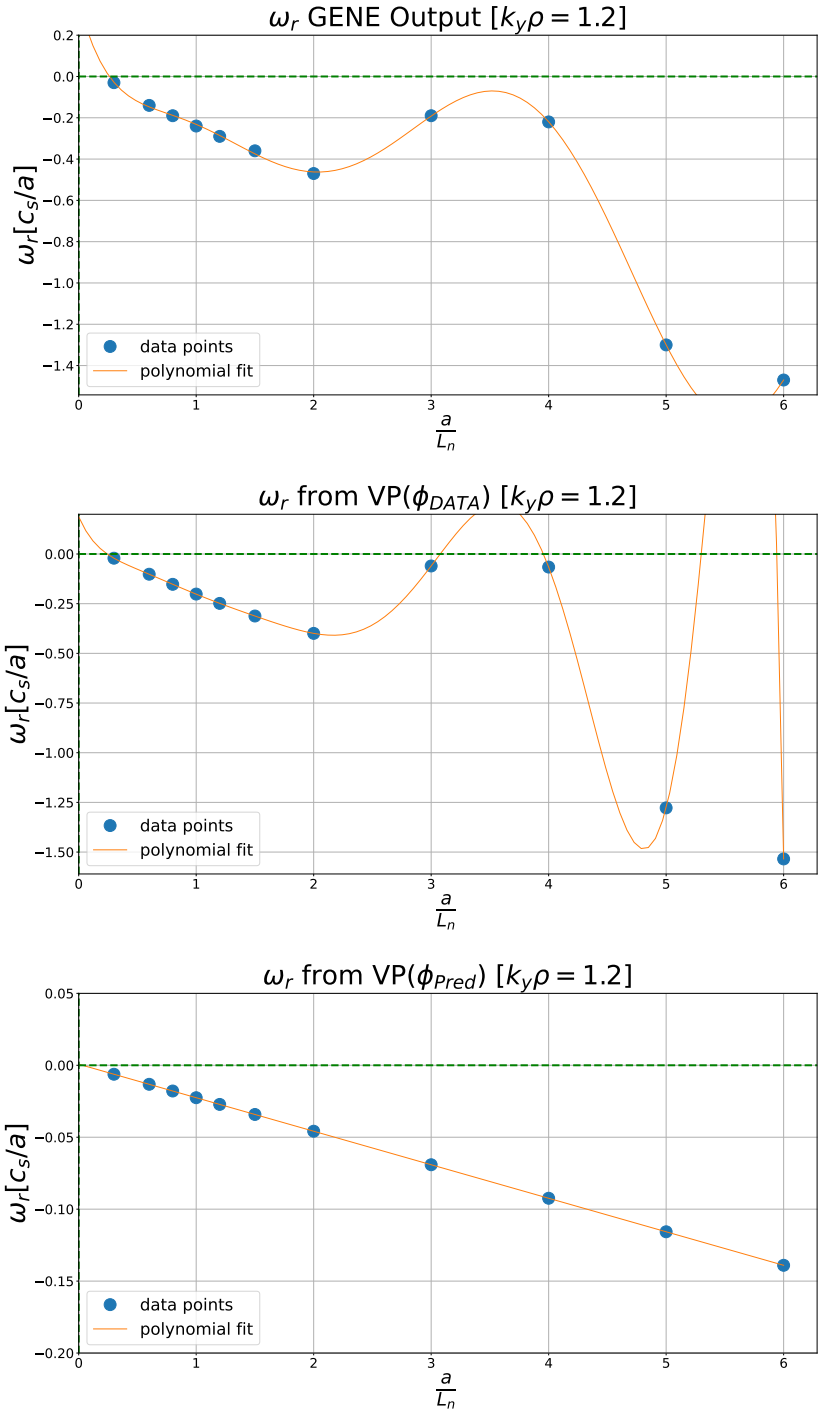

Figure 7.150: *Plots of the real mode frequency ω_r in W7-X (LM) from: (i) GENE, (ii) the variational principle using ϕ-data, and (iii) the variational principle using $\phi_{(Pred)}$.*

HSX

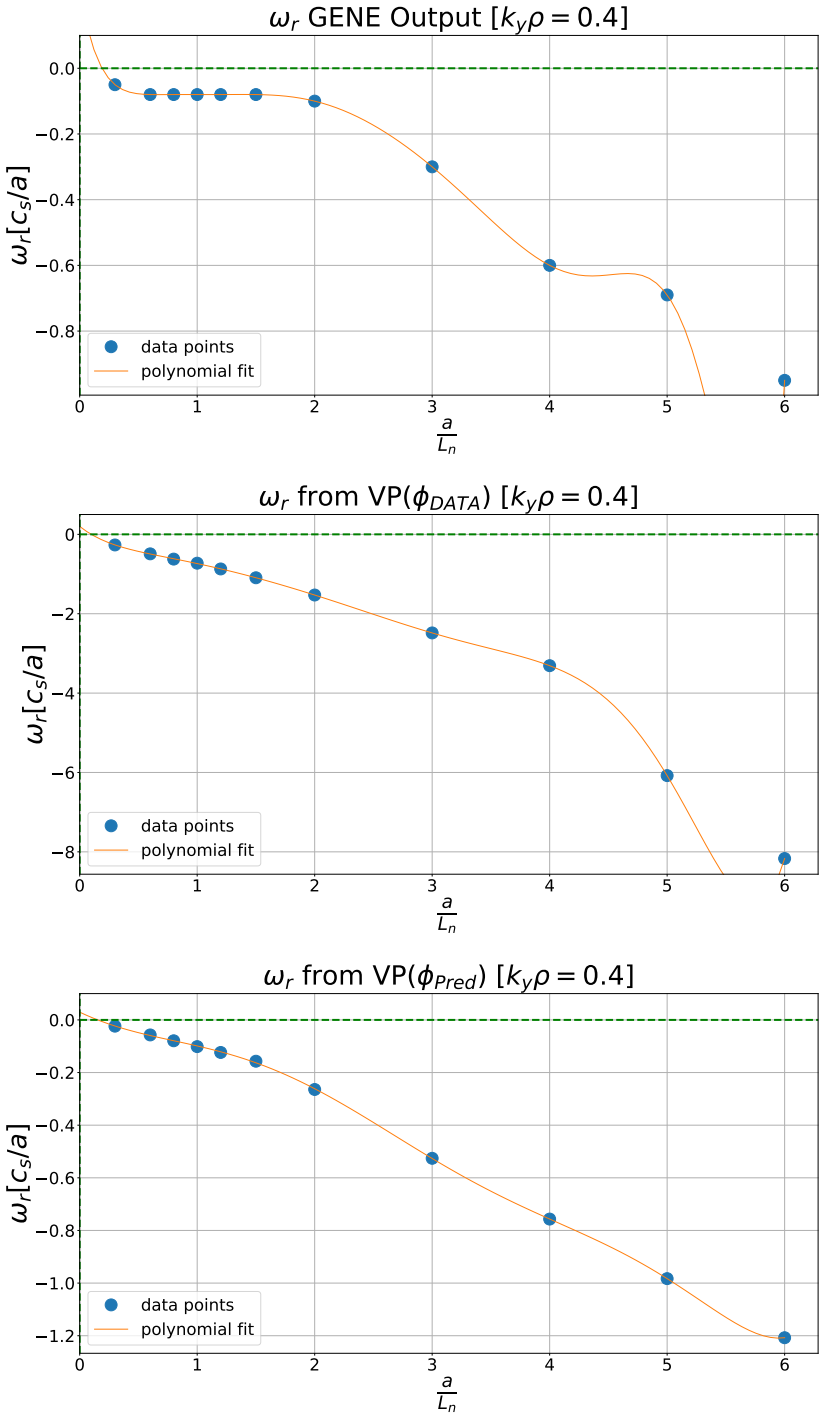

Figure 7.151: *Plots of the real mode frequency ω_r in HSX from: (i) GENE, (ii) the variational principle using ϕ-data, and (iii) the variational principle using $\phi_{(Pred)}$.*

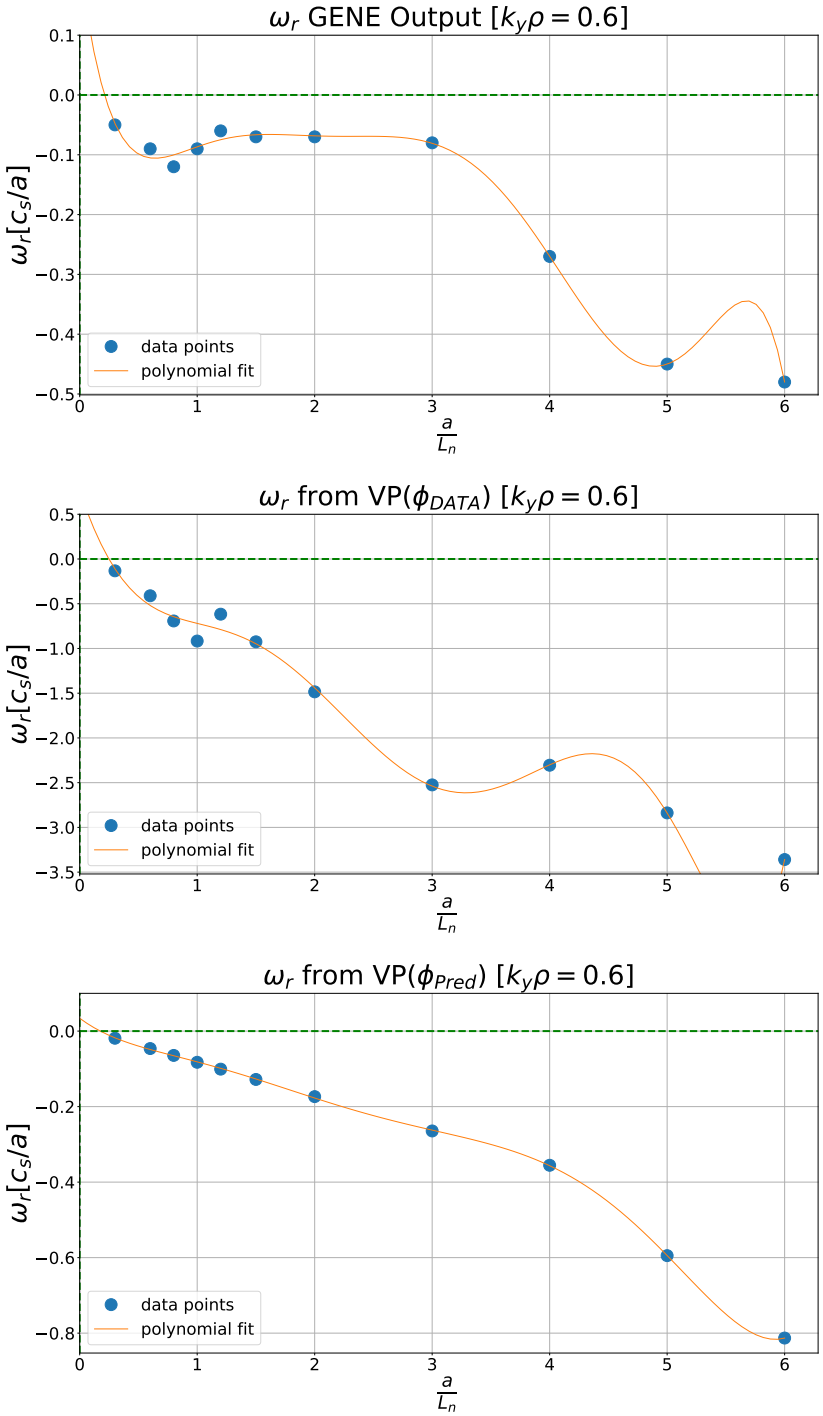

Figure 7.152: *Plots of the real mode frequency ω_r in HSX from: (i) GENE, (ii) the variational principle using ϕ-data, and (iii) the variational principle using $\phi_{(Pred)}$.*

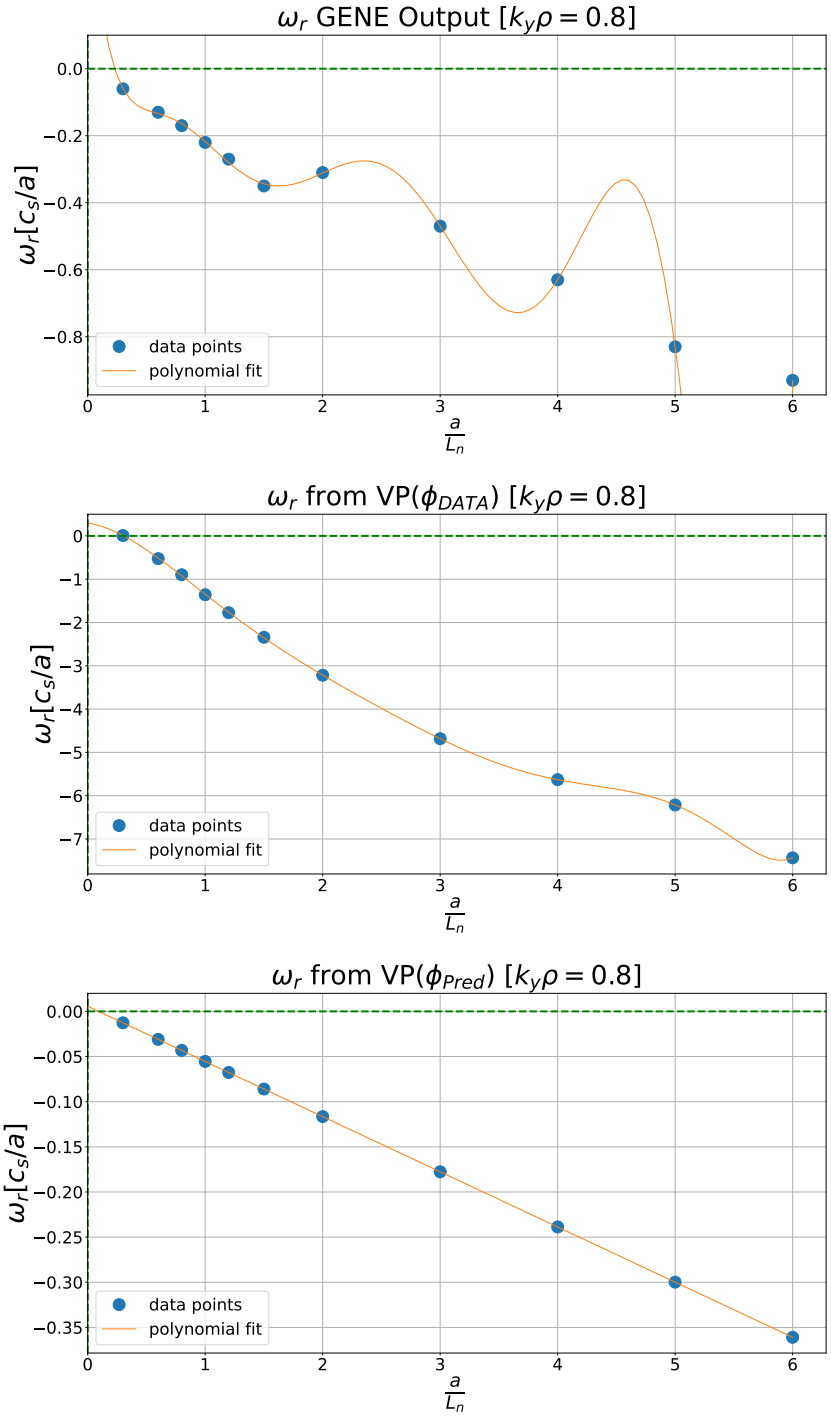

Figure 7.153: *Plots of the real mode frequency ω_r in HSX from: (i) GENE, (ii) the variational principle using ϕ-data, and (iii) the variational principle using $\phi_{(Pred)}$.*

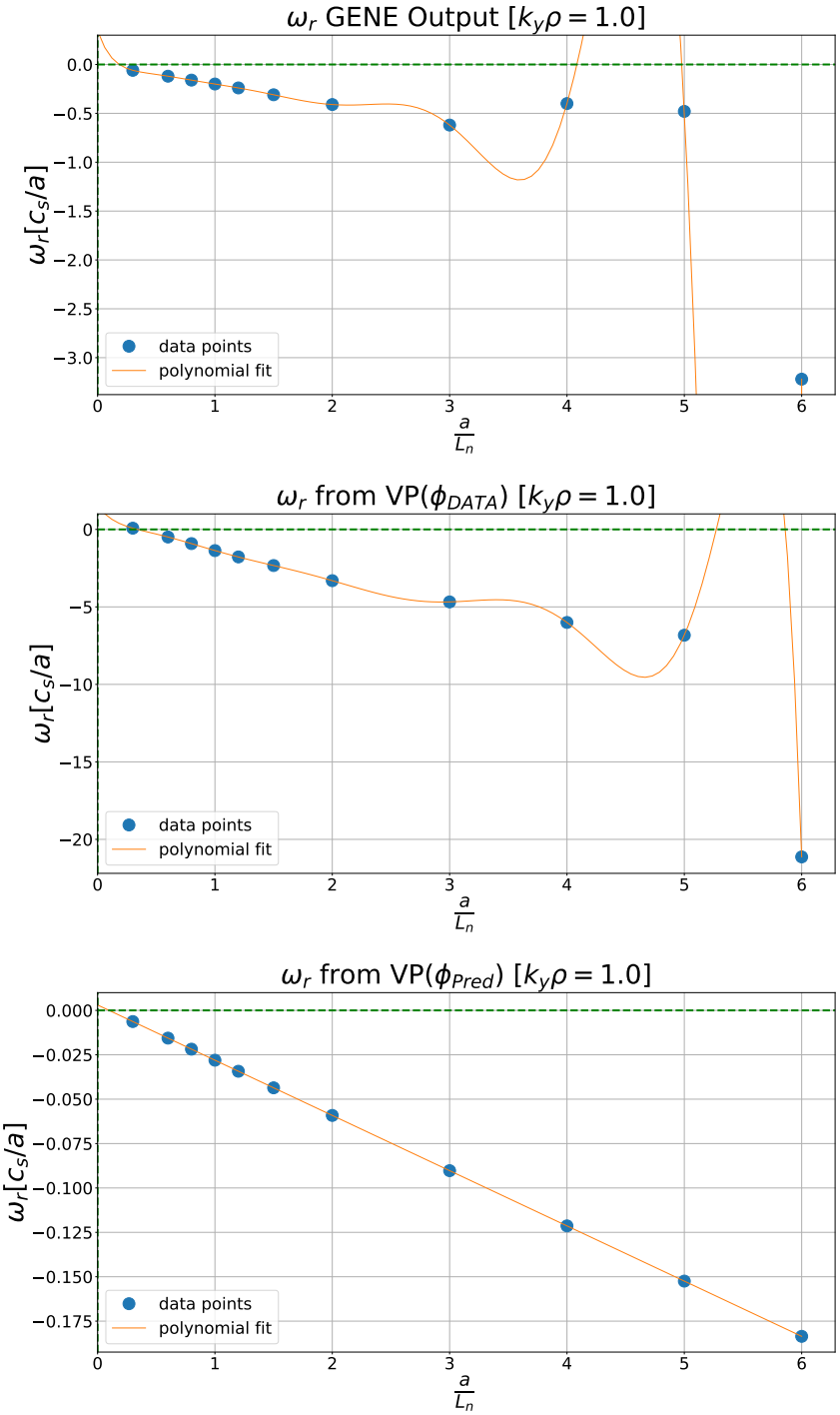

Figure 7.154: *Plots of the real mode frequency ω_r in HSX from: (i) GENE, (ii) the variational principle using ϕ-data, and (iii) the variational principle using $\phi_{(Pred)}$.*

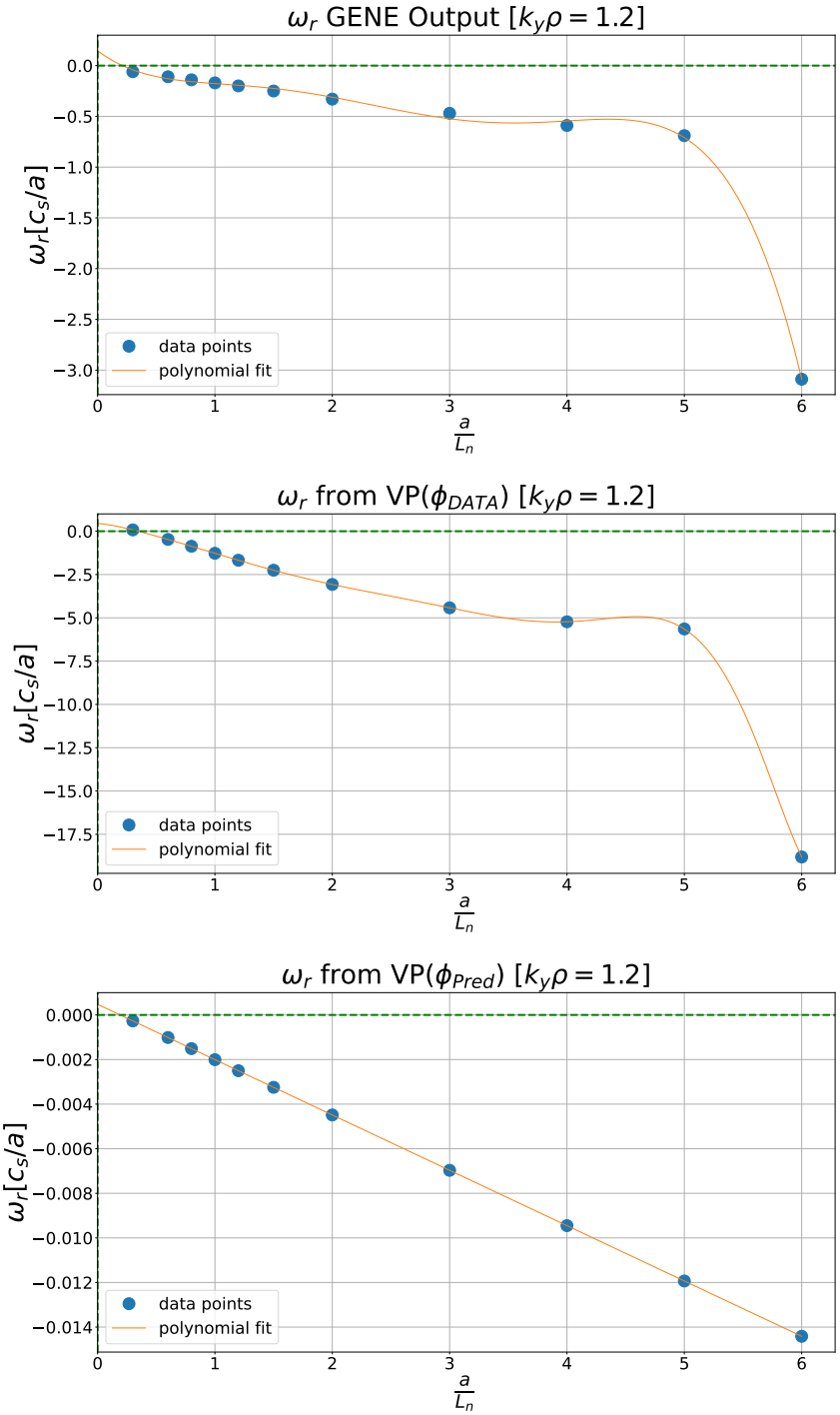

Figure 7.155: *Plots of the real mode frequency ω_r in HSX from: (i) GENE, (ii) the variational principle using ϕ-data, and (iii) the variational principle using $\phi_{(Pred)}$.*

Discussion of Alternative Approach

We now discuss the results of this alternative approach to approximating the critical density gradient. So far, we have presented three separate forms of the real mode frequency ω_r for each wavenumber in all geometric configurations considered. As already stated earlier in this section, each of these plots of ω_r has been derived by different means - the first uses GENE directly, the second uses our variational principle and GENE data for ϕ, and finally, the third uses our variational principle and the predicted mode structure $\phi_{(Pred)}$. The next step was to calculate the lowest positive root for each of these plots. The results of this step are compiled in Table 7.2, where we compare these approximate critical density gradient values with those obtained using the growth rates γ from GENE directly. Following from this table, scatter-correlation plots are presented comparing the critical density gradient values as obtained from the GENE growth rates, γ, and those from setting $\omega_{r(GENE)} = 0$. This is the idealised case for this proxy, as it relies totally on GENE data for ω_r. Regardless, these plots should provide some insight on whether the underlying basis for this proxy is correct, i.e., $\omega_r \stackrel{!}{=} \gamma \stackrel{!}{=} 0$ at marginal stability. We do not provide scatter-correlation plots for the remaining columns in Table 7.2, as they do not shed further light on the basis of this alternative proxy.

As we can see in the last column of Table 7.2 ($VP_{(\phi_{Pred})}$ column), which corresponds to the case of using a predicted mode structure as the input for our variational principle, we have exact agreement between some of these results and those obtained by the original proxy (see Table 7.1). More specifically, there is full agreement for all of the DIII-D tokamak values in both tables, and partial agreement for the other geometric configurations. This is most likely due to the fact that both of these procedures relied on the same predicted mode structure profiles, and both yield their solution when $\omega_r = 0$. The discrepancies may be explained by the fact that the original and alternative methods obtained these proxy results by different means. The former utilised Eqn. 6.87 to find precise values for the proxy, which agreed with the plotted results in section 7.2.2. The latter method relied on finding the roots using fitted polynomials, which may have been subject to some error in measurement. Despite these discrepancies, the overall similarity in results may indicate that our alternative method for approximating the critical density gradient - although more simplistic and arguably more expedient - may be just as effective as our more laborious approach taken in our original method.

Looking again to Table 7.2, we see that the results from the growth rate γ are often in the same neighbourhood as those obtained from the GENE output of ω_r. This can be seen more visually in the scatter-correlation plots (see Figures 7.156, 7.157, 7.158 and 7.159). These plots show that we have moderate-to-strong positive correlations for all wavenumbers considered, which is a good indicator that the basis for this proxy may be correct. Perfect agreement was not expected, or even possible, due to the fact that both of these quantities (γ and ω_r from GENE) are subject to error in measurement from our polynomial-fitting procedure. However, the approximate agreement here *may* indicate that our theoretical result in section 6.2 ($\omega_r \stackrel{!}{=} \gamma \stackrel{!}{=} 0$ at marginal stability) is

validated. To be clear, we are not claiming this to be true with full certainty, but we are proposing that it *may* hold truth. A deeper investigation into this would be needed to see if this claim holds under further scrutiny. A potential means to following through with this would be to obtain more high resolution GENE data for lower density gradient values (closer to marginal stability), in order to remove some of the uncertainty in our measurement procedure.
When looking to our results obtained using the variational principle and ϕ-data from GENE as an input ($VP_{(\phi_{DATA})}$ column), we see some moderate agreement between these values and those from the GENE growth rates. In particular, NCSX, W7-X (SC) and W7-X (LM) perhaps show the best agreement for this comparison. For most geometries (with perhaps the exceptions of DIII-D and HSX), the spread of values for different wavenumbers is relatively low within a given configuration, which is consistent with our benchmark γ column. This may indicate that there is greater systematic error present, compared to random error. Our procedure in this case relied on the idealised trial functions of ϕ-data from GENE, so any discrepancies are most likely due to our overall procedure as opposed to our mode structure input.
Finally, when looking to our results obtained using the variational principle and $\phi_{(Pred)}$ as an input ($VP_{(\phi_{Pred})}$ column), we see less agreement than in our previous two case with the γ column. This is most likely due to some systematic error in our procedure overall, but also due to our heavy dependence on the mode frequency proxy, which in turn depended on the mode structure prediction. Controllable random error could then be reduced if an enhanced prediction for $\phi_{(Pred)}$ was utilised, thus improving our mode frequency proxy. However, some systematic error would still be present after this, as was found in the previous case where the trial function was idealised.

If our work here is deemed to be valid and worth further investigation, the next steps to take beyond these results would be as follows. In order to find an optimal geometry that maximises the critical density gradient - thus delaying the onset of the problematic TEM instability - we need an analytical expression for the critical density gradient, which depends on the geometric quantities that we can manipulate. These are the magnetic field strength B and the curvature κ. From our alternative method of approximating the critical density gradient (section 6.2), we found an expression that meets this criterion:

$$\left(\frac{a}{L_{n_e}}\right)_{Crit} = \frac{\left(\frac{eBa}{k_\alpha T_e}\right)\left\{\int_{-\infty}^{\infty}\left[2\Gamma_0 - b\left(\Gamma_0 - \Gamma_1\right)\right]\frac{\hat{\omega}_{di}}{2}|\phi|^2\frac{dl}{B} + \frac{1}{2}\int_{\frac{1}{B_{max}}}^{\frac{1}{B_{min}}}\sum_{\text{wells}}\tau(\lambda)\left(\frac{3}{2}F_e\overline{G(\lambda)}\right)|\overline{\phi}|^2 d\lambda\right\}}{\frac{1}{2}\int_{\frac{1}{B_{max}}}^{\frac{1}{B_{min}}}\sum_{\text{wells}}\tau(\lambda)|\overline{\phi}|^2 d\lambda - \int_{-\infty}^{\infty}\left[\Gamma_0 - \eta_i b\left(\Gamma_0 - \Gamma_1\right)\right]|\phi|^2\frac{dl}{B}} \tag{7.11}$$

This expression can now be inserted into a stellarator optimisation code (STELLOPT), which is instructed to generate a geometry in configuration space (i.e., manipulate B and κ), such that the right-hand side of Eqn. 7.11 is maximised. The resulting geometry can then be tested with GENE to investigate whether the energy lost due to transport caused by TEM-driven turbulence is reduced. If this is achieved, then our research efforts here will be proven successful.

Geometry	Critical Density Gradient Values			
	γ GENE	ω_r GENE	$\mathrm{VP}_{(\phi_{DATA})}$	$\mathrm{VP}_{(\phi_{Pred})}$
DIII-D ($k_y\rho = 0.6$)	0.3182	0.2208	0.4379	0.4470
DIII-D ($k_y\rho = 0.8$)	0.3051	0.3002	0.3685	0.1562
DIII-D ($k_y\rho = 1.0$)	0.3073	0.2994	0.2052	0.9259
DIII-D ($k_y\rho = 1.2$)	0.3080	0.2999	0.0678	0.6448
NCSX ($k_y\rho = 0.6$)	0.2980	0.2591	0.2743	0.0340
NCSX ($k_y\rho = 0.8$)	0.2961	0.2648	0.2960	0.2064
NCSX ($k_y\rho = 1.0$)	0.2776	0.2588	0.3138	0.1428
NCSX ($k_y\rho = 1.2$)	0.2495	0.2822	0.3128	0.5688
W7-X (SC) ($k_y\rho = 0.6$)	0.1783	0.2758	0.2692	0.1970
W7-X (SC) ($k_y\rho = 0.8$)	0.2014	0.2171	0.2076	0.1992
W7-X (SC) ($k_y\rho = 1.0$)	0.2021	0.2244	0.2650	0.0367
W7-X (SC) ($k_y\rho = 1.2$)	0.1617	0.1459	0.1941	0.1958
W7-X (HM) ($k_y\rho = 0.6$)	0.1624	0.1746	0.2590	0.1921
W7-X (HM) ($k_y\rho = 0.8$)	0.1472	0.1747	0.2111	0.0564
W7-X (HM) ($k_y\rho = 1.0$)	0.1559	0.3003	0.2975	12.1527
W7-X (HM) ($k_y\rho = 1.2$)	0.2265	0.2999	0.2737	-0.0159
W7-X (LM) ($k_y\rho = 0.6$)	0.2975	0.2070	0.2456	0.1407
W7-X (LM) ($k_y\rho = 0.8$)	0.3015	0.2363	0.2731	0.1929
W7-X (LM) ($k_y\rho = 1.0$)	0.2858	0.2930	0.2687	0.0814
W7-X (LM) ($k_y\rho = 1.2$)	0.2264	0.2140	0.2429	0.0326
HSX ($k_y\rho = 0.4$)	0.2106	0.1901	0.0985	0.1532
HSX ($k_y\rho = 0.6$)	0.1725	0.2119	0.2489	0.1754
HSX ($k_y\rho = 0.8$)	0.2401	0.2305	0.3051	0.0930
HSX ($k_y\rho = 1.0$)	0.2146	0.1847	0.3377	0.0980
HSX ($k_y\rho = 1.2$)	0.2115	0.2116	0.3448	0.1919

Table 7.2: *Critical density gradient values from GENE data and from the real mode frequency ω_r using different methods.*

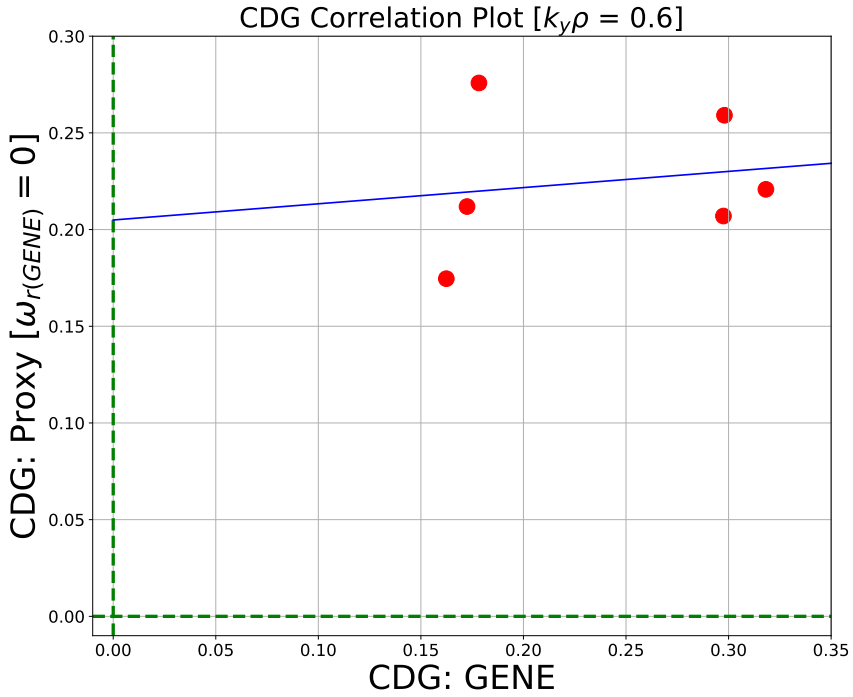

Figure 7.156: *Scatter-correlation plot comparing our critical-density-gradient proxy results with GENE. The proxy here is based on finding the density gradient value corresponding to* $\omega_{r(GENE)} = 0$.

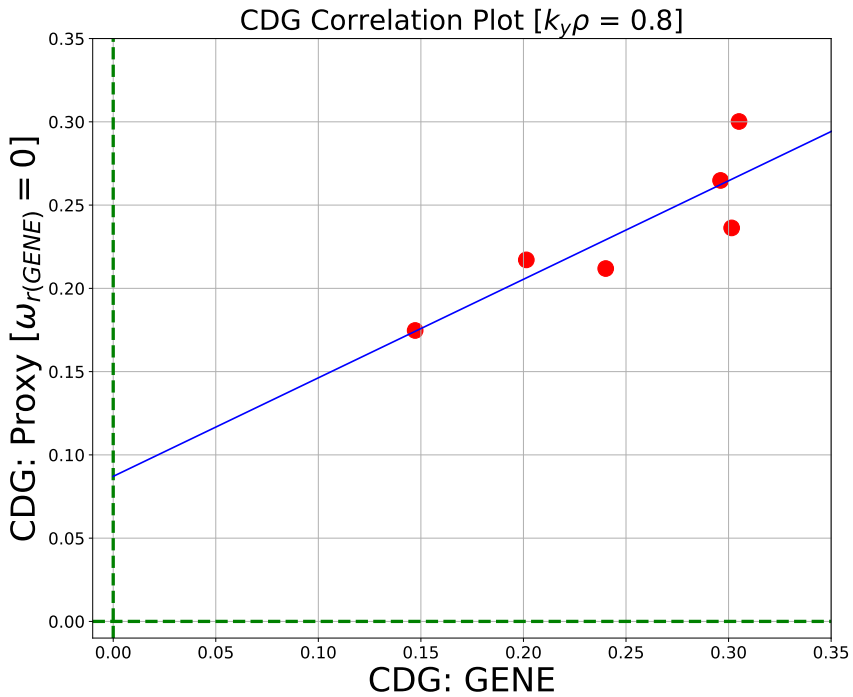

Figure 7.157: *Scatter-correlation plot comparing our critical-density-gradient proxy results with GENE. The proxy here is based on finding the density gradient value corresponding to* $\omega_{r(GENE)} = 0$.

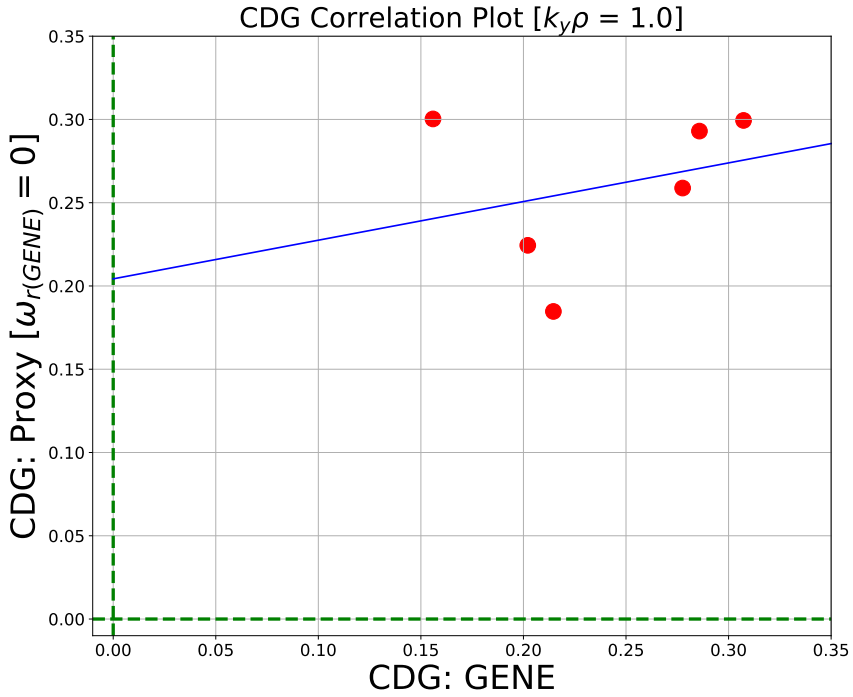

Figure 7.158: *Scatter-correlation plot comparing our critical-density-gradient proxy results with GENE. The proxy here is based on finding the density gradient value corresponding to* $\omega_{r(GENE)} = 0$.

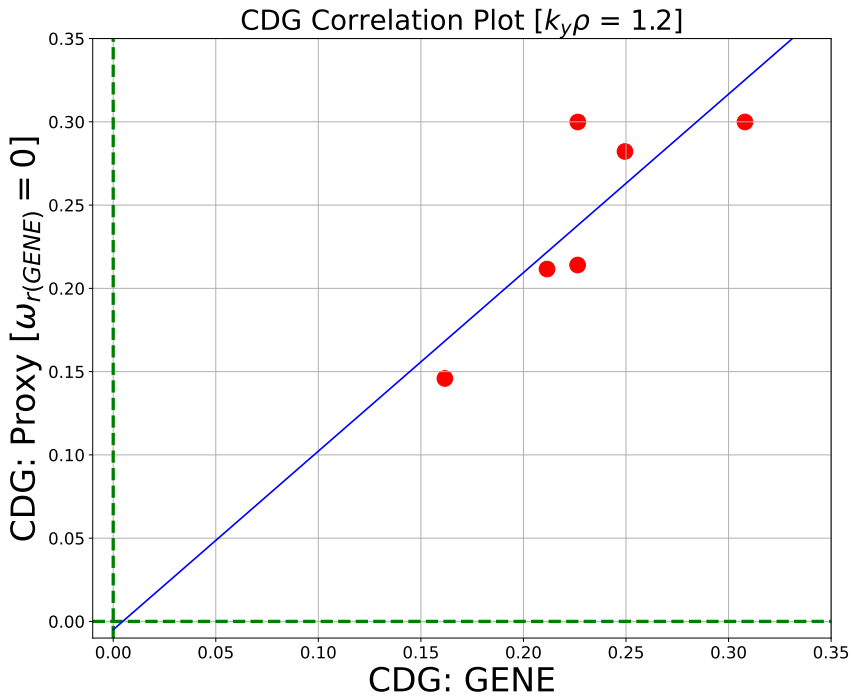

Figure 7.159: *Scatter-correlation plot comparing our critical-density-gradient proxy results with GENE. The proxy here is based on finding the density gradient value corresponding to* $\omega_{r(GENE)} = 0$.

Chapter 8

Conclusion & Outlook

We now arrive to the conclusion of this thesis report. We can summarise the work carried out here very concisely into three main stages of results.

1. We showed that a variational principle technique can be utilised to accurately predict the real mode frequency of the TEM plasma micro-instability in the complex geometries of stellarators (see section 5.2 for the derivation). Prior to this work, this same technique had only been known to work in the simpler tokamak geometry. Thus, this is an important and highly useful finding. Perhaps in future, a similar technique could be applied to the investigation of other micro-instabilities also, e.g., the trapped-ion mode, the ion-temperature gradient mode.

2. We showed that the mode structure ϕ can be very roughly predicted based purely on the geometrical characteristics of the stellarator or tokamak configuration. This prediction can then be inserted as a trial function into a variational principle result, in order to calculate the approximate real mode frequency. The significance of this would be that it alleviates the dependence on procuring costly and time-consuming supercomputer simulation data. The version of this technique presented in this thesis is only a first attempt so as to prove the principle of the method - further modification and refinement is most certainly required before this technique can be used reliably.

3. Finally, we presented two procedures for how a potential proxy for the critical density gradient can be developed using the gyrokinetic framework which describes the nature of plasma micro-instabilities. Our proxies were heavily dependent on the accuracy of the mode frequency proxy, and thus, dependent on the mode structure prediction. Therefore, a propagation of error is inevitably present. This is why we must emphasise, once again, the importance of enhancing the procedure for predicting the mode structure. An improvement in this effort will lead to a more accurate mode frequency proxy, and in turn, to more

efficacious critical-density-gradient proxies.

With these results now concisely summarised, it is worth discussing the outlook of their utility and future implementation. As stated already in this report, the work carried out here depended heavily on the accuracy of a very early approximation for the mode structure of the TEM. We should then acknowledge that use of such a prediction inevitably lead to a lower resolution representation of the actual physical behaviour at play. Regardless, this compromise of losing predictive power in exchange for gaining cheaper and faster means to geometrical optimisation may prove to be highly useful once the method has been further developed. Thus, it may be the case that strong predictive power is not necessarily essential for optimising stellarator geometries against micro-instabilities, such as the TEM.
The efficacy of this work should then be tested as follows. Our analytical results (Eqn. 7.11, in particular) should be implemented in a stellarator optimisation routine (STELLOPT), so as to generate a new stellarator geometry in configuration space which seeks to maximise the value of the critical density gradient of the TEM. Ideally, this would then delay the onset of this problematic instability, and the subsequent transport caused by it. This strategy of optimisation may provide our plasma with prolonged stability and thus, a higher confinement time, so that it may eventually reach the necessary fusion-temperatures at its core.

It is worth noting that this project focused solely on one of a plethora of challenges facing magnetic confinement fusion today. The expansive field of nuclear fusion research clearly still has a long road ahead before it can hope to create efficacious, self-sustaining, and reliable fusion reactors. However, despite the daunting nature of this task, progress is undeniably being made and obstacles facing nuclear fusion optimisation are consistently being overcome. It is only with this persistent and rigorous work ethic that we can ever hope to achieve our goals here in this lifetime. It is thus my hope that the work carried out in this project will contribute in some small part, directly or otherwise, to the wider effort being diligently made by the dedicated fusion community.

Finally, we will conclude this report with one last note of optimistic motivation. With pressing matters such as climate change and other negative environmental impacts occupying a large part of our collective consciousness on a daily basis, the need for clean energy production has never been stronger. Fusion may be the most cogent of means to a cleaner, safer, and more sustainable future. And with the truly innovative design, combined with the huge potential, of the stellarator, we may just hold the key to that brighter - and longer lasting - future.

Appendix A

Alternative Mode Frequency Proxy

In this appendix, we derive a proxy for the mode frequency ω of the TEM instability in stellarator geometry, where only the trapped portions of each particle species (ions and electrons) are being considered. This choice was made due to fact that the TEM instability arises in the system purely because of resonance induced by trapped particle behaviour [12]. As already mentioned, the proxy for ω developed here is not utilised elsewhere in this project, and serves only as an alternative to the proxy developed in section 5.2. Nevertheless, the procedure carried out here is relevant to that section, and so is worth understanding in conjunction with the ω proxy pertaining to passing ions and trapped electrons.

To begin, we state the bounce-averaged solution (i.e., trapped particles only) of the gyrokinetic equation, given by the following expression for g_a

$$\boxed{g_{a(Trapped)} = \frac{e_a}{T_a}\overline{J_0\phi}\frac{(\omega - \omega_{*a}^T)}{(\omega - \overline{\omega}_{da})}f_{a0}} \tag{A.1}$$

and we recall that this expression corresponds to the non-adiabatic portion of the distribution function. We can insert this into the QN condition, given by

$$\boxed{\sum_{a=i,e}\frac{n_a e_a^2}{T_a}\phi = \sum_{a=i,e} e_a \int g_a(\mathbf{R},\mathcal{E},\mu)J_0\left(\frac{k_\perp v_\perp}{\omega_a}\right)d\mathbf{v}} \tag{A.2}$$

This substitution yields

$$\sum_{a=i,e}\frac{n_a e_a^2}{T_a}\phi = \sum_{a=i,e} e_a \int_{trapped}\left(\frac{e_a}{T_a}\overline{J_0\phi}\frac{(\omega - \omega_{*a}^T)}{(\omega - \overline{\omega}_{da})}f_{a0}\right)J_0 d\mathbf{v} \tag{A.3}$$

To simplify matters, the Bessel function J_0 for trapped particles can be set equal to one [12]. This approximation is suitable for long perpendicular wavelengths, $k_\perp \rho_a \ll 1$. Let's now look more carefully at how the bounce-averaging works, which is indicated by the presence of a 'bar' over certain terms. We will do this in the following aside.

ASIDE

For some quantity Q which will be bounce-averaged, then

$$\overline{Q} = \frac{1}{\tau_{ba}(\lambda)} \oint Q \frac{dl}{|v_\parallel|} \tag{A.4}$$

where

$$\begin{aligned} \tau_{ba}(\lambda) &= \oint \frac{dl}{|v_\parallel|} \\ |v_\parallel| &= x v_{Ta} \sqrt{1 - \lambda B} \end{aligned} \tag{A.5}$$

such that

$$\overline{Q} = \frac{1}{\left(\oint \frac{dl}{x v_{Ta} \sqrt{1 - \lambda B}} \right)} \oint Q \frac{dl}{x v_{Ta} \sqrt{1 - \lambda B}} \tag{A.6}$$

Remember, $x v_{Ta} = v = \sqrt{\frac{2\mathcal{E}}{m_a}}$, which isn't dependent on the field line coordinate l, so we can pull these terms out of our integrals and they cancel:

$$\overline{Q} = \frac{1}{\left(\oint \frac{dl}{\sqrt{1 - \lambda B(l)}} \right)} \oint Q \frac{dl}{\sqrt{1 - \lambda B(l)}} \tag{A.7}$$

This shows that bounce-averaging doesn't introduce any hidden or implicit species-dependence to our quantities. We will end this aside by introducing a neat shorthand for this species-independent bounce time expression:

$$\tau(\lambda) = \oint \frac{dl}{\sqrt{1 - \lambda B}} \tag{A.8}$$

such that the bounce-average procedure becomes

$$\overline{Q} = \frac{1}{\tau(\lambda)} \oint Q \frac{dl}{\sqrt{1 - \lambda B(l)}} \tag{A.9}$$

For clarity during the derivations of this report, we will primarily use the more explicit expression given in Eqn. A.7.

Based on this aside, we can now see that the bounce-averaged term in Eqn. 6.3 can be expressed as follows

$$\begin{aligned}\overline{\phi} &= \frac{1}{\tau_{ba}(\lambda)} \oint \phi \frac{dl}{|v_{\parallel}|} \\ &= \frac{1}{\left(\oint \frac{dl}{\sqrt{1-\lambda B(l)}}\right)} \oint \phi \frac{dl}{\sqrt{1-\lambda B(l)}}\end{aligned}$$

In order to obtain a purely real left-hand side, Eqn. A.3 is multiplied across by ϕ^* and subsequently integrated along the field line. Note, this step does not necessarily need to be carried out at this point in the derivation, but we are mirroring the procedure carried in Chapter 6, which has some overlap with this section. This gives

$$\begin{aligned}\sum_a \frac{n_a e_a^2}{T_a}\langle|\phi|^2\rangle &= \sum_a \sum_{\text{wells}} e_a \oint \frac{dl}{B} \int \frac{e_a}{T_a}\overline{\phi}\phi^* \frac{(\omega-\omega_{*a}^T)}{(\omega-\overline{\omega}_{da})} f_{a0} d\mathbf{v} \Big/ \oint \frac{dl}{B} \\ &= \sum_a \sum_{\text{wells}} e_a \oint \frac{dl}{B} \int_{trapped} \frac{e_a}{T_a}\overline{\phi}\phi^* \frac{(\omega-\omega_{*a}^T)}{(\omega-\overline{\omega}_{da})} f_{a0} \frac{2\pi B v^3 dv d\lambda}{|v_{\parallel}|} \Big/ \oint \frac{dl}{B} \\ &= \sum_a \sum_{\text{wells}} e_a \int_{\frac{1}{B_{max}}}^{\frac{1}{B_{min}}} d\lambda \int_0^{\infty} 2\pi v^3 dv \oint \frac{dl}{|v_{\parallel}|} \frac{e_a}{T_a}\overline{\phi}\phi^* \frac{(\omega-\omega_{*a}^T)}{(\omega-\overline{\omega}_{da})} f_{a0} \Big/ \oint \frac{dl}{B} \\ &= \sum_a \sum_{\text{wells}} e_a \int_{\frac{1}{B_{max}}}^{\frac{1}{B_{min}}} d\lambda \int_0^{\infty} 2\pi v^3 dv \frac{e_a}{T_a}(\overline{\phi})(\overline{\phi^*})\tau_{ba}(\lambda) \frac{(\omega-\omega_{*a}^T)}{(\omega-\overline{\omega}_{da})} f_{a0} \Big/ \oint \frac{dl}{B} \\ &= \sum_a \sum_{\text{wells}} \int_{\frac{1}{B_{max}}}^{\frac{1}{B_{min}}} d\lambda \int_0^{\infty} 2\pi v^3 dv \frac{e_a^2}{T_a}|\overline{\phi}|^2 \tau_{ba}(\lambda) \frac{(\omega-\omega_{*a}^T)}{(\omega-\overline{\omega}_{da})} f_{a0} \Big/ \oint \frac{dl}{B}\end{aligned} \tag{A.10}$$

where the following expressions have been used

$$\begin{aligned}\langle ... \rangle &= \oint ... \frac{dl}{B} \Big/ \oint \frac{dl}{B} \\ \oint \frac{dl}{|v_{\parallel}|}\phi^* &= \overline{\phi^*}\tau_{ba} \\ \tau_{ba}(\lambda) &= \oint \frac{dl}{|v_{\parallel}|} = \oint \frac{dl}{x v_{Ta}\sqrt{1-\lambda B}}\end{aligned} \tag{A.11}$$

as well as

$$d\mathbf{v} = 2\pi v_{\perp} dv_{\perp} dv_{\parallel} = \sum_{\sigma} \frac{B\pi v^3 dv d\lambda}{|v_{\parallel}|} \tag{A.12}$$

with

$$\begin{aligned}\lambda &= \frac{v_{\perp}^2}{v^2 B} = \frac{\mu}{\mathcal{E}} \\ \sigma &= \frac{v_{\parallel}}{|v_{\parallel}|}\end{aligned} \tag{A.13}$$

The left-hand side of Eqn. A.10 is purely real, and so the right-hand side consequently has to be purely real also. By introducing the normalised velocity coordinate $x = \frac{v}{v_{Ta}}$, the bounce-averaged

magnetic drift can be expressed in terms of this normalised velocity and a factor that depends on the pitch angle λ and the particle species a,

$$\begin{aligned}\overline{\omega}_{da} &= \overline{\mathbf{k}_\perp \cdot \left[\hat{\mathbf{b}} \times \left(\frac{v_\perp^2}{2}\nabla \ln B + v_\parallel^2 \vec{\kappa}\right)\frac{1}{\Omega_a}\right]} \\ &= \overline{\mathbf{k}_\perp \cdot \left[\hat{\mathbf{b}} \times \left(\frac{\lambda B v^2}{2}\nabla \ln B + v^2(1-\lambda B)\vec{\kappa}\right)\frac{1}{\Omega_a}\right]} \\ &= \left(x^2 v_{Ta}^2\right)\overline{\mathbf{k}_\perp \cdot \left[\hat{\mathbf{b}} \times \left(\frac{\lambda B}{2}\nabla \ln B + (1-\lambda B)\vec{\kappa}\right)\frac{1}{\Omega_a}\right]} \\ &= x^2 D_a(\lambda)\end{aligned} \tag{A.14}$$

such that $D_a(\lambda)$ is defined as

$$D_a(\lambda) \equiv v_{Ta}^2 \overline{\mathbf{k}_\perp \cdot \left[\hat{\mathbf{b}} \times \left(\frac{\lambda B}{2}\nabla \ln B + (1-\lambda B)\vec{\kappa}\right)\frac{1}{\Omega_a}\right]} \tag{A.15}$$

where $\vec{\kappa} = \hat{\mathbf{b}} \cdot \nabla \hat{\mathbf{b}}$ describes the curvature. In the following aside, Eqn. A.15 is parsed further such that its species-dependent and λ-dependent components can be defined separately.

ASIDE

Looking more closely at Eqn. A.15, the species-dependent terms can be expanded as follows:

$$\begin{aligned} v_{Ta} &= \sqrt{\frac{2T_a}{m_a}} \\ \overline{\Omega_a} &= \overline{\left(\frac{e_a B}{m_a}\right)} = \frac{e_a \overline{B}}{m_a} \end{aligned} \tag{A.16}$$

Now, going back to the expression for $D_a(\lambda)$

$$D_a(\lambda) \equiv v_{Ta}^2 \overline{\mathbf{k}_\perp \cdot \left[\hat{\mathbf{b}} \times \left(\frac{\lambda B}{2} \nabla \ln B + (1 - \lambda B)\vec{\kappa}\right) \frac{1}{\Omega_a}\right]} \tag{A.17}$$

we can insert our expressions from Eqn. A.16 to obtain

$$\begin{aligned} D_a(\lambda) &= \left(\frac{2T_a}{m_a}\right) \overline{\mathbf{k}_\perp \cdot \left[\hat{\mathbf{b}} \times \left(\frac{\lambda B}{2} \nabla \ln B + (1 - \lambda B)\vec{\kappa}\right) \frac{m_a}{e_a B}\right]} \\ &= \left(\frac{2T_a}{m_a}\right) \left(\frac{m_a}{e_a}\right) \overline{\mathbf{k}_\perp \cdot \left[\hat{\mathbf{b}} \times \left(\frac{\lambda B}{2} \nabla \ln B + (1 - \lambda B)\vec{\kappa}\right) \frac{1}{B}\right]} \\ &= \left(\frac{2T_a}{e_a}\right) \overline{\mathbf{k}_\perp \cdot \left[\hat{\mathbf{b}} \times \left(\frac{\lambda B}{2} \nabla \ln B + (1 - \lambda B)\vec{\kappa}\right) \frac{1}{B}\right]} \\ &= F_a \overline{G(\lambda)} \end{aligned} \tag{A.18}$$

where in the final step, $D_a(\lambda)$ has been split into a species-dependent part F_a, and a λ-dependent part $\overline{G(\lambda)}$.

To prevent resonance from occurring in this derivation, an ordering scheme is assumed involving the bounced-averaged magnetic drift frequency and the mode frequency, as follows:

$$\overline{\omega}_{da} \ll \omega \implies \frac{\overline{\omega}_{da}}{\omega} \ll 1 \tag{A.19}$$

This assumption is not too crude in some stellarator geometries, particularly those approaching QI (W7-X and QIPC) [12]. This then facilitates carrying out a Taylor expansion of the following term:

$$\frac{(\omega - \omega^T_{*a})}{(\omega - \overline{\omega}_{da})} = \frac{\omega}{\omega}\frac{\left(1 - \frac{\omega^T_{*a}}{\omega}\right)}{\left(1 - \frac{\overline{\omega}_{da}}{\omega}\right)} \simeq \left(1 - \frac{\omega^T_{*a}}{\omega}\right)\left(1 + \frac{\overline{\omega}_{da}}{\omega} + \mathcal{O}\left(\frac{\overline{\omega}^2_{da}}{\omega^2}\right)\right) \tag{A.20}$$

which can be expanded to first order in $\overline{\omega}_{da}$ to give

$$\frac{(\omega - \omega^T_{*a})}{(\omega - \overline{\omega}_{da})} \simeq \left(1 - \frac{\omega^T_{*a}}{\omega} + \frac{\overline{\omega}_{da}}{\omega} - \frac{\omega^T_{*a}\overline{\omega}_{da}}{\omega^2}\right) \tag{A.21}$$

Using both Eqn. A.14 and Eqn. A.18 then changes this to

$$\frac{(\omega - \omega^T_{*a})}{(\omega - \overline{\omega}_{da})} \simeq \left(1 - \frac{\omega^T_{*a}}{\omega} + \frac{x^2 F_a \overline{G(\lambda)}}{\omega} - \frac{\omega^T_{*a} x^2 F_a \overline{G(\lambda)}}{\omega^2}\right) \tag{A.22}$$

Returning to Eqn. A.10

$$\sum_a \frac{n_a e_a^2}{T_a}\langle|\phi|^2\rangle = \sum_a \sum_{\text{wells}} \int_{\frac{1}{B_{max}}}^{\frac{1}{B_{min}}} d\lambda \int_0^\infty 2\pi v^3 dv \frac{e_a^2}{T_a}|\overline{\phi}|^2 \tau_{ba}(\lambda)\frac{(\omega - \omega^T_{*a})}{(\omega - \overline{\omega}_{da})} f_{a0} / \oint \frac{dl}{B} \tag{A.23}$$

inserting Eqn. A.22 then gives

$$\begin{aligned}\sum_a \frac{n_a e_a^2}{T_a}\langle|\phi|^2\rangle = \sum_a \sum_{\text{wells}} \int_{\frac{1}{B_{max}}}^{\frac{1}{B_{min}}} d\lambda \int_0^\infty 2\pi v^3 dv \frac{e_a^2}{T_a}|\overline{\phi}|^2 \tau_{ba}(\lambda) \times \\ \times \left(1 - \frac{\omega^T_{*a}}{\omega} + \frac{x^2 F_a \overline{G(\lambda)}}{\omega} - \frac{\omega^T_{*a} x^2 F_a \overline{G(\lambda)}}{\omega^2}\right) f_{a0} / \oint \frac{dl}{B}\end{aligned} \tag{A.24}$$

Now, using the expression for the normalised velocity $x = \frac{v}{v_{Ta}}$, the result can be rewritten as

$$\begin{aligned}\sum_a \frac{n_a e_a^2}{T_a}\langle|\phi|^2\rangle = \sum_a \sum_{\text{wells}} \int_{\frac{1}{B_{max}}}^{\frac{1}{B_{min}}} d\lambda \int_0^\infty 2\pi \left(v_{Ta}^3 x^3\right)\left(v_{Ta} dx\right) \frac{e_a^2}{T_a}|\overline{\phi}|^2 \tau_{ba}(\lambda) \times \\ \times \left(1 - \frac{\omega^T_{*a}}{\omega} + \frac{x^2 F_a \overline{G(\lambda)}}{\omega} - \frac{\omega^T_{*a} x^2 F_a \overline{G(\lambda)}}{\omega^2}\right) f_{a0} / \oint \frac{dl}{B}\end{aligned} \tag{A.25}$$

The following expression for the equilibrium Maxwellian distribution

$$f_{a0} = \left[n_a \left(\frac{1}{\pi v_{Ta}^2}\right)^{\frac{3}{2}} e^{-x^2}\right] \tag{A.26}$$

can also be inserted, giving

$$\sum_a \frac{n_a e_a^2}{T_a}\langle|\phi|^2\rangle = \sum_a \sum_{\text{wells}} \int_{\frac{1}{B_{max}}}^{\frac{1}{B_{min}}} d\lambda \int_0^\infty 2\pi \left(v_{Ta}^3 x^3\right)(v_{Ta}dx)\frac{e_a^2}{T_a}|\overline{\phi}|^2\tau_{ba}(\lambda)\times \\ \times\left(1-\frac{\omega_{*a}^T}{\omega}+\frac{x^2F_a\overline{G(\lambda)}}{\omega}-\frac{\omega_{*a}^T x^2 F_a\overline{G(\lambda)}}{\omega^2}\right)\left[n_a\left(\frac{1}{\pi v_{Ta}^2}\right)^{\frac{3}{2}}e^{-x^2}\right]/\oint\frac{dl}{B} \tag{A.27}$$

Furthermore, the following definition for the bounce time $\tau_{ba}(\lambda)$

$$\tau_{ba}(\lambda) = \oint \frac{dl}{|v_\parallel|} \\ |v_\parallel| = x v_{Ta}\sqrt{1-\lambda B} \tag{A.28}$$

which can be rewritten as

$$\tau_{ba}(\lambda) = \oint \frac{dl}{x v_{Ta}\sqrt{1-\lambda B}} \tag{A.29}$$

can now be inserted into Eqn. A.27 to give

$$\sum_a \frac{n_a e_a^2}{T_a}\langle|\phi|^2\rangle = \sum_a \sum_{\text{wells}} \int_{\frac{1}{B_{max}}}^{\frac{1}{B_{min}}} d\lambda \int_0^\infty 2\pi \left(v_{Ta}^3 x^3\right)(v_{Ta}dx)\frac{e_a^2}{T_a}|\overline{\phi}|^2 \oint\frac{dl}{x v_{Ta}\sqrt{1-\lambda B}}\times \\ \times\left(1-\frac{\omega_{*a}^T}{\omega}+\frac{x^2F_a\overline{G(\lambda)}}{\omega}-\frac{\omega_{*a}^T x^2 F_a\overline{G(\lambda)}}{\omega^2}\right)\left[n_a\left(\frac{1}{\pi v_{Ta}^2}\right)^{\frac{3}{2}}e^{-x^2}\right]/\oint\frac{dl}{B} \tag{A.30}$$

Here, all of the thermal velocity terms v_{Ta} cancel, which results in

$$\sum_a \frac{n_a e_a^2}{T_a}\langle|\phi|^2\rangle = \frac{2\pi}{\pi^{\frac{3}{2}}}\sum_a \frac{n_a e_a^2}{T_a}\sum_{\text{wells}}\int_{\frac{1}{B_{max}}}^{\frac{1}{B_{min}}} d\lambda \int_0^\infty x^2 e^{-x^2}dx|\overline{\phi}|^2\oint\frac{dl}{\sqrt{1-\lambda B}}\times \\ \times \underbrace{\left(1-\frac{\omega_{*a}^T}{\omega}+\frac{x^2F_a\overline{G(\lambda)}}{\omega}-\frac{\omega_{*a}^T x^2 F_a\overline{G(\lambda)}}{\omega^2}\right)}_{\dagger}/\oint\frac{dl}{B} \tag{A.31}$$

Using the following definition of the temperature-dependent diamagnetic drift frequency

$$\omega_{*a}^T = \omega_{*a}\left[1+\eta_a\left(\frac{\mathcal{E}_a}{T_a}-\frac{3}{2}\right)\right] \tag{A.32}$$

and also

$$\frac{\mathcal{E}_a}{T_a} = \frac{m_a v^2}{2T_a} = \frac{v^2}{v_{Ta}^2} = x^2 \tag{A.33}$$

leads Eqn. A.32 to become

$$\omega_{*a}^T = \omega_{*a}\left[1+\eta_a\left(x^2-\frac{3}{2}\right)\right] = \left[\omega_{*a}+\omega_{*a}\eta_a x^2-\frac{3}{2}\omega_{*a}\eta_a\right] \tag{A.34}$$

Implementing this expansion into † from Eqn. A.31 then gives

$$\begin{aligned}\dagger =& \left(1-\frac{\left[\omega_{*a}+\omega_{*a}\eta_a x^2-\frac{3}{2}\omega_{*a}\eta_a\right]}{\omega}+\frac{x^2F_a\overline{G(\lambda)}}{\omega}-\frac{\left[\omega_{*a}+\omega_{*a}\eta_a x^2-\frac{3}{2}\omega_{*a}\eta_a\right]x^2F_a\overline{G(\lambda)}}{\omega^2}\right)\\ =&\left(1-\frac{\omega_{*a}}{\omega}-\frac{\omega_{*a}\eta_a x^2}{\omega}+\frac{\frac{3}{2}\omega_{*a}\eta_a}{\omega}+\frac{x^2F_a\overline{G(\lambda)}}{\omega}-\frac{\omega_{*a}x^2F_a\overline{G(\lambda)}}{\omega^2}\right.\\ &\left.-\frac{\omega_{*a}\eta_a x^4F_a\overline{G(\lambda)}}{\omega^2}+\frac{\frac{3}{2}\omega_{*a}\eta_a x^2F_a\overline{G(\lambda)}}{\omega^2}\right)\end{aligned} \tag{A.35}$$

This expansion, when inserted into Eqn. A.31, helps to reveal all of the x-dependent terms in the derivation:

$$\begin{aligned}\sum_a\frac{n_ae_a^2}{T_a}\langle|\phi|^2\rangle =&\frac{2}{\sqrt{\pi}}\sum_a\frac{n_ae_a^2}{T_a}\sum_{\text{wells}}\int_{\frac{1}{B_{max}}}^{\frac{1}{B_{min}}}d\lambda\int_0^\infty x^2e^{-x^2}dx|\overline{\phi}|^2\oint\frac{dl}{\sqrt{1-\lambda B}}\times\\ &\left(1-\frac{\omega_{*a}}{\omega}-\frac{\omega_{*a}\eta_a x^2}{\omega}+\frac{\frac{3}{2}\omega_{*a}\eta_a}{\omega}+\frac{x^2F_a\overline{G(\lambda)}}{\omega}-\frac{\omega_{*a}x^2F_a\overline{G(\lambda)}}{\omega^2}\right.\\ &\left.-\frac{\omega_{*a}\eta_a x^4F_a\overline{G(\lambda)}}{\omega^2}+\frac{\frac{3}{2}\omega_{*a}\eta_a x^2F_a\overline{G(\lambda)}}{\omega^2}\right)\times\frac{1}{\oint\frac{dl}{B}}\end{aligned} \tag{A.36}$$

Now, noting that all of the x-integrals are even, the integration limits can be modified as follows:

$$2\int_0^\infty dx\equiv\int_{-\infty}^\infty dx \tag{A.37}$$

such that the following integrals can be utilised:

$$\begin{aligned}\int_{-\infty}^\infty x^2e^{-x^2}dx&=\frac{\sqrt{\pi}}{2}\\ \int_{-\infty}^\infty x^4e^{-x^2}dx&=\frac{3}{4}\sqrt{\pi}\\ \int_{-\infty}^\infty x^6e^{-x^2}dx&=\frac{15}{8}\sqrt{\pi}\end{aligned} \tag{A.38}$$

Now, the x-integration is calculated piece by piece. First, we can group together the relevant parts of Eqn. A.36 based on the degree of x. For instance, the terms with no x component in the large parenthesis of Eqn. A.36 are

$$\left(1-\frac{\omega_{*a}}{\omega}+\frac{\frac{3}{2}\omega_{*a}\eta_a}{\omega}\right) \tag{A.39}$$

such that, applying the x-integration gives

$$\int_{-\infty}^\infty x^2e^{-x^2}dx\left(1-\frac{\omega_{*a}}{\omega}+\frac{\frac{3}{2}\omega_{*a}\eta_a}{\omega}\right)=\frac{\sqrt{\pi}}{2}\left(1-\frac{\omega_{*a}}{\omega}+\frac{\frac{3}{2}\omega_{*a}\eta_a}{\omega}\right) \tag{A.40}$$

Similarly, the terms with an x^2 component in the large parenthesis of Eqn. A.36 are

$$\left(-\frac{\omega_{*a}\eta_a x^2}{\omega}+\frac{x^2F_a\overline{G(\lambda)}}{\omega}-\frac{\omega_{*a}x^2F_a\overline{G(\lambda)}}{\omega^2}+\frac{\frac{3}{2}\omega_{*a}\eta_a x^2F_a\overline{G(\lambda)}}{\omega^2}\right)= x^2\left(-\frac{\omega_{*a}\eta_a}{\omega}+\frac{F_a\overline{G(\lambda)}}{\omega}-\frac{\omega_{*a}F_a\overline{G(\lambda)}}{\omega^2}+\frac{\frac{3}{2}\omega_{*a}\eta_aF_a\overline{G(\lambda)}}{\omega^2}\right) \tag{A.41}$$

such that

$$\int_{-\infty}^{\infty}x^4e^{-x^2}dx\left(-\frac{\omega_{*a}\eta_a}{\omega}+\frac{F_a\overline{G(\lambda)}}{\omega}-\frac{\omega_{*a}F_a\overline{G(\lambda)}}{\omega^2}+\frac{\frac{3}{2}\omega_{*a}\eta_aF_a\overline{G(\lambda)}}{\omega^2}\right)= \frac{3}{4}\sqrt{\pi}\left(-\frac{\omega_{*a}\eta_a}{\omega}+\frac{F_a\overline{G(\lambda)}}{\omega}-\frac{\omega_{*a}F_a\overline{G(\lambda)}}{\omega^2}+\frac{\frac{3}{2}\omega_{*a}\eta_aF_a\overline{G(\lambda)}}{\omega^2}\right) \tag{A.42}$$

Finally, integrating the last remaining term, which has an x^4 component in the large parenthesis of Eqn. A.36, gives

$$\int_{-\infty}^{\infty}x^6e^{-x^2}dx\left(-\frac{\omega_{*a}\eta_aF_a\overline{G(\lambda)}}{\omega^2}\right)=\frac{15}{8}\sqrt{\pi}\left(-\frac{\omega_{*a}\eta_aF_a\overline{G(\lambda)}}{\omega^2}\right) \tag{A.43}$$

Notice that the $\sqrt{\pi}$ terms common to these results can be pulled out, so as to cancel with the $\frac{1}{\sqrt{\pi}}$ term in the prefactor of Eqn. A.36. Thus, these terms are now dropped.

Combining the results from Eqn. A.40, A.42 and A.43 now gives

$$\begin{aligned}&\frac{1}{2}\left(1-\frac{\omega_{*a}}{\omega}+\frac{\frac{3}{2}\omega_{*a}\eta_a}{\omega}\right)+\\&\frac{3}{4}\left(-\frac{\omega_{*a}\eta_a}{\omega}+\frac{F_a\overline{G(\lambda)}}{\omega}-\frac{\omega_{*a}F_a\overline{G(\lambda)}}{\omega^2}+\frac{\frac{3}{2}\omega_{*a}\eta_aF_a\overline{G(\lambda)}}{\omega^2}\right)+\\&\frac{15}{8}\left(-\frac{\omega_{*a}\eta_aF_a\overline{G(\lambda)}}{\omega^2}\right)\end{aligned} \tag{A.44}$$

which can now be expanded fully as follows:

$$\frac{1}{2}-\frac{1}{2}\frac{\omega_{*a}}{\omega}+\frac{3}{4}\frac{\omega_{*a}\eta_a}{\omega}-\frac{3}{4}\frac{\omega_{*a}\eta_a}{\omega}+\frac{3}{4}\frac{F_a\overline{G(\lambda)}}{\omega}-\frac{3}{4}\frac{\omega_{*a}F_a\overline{G(\lambda)}}{\omega^2}+\frac{9}{8}\frac{\omega_{*a}\eta_aF_a\overline{G(\lambda)}}{\omega^2}-\frac{15}{8}\frac{\omega_{*a}\eta_aF_a\overline{G(\lambda)}}{\omega^2} \tag{A.45}$$

which can be simplified somewhat to

$$\frac{1}{2}-\frac{1}{2}\frac{\omega_{*a}}{\omega}+\frac{3}{4}\frac{F_a\overline{G(\lambda)}}{\omega}-\frac{3}{4}\frac{\omega_{*a}F_a\overline{G(\lambda)}}{\omega^2}-\frac{3}{4}\frac{\omega_{*a}\eta_aF_a\overline{G(\lambda)}}{\omega^2} \tag{A.46}$$

and pulling out a factor of $\frac{1}{2}$

$$\frac{1}{2}\left[1-\frac{\omega_{*a}}{\omega}+\frac{3}{2}\frac{F_a\overline{G(\lambda)}}{\omega}-\frac{3}{2}\frac{\omega_{*a}F_a\overline{G(\lambda)}}{\omega^2}-\frac{3}{2}\frac{\omega_{*a}\eta_aF_a\overline{G(\lambda)}}{\omega^2}\right] \tag{A.47}$$

and tidying some more

$$\frac{1}{2}\left[1-\frac{\omega_{*a}}{\omega}+\frac{3}{2}\frac{F_a\overline{G(\lambda)}}{\omega}\left(1-\frac{\omega_{*a}}{\omega}-\frac{\omega_{*a}\eta_a}{\omega}\right)\right] \tag{A.48}$$

which can be written more concisely as

$$\frac{1}{2}\left[1-\frac{\omega_{*a}}{\omega}+\frac{3}{2}\frac{F_a\overline{G(\lambda)}}{\omega}\left(1-\frac{\omega_{*a}}{\omega}\left[1+\eta_a\right]\right)\right] \tag{A.49}$$

Eqn. A.49 will be recalled again later, so it is convenient to define it as $U_a(\omega,\lambda)$:

$$U_a(\omega,\lambda)\equiv\frac{1}{2}\left[1-\frac{\omega_{*a}}{\omega}+\frac{3}{2}\frac{F_a\overline{G(\lambda)}}{\omega}\left(1-\frac{\omega_{*a}}{\omega}\left[1+\eta_a\right]\right)\right] \tag{A.50}$$

Substituting this into Eqn. A.36 now gives

$$\sum_a\frac{n_ae_a^2}{T_a}\langle|\phi|^2\rangle=\sum_a\frac{n_ae_a^2}{T_a}\sum_{\text{wells}}\int_{\frac{1}{B_{max}}}^{\frac{1}{B_{min}}}d\lambda U_a(\omega,\lambda)|\overline{\phi}|^2\oint\frac{dl}{\sqrt{1-\lambda B}}/\oint\frac{dl}{B} \tag{A.51}$$

Recalling that

$$\langle|\phi|^2\rangle=\oint|\phi|^2\frac{dl}{B}/\oint\frac{dl}{B} \tag{A.52}$$

we see that a common factor of $\frac{1}{\oint\frac{dl}{B}}$ is present on both sides of Eqn. A.51. This term isn't species-dependent, so it can be dropped without affecting our species-summation. This means that Eqn. A.51 can now be rewritten as

$$\sum_a\frac{n_ae_a^2}{T_a}\oint|\phi|^2\frac{dl}{B}=\sum_a\frac{n_ae_a^2}{T_a}\sum_{\text{wells}}\int_{\frac{1}{B_{max}}}^{\frac{1}{B_{min}}}d\lambda U_a(\omega,\lambda)|\overline{\phi}|^2\oint\frac{dl}{\sqrt{1-\lambda B}} \tag{A.53}$$

Now, expanding this expression for both particle species:

$$\begin{aligned}&\frac{n_ie_i^2}{T_i}\oint|\phi|^2\frac{dl}{B}+\frac{n_ee_e^2}{T_e}\oint|\phi|^2\frac{dl}{B}=\\&\frac{n_ie_i^2}{T_i}\sum_{\text{wells}}\int_{\frac{1}{B_{max}}}^{\frac{1}{B_{min}}}d\lambda U_i(\omega,\lambda)|\overline{\phi}|^2\oint\frac{dl}{\sqrt{1-\lambda B}}+\frac{n_ee_e^2}{T_e}\sum_{\text{wells}}\int_{\frac{1}{B_{max}}}^{\frac{1}{B_{min}}}d\lambda U_e(\omega,\lambda)|\overline{\phi}|^2\oint\frac{dl}{\sqrt{1-\lambda B}}\end{aligned} \tag{A.54}$$

We can assume equal species density and note the equivalence of the square of the ion/electron charge as follows:

$$\begin{aligned}n_i&=n_e=n\\e_i^2&=e_e^2=e^2\end{aligned} \tag{A.55}$$

Using these then changes Eqn. A.54 to

$$\begin{aligned}&\frac{ne^2}{T_i}\oint|\phi|^2\frac{dl}{B}+\frac{ne^2}{T_e}\oint|\phi|^2\frac{dl}{B}=\\&\frac{ne^2}{T_i}\sum_{\text{wells}}\int_{\frac{1}{B_{max}}}^{\frac{1}{B_{min}}}d\lambda U_i(\omega,\lambda)|\overline{\phi}|^2\oint\frac{dl}{\sqrt{1-\lambda B}}+\frac{ne^2}{T_e}\sum_{\text{wells}}\int_{\frac{1}{B_{max}}}^{\frac{1}{B_{min}}}d\lambda U_e(\omega,\lambda)|\overline{\phi}|^2\oint\frac{dl}{\sqrt{1-\lambda B}}\end{aligned} \tag{A.56}$$

Multiplying across by $\frac{T_e}{ne^2}$ and rearranging slightly gives

$$\begin{aligned}&\left(\frac{T_e}{T_i}+1\right)\oint|\phi|^2\frac{dl}{B}=\\&\frac{T_e}{T_i}\sum_{\text{wells}}\int_{\frac{1}{B_{max}}}^{\frac{1}{B_{min}}}d\lambda U_i(\omega,\lambda)|\overline{\phi}|^2\oint\frac{dl}{\sqrt{1-\lambda B}}+\sum_{\text{wells}}\int_{\frac{1}{B_{max}}}^{\frac{1}{B_{min}}}d\lambda U_e(\omega,\lambda)|\overline{\phi}|^2\oint\frac{dl}{\sqrt{1-\lambda B}}\end{aligned}\tag{A.57}$$

Now, we can inspect the U_i and U_e terms more closely. Noting the definition of the temperature-independent diamagnetic drift frequency

$$\omega_{*a}=\frac{T_a k_\alpha}{e_a}\frac{d\ln n_a}{d\psi}\tag{A.58}$$

we can make use of Eqn. A.55 here to give

$$\omega_{*i}=-\frac{\omega_{*e}}{\tau}\tag{A.59}$$

where $\tau=\frac{Te}{Ti}$. Note, this τ is not to be confused with the species-dependent bounce time expression $\tau_{ba}(\lambda)$.

At this point, it is also useful to notice the following relation

$$\begin{aligned}F_a&=\frac{2T_a}{e_a}\\\implies F_i&=-\frac{F_e}{\tau}\end{aligned}\tag{A.60}$$

Now, with these relations in mind, and recalling the definition of U_a

$$U_a(\omega,\lambda)=\frac{1}{2}\left[1-\frac{\omega_{*a}}{\omega}+\frac{3}{2}\frac{F_a\overline{G(\lambda)}}{\omega}\left(1-\frac{\omega_{*a}}{\omega}\left[1+\eta_a\right]\right)\right]\tag{A.61}$$

for the ions, this expression becomes

$$U_i(\omega,\lambda)=\frac{1}{2}\left[1-\frac{\omega_{*i}}{\omega}+\frac{3}{2}\frac{F_i\overline{G(\lambda)}}{\omega}\left(1-\frac{\omega_{*i}}{\omega}\left[1+\eta_i\right]\right)\right]\tag{A.62}$$

and inserting the relations from Eqn. A.59 and Eqn. A.60 gives

$$U_i(\omega,\lambda)=\frac{1}{2}\left[1+\frac{\omega_{*e}}{\tau\omega}-\frac{3}{2}\frac{F_e\overline{G(\lambda)}}{\tau\omega}\left(1+\frac{\omega_{*e}}{\tau\omega}\left[1+\eta_i\right]\right)\right]\tag{A.63}$$

By fully expanding the content in brackets, we get

$$U_i(\omega,\lambda)=\frac{1}{2}\left[1+\frac{\omega_{*e}}{\tau\omega}-\frac{3}{2}\frac{F_e\overline{G(\lambda)}}{\tau\omega}-\frac{3}{2}\frac{F_e\overline{G(\lambda)}}{\tau\omega}\frac{\omega_{*e}}{\tau\omega}-\frac{3}{2}\frac{F_e\overline{G(\lambda)}}{\tau\omega}\frac{\omega_{*e}}{\tau\omega}\eta_i\right]\tag{A.64}$$

Now, looking at U_e

$$U_e(\omega,\lambda)=\frac{1}{2}\left[1-\frac{\omega_{*e}}{\omega}+\frac{3}{2}\frac{F_e\overline{G(\lambda)}}{\omega}\left(1-\frac{\omega_{*e}}{\omega}\left[1+\eta_e\right]\right)\right]\tag{A.65}$$

and fully expanding the content in brackets again

$$U_e(\omega,\lambda) = \frac{1}{2}\left[1 - \frac{\omega_{*e}}{\omega} + \frac{3}{2}\frac{F_e\overline{G(\lambda)}}{\omega} - \frac{3}{2}\frac{F_e\overline{G(\lambda)}}{\omega}\frac{\omega_{*e}}{\omega} - \frac{3}{2}\frac{F_e\overline{G(\lambda)}}{\omega}\frac{\omega_{*e}}{\omega}\eta_e\right] \tag{A.66}$$

Putting all of these expanded terms into Eqn. A.57 results in

$$\begin{aligned}
&(\tau+1)\oint|\phi|^2\frac{dl}{B} = \\
&\frac{\tau}{2}\sum_{\text{wells}}\int_{\frac{1}{B_{max}}}^{\frac{1}{B_{min}}} d\lambda\left[1 + \frac{\omega_{*e}}{\tau\omega} - \frac{3}{2}\frac{F_e\overline{G(\lambda)}}{\tau\omega} - \frac{3}{2}\frac{F_e\overline{G(\lambda)}}{\tau\omega}\frac{\omega_{*e}}{\tau\omega} - \frac{3}{2}\frac{F_e\overline{G(\lambda)}}{\tau\omega}\frac{\omega_{*e}}{\tau\omega}\eta_i\right]|\overline{\phi}|^2\oint\frac{dl}{\sqrt{1-\lambda B}} + \\
&\frac{1}{2}\sum_{\text{wells}}\int_{\frac{1}{B_{max}}}^{\frac{1}{B_{min}}} d\lambda\left[1 - \frac{\omega_{*e}}{\omega} + \frac{3}{2}\frac{F_e\overline{G(\lambda)}}{\omega} - \frac{3}{2}\frac{F_e\overline{G(\lambda)}}{\omega}\frac{\omega_{*e}}{\omega} - \frac{3}{2}\frac{F_e\overline{G(\lambda)}}{\omega}\frac{\omega_{*e}}{\omega}\eta_e\right]|\overline{\phi}|^2\oint\frac{dl}{\sqrt{1-\lambda B}}
\end{aligned} \tag{A.67}$$

Noticing that all terms and integrals outside of the brackets are equivalent in the middle and bottom lines of Eqn. A.67, the bracketed terms can be combined as follows:

$$\begin{aligned}
&\tau\left[1 + \frac{\omega_{*e}}{\tau\omega} - \frac{3}{2}\frac{F_e\overline{G(\lambda)}}{\tau\omega} - \frac{3}{2}\frac{F_e\overline{G(\lambda)}}{\tau\omega}\frac{\omega_{*e}}{\tau\omega} - \frac{3}{2}\frac{F_e\overline{G(\lambda)}}{\tau\omega}\frac{\omega_{*e}}{\tau\omega}\eta_i\right] + \\
&\left[1 - \frac{\omega_{*e}}{\omega} + \frac{3}{2}\frac{F_e\overline{G(\lambda)}}{\omega} - \frac{3}{2}\frac{F_e\overline{G(\lambda)}}{\omega}\frac{\omega_{*e}}{\omega} - \frac{3}{2}\frac{F_e\overline{G(\lambda)}}{\omega}\frac{\omega_{*e}}{\omega}\eta_e\right]
\end{aligned} \tag{A.68}$$

where the τ can be multiplied by the terms in the bracket of the top line, giving

$$\begin{aligned}
&\left[\tau + \frac{\omega_{*e}}{\omega} - \frac{3}{2}\frac{F_e\overline{G(\lambda)}}{\omega} - \frac{3}{2}\frac{F_e\overline{G(\lambda)}}{\tau\omega}\frac{\omega_{*e}}{\omega} - \frac{3}{2}\frac{F_e\overline{G(\lambda)}}{\tau\omega}\frac{\omega_{*e}}{\omega}\eta_i\right] + \\
&\left[1 - \frac{\omega_{*e}}{\omega} + \frac{3}{2}\frac{F_e\overline{G(\lambda)}}{\omega} - \frac{3}{2}\frac{F_e\overline{G(\lambda)}}{\omega}\frac{\omega_{*e}}{\omega} - \frac{3}{2}\frac{F_e\overline{G(\lambda)}}{\omega}\frac{\omega_{*e}}{\omega}\eta_e\right]
\end{aligned} \tag{A.69}$$

and merging these brackets then leads to the cancellation of the second and third terms in each line, and the remainder gives

$$\left[\tau - \frac{3}{2}\frac{F_e\overline{G(\lambda)}}{\tau\omega}\frac{\omega_{*e}}{\omega} - \frac{3}{2}\frac{F_e\overline{G(\lambda)}}{\tau\omega}\frac{\omega_{*e}}{\omega}\eta_i + 1 - \frac{3}{2}\frac{F_e\overline{G(\lambda)}}{\omega}\frac{\omega_{*e}}{\omega} - \frac{3}{2}\frac{F_e\overline{G(\lambda)}}{\omega}\frac{\omega_{*e}}{\omega}\eta_e\right] \tag{A.70}$$

which can be rearranged further to give

$$\left[\tau + 1 - \frac{3}{2}\frac{F_e\overline{G(\lambda)}}{\omega}\frac{\omega_{*e}}{\omega}\left(1 + \eta_e + \frac{1+\eta_i}{\tau}\right)\right] \tag{A.71}$$

All of this transforms Eqn. A.67 into the following concise form

$$(\tau+1)\oint|\phi|^2\frac{dl}{B} = \frac{1}{2}\sum_{\text{wells}}\int_{\frac{1}{B_{max}}}^{\frac{1}{B_{min}}} d\lambda\left[(\tau+1) - \frac{3}{2}F_e\overline{G(\lambda)}\frac{\omega_{*e}}{\omega^2}\left(1 + \eta_e + \frac{1+\eta_i}{\tau}\right)\right]|\overline{\phi}|^2\oint\frac{dl}{\sqrt{1-\lambda B}} \tag{A.72}$$

This result can now be rearranged to find an expression for $\frac{\omega^2}{\omega_{*e}}$ in terms of the remaining quantities. Focusing on the right-hand side of Eqn. A.72, this is expanded as follows:

$$\begin{aligned}&\frac{1}{2}\sum_{\text{wells}}\int_{\frac{1}{B_{max}}}^{\frac{1}{B_{min}}} d\lambda\left[(\tau+1)-\frac{3}{2}F_e\overline{G(\lambda)}\frac{\omega_{*e}}{\omega^2}\left(1+\eta_e+\frac{1+\eta_i}{\tau}\right)\right]|\overline{\phi}|^2\oint\frac{dl}{\sqrt{1-\lambda B}}=\\&\frac{\tau+1}{2}\sum_{\text{wells}}\int_{\frac{1}{B_{max}}}^{\frac{1}{B_{min}}} d\lambda|\overline{\phi}|^2\oint\frac{dl}{\sqrt{1-\lambda B}}-\\&\frac{\omega_{*e}}{\omega^2}\frac{3}{4}\left(1+\eta_e+\frac{1+\eta_i}{\tau}\right)\sum_{\text{wells}}\int_{\frac{1}{B_{max}}}^{\frac{1}{B_{min}}} d\lambda F_e\overline{G(\lambda)}|\overline{\phi}|^2\oint\frac{dl}{\sqrt{1-\lambda B}}\end{aligned}\tag{A.73}$$

Now, inserting this expanded expression back into Eqn. A.72 gives

$$\begin{aligned}&(\tau+1)\oint|\phi|^2\frac{dl}{B}=\\&\frac{(\tau+1)}{2}\sum_{\text{wells}}\int_{\frac{1}{B_{max}}}^{\frac{1}{B_{min}}} d\lambda|\overline{\phi}|^2\oint\frac{dl}{\sqrt{1-\lambda B}}-\\&\frac{\omega_{*e}}{\omega^2}\frac{3}{4}\left(1+\eta_e+\frac{1+\eta_i}{\tau}\right)\sum_{\text{wells}}\int_{\frac{1}{B_{max}}}^{\frac{1}{B_{min}}} d\lambda F_e\overline{G(\lambda)}|\overline{\phi}|^2\oint\frac{dl}{\sqrt{1-\lambda B}}\end{aligned}\tag{A.74}$$

which can be rearranged to give

$$\begin{aligned}&\frac{\omega_{*e}}{\omega^2}\frac{3}{4}\left(1+\eta_e+\frac{1+\eta_i}{\tau}\right)\sum_{\text{wells}}\int_{\frac{1}{B_{max}}}^{\frac{1}{B_{min}}} d\lambda F_e\overline{G(\lambda)}|\overline{\phi}|^2\oint\frac{dl}{\sqrt{1-\lambda B}}=\\&\frac{(\tau+1)}{2}\sum_{\text{wells}}\int_{\frac{1}{B_{max}}}^{\frac{1}{B_{min}}} d\lambda|\overline{\phi}|^2\oint\frac{dl}{\sqrt{1-\lambda B}}-(\tau+1)\oint|\phi|^2\frac{dl}{B}\end{aligned}\tag{A.75}$$

and continuing to rearrange gives

$$\frac{\omega_{*e}}{\omega^2}=\frac{\frac{(\tau+1)}{2}\sum_{\text{wells}}\int_{\frac{1}{B_{max}}}^{\frac{1}{B_{min}}} d\lambda|\overline{\phi}|^2\oint\frac{dl}{\sqrt{1-\lambda B}}-(\tau+1)\oint|\phi|^2\frac{dl}{B}}{\frac{3}{4}\left(1+\eta_e+\frac{1+\eta_i}{\tau}\right)\sum_{\text{wells}}\int_{\frac{1}{B_{max}}}^{\frac{1}{B_{min}}} d\lambda F_e\overline{G(\lambda)}|\overline{\phi}|^2\oint\frac{dl}{\sqrt{1-\lambda B}}}\tag{A.76}$$

Finally, inverting this expression gives a form of the ω proxy:

$$\boxed{\frac{\omega^2}{\omega_{*e}}=\frac{\frac{3}{4}\left(1+\eta_e+\frac{1+\eta_i}{\tau}\right)\sum_{\text{wells}}\int_{\frac{1}{B_{max}}}^{\frac{1}{B_{min}}} d\lambda F_e\overline{G(\lambda)}|\overline{\phi}|^2\oint\frac{dl}{\sqrt{1-\lambda B}}}{\frac{(\tau+1)}{2}\sum_{\text{wells}}\int_{\frac{1}{B_{max}}}^{\frac{1}{B_{min}}} d\lambda|\overline{\phi}|^2\oint\frac{dl}{\sqrt{1-\lambda B}}-(\tau+1)\oint|\phi|^2\frac{dl}{B}}}\tag{A.77}$$

With the ω proxy for trapped ions and trapped electrons now fully derived, it is necessary to verify that this expression is compatible for use with the variational principle before being utilised further. If Eqn. A.77 does not possess the required variational property that this principle relies on, then the relation cannot be used to predict the mode frequency. The investigation of this requirement can be found in Appendix B.1. In that discussion, it is shown that Eqn. A.77 does indeed satisfy the variational principle requirement.

Appendix B

Verifying Validity of using the Variational Principle

In this appendix, we present the explicit compatibility of the variational principle with our two proxies for the mode frequency ω of the TEM instability. As before, our first ω proxy considered only the effect of trapped ions and trapped electrons in the system. Our second ω proxy considered the effect of passing ions and trapped electrons in the system. Both proxies have proved to be applicable for use with the variational principle, but only the latter proxy was utilised for the main results of this project.

B.1 Variational Principle for Trapped Particles Only

In this section, we investigate to see if the ω proxy for trapped ions and trapped electrons is applicable for use with the variational principle approach.

We will restate that ω proxy here:

$$\boxed{\frac{\omega^2}{\omega_{*e}} = \frac{\frac{3}{4}\left(1+\eta_e+\frac{1+\eta_i}{\tau}\right)\sum_{\text{wells}}\int_{\frac{1}{B_{max}}}^{\frac{1}{B_{min}}} d\lambda F_e \overline{G(\lambda)}|\overline{J_0\phi}|^2 \oint \frac{dl}{\sqrt{1-\lambda B}}}{\frac{(\tau+1)}{2}\sum_{\text{wells}}\int_{\frac{1}{B_{max}}}^{\frac{1}{B_{min}}} d\lambda |\overline{J_0\phi}|^2 \oint \frac{dl}{\sqrt{1-\lambda B}} - (\tau+1)\oint |\phi|^2 \frac{dl}{B}}} \tag{B.1}$$

As will become clear soon, we will use Eqn. A.74 as our starting point, instead of the fully derived

relation in Eqn. B.1:

$$\begin{aligned}&(\tau+1)\oint|\phi|^2\frac{dl}{B}=\\&\frac{(\tau+1)}{2}\sum_{\text{wells}}\int_{\frac{1}{B_{max}}}^{\frac{1}{B_{min}}}d\lambda|\overline{\phi}|^2\oint\frac{dl}{\sqrt{1-\lambda B}}-\\&\frac{\omega_{*e}}{\omega^2}\frac{3}{4}\left(1+\eta_e+\frac{1+\eta_i}{\tau}\right)\sum_{\text{wells}}\int_{\frac{1}{B_{max}}}^{\frac{1}{B_{min}}}d\lambda F_e\overline{G(\lambda)}|\overline{\phi}|^2\oint\frac{dl}{\sqrt{1-\lambda B}}\end{aligned}\tag{B.2}$$

This can be rearranged slightly to give

$$\begin{aligned}&\omega^2(\tau+1)\left[\oint|\phi|^2\frac{dl}{B}-\frac{1}{2}\sum_{\text{wells}}\int_{\frac{1}{B_{max}}}^{\frac{1}{B_{min}}}d\lambda|\overline{\phi}|^2\oint\frac{dl}{\sqrt{1-\lambda B}}\right]=\\&-\omega_{*e}\frac{3}{4}\left(1+\eta_e+\frac{1+\eta_i}{\tau}\right)\sum_{\text{wells}}\int_{\frac{1}{B_{max}}}^{\frac{1}{B_{min}}}d\lambda F_e\overline{G(\lambda)}|\overline{\phi}|^2\oint\frac{dl}{\sqrt{1-\lambda B}}\end{aligned}\tag{B.3}$$

Let's now vary this expression with respect to ϕ:

$$\begin{aligned}&2\omega\delta\omega(\tau+1)\left[\oint|\phi|^2\frac{dl}{B}-\frac{1}{2}\sum_{\text{wells}}\int_{\frac{1}{B_{max}}}^{\frac{1}{B_{min}}}d\lambda|\overline{\phi}|^2\oint\frac{dl}{\sqrt{1-\lambda B}}\right]+\\&\omega^2(\tau+1)\left[\oint 2\phi\delta\phi\frac{dl}{B}-\frac{1}{2}\sum_{\text{wells}}\int_{\frac{1}{B_{max}}}^{\frac{1}{B_{min}}}d\lambda 2\overline{\phi}\delta\overline{\phi}\oint\frac{dl}{\sqrt{1-\lambda B}}\right]=\\&-\omega_{*e}\frac{3}{4}\left(1+\eta_e+\frac{1+\eta_i}{\tau}\right)\sum_{\text{wells}}\int_{\frac{1}{B_{max}}}^{\frac{1}{B_{min}}}d\lambda F_e\overline{G(\lambda)}2\overline{\phi}\delta\overline{\phi}\oint\frac{dl}{\sqrt{1-\lambda B}}\end{aligned}\tag{B.4}$$

We can now make use of the bounce-averaging procedure as follows:

$$\delta\overline{\phi}=\frac{1}{\oint\frac{dl}{\sqrt{1-\lambda B}}}\oint\delta\phi\frac{dl}{\sqrt{1-\lambda B}}\tag{B.5}$$

which can be inserted into our main expression to give

$$\begin{aligned}&2\omega\delta\omega(\tau+1)\left[\oint|\phi|^2\frac{dl}{B}-\frac{1}{2}\sum_{\text{wells}}\int_{\frac{1}{B_{max}}}^{\frac{1}{B_{min}}}d\lambda|\overline{\phi}|^2\oint\frac{dl}{\sqrt{1-\lambda B}}\right]+\\&\omega^2(\tau+1)\left[\oint 2\phi\delta\phi\frac{dl}{B}-\frac{1}{2}\sum_{\text{wells}}\int_{\frac{1}{B_{max}}}^{\frac{1}{B_{min}}}d\lambda 2\overline{\phi}\left(\frac{1}{\oint\frac{dl}{\sqrt{1-\lambda B}}}\oint\delta\phi\frac{dl}{\sqrt{1-\lambda B}}\right)\oint\frac{dl}{\sqrt{1-\lambda B}}\right]=\\&-\omega_{*e}\frac{3}{4}\left(1+\eta_e+\frac{1+\eta_i}{\tau}\right)\sum_{\text{wells}}\int_{\frac{1}{B_{max}}}^{\frac{1}{B_{min}}}d\lambda F_e\overline{G(\lambda)}2\overline{\phi}\left(\frac{1}{\oint\frac{dl}{\sqrt{1-\lambda B}}}\oint\delta\phi\frac{dl}{\sqrt{1-\lambda B}}\right)\oint\frac{dl}{\sqrt{1-\lambda B}}\end{aligned}\tag{B.6}$$

This can be simplified as follows:

$$\begin{aligned}&2\omega\delta\omega(\tau+1)\left[\oint|\phi|^2\frac{dl}{B}-\frac{1}{2}\sum_{\text{wells}}\int_{\frac{1}{B_{max}}}^{\frac{1}{B_{min}}}d\lambda|\overline{\phi}|^2\oint\frac{dl}{\sqrt{1-\lambda B}}\right]+\\&\omega^2(\tau+1)\left[\oint 2\phi\delta\phi\frac{dl}{B}-\frac{1}{2}\sum_{\text{wells}}\int_{\frac{1}{B_{max}}}^{\frac{1}{B_{min}}}d\lambda 2\overline{\phi}a\oint\delta\phi\frac{dl}{\sqrt{1-\lambda B}}\right]=\\&-\omega_{*e}\frac{3}{4}\left(1+\eta_e+\frac{1+\eta_i}{\tau}\right)\sum_{\text{wells}}\int_{\frac{1}{B_{max}}}^{\frac{1}{B_{min}}}d\lambda F_e\overline{G(\lambda)}2\overline{\phi}\oint\delta\phi\frac{dl}{\sqrt{1-\lambda B}}\end{aligned}\tag{B.7}$$

Rearranging then gives

$$\begin{aligned}
&2\omega\delta\omega\,(\tau+1)\left[\oint|\phi|^2\frac{dl}{B}-\frac{1}{2}\sum_{\text{wells}}\int_{\frac{1}{B_{max}}}^{\frac{1}{B_{min}}}d\lambda|\overline{\phi}|^2\oint\frac{dl}{\sqrt{1-\lambda B}}\right]=\\
&-2\omega^2\,(\tau+1)\left[\oint\phi\delta\phi\frac{dl}{B}-\frac{1}{2}\sum_{\text{wells}}\int_{\frac{1}{B_{max}}}^{\frac{1}{B_{min}}}d\lambda\overline{\phi}\oint\delta\phi\frac{dl}{\sqrt{1-\lambda B}}\right]\\
&-2\omega_{*e}\frac{3}{4}\left(1+\eta_e+\frac{1+\eta_i}{\tau}\right)\sum_{\text{wells}}\int_{\frac{1}{B_{max}}}^{\frac{1}{B_{min}}}d\lambda F_e\overline{G(\lambda)}\overline{\phi}\oint\delta\phi\frac{dl}{\sqrt{1-\lambda B}}
\end{aligned}\tag{B.8}$$

Dividing across by 2 and rearranging further now gives

$$\begin{aligned}
&\omega\delta\omega\,(\tau+1)\left[\oint|\phi|^2\frac{dl}{B}-\frac{1}{2}\sum_{\text{wells}}\int_{\frac{1}{B_{max}}}^{\frac{1}{B_{min}}}d\lambda|\overline{\phi}|^2\oint\frac{dl}{\sqrt{1-\lambda B}}\right]=\\
&-\oint\delta\phi\frac{dl}{B}\left\{\omega^2\,(\tau+1)\left[\phi-\frac{1}{2}B\int_{\frac{1}{B_{max}}}^{\frac{1}{B_{min}}}\frac{d\lambda}{\sqrt{1-\lambda B}}\overline{\phi}\right]\right.\\
&\left.+\omega_{*e}\frac{3}{4}\left(1+\eta_e+\frac{1+\eta_i}{\tau}\right)B\int_{\frac{1}{B_{max}}}^{\frac{1}{B_{min}}}\frac{d\lambda}{\sqrt{1-\lambda B}}F_e\overline{G(\lambda)}\overline{\phi}\right\}
\end{aligned}\tag{B.9}$$

Before seeing how the variational principle will work here, let's go back to Eqn. B.2:

$$\begin{aligned}
&(\tau+1)\oint|\phi|^2\frac{dl}{B}=\\
&\frac{(\tau+1)}{2}\sum_{\text{wells}}\int_{\frac{1}{B_{max}}}^{\frac{1}{B_{min}}}d\lambda|\overline{\phi}|^2\oint\frac{dl}{\sqrt{1-\lambda B}}-\\
&\frac{\omega_{*e}}{\omega^2}\frac{3}{4}\left(1+\eta_e+\frac{1+\eta_i}{\tau}\right)\sum_{\text{wells}}\int_{\frac{1}{B_{max}}}^{\frac{1}{B_{min}}}d\lambda F_e\overline{G(\lambda)}|\overline{\phi}|^2\oint\frac{dl}{\sqrt{1-\lambda B}}
\end{aligned}\tag{B.10}$$

We need to remind ourselves of the following subtlety that arose when calculating the ω proxy given by Eqn. B.1. Near the beginning of that derivation, we multiplied our QN equation by $\frac{\phi^*}{B}$ and integrated over the entire field line. As stated at this point in that derivation, this was carried out to mirror a similar procedure which will be encountered in Chapter **??**. However, in order to truly see the variational property of this ω proxy, we need to **undo** this step of multiplying across by $\frac{\phi^*}{B}$ and integrating over the entire field line. This will provide us with an integral equation expression which is essential to understanding how the variational principle can be applied.

Thus, we will now undo this step in Eqn. B.10, which can be seen by rewriting the following relevant terms:

$$\oint|\phi|^2\frac{dl}{B}=\oint\phi\cdot\phi^*\frac{dl}{B}=\oint\phi^*\frac{dl}{B}(\phi)\tag{B.11}$$

and

$$\begin{aligned}
\sum_{\text{wells}}\int_{\frac{1}{B_{max}}}^{\frac{1}{B_{min}}}d\lambda\underbrace{|\overline{\phi}|^2}_{\overline{\phi}\cdot\overline{\phi^*}}\oint\frac{dl}{\sqrt{1-\lambda B}}&=\sum_{\text{wells}}\int_{\frac{1}{B_{max}}}^{\frac{1}{B_{min}}}d\lambda\overline{\phi}\oint\phi^*\frac{dl}{\sqrt{1-\lambda B}}\\
&=\oint\phi^*\frac{dl}{B}\left(B\int_{\frac{1}{B_{max}}}^{\frac{1}{B_{min}}}\frac{d\lambda}{\sqrt{1-\lambda B}}\overline{\phi}\right)
\end{aligned}\tag{B.12}$$

where in Eqn. B.12, we used

$$\overline{\phi^*} = \frac{1}{\oint \frac{dl}{\sqrt{1-\lambda B}}} \oint \phi^* \frac{dl}{\sqrt{1-\lambda B}} \implies \overline{\phi^*} \oint \frac{dl}{\sqrt{1-\lambda B}} = \oint \phi^* \frac{dl}{\sqrt{1-\lambda B}} \tag{B.13}$$

and also, for trapped particles we have

$$\int_{-\infty}^{\infty} \equiv \sum_{wells} \oint \tag{B.14}$$

These changes can be implemented to Eqn. B.10, giving

$$\begin{aligned} &\oint \phi^* \frac{dl}{B} \left[(\tau+1)\, \phi \right] = \\ &\oint \phi^* \frac{dl}{B} \left[\frac{(\tau+1)}{2} B \int_{\frac{1}{B_{max}}}^{\frac{1}{B_{min}}} \frac{d\lambda}{\sqrt{1-\lambda B}} \overline{\phi} \right] - \\ &\oint \phi^* \frac{dl}{B} \left[\frac{\omega_{*e}}{\omega^2} \frac{3}{4} \left(1 + \eta_e + \frac{1+\eta_i}{\tau} \right) B \int_{\frac{1}{B_{max}}}^{\frac{1}{B_{min}}} \frac{d\lambda}{\sqrt{1-\lambda B}} F_e \overline{G(\lambda)} \overline{\phi} \right] \end{aligned} \tag{B.15}$$

And so, if we now **undo this step** of multiplying across by $\frac{\phi^*}{B}$ and integrating over the entire field line, we are left with the following integral equation:

$$\begin{aligned} &(\tau+1)\, \phi = \\ &\frac{(\tau+1)}{2} B \int_{\frac{1}{B_{max}}}^{\frac{1}{B_{min}}} \frac{d\lambda}{\sqrt{1-\lambda B}} \overline{\phi} - \\ &\frac{\omega_{*e}}{\omega^2} \frac{3}{4} \left(1 + \eta_e + \frac{1+\eta_i}{\tau} \right) B \int_{\frac{1}{B_{max}}}^{\frac{1}{B_{min}}} \frac{d\lambda}{\sqrt{1-\lambda B}} F_e \overline{G(\lambda)} \overline{\phi} \end{aligned} \tag{B.16}$$

Multiplying across by ω^2 and rearranging then gives us

$$\begin{aligned} &\omega^2 (\tau+1) \left[\phi - \frac{1}{2} B \int_{\frac{1}{B_{max}}}^{\frac{1}{B_{min}}} \frac{d\lambda}{\sqrt{1-\lambda B}} \overline{\phi} \right] = \\ &- \omega_{*e} \frac{3}{4} \left(1 + \eta_e + \frac{1+\eta_i}{\tau} \right) B \int_{\frac{1}{B_{max}}}^{\frac{1}{B_{min}}} \frac{d\lambda}{\sqrt{1-\lambda B}} F_e \overline{G(\lambda)} \overline{\phi} \end{aligned} \tag{B.17}$$

which implies

$$\begin{aligned} &\omega^2 (\tau+1) \left[\phi - \frac{1}{2} B \int_{\frac{1}{B_{max}}}^{\frac{1}{B_{min}}} \frac{d\lambda}{\sqrt{1-\lambda B}} \overline{\phi} \right] + \\ &\omega_{*e} \frac{3}{4} \left(1 + \eta_e + \frac{1+\eta_i}{\tau} \right) B \int_{\frac{1}{B_{max}}}^{\frac{1}{B_{min}}} \frac{d\lambda}{\sqrt{1-\lambda B}} F_e \overline{G(\lambda)} \overline{\phi} = 0 \end{aligned} \tag{B.18}$$

Now reminding ourselves of our main derivation here, Eqn. B.9 reads as:

$$\begin{aligned} &\omega \delta\omega (\tau+1) \left[\oint |\phi|^2 \frac{dl}{B} - \frac{1}{2} \sum_{\text{wells}} \int_{\frac{1}{B_{max}}}^{\frac{1}{B_{min}}} d\lambda |\overline{\phi}|^2 \oint \frac{dl}{\sqrt{1-\lambda B}} \right] \\ &= - \oint \delta\phi \frac{dl}{B} \left\{ \omega^2 (\tau+1) \left[\phi - \frac{1}{2} B \int_{\frac{1}{B_{max}}}^{\frac{1}{B_{min}}} \frac{d\lambda}{\sqrt{1-\lambda B}} \overline{\phi} \right] + \right. \\ &\left. \omega_{*e} \frac{3}{4} \left(1 + \eta_e + \frac{1+\eta_i}{\tau} \right) B \int_{\frac{1}{B_{max}}}^{\frac{1}{B_{min}}} \frac{d\lambda}{\sqrt{1-\lambda B}} F_e \overline{G(\lambda)} \overline{\phi} \right\} \end{aligned} \tag{B.19}$$

As we can see, the term in curly brackets here is exactly Eqn. B.18. And so, we immediately obtain $\delta\omega = 0$ when our integral equation is fulfilled. In other words, the mode structure ϕ that solves the integral equation (Eqn. B.16 or Eqn. B.17) also minimises the expression for ω.

B.2 Variational Principle for Passing Ions and Trapped Electrons

In this section, we investigate to see if the ω proxy for passing ions and trapped electrons is applicable for use with the variational principle approach. Instead of using our fully expanded final result Eqn. 5.101 for this proxy, let's use the more concise version Eqn. 5.98:

$$\begin{aligned}
&\frac{\omega^2}{\omega_{*e}^2}\left\{\int_{-\infty}^{\infty}\left(1+\tau\left[1-Z_1\right]\right)|\phi|^2\frac{dl}{B}-\int_{\frac{1}{B_{max}}}^{\frac{1}{B_{min}}}\int_{-\infty}^{\infty}\frac{dl}{\sqrt{1-\lambda B}}\frac{1}{2}|\overline{\phi}|^2 d\lambda\right\}= \\
&\frac{\omega}{\omega_{*e}}\left\{\int_{-\infty}^{\infty}\left[Z_1\left(1-\eta_i+\frac{\hat{\omega}_{di}\tau}{2\omega_{*e}}\right)+Z_2\left(\eta_i+\frac{\hat{\omega}_{di}\tau}{2\omega_{*e}}\right)\right]|\phi|^2\frac{dl}{B}+\right. \\
&\left.\int_{\frac{1}{B_{max}}}^{\frac{1}{B_{min}}}\int_{-\infty}^{\infty}\frac{dl}{\sqrt{1-\lambda B}}\frac{1}{2}\left(-1+\frac{3}{2}\frac{F_e\overline{G(\lambda)}}{\omega_{*e}}\right)|\overline{\phi}|^2 d\lambda\right\} \\
&+\int_{-\infty}^{\infty}\left[\left(\frac{\hat{\omega}_{di}}{2\omega_{*e}}\right)\times\left(Z_1+Z_2+Z_3\right)\right]|\phi|^2\frac{dl}{B} \\
&+\int_{\frac{1}{B_{max}}}^{\frac{1}{B_{min}}}\int_{-\infty}^{\infty}\frac{dl}{\sqrt{1-\lambda B}}\frac{1}{2}\left(-\frac{3}{2}\frac{F_e\overline{G(\lambda)}}{\omega_{*e}}\left[1+\eta_e\right]\right)|\overline{\phi}|^2 d\lambda
\end{aligned} \tag{B.20}$$

Varying this expression with respect to ϕ gives

$$\begin{aligned}
&\frac{2\omega}{\omega_{*e}^2}\delta\omega\left\{\int_{-\infty}^{\infty}\left(1+\tau\left[1-Z_1\right]\right)|\phi|^2\frac{dl}{B}-\int_{\frac{1}{B_{max}}}^{\frac{1}{B_{min}}}\int_{-\infty}^{\infty}\frac{dl}{\sqrt{1-\lambda B}}\frac{1}{2}|\overline{\phi}|^2d\lambda\right\}+\\
&\frac{\omega^2}{\omega_{*e}^2}\left\{\int_{-\infty}^{\infty}\left(1+\tau\left[1-Z_1\right]\right)2\phi\delta\phi\frac{dl}{B}-\int_{\frac{1}{B_{max}}}^{\frac{1}{B_{min}}}\int_{-\infty}^{\infty}\frac{dl}{\sqrt{1-\lambda B}}\frac{1}{2}2\overline{\phi}\delta\overline{\phi}d\lambda\right\}=\\
&\frac{\delta\omega}{\omega_{*e}}\left\{\int_{-\infty}^{\infty}\left[Z_1\left(1-\eta_i+\frac{\hat{\omega}_{di}\tau}{2\omega_{*e}}\right)+Z_2\left(\eta_i+\frac{\hat{\omega}_{di}\tau}{2\omega_{*e}}\right)\right]|\phi|^2\frac{dl}{B}\right.\\
&\left.+\int_{\frac{1}{B_{max}}}^{\frac{1}{B_{min}}}\int_{-\infty}^{\infty}\frac{dl}{\sqrt{1-\lambda B}}\frac{1}{2}\left(-1+\frac{3}{2}\frac{F_e\overline{G(\lambda)}}{\omega_{*e}}\right)|\overline{\phi}|^2d\lambda\right\}+\\
&\frac{\omega}{\omega_{*e}}\left\{\int_{-\infty}^{\infty}\left[Z_1\left(1-\eta_i+\frac{\hat{\omega}_{di}\tau}{2\omega_{*e}}\right)+Z_2\left(\eta_i+\frac{\hat{\omega}_{di}\tau}{2\omega_{*e}}\right)\right]2\phi\delta\phi\frac{dl}{B}\right.\\
&\left.+\int_{\frac{1}{B_{max}}}^{\frac{1}{B_{min}}}\int_{-\infty}^{\infty}\frac{dl}{\sqrt{1-\lambda B}}\frac{1}{2}\left(-1+\frac{3}{2}\frac{F_e\overline{G(\lambda)}}{\omega_{*e}}\right)2\overline{\phi}\delta\overline{\phi}d\lambda\right\}\\
&+\int_{-\infty}^{\infty}\left[\left(\frac{\hat{\omega}_{di}}{2\omega_{*e}}\right)\times\left(Z_1+Z_2+Z_3\right)\right]2\phi\delta\phi\frac{dl}{B}\\
&+\int_{\frac{1}{B_{max}}}^{\frac{1}{B_{min}}}\int_{-\infty}^{\infty}\frac{dl}{\sqrt{1-\lambda B}}\frac{1}{2}\left(-\frac{3}{2}\frac{F_e\overline{G(\lambda)}}{\omega_{*e}}\left[1+\eta_e\right]\right)2\overline{\phi}\delta\overline{\phi}d\lambda
\end{aligned}\tag{B.21}$$

which can be quickly tidied up by implementing the following:

$$\delta\overline{\phi}=\frac{1}{\oint\frac{dl}{\sqrt{1-\lambda B}}}\oint\delta\phi\frac{dl}{\sqrt{1-\lambda B}}\implies\oint\frac{dl}{\sqrt{1-\lambda B}}\delta\overline{\phi}=\oint\delta\phi\frac{dl}{\sqrt{1-\lambda B}}\tag{B.22}$$

giving us

$$\begin{aligned}
&\frac{2\omega}{\omega_{*e}^2}\delta\omega\left\{\int_{-\infty}^{\infty}\left(1+\tau\left[1-Z_1\right]\right)|\phi|^2\frac{dl}{B}-\int_{\frac{1}{B_{max}}}^{\frac{1}{B_{min}}}\int_{-\infty}^{\infty}\frac{dl}{\sqrt{1-\lambda B}}\frac{1}{2}|\overline{\phi}|^2d\lambda\right\}+\\
&\frac{\omega^2}{\omega_{*e}^2}\left\{\int_{-\infty}^{\infty}\left(1+\tau\left[1-Z_1\right]\right)2\phi\delta\phi\frac{dl}{B}-\int_{\frac{1}{B_{max}}}^{\frac{1}{B_{min}}}\int_{-\infty}^{\infty}\frac{dl}{\sqrt{1-\lambda B}}\frac{1}{2}2\overline{\phi}\delta\phi d\lambda\right\}=\\
&\frac{\delta\omega}{\omega_{*e}}\left\{\int_{-\infty}^{\infty}\left[Z_1\left(1-\eta_i+\frac{\hat{\omega}_{di}\tau}{2\omega_{*e}}\right)+Z_2\left(\eta_i+\frac{\hat{\omega}_{di}\tau}{2\omega_{*e}}\right)\right]|\phi|^2\frac{dl}{B}+\right.\\
&\left.\int_{\frac{1}{B_{max}}}^{\frac{1}{B_{min}}}\int_{-\infty}^{\infty}\frac{dl}{\sqrt{1-\lambda B}}\frac{1}{2}\left(-1+\frac{3}{2}\frac{F_e\overline{G(\lambda)}}{\omega_{*e}}\right)|\overline{\phi}|^2d\lambda\right\}+\\
&\frac{\omega}{\omega_{*e}}\left\{\int_{-\infty}^{\infty}\left[Z_1\left(1-\eta_i+\frac{\hat{\omega}_{di}\tau}{2\omega_{*e}}\right)+Z_2\left(\eta_i+\frac{\hat{\omega}_{di}\tau}{2\omega_{*e}}\right)\right]2\phi\delta\phi\frac{dl}{B}+\right.\\
&\left.\int_{\frac{1}{B_{max}}}^{\frac{1}{B_{min}}}\int_{-\infty}^{\infty}\frac{dl}{\sqrt{1-\lambda B}}\frac{1}{2}\left(-1+\frac{3}{2}\frac{F_e\overline{G(\lambda)}}{\omega_{*e}}\right)2\overline{\phi}\delta\phi d\lambda\right\}+\\
&\int_{-\infty}^{\infty}\left[\left(\frac{\hat{\omega}_{di}}{2\omega_{*e}}\right)\times\left(Z_1+Z_2+Z_3\right)\right]2\phi\delta\phi\frac{dl}{B}+\\
&\int_{\frac{1}{B_{max}}}^{\frac{1}{B_{min}}}\int_{-\infty}^{\infty}\frac{dl}{\sqrt{1-\lambda B}}\frac{1}{2}\left(-\frac{3}{2}\frac{F_e\overline{G(\lambda)}}{\omega_{*e}}\left[1+\eta_e\right]\right)2\overline{\phi}\delta\phi d\lambda
\end{aligned}\tag{B.23}$$

where once again, we will note that $\int_{-\infty}^{\infty} \equiv \sum_{\text{wells}} \oint$ for the trapped particles.

Let's rearrange slightly to give

$$\begin{aligned}
&\delta\omega\left[\frac{2\omega}{\omega_{*e}^2}\left\{\int_{-\infty}^{\infty}\left(1+\tau\left[1-Z_1\right]\right)|\phi|^2\frac{dl}{B}-\int_{\frac{1}{B_{max}}}^{\frac{1}{B_{min}}}\int_{-\infty}^{\infty}\frac{dl}{\sqrt{1-\lambda B}}\frac{1}{2}|\overline{\phi}|^2 d\lambda\right\}-\right.\\
&\frac{1}{\omega_{*e}}\left\{\int_{-\infty}^{\infty}\left[Z_1\left(1-\eta_i+\frac{\hat{\omega}_{di}\tau}{2\omega_{*e}}\right)+Z_2\left(\eta_i+\frac{\hat{\omega}_{di}\tau}{2\omega_{*e}}\right)\right]|\phi|^2\frac{dl}{B}+\right.\\
&\left.\left.\int_{\frac{1}{B_{max}}}^{\frac{1}{B_{min}}}\int_{-\infty}^{\infty}\frac{dl}{\sqrt{1-\lambda B}}\frac{1}{2}\left(-1+\frac{3}{2}\frac{F_e\overline{G(\lambda)}}{\omega_{*e}}\right)|\overline{\phi}|^2 d\lambda\right\}\right]=\\
&-2\int_{-\infty}^{\infty}\delta\phi\frac{dl}{B}\left[\frac{\omega^2}{\omega_{*e}^2}\left\{\left(1+\tau\left[1-Z_1\right]\right)\phi-\frac{1}{2}B\int_{\frac{1}{B_{max}}}^{\frac{1}{B_{min}}}\frac{d\lambda}{\sqrt{1-\lambda B}}\overline{\phi}\right\}-\right.\\
&\frac{\omega}{\omega_{*e}}\left\{\left[Z_1\left(1-\eta_i+\frac{\hat{\omega}_{di}\tau}{2\omega_{*e}}\right)+Z_2\left(\eta_i+\frac{\hat{\omega}_{di}\tau}{2\omega_{*e}}\right)\right]\phi+\frac{1}{2}B\int_{\frac{1}{B_{max}}}^{\frac{1}{B_{min}}}\frac{d\lambda}{\sqrt{1-\lambda B}}\left(-1+\frac{3}{2}\frac{F_e\overline{G(\lambda)}}{\omega_{*e}}\right)\overline{\phi}\right\}\\
&\left.-\left[\left(\frac{\hat{\omega}_{di}}{2\omega_{*e}}\right)\times\left(Z_1+Z_2+Z_3\right)\right]\phi+\frac{1}{2}B\int_{\frac{1}{B_{max}}}^{\frac{1}{B_{min}}}\frac{d\lambda}{\sqrt{1-\lambda B}}\left(\frac{3}{2}\frac{F_e\overline{G(\lambda)}}{\omega_{*e}}\left[1+\eta_e\right]\right)\overline{\phi}\right]
\end{aligned} \tag{B.24}$$

The significance of this large expression in square brackets will become clear in a moment. Let's now take a gentle detour to tie up this argument. Reminding ourselves of our integral equation, given by Eqn. 5.76, and the expansion of $[Y_0+Y_1]$, given by Eqn. 5.87:

$$\begin{aligned}
&\implies \left[1+\tau\left(1-\left[Y_0+Y_1\right]\right)\right]\phi = B\int_{\frac{1}{B_{max}}}^{\frac{1}{B_{min}}}U_e(\omega,\lambda)\overline{\phi}\frac{d\lambda}{\sqrt{1-\lambda B}}\\
&\implies \left[Y_0+Y_1\right]=\\
&\quad Z_1+\frac{1}{\omega}\left[Z_1\left(-\omega_{*i}+\omega_{*i}\eta_i+\frac{\hat{\omega}_{di}}{2}\right)+Z_2\left(-\omega_{*i}\eta_i+\frac{\hat{\omega}_{di}}{2}\right)\right]+\\
&\quad\frac{1}{\omega^2}\left[\left(-\frac{\omega_{*i}\hat{\omega}_{di}}{2}\right)\times\left(Z_1+Z_2+Z_3\right)\right]
\end{aligned} \tag{B.25}$$

where

$$\begin{aligned}
U_e(\omega,l) &= \frac{1}{2}\left[1-\frac{\omega_{*e}}{\omega}+\frac{3}{2}\frac{F_e\overline{G(\lambda)}}{\omega}\left(1-\frac{\omega_{*e}}{\omega}\left[1+\eta_e\right]\right)\right]\\
&= \frac{1}{2}\left[1-\frac{\omega_{*e}}{\omega}+\frac{3}{2}\frac{F_e\overline{G(\lambda)}}{\omega}-\frac{3}{2}\frac{F_e\overline{G(\lambda)}\omega_{*e}}{\omega^2}\left[1+\eta_e\right]\right]
\end{aligned} \tag{B.26}$$

We can expand our first expression in Eqn. B.25 here as follows:

$$\begin{aligned}
&(1+\tau)\phi-\tau Z_1\phi-\tau\frac{1}{\omega}\left[Z_1\left(-\omega_{*i}+\omega_{*i}\eta_i+\frac{\hat{\omega}_{di}}{2}\right)+Z_2\left(-\omega_{*i}\eta_i+\frac{\hat{\omega}_{di}}{2}\right)\right]\phi-\\
&\tau\frac{1}{\omega^2}\left[\left(-\frac{\omega_{*i}\hat{\omega}_{di}}{2}\right)\times\left(Z_1+Z_2+Z_3\right)\right]\phi=\\
&B\int_{\frac{1}{B_{max}}}^{\frac{1}{B_{min}}}\frac{1}{2}\left[1-\frac{\omega_{*e}}{\omega}+\frac{3}{2}\frac{F_e\overline{G(\lambda)}}{\omega}-\frac{3}{2}\frac{F_e\overline{G(\lambda)}\omega_{*e}}{\omega^2}\left[1+\eta_e\right]\right]\overline{\phi}\frac{d\lambda}{\sqrt{1-\lambda B}}
\end{aligned} \tag{B.27}$$

Again, we will now make use of the fact that:

$$\begin{aligned}\omega_{*i} &= -\frac{\omega_{*e}}{\tau} \\ \tau &= \frac{T_e}{T_i}\end{aligned} \tag{B.28}$$

which gives

$$\begin{aligned}&(1+\tau)\phi - \tau Z_1\phi - \tau\frac{1}{\omega}\left[Z_1\left(\frac{\omega_{*e}}{\tau} - \frac{\omega_{*e}}{\tau}\eta_i + \frac{\hat{\omega}_{di}}{2}\right) + Z_2\left(\frac{\omega_{*e}}{\tau}\eta_i + \frac{\hat{\omega}_{di}}{2}\right)\right]\phi - \\ &\tau\frac{1}{\omega^2}\left[\left(\frac{\omega_{*e}\hat{\omega}_{di}}{2\tau}\right)\times(Z_1+Z_2+Z_3)\right]\phi = \\ &B\int_{\frac{1}{B_{max}}}^{\frac{1}{B_{min}}}\frac{1}{2}\left[1 - \frac{\omega_{*e}}{\omega} + \frac{3}{2}\frac{F_e\overline{G(\lambda)}}{\omega} - \frac{3}{2}\frac{F_e\overline{G(\lambda)}\omega_{*e}}{\omega^2}\left[1+\eta_e\right]\right]\overline{\phi}\frac{d\lambda}{\sqrt{1-\lambda B}}\end{aligned} \tag{B.29}$$

and tidying more gives

$$\begin{aligned}&(1+\tau[1-Z_1])\phi - \frac{1}{\omega}\left[Z_1\left(\omega_{*e} - \omega_{*e}\eta_i + \frac{\hat{\omega}_{di}\tau}{2}\right) + Z_2\left(\omega_{*e}\eta_i + \frac{\hat{\omega}_{di}\tau}{2}\right)\right]\phi - \\ &\frac{1}{\omega^2}\left[\left(\frac{\omega_{*e}\hat{\omega}_{di}}{2}\right)\times(Z_1+Z_2+Z_3)\right]\phi = \\ &B\int_{\frac{1}{B_{max}}}^{\frac{1}{B_{min}}}\frac{1}{2}\left[1 - \frac{\omega_{*e}}{\omega} + \frac{3}{2}\frac{F_e\overline{G(\lambda)}}{\omega} - \frac{3}{2}\frac{F_e\overline{G(\lambda)}\omega_{*e}}{\omega^2}\left[1+\eta_e\right]\right]\overline{\phi}\frac{d\lambda}{\sqrt{1-\lambda B}}\end{aligned} \tag{B.30}$$

and more

$$\begin{aligned}&(1+\tau[1-Z_1])\phi - \frac{\omega_{*e}}{\omega}\left[Z_1\left(1 - \eta_i + \frac{\hat{\omega}_{di}\tau}{2\omega_{*e}}\right) + Z_2\left(\eta_i + \frac{\hat{\omega}_{di}\tau}{2\omega_{*e}}\right)\right]\phi - \\ &\frac{\omega_{*e}^2}{\omega^2}\left[\left(\frac{\hat{\omega}_{di}}{2\omega_{*e}}\right)\times(Z_1+Z_2+Z_3)\right]\phi = \\ &B\int_{\frac{1}{B_{max}}}^{\frac{1}{B_{min}}}\frac{1}{2}\left[1 - \frac{\omega_{*e}}{\omega} + \frac{3}{2}\frac{F_e\overline{G(\lambda)}}{\omega} - \frac{3}{2}\frac{F_e\overline{G(\lambda)}\omega_{*e}}{\omega^2}\left[1+\eta_e\right]\right]\overline{\phi}\frac{d\lambda}{\sqrt{1-\lambda B}}\end{aligned} \tag{B.31}$$

Now multiplying across by $\frac{\omega^2}{\omega_{*e}^2}$ gives

$$\begin{aligned}&\frac{\omega^2}{\omega_{*e}^2}\left(1+\tau[1-Z_1]\right)\phi - \frac{\omega}{\omega_{*e}}\left[Z_1\left(1 - \eta_i + \frac{\hat{\omega}_{di}\tau}{2\omega_{*e}}\right) + Z_2\left(\eta_i + \frac{\hat{\omega}_{di}\tau}{2\omega_{*e}}\right)\right]\phi - \\ &\left[\left(\frac{\hat{\omega}_{di}}{2\omega_{*e}}\right)\times(Z_1+Z_2+Z_3)\right]\phi = \\ &B\int_{\frac{1}{B_{max}}}^{\frac{1}{B_{min}}}\frac{1}{2}\left[\frac{\omega^2}{\omega_{*e}^2} - \frac{\omega}{\omega_{*e}} + \frac{\omega}{\omega_{*e}^2}\frac{3}{2}F_e\overline{G(\lambda)} - \frac{3}{2}\frac{F_e\overline{G(\lambda)}}{\omega_{*e}}\left[1+\eta_e\right]\right]\overline{\phi}\frac{d\lambda}{\sqrt{1-\lambda B}}\end{aligned} \tag{B.32}$$

Focusing on the right-hand side here, it can be fully expanded out to give

$$\begin{aligned}&B\int_{\frac{1}{B_{max}}}^{\frac{1}{B_{min}}}\frac{1}{2}\left[\frac{\omega^2}{\omega_{*e}^2} - \frac{\omega}{\omega_{*e}} + \frac{\omega}{\omega_{*e}^2}\frac{3}{2}F_e\overline{G(\lambda)} - \frac{3}{2}\frac{F_e\overline{G(\lambda)}}{\omega_{*e}}\left[1+\eta_e\right]\right]\overline{\phi}\frac{d\lambda}{\sqrt{1-\lambda B}} = \\ &\frac{\omega^2}{\omega_{*e}^2}\frac{1}{2}B\int_{\frac{1}{B_{max}}}^{\frac{1}{B_{min}}}\overline{\phi}\frac{d\lambda}{\sqrt{1-\lambda B}} + \frac{\omega}{\omega_{*e}}\frac{1}{2}B\int_{\frac{1}{B_{max}}}^{\frac{1}{B_{min}}}\overline{\phi}\left(-1 + \frac{3}{2}\frac{F_e\overline{G(\lambda)}}{\omega_{*e}}\right)\frac{d\lambda}{\sqrt{1-\lambda B}} \\ &-\frac{1}{2}B\int_{\frac{1}{B_{max}}}^{\frac{1}{B_{min}}}\overline{\phi}\left(\frac{3}{2}\frac{F_e\overline{G(\lambda)}}{\omega_{*e}}\left[1+\eta_e\right]\right)\frac{d\lambda}{\sqrt{1-\lambda B}}\end{aligned} \tag{B.33}$$

Reinserting this expanded right-hand side into Eqn. B.32 now gives

$$\begin{aligned}
&\frac{\omega^2}{\omega_{*e}^2}\left(1+\tau[1-Z_1]\right)\phi-\frac{\omega}{\omega_{*e}}\left[Z_1\left(1-\eta_i+\frac{\hat{\omega}_{di}\tau}{2\omega_{*e}}\right)+Z_2\left(\eta_i+\frac{\hat{\omega}_{di}\tau}{2\omega_{*e}}\right)\right]\phi- \\
&\left[\left(\frac{\hat{\omega}_{di}}{2\omega_{*e}}\right)\times(Z_1+Z_2+Z_3)\right]\phi= \\
&\frac{\omega^2}{\omega_{*e}^2}\frac{1}{2}B\int_{\frac{1}{B_{max}}}^{\frac{1}{B_{min}}}\overline{\phi}\frac{d\lambda}{\sqrt{1-\lambda B}}+\frac{\omega}{\omega_{*e}}\frac{1}{2}B\int_{\frac{1}{B_{max}}}^{\frac{1}{B_{min}}}\overline{\phi}\left(-1+\frac{3}{2}\frac{F_e\overline{G(\lambda)}}{\omega_{*e}}\right)\frac{d\lambda}{\sqrt{1-\lambda B}} \\
&-\frac{1}{2}B\int_{\frac{1}{B_{max}}}^{\frac{1}{B_{min}}}\overline{\phi}\left(\frac{3}{2}\frac{F_e\overline{G(\lambda)}}{\omega_{*e}}\left[1+\eta_e\right]\right)\frac{d\lambda}{\sqrt{1-\lambda B}}
\end{aligned} \tag{B.34}$$

Now let's bring everything over to the left-hand side and group together similar terms

$$\begin{aligned}
&\frac{\omega^2}{\omega_{*e}^2}\left\{\left(1+\tau[1-Z_1]\right)\phi-\frac{1}{2}B\int_{\frac{1}{B_{max}}}^{\frac{1}{B_{min}}}\overline{\phi}\frac{d\lambda}{\sqrt{1-\lambda B}}\right\}- \\
&\frac{\omega}{\omega_{*e}}\left\{\left[Z_1\left(1-\eta_i+\frac{\hat{\omega}_{di}\tau}{2\omega_{*e}}\right)+Z_2\left(\eta_i+\frac{\hat{\omega}_{di}\tau}{2\omega_{*e}}\right)\right]\phi+\frac{1}{2}B\int_{\frac{1}{B_{max}}}^{\frac{1}{B_{min}}}\frac{d\lambda}{\sqrt{1-\lambda B}}\left(-1+\frac{3}{2}\frac{F_e\overline{G(\lambda)}}{\omega_{*e}}\right)\overline{\phi}\right\} \\
&-\left[\left(\frac{\hat{\omega}_{di}}{2\omega_{*e}}\right)\times(Z_1+Z_2+Z_3)\right]\phi+\frac{1}{2}B\int_{\frac{1}{B_{max}}}^{\frac{1}{B_{min}}}\frac{d\lambda}{\sqrt{1-\lambda B}}\left(\frac{3}{2}\frac{F_e\overline{G(\lambda)}}{\omega_{*e}}\left[1+\eta_e\right]\right)\overline{\phi}=0
\end{aligned} \tag{B.35}$$

Now let's remind ourselves of the long expression in square brackets from Eqn. B.24:

$$\begin{aligned}
&\left[\frac{\omega^2}{\omega_{*e}^2}\left\{\left(1+\tau\left[1-Z_1\right]\right)\phi-\frac{1}{2}B\int_{\frac{1}{B_{max}}}^{\frac{1}{B_{min}}}\frac{d\lambda}{\sqrt{1-\lambda B}}\overline{\phi}\right\}-\right. \\
&\frac{\omega}{\omega_{*e}}\left\{\left[Z_1\left(1-\eta_i+\frac{\hat{\omega}_{di}\tau}{2\omega_{*e}}\right)+Z_2\left(\eta_i+\frac{\hat{\omega}_{di}\tau}{2\omega_{*e}}\right)\right]\phi+\frac{1}{2}B\int_{\frac{1}{B_{max}}}^{\frac{1}{B_{min}}}\frac{d\lambda}{\sqrt{1-\lambda B}}\left(-1+\frac{3}{2}\frac{F_e\overline{G(\lambda)}}{\omega_{*e}}\right)\overline{\phi}\right\} \\
&\left.-\left[\left(\frac{\hat{\omega}_{di}}{2\omega_{*e}}\right)\times(Z_1+Z_2+Z_3)\right]\phi+\frac{1}{2}B\int_{\frac{1}{B_{max}}}^{\frac{1}{B_{min}}}\frac{d\lambda}{\sqrt{1-\lambda B}}\left(\frac{3}{2}\frac{F_e\overline{G(\lambda)}}{\omega_{*e}}\left[1+\eta_e\right]\right)\overline{\phi}\right]
\end{aligned} \tag{B.36}$$

We can now clearly see that Eqn. B.35 and Eqn. B.36 match. Thus, to obtain $\delta\omega=0$ in Eqn. B.24, our original integral equation given by Eqn. 5.76 (and again in Eqn. B.25) must be fulfilled. In other words, the solution ϕ to the integral equation (Eqn. 5.76 and Eqn. B.25) also minimises the expression for ω. This explicitly shows the variational property possessed by the ω proxy for passing ions and trapped electrons.

Bibliography

[1] Jeffrey P Freidberg. *Plasma physics and fusion energy*. Cambridge university press, 2008.

[2] Daniel Told. *Gyrokinetic microturbulence in transport barriers*. PhD thesis, Universität Ulm, 2012.

[3] Georges Audi, Olivier Bersillon, Jean Blachot, and Aaldert Hendrik Wapstra. The nubase evaluation of nuclear and decay properties. *Nuclear Physics A*, 624:1–124, 2003.

[4] John Wesson and David J Campbell. *Tokamaks*, volume 149. Oxford university press, 2011.

[5] John D Lawson. Some criteria for a power producing thermonuclear reactor. *Proceedings of the physical society. Section B*, 70(1):6, 1957.

[6] F Winterberg. Case institute of technology plasma research program. Technical report, Technical Report, 1963.

[7] Stefanie Braun. *Effect of impurities on kinetic transport processes in fusion plasmas*. PhD thesis, 2010.

[8] B Coppi and W Sadowski. Proceedings of the finite beta theory workshop.[proceedings of the finite beta theory workshop]. Technical report, Department of Energy, Washington, DC (USA). Office of Fusion Energy, 1977.

[9] Per Helander. Theory of plasma confinement in non-axisymmetric magnetic fields. *Reports on Progress in Physics*, 77(8):087001, 2014.

[10] T Klinger, T Andreeva, S Bozhenkov, C Brandt, R Burhenn, B Buttenschön, G Fuchert, B Geiger, O Grulke, HP Laqua, et al. Overview of first wendelstein 7-x high-performance operation. *Nuclear Fusion*, 59(11):112004, 2019.

[11] GD Conway. Turbulence measurements in fusion plasmas. *Plasma Physics and Controlled Fusion*, 50(12):124026, 2008.

[12] Josefine Henriette Elise Proll. *Trapped-particle instabilities in quasi-isodynamic stellarators*. PhD thesis, 2014.

[13] Xavier Garbet. Introduction to turbulent transport in fusion plasmas. *Comptes Rendus Physique*, 7(6):573–583, 2006.

[14] HE Mynick, N Pomphrey, and P Xanthopoulos. Optimizing stellarators for turbulent transport. *Physical review letters*, 105(9):095004, 2010.

[15] JC Adam, WM Tang, and PH Rutherford. Destabilization of the trapped-electron mode by magnetic curvature drift resonances. *The Physics of Fluids*, 19(4):561–566, 1976.

[16] JW Connor, RJ Hastie, and P Helander. Stability of the trapped electron mode in steep density and temperature gradients. *Plasma physics and controlled fusion*, 48(6):885, 2006.

[17] Josefine Henriette Elise Proll, Per Helander, John William Connor, and GG Plunk. Resilience of quasi-isodynamic stellarators against trapped-particle instabilities. *Physical Review Letters*, 108(24):245002, 2012.

[18] Per Helander, Josefine Henriette Elise Proll, and Gabriel Galad Plunk. Collisionless microinstabilities in stellarators. i. analytical theory of trapped-particle modes. *Physics of Plasmas*, 20(12):122505, 2013.

[19] Josefine Henriette Elise Proll, Pavlos Xanthopoulos, and Per Helander. Collisionless microinstabilities in stellarators. ii. numerical simulations. *Physics of Plasmas*, 20(12):122506, 2013.

[20] JHE Proll, HE Mynick, P Xanthopoulos, SA Lazerson, and BJ Faber. Tem turbulence optimisation in stellarators. *Plasma Physics and Controlled Fusion*, 58(1):014006, 2015.

[21] JHE Proll, P Xanthopoulos, P Helander, GG Plunk, BJ Faber, T Görler, HM Smith, and MJ Pueschel. Suppression of turbulence by trapped electrons in optimised stellarators. *arXiv preprint arXiv:2002.10484*, 2020.

[22] B Coppi, MN Rosenbluth, and RZ Sagdeev. Instabilities due to temperature gradients in complex magnetic field configurations. *The Physics of Fluids*, 10(3):582–587, 1967.

[23] Ft Romanelli. Ion temperature-gradient-driven modes and anomalous ion transport in tokamaks. *Physics of Fluids B: Plasma Physics*, 1(5):1018–1025, 1989.

[24] Steven C Cowley, RM Kulsrud, and R Sudan. Considerations of ion-temperature-gradient-driven turbulence. *Physics of Fluids B: Plasma Physics*, 3(10):2767–2782, 1991.

[25] Michael Alan Beer. *Gyrofluid models of turbulent transport in tokamaks*. PhD thesis, Princeton University, 1995.

[26] Michael Alan Beer and Gregory Wayne Hammett. Toroidal gyrofluid equations for simulations of tokamak turbulence. *Physics of Plasmas*, 3(11):4046–4064, 1996.

[27] A Zocco, P Xanthopoulos, H Doerk, JW Connor, and P Helander. Threshold for the destabilisation of the ion-temperature-gradient mode in magnetically confined toroidal plasmas. *Journal of Plasma Physics*, 84(1), 2018.

[28] A Zocco, GG Plunk, P Xanthopoulos, and P Helander. Geometric stabilization of the electrostatic ion-temperature-gradient driven instability. i. nearly axisymmetric systems. *Physics of Plasmas*, 23(8):082516, 2016.

[29] A Zocco, GG Plunk, and P Xanthopoulos. Geometric stabilization of the electrostatic ion-temperature-gradient driven instability. ii. non-axisymmetric systems. *Physics of Plasmas*, 27(2):022507, 2020.

[30] Robert J Goldston and Paul Harding Rutherford. *Introduction to plasma physics*. CRC Press, 1995.

[31] P Xanthopoulos, HE Mynick, P Helander, Yu Turkin, GG Plunk, F Jenko, T Görler, D Told, T Bird, and JHE Proll. Controlling turbulence in present and future stellarators. *Physical review letters*, 113(15):155001, 2014.

[32] P Xanthopoulos, GG Plunk, A Zocco, and P Helander. Intrinsic turbulence stabilization in a stellarator. *Physical Review X*, 6(2):021033, 2016.

[33] HE Mynick, AH Boozer, and LP Ku. Improving confinement in quasi-axisymmetric stellarators. *Physics of plasmas*, 13(6):064505, 2006.

[34] HE Mynick, P Xanthopoulos, and AH Boozer. Geometry dependence of stellarator turbulence. *Physics of Plasmas*, 16(11):110702, 2009.

[35] PW Terry. Suppression of turbulence and transport by sheared flow. *Reviews of Modern Physics*, 72(1):109, 2000.

[36] HE Mynick, N Pomphrey, and P Xanthopoulos. Reducing turbulent transport in toroidal configurations via shaping. *Physics of Plasmas*, 18(5):056101, 2011.

[37] Robert S Cohen, Lyman Spitzer Jr, and Paul McR Routly. The electrical conductivity of an ionized gas. *Physical Review*, 80(2):230, 1950.

[38] John A Krommes. The gyrokinetic description of microturbulence in magnetized plasmas. *Annual review of fluid mechanics*, 44:175–201, 2012.

[39] Xavier Garbet, Yasuhiro Idomura, L Villard, and TH Watanabe. Gyrokinetic simulations of turbulent transport. *Nuclear Fusion*, 50(4):043002, 2010.

[40] JW Connor and RJ Hastie. Low frequency stability theory of axisymmetric toroidal plasma. i. general theory. *Plasma Physics*, 17(2):97, 1975.

[41] Thomas M Antonsen Jr and Barton Lane. Kinetic equations for low frequency instabilities in inhomogeneous plasmas. *The Physics of Fluids*, 23(6):1205–1214, 1980.

[42] Robert L Dewar and AH Glasser. Ballooning mode spectrum in general toroidal systems. *The Physics of fluids*, 26(10):3038–3052, 1983.

[43] Per Helander, CD Beidler, TM Bird, M Drevlak, Y Feng, R Hatzky, F Jenko, R Kleiber, JHE Proll, Yu Turkin, et al. Stellarator and tokamak plasmas: a comparison. *Plasma Physics and Controlled Fusion*, 54(12):124009, 2012.

[44] Paul Harding Rutherford and EA Frieman. Drift instabilities in general magnetic field configurations. *The Physics of Fluids*, 11(3):569–585, 1968.

[45] KV Roberts and JB Taylor. Gravitational resistive instability of an incompressible plasma in a sheared magnetic field. *The Physics of Fluids*, 8(2):315–322, 1965.

[46] JB Taylor. Plasma physics and controlled nuclear fusion research. In *Proc. 5th Int. Conf. Tokyo*, volume 1, page 161. IAEA, 1975.

[47] JW Connor, RJ Hastie, and JB Taylor. Shear, periodicity, and plasma ballooning modes. *Physical Review Letters*, 40(6):396, 1978.

[48] John William Connor, RJ Hastie, and John Bryan Taylor. High mode number stability of an axisymmetric toroidal plasma. *Proceedings of the Royal Society of London. A. Mathematical and Physical Sciences*, 365(1720):1–17, 1979.

[49] Jason Parisi. Ballooning transformation introduction. *https://jason-parisi.com/wp-content/uploads/2018/06/BallooningFormalismIntro.pdf*, 2018.

[50] P.T. Mulholland. Nuclear fusion in stellarators: Theory for technology report. *(Available upon request)*, 2020.

[51] Izrail Moiseevitch Gelfand, Richard A Silverman, et al. *Calculus of variations*. Courier Corporation, 2000.

[52] GG Plunk, JW Connor, and P Helander. Collisionless microinstabilities in stellarators. part 4. the ion-driven trapped-electron mode. *Journal of Plasma Physics*, 83(4), 2017.

[53] J Nührenberg, W Lotz, P Merkel, C Nührenberg, U Schwenn, E Strumberger, and T Hayashi. Overview on wendelstein 7-x theory. *Fusion Technology*, 27(3T):71–78, 1995.

[54] Abdulgader F Almagri, David T Anderson, F Simon B Anderson, Paul H Probert, J Leon Shohet, and Joseph N Talmadge. A helically symmetric stellarator (hsx). *IEEE Transactions on Plasma Science*, 27(1):114–115, 1999.

[55] B. J. Faber, M. J. Pueschel, P. W. Terry, C. C. Hegna, and J. E. Roman. Stellarator microinstabilities and turbulence at low magnetic shear. *Journal of Plasma Physics*, 84(5):905840503, 2018.

[56] P Xanthopoulos and F Jenko. Gyrokinetic analysis of linear microinstabilities for the stellarator wendelstein 7-x. *Physics of plasmas*, 14(4):042501, 2007.